

REPORT DOCUMENTATION PAGEForm Approved
OMB No. 0704-0188

Public reporting burden for this collection of information is estimated to average 1 hour per response, including the time for reviewing instructions, searching existing data sources, gathering and maintaining the data needed, and completing and reviewing this collection of information. Send comments regarding this burden estimate or any other aspect of this collection of information, including suggestions for reducing this burden to Department of Defense, Washington Headquarters Services, Directorate for Information Operations and Reports (0704-0188), 1215 Jefferson Davis Highway, Suite 1204, Arlington, VA 22202-4302. Respondents should be aware that notwithstanding any other provision of law, no person shall be subject to any penalty for failing to comply with a collection of information if it does not display a currently valid OMB control number. **PLEASE DO NOT RETURN YOUR FORM TO THE ABOVE ADDRESS.**

1. REPORT DATE (DD-MM-YYYY) 03-17-10		2. REPORT TYPE Final		3. DATES COVERED (From - To) 2/4/2009-12/31/2009	
4. TITLE AND SUBTITLE The Thirteenth International Conference on Defects- Imaging and Physics in Semiconductors (DRIP XIII)				5a. CONTRACT NUMBER	
				5b. GRANT NUMBER N00014-09-1-0624	
				5c. PROGRAM ELEMENT NUMBER	
6. AUTHOR(S) The Minerals, Metals & Materials Society				5d. PROJECT NUMBER	
				5e. TASK NUMBER	
				5f. WORK UNIT NUMBER	
7. PERFORMING ORGANIZATION NAME(S) AND ADDRESS(ES) The Minerals, Metals and Materials Society, Inc. 184 Thorn Hill Road Warrendale, PA 15086				8. PERFORMING ORGANIZATION REPORT NUMBER	
9. SPONSORING / MONITORING AGENCY NAME(S) AND ADDRESS(ES) Office of Naval Research 875 North Randolph Street Arlington, VA 22203-1995				10. SPONSOR/MONITOR'S ACRONYM(S) ONR	
				11. SPONSOR/MONITOR'S REPORT NUMBER(S)	
12. DISTRIBUTION / AVAILABILITY STATEMENT Approved for Publication Release					
13. SUPPLEMENTARY NOTES Semiconductor, defect recognition					
14. ABSTRACT The Thirteenth International Conference on Defects-Recognition, Imaging and Physics in Semiconductors (DRIP XIII) was a conference on the physics of semiconductors with special emphasis on defects. It covered application aspects as well as fundamental questions regarding the physics of defects. The conference took place September 13-17, 2009, at the Olgebay Conference Center and Resort, Wheeling, West Virginia.					
15. SUBJECT TERMS					
16. SECURITY CLASSIFICATION OF:			17. LIMITATION OF ABSTRACT U	18. NUMBER OF PAGES 2	19a. NAME OF RESPONSIBLE PERSON Marleen Schrader
a. REPORT U	b. ABSTRACT U	c. THIS PAGE U			19b. TELEPHONE NUMBER (include area code) 724-814-3178

20100623234

The Thirteenth International Conference on Defects-Recognition, Imaging and Physics in Semiconductors (DRIP XIII) was a conference on the physics of semiconductors with special emphasis on defects. It covered application aspects as well as fundamental questions regarding the physics of defects. The conference took place September 13-17, 2009, at the Olgebay Conference Center and Resort, Wheeling, West Virginia.

Main areas of interest were:

- The physics of active defects in elemental and compound semiconductors
- Experimental ways to get information on defects by means of imaging and spectroscopy
- The effects of imperfections on properties of bulk semiconductors, epitaxial layers, and interfaces
- The qualification and reliability of electronic or optoelectronic devices in relation to defects or imperfections in the materials assessed by imaging or mapping

DRIP is particularly suited for anyone working, having specific needs, or simply being interested in getting up-to-date with the fields of visualization, imaging, identification, and understanding defects which affect the operation of semiconductor devices. The trend towards features with smaller and smaller critical dimensions, with all the associated physics involved (such as novel quantum effects...) is one of the important driving forces behind this. At the other end of the scale, there is a need for development of tools capable of producing images over whole wafers of increasing size. The field covered by DRIP can be described as "going from the extremely small to the extremely large", a concept now familiar to any other area of science. The main challenge of this conference was to link defect images, transport/optical properties, and performances of the actual devices.

The purpose of DRIP is to provide a forum for scientists/engineers from universities, government institutes, and industry to meet and discuss methods used for the recognition and imaging of defects in semiconductor materials and semiconductor devices. The conference included investigations of defects in the raw materials (wafer level), process-induced defects, and defects that appear during operation (burn-in, aging tests,...) The primary concern of DRIP was the methodology and the physics of measurement procedures, together with specific developments in instrumentation.

Authors presenting their work at the DRIP XIII Conference were encouraged to submit a manuscript for consideration for publication in the conference proceedings. Proceedings will appear as a special issue of the Journal of Electronic Materials (*JEM*), the estimated publishing date is June 2010.

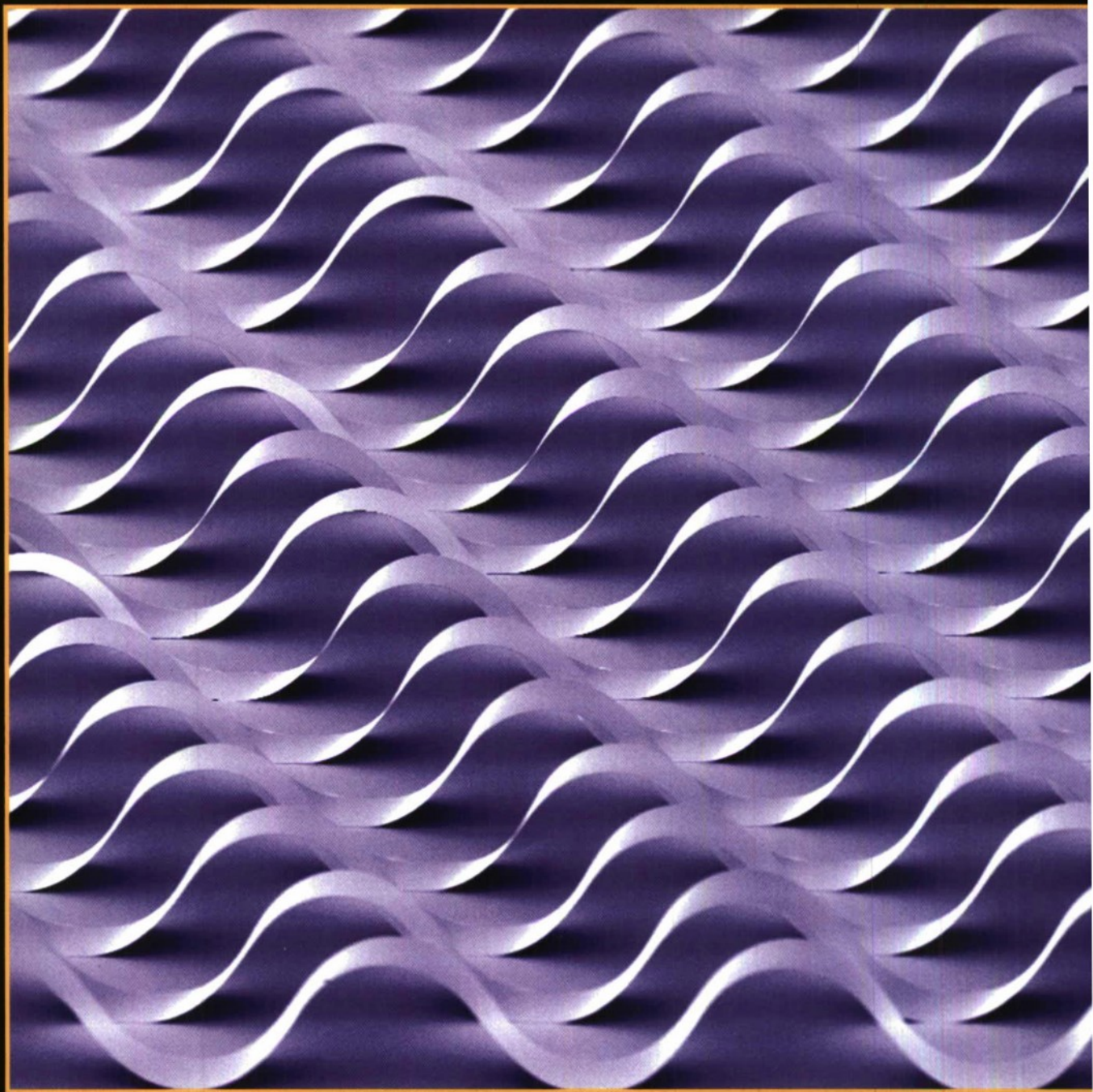
JOM

**TMS 2011
ANNUAL
MEETING:
Symposia
Listing Inside**

JUNE 2010

A publication of The Minerals, Metals & Materials Society

www.tms.org/jom.html



SURFACE ENGINEERING

- Thin Films and Coatings
- Corrosion
- Multiscale Phenomena in Surfaces



Your Professional Partner for Career Advancement

Introducing 4 more reasons to renew your TMS membership in 2010!

- 1.** E-mentoring – Designed to assist colleagues at every career level with professional development.
- 2.** Consultant Resources – A compendium of tools, templates, and tips to ensure your business infrastructure is sound.
- 3.** TMS On Reserve – An anthology of 12 newly-digitalized, library archive volumes of foundational documents and select conference proceedings from the American Institute of Mining, Metallurgy, and Petroleum Engineers (AIME).
- 4.** OneMine – A collaborative effort among societies to create a single global resource for mining and minerals research. TMS members receive a special subscription rate.

Enjoy these and the numerous other TMS benefits you've come to value by accessing our sleek, redesigned Members Only Web pages.

Discover how all of your TMS professional essentials are just a click away!

<http://members.tms.org>

LEARN • NETWORK • ADVANCE

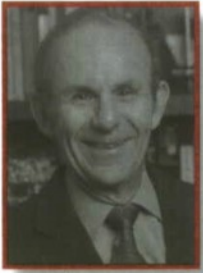
www.tms.org



Member News

Updates on friends and colleagues in the materials community

David N. Seidman to Deliver 2011 Institute of Metals Lecture




David N. Seidman, Walter P. Murphy Professor of Materials Science and Engineering, Northwestern University, and 1997 TMS Fellow, has been selected to give the Institute of Metals Lecture and receive the Robert Franklin Mehl Award for outstanding scientific leadership at the TMS 2011 Annual Meeting in San Diego, February 27–March 3. Seidman's lecture is tentatively titled, "The Ubiquitous Interfacial Free Energy in Materials Science."

Seidman is considered one of the world's leading authorities in atom-probe tomography, and is credited for

designing the first atom-probe field ion microscope (FIM) with full computer control for high mass resolution, setting the standard for future instrument design. His research has led to major advances in the understanding of the behavior of vacancies and self-interstitial atoms in metals, particularly in connection with radiation damage and dislocation interactions. The founding director of the Northwestern University Center for Atom-Probe Tomography, Seidman has pioneered the use of FIM and three-dimensional atom probe tomography to study interfaces, segregation, and precipitation in metals and metal alloy systems on an atomic scale. He has earned numerous awards, honors, and professional recognitions, most recently being named a 2010 Fellow by the Materials Research Society.

Iver Anderson Recognized for Excellence in Technology Transfer



Iver Anderson, senior metallurgist at the U.S. Department of Energy's (DOE) Ames Laboratory and chair of the TMS Materials and Society Committee, recently received a national Excellence in Technology Transfer Award from the Federal Laboratory Consortium (FLC). He was recognized for his work on a lead-free solder alloy with wide industry acceptance. A durable, environmentally safe alternative to traditional

tin-lead solder for joining electronic micro-circuits and electrical contacts, the alloy is Ames Laboratory's most successful technology to date. It is currently licensed to more than 50 companies worldwide and has generated more than \$20 million in royalties.

The FLC is a nationwide network of more than 700 major federal laboratories and centers, as well as their parent departments and agencies. Anderson's was one of five DOE technology transfer successes selected in 2010 for the national FLC award from across all federal government research laboratories.


TMS Announces JEM Best Paper Award

To recognize outstanding scientific or engineering contributions in the electronic materials field, TMS has established the *Journal of Electronic Materials* (JEM) Best Paper Award. Papers published in JEM between July 2009 and June 2010 are eligible for the inaugural award. The winner can accept the award at either the TMS 2011

Annual Meeting or the 2011 Electronic Materials Conference.

To nominate a paper, send a copy of the article, along with the nominator's letter of endorsement and recommendation to Deborah Price, TMS student affairs & awards administrator, at price@tms.org. The deadline for nominations is October 15, 2010.

DIRAN APELIAN EARNS BRITISH FOUNDRY MEDAL



Diran Apelian, 2008 TMS president, has been awarded the 2010 British Foundry Medal for his paper, "Pressure Assisted Processes for High Integrity Aluminum Castings." Parts 1 and 2 of the paper were published in the October and November 2009 issues of *Foundry Trade Journal*. He will receive the medal at the Institute of Cast Metals Engineers awards ceremony in October. Apelian is the Howmet Professor of Mechanical Engineering and director of the Metal Processing Institute at Worcester Polytechnic Institute.

IN MEMORY OF BILL BUCKMAN

Raymond W. "Bill" Buckman, a TMS member since 1961, passed away at his home in Pleasant Hills, Pennsylvania, on April 16, 2010. He was 79.

A metallurgical engineer specializing in advanced materials, Buckman was employed by Westinghouse Electric Corporation for more than 30 years, where he managed a variety of projects and initiatives. His work ranged from developing wind turbine, fuel cell, and solar technology, to inventing and characterizing refractory metal alloys, to helping design a nuclear-powered rocket for propelling spacecraft to the outer planets. He eventually held about two dozen patents and authored more than 100 technical papers.

Upon leaving Westinghouse, Buckman formed a consulting company, Refractory Metals Technologies. In recent years, he developed a new metal alloy for stents used in heart surgery, prompting him to remark to friends and colleagues, "My career has gone from outer space to inner space." The library at the former Westinghouse Astronuclear Laboratory in Large, Pennsylvania, where Buckman spent most of his career at Westinghouse, has been named in his honor.



TMS Member Profiles

Meet a Member: Jay Narayan Named 2011 *Acta Materialia* Gold Medal Recipient

By Lynne Robinson

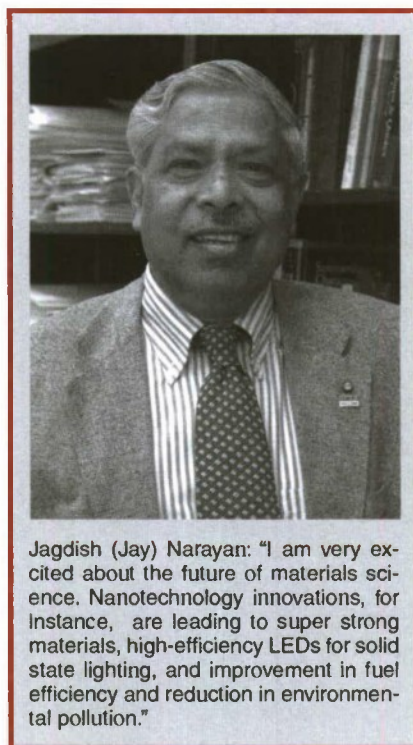
"Materials science is an enabling science which connects us to technology and society. This aspect of materials fascinated me the most," recalls Jagdish (Jay) Narayan of his decision to switch from mechanical engineering to materials as an undergraduate student at the Indian Institute of Technology Kanpur. "I realized that major changes in our civilization have occurred as a result of materials revolutions—from stone, to iron, to bronze, to semiconductor. Everything is made out of materials—and the bottleneck for every new technology is often materials."

Breaking those bottlenecks has been Narayan's professional mission for nearly 40 years, with his many contributions most recently being recognized with the 2011 *Acta Materialia* Gold Medal and Prize. *Acta Materialia*, Inc. represents 33 professional societies worldwide in publishing two highly regarded international journals. Awarded by the *Acta Materialia* Board of Governors, the Gold Medal honors one exceptional person annually for lifetime achievements in materials science research and leadership. "I am deeply honored and profoundly humbled by this international recognition by my peers," said Narayan, the North Carolina State University John C.C. Fan Family Distinguished Chair Professor, Materials Science and Engineering. "This is also very special because I published my first three papers in *Acta* journals."

The path leading Narayan to many of his discoveries began at the University of California, Berkeley, where he earned both his master's degree and Ph.D. in just two years. "I realized very quickly that the property of every solid state material is controlled largely by defects and interfaces, grain boundaries included," he said. "Using laser-based processing methods, it was possible for me to control the micro-

structure and create exciting materials with unique properties and profound implications for solid state devices."

Since then, Narayan has made fundamental contributions in defects, diffusion, ion implantation, and laser-solid interactions. These, in turn, have led to



Jagdish (Jay) Narayan: "I am very excited about the future of materials science. Nanotechnology innovations, for instance, are leading to super strong materials, high-efficiency LEDs for solid state lighting, and improvement in fuel efficiency and reduction in environmental pollution."

major materials breakthroughs, including laser-diffused solar cells, formation of supersaturated semiconductor alloys, metal-ceramic nanocomposites, novel ZnMgO and ZnCdO alloys, ZnO-based transparent conductors, and new nanostructured materials with improved properties. Narayan said he is particularly pleased with his invention of domain matching epitaxy, which is based on matching integral multiples of lattice planes across the film-substrate interface to address epitaxial growth across the misfit scale on polar, as well as nonpolar, substrates. He also cites his development of quantum-confined GaN-based NanoPocket LEDs as

another career highlight. "These stand to revolutionize next-generation solid state devices with integrated functionality," he said.

Mostly, looking back on his career, Narayan said he feels "very fortunate to have a large number of very talented graduate students, post docs, and collaborators worldwide."

A TMS Life Member and 1999 TMS Fellow, Narayan notes that, in his experience, few achievements come without first having to overcome any number of challenges. It's important, he cautions, that scientists and engineers just entering the field learn to take these in stride. "Sometimes, you have to stop pursuing certain research, no matter how exciting it is, because funding for it has ended," he said. "You have to spend a lot more time managing your research now—it leaves that much less time for innovative thinking and takes time away from your family and personal life, which is unhealthy and unsustainable. It is important to find a balance, have fun, and do some good for society through your research innovations."

Making an impact on society, whether improving health and healing through biomedical advances or addressing global energy and sustainability issues, is well within the grasp of any materials scientist and engineer, said Narayan, observing, "For every advanced technology, there is a materials problem which needs a solution."

Details on events and symposia celebrating this pinnacle achievement in Narayan's career will be announced at a later date.

Each month, *JOM* profiles a TMS member and his or her activities both in and out of the realm of materials science and engineering. To suggest a candidate for this feature, contact Maureen Byko, *JOM* editor, at mbyko@tms.org.

**THIN FILMS AND
COATINGS**

- 9:** Flexible Film Systems: Current Understanding and Future Prospects: Megan J. Cordill
- 15:** Applications of Porous Silicon Thin Films in Solar Cells and Biosensors: Priyanka Singh, Shailesh N. Sharma, and N.M. Ravindra
- 25:** Effects of Substrate Temperature and RF Power on the Formation of Aligned Nanorods in ZnO Thin Films: Sudhakar Shet, Kwang-Soon Ahn, Ravindra Nugehalli, Yanfa Yan, John Turner, and Mowafak Al-Jassim

CORROSION

- 31:** Corrosion as a Nanostructure Synthesis Strategy: M.P. Brady
- 32:** Materials "Alchemy": Shape-Preserving Chemical Transformation of Micro-to-Macroscopic 3-D Structures: Kenneth H. Sandhage
- 44:** Processing of Porous Carbon with Tunable Pore Structure by the Carbide-derived Carbon Method: Nadejda Popovska and Martina Kormann

- 50:** Structure/Processing Relationships in the Fabrication of Nanoporous Gold: F. Kertis, J. Snyder, Lata Govada, Sahir Khurshid, N. Chayen, and J. Erlebacher

- 57:** The Anodization of Aluminum for Nanotechnology Applications: Woo Lee

**MULTISCALE PHENOMENA
IN SURFACES**

- 64:** Surface Engineering for Amorphous-, Nanocrystalline-, and Bio-materials: Sandip P. Harimkar, Arvind Agarwal, Sudipta Seal, and Narendra B. Dahotre
- 65:** Spark Plasma Sintering for Multi-scale Surface Engineering of Materials: Mrinalini Mulukutla, Ashish Singh, and Sandip P. Harimkar
- 72:** Electrophoretic Deposition of Hyaluronic Acid and Composite Films for Biomedical Applications: R. Ma, Y. Li, and I. Zhitomirsky
- 76:** Laser Process Effects on Physical Texture and Wetting in Implantable Ti-Alloys: Sameer R. Paital, Wei He, Claus Daniel, and Narendra B. Dahotre

- 84:** Characteristics of Hemocompatible TiO₂ Nano-films Produced by the Sol-gel and Anodic Oxidation Techniques: C.E. Schvezov, M.A. Alterach, M.L. Vera, M.R. Rosenberger, and A.E. Ares
- 88:** Effect of Current Density on the Pulsed Co-electrodeposition of Nanocrystalline Nickel-copper Alloys: Mansi Agarwal, Vinod Kumar, S.R.K. Malladi, R. Balasubramaniam, and Kantesh Balani

FEATURE

- 7:** The Structural Materials Division: Adding Strength to TMS and Its Membership Since 1988: Eric M. Taleff

ALSO IN THIS ISSUE**insert: Member News**

- 2:** In the Final Analysis
- 3:** News & Update
- 93:** Meetings Calendar
- 94:** Materials Resource Center: Jobs, Consultants, Marketplace
- 96:** End Notes: "Multi-society Publication Underscores MSE Role in Securing Energy Solutions:" Lynne Robinson

About the Cover: Flexible electronic structures are being developed by researchers at Argonne National Laboratory and the University of Illinois at Urbana-Champaign. Shown are semiconductor ribbons with buckled profiles on polydimethylsiloxane surfaces that are functionalized for surface chemical bonding. These flexible structures could find applications as sensors and as electronic devices that can be integrated into artificial muscles or biological tissues. Read about flexible film systems in the article on page 9 by Megan J. Cordill. Photo courtesy of Argonne National Laboratory.

In the Final Analysis

"I like to compare the holiday season with the way a child listens to a favorite story. The pleasure is in the familiar way the story begins, the anticipation of familiar turns it takes, the familiar moments of suspense, and the familiar climax and ending."

— (Mr.) Fred Rogers

One of the joys of being a Pittsburgher is the tremendous civic pride that comes from having a brilliant pioneer of children's television as, quite literally, a resident of our neighborhood. If you never had the experience of viewing a telecast by Mr. Rogers of *Mr. Rogers' Neighborhood* fame, suffice to say he was a good guy who spoke to children for decades like they were all good guys and girls as well.

As a kid, I appreciated Mr. Rogers' imagination-provoking journeys into the land of make believe. As an adult, I appreciate all of the good work that he did to help shape two generations of young people with an uplifting, but never treacly, message. As a columnist, I appreciate that I can take Mr. Rogers' thoughtful reflection on the psychology of children and leverage it into an editorial. In this case, I find that if we substitute "TMS Annual Meeting" for "holiday season," we end up with the warp and woof of the society's conference-organization experience.

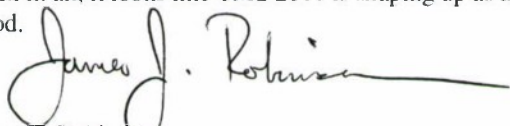
In terms of significance, the TMS Annual Meeting is the society's capstone event. It is the holiday season of all holiday seasons on the materials calendar from our perspective. Every day in some essential way, there is a cadre of volunteers and staff endeavoring to help the society prepare for it. They're all doing a great job.

Of all of the preparatory activities with which we busy ourselves, perhaps the most significant happened but a few days before the penning of this column. The editor even stopped the presses to work the breaking news into this issue's News & Update. What's the event? It is the finalization by the TMS Program Committee of what symposia will be presented at the TMS 2011 Annual Meeting. As you read, these symposia are opening for the submission of abstracts in the society's ProgramMaster website. If the still-distant TMS 2011 Annual Meeting is to be a success, it will be because of what happens from now to late July when the appeal for abstracts closes and the organization of thousands of presentations into sessions begins.

I'm already intrigued by several elements of the emergent programming plans. Accounting for my personal biases and in full recognition that everything at this point is subject to change, here's a quick peek at how the TMS 2011 neighborhood is taking shape:

- Seven programming tracks have been created to hold a record 72 (!) symposia: Aluminum and Magnesium; Advanced Characterization, Modeling, and Materials Performance; High-Performance Materials; Materials and Society (Energy and Sustainable Production); Materials Processing and Production; Nanoscale and Amorphous Materials; Professional Development.
- The Materials and Society Committee is looking to hold a plenary session to open the meeting with a cross-cutting program. A broad plenary session by the Light Metals Division is under discussion as well.
- Two honorary symposia are under development: The David Pope Honorary Symposium on Fundamentals of Deformation and Fracture of Advanced Metallic Materials, and Polycrystal Modeling with Experimental Integration: A Symposium Honoring Carlos Tome.
- It looks to be a big year in computational materials science and engineering, with nearly ten symposia that fit under that broad umbrella. One that I look forward to based on title alone: Massively Parallel Simulations of Materials Responses.
- I ask your indulgence as I give a shout out to my friend Jud Ready for busting a rhyme with his symposium *Geek Speak on the Hill*. Succinct and syncopated!

All in all, it looks like TMS 2011 is shaping up as five beautiful days in the neighborhood.



James J. Robinson
Publisher

JOM

184 Thorn Hill Road,
Warrendale, PA 15086, USA

Telephone: (724) 776-9000

Fax: (724) 776-3770

Web: www.tms.org/jom.html

E-Mail: jom@tms.org

PUBLISHER

James J. Robinson

JUNE ADVISORS:

Thin Films and Coatings

Thins Films and Interfaces Committee

Choong-un Kim, University of Texas at Arlington

Nancy L. Michael,

University of Texas at Arlington

Corrosion

Corrosion and Environmental Effects Committee

Michael P. Brady,

Oak Ridge National Laboratory

Multiscale Phenomena in Surfaces

Surface Engineering Committee

Sandip P. Harimkar, Oklahoma State University

Arvind Agarwal, Florida International University

Sudipta Seal, University of Central Florida

Narendra Dahotre, University of North Texas

EDITORIAL STAFF

Maureen Byko, Editor

Cheryl M. Geier, Senior Graphic Designer

Shirley A. Litzinger, Production Editor

Elizabeth Rossi, Web Developer

PARTNER RELATIONS AND ADVERTISING STAFF

Trudi Dunlap, Director

Colleen Leary, Sales Representative

JOM (ISSN 1047-4838) is published monthly by Springer Sciences & Business Media, LLC (Springer) 233 Spring St., New York, NY 10013 in cooperation with The Minerals, Metals & Materials Society (TMS).

DISCLAIMER: The opinions and statements expressed in JOM are those of the authors only and are not necessarily those of TMS or the editorial staff. No confirmations or endorsements are intended or implied.

SUBSCRIPTIONS, ORDERS, AND OTHER FULFILLMENT INQUIRIES: In the Americas, contact Journals Customer Service, P.O. Box 2485, Secaucus, NJ 07096, USA; telephone (800) 777-4643 (in North America) or (212) 460-1500 (outside North America); e-mail journals-ny@springer.com. Outside the Americas, contact Journals Customer Service, Springer Distribution Center, Haberstr. 7, 69126 Heidelberg, Germany; telephone 49-6221-345-4303; e-mail subscriptions@springer.com.

TMS MEMBERS: Access this and back issues of JOM on-line at no charge via members.tms.org

POSTMASTER: Send address changes to: JOM, Springer, 233 Spring Street, New York, NY 10013, USA. Periodicals postage paid at New York, NY, and additional mailing offices.

Symposia Announced for TMS 2011

Abstracts Now Being Accepted

Insights into enhancing established technologies to address new demands and challenges. Groundbreaking research on emerging fields and their implications for the future. A sharing of knowledge and expertise on computational methods and other tools and approaches to push materials science and engineering to a new level of development. These and many other learning and networking opportunities inform the initial symposia plan announced by the TMS Program Committee for the TMS 2011 Annual Meeting, February 27–March 3, in San Diego.

Within the broad theme of “Linking Science and Technology for Global Solutions,” the symposia will present the latest developments in materials science and engineering in six technical tracks: Aluminum and Magnesium;



Advanced Characterization, Modeling, and Materials Performance; High Performance Materials; Materials and Society; Materials Processing and Production; Nanoscale and Amorphous Materials. In addition, a new, nontechnical track, Professional Development, has been added for 2011. Abstracts are being accepted via ProgramMaster, accessed at the TMS 2011 home page, <http://www.tms.org/meetings/annual-11/AM11home.aspx>, until July 15, 2010.

To assist with determining the

symposium that would make the best fit for a particular abstract topic, a current listing of TMS 2011 symposia in alphabetical order, along with their organizers, follows. Additional information and descriptions of the symposia topics can be accessed in ProgramMaster. Symposia topics are subject to change, so please check back on the TMS 2011 website regularly for updated symposia information, as well as news and announcements of other TMS 2011 events.

TMS 2011 Symposia

2011 Functional and Structural Nanomaterials: Fabrication, Properties, Applications and Implications—Jiyoung Kim, University of Texas; David W. Stollberg, Georgia Tech Research Institute; Seong Jin Koh, University of Texas at Arlington; Nitin Chopra, The University of Alabama; Suveen Nigel Mathaudhu, U.S. Army Research Laboratory

2nd International Symposium on High-Temperature Metallurgical Processing—Jiann-Yang Hwang, Michigan Technological University; Jerome P. Downey, Montana Tech; Jaroslav Drellich, Michigan Technological University; Tao Jiang, Central South University; Mark Cooksey, Commonwealth Scientific and Industrial Research Organisation (CSIRO)

4th International Shape Casting Symposium—Murat Tiryakioglu, Robert Morris University; Paul Crepeau, General Motors Corporation; John Campbell, University of Birmingham

Advances in Mechanics of One-Dimensional Micro/Nano Materials—Reza Shahbazian-Yassar, Michigan Technologi-

cal University; Katerina Aifantis, Aristotle University of Thessaloniki; Seung Min J. Han, Stanford University

Advances in Science-Based Processing of Superalloys for Cost and Sustainment—Donna Ballard, U.S. Air Force; David Ulrich Furrer, Rolls-Royce; Paul D. Jablonski, U.S. Department of Energy; Christopher F. Woodward, Air Force Research Laboratory (AFRL); Jeff Simmons, AFRL

Alumina and Bauxite—James B. Metson, University of Auckland; Carlos Enrique Suarez, Hatch Associates Inc.

Aluminum Alloys: Fabrication, Characterization and Applications—Subodh K. Das, Phinix LLC; Zhengdong Long, Kaiser Aluminum; Tongguang Zhai, University of Kentucky

Aluminum Reduction Technology—Mohd Mahmood, Aluminium Bahrain; Abdulla Habib Ahmed, Aluminium Bahrain (Alba); Charles Mark Read, Bechtel Corporation

Aluminum Rolling—Kai F. Karhausen, Hydro Aluminium Deutschland GmbH

Approaches for Investigating Phase Transformations at the Atomic Scale—Neal D.

Evans, Oak Ridge National Laboratory; Francisca Caballero, Spanish National Research Center for Metallurgy (CENIM-CSIC); Chris Wolverton, Northwestern University; David Seidman, Northwestern University; Rajarshi Banerjee, University of North Texas

Battery Recycling—Gregory K. Krumdiek, Argonne National Laboratory

Biological Materials Science—Jamie J. Kruzic, Oregon State University; Nima Rahbar, University of Massachusetts, Dartmouth; Po-Yu Chen, University of California, San Diego; Candan Tamerler, University of Washington

Bridging Microstructure, Properties and Processing of Polymer Based Advanced Materials—Dongsheng Li, Pacific Northwest National Laboratory; Said Ahzi, Université Louis Pasteur; Moe Kahleel, Pacific Northwest National Laboratory

Bulk Metallic Glasses VIII—Gongyao Wang, University of Tennessee; Peter K. Liaw, University of Tennessee; Hahn Choo, University of Tennessee; Yanfei Gao, University of Tennessee

Carbon Dioxide and Other Greenhouse

Gas Reduction Metallurgy-2011—Neale R. Neelameggham, US Magnesium LLC; Ramana G. Reddy, The University of Alabama; Maria D. Salazar-Villalpando, National Energy Technology Laboratory; James A Yurko, 22Ti LLC; Malti Goel, INSA

Cast Shop for Aluminum Production—Geoffrey Alan Brooks, Swinburne University of Technology; John F. Grandfield, Grandfield Technology Pty. Ltd.

Challenges in Mechanical Performances of Materials in Next Generation Nuclear Power Plants—Faramarz Zarandi, CANMET-Materials Technology Laboratory

Characterization of Minerals, Metals, and Materials—Sergio Neves Monteiro, State University of Northern Rio de Janeiro—UENF

Chloride 2011: Practice and Theory of Chloride-Based Metallurgy—Dirk E. Verhulst, Consultant, Extractive Metallurgy; V.I. (Lucky) Lakshmanan, Process Research Ortech, Inc.

Coatings for Structural, Biological, and Electronic Applications II—Nuggehalli M. Ravindra, New Jersey Institute of Technology; Choong-Un Kim, University of Texas at Arlington; Naney L. Michael, University of Texas at Arlington; Gregory K. Krumdick, Argonne National Laboratory; Roger J. Narayan, University of North Carolina & North Carolina State University

Commonality of Phenomena in Composite Materials II—Meisha Shofner, Georgia Institute of Technology; Carl Boehlert, Michigan State University

Computational Plasticity—Remi Dingreville, Polytechnic Institute of New York University; Koen Janssens, Paul Scherrer Institute

Computational Thermodynamics and Kinetics—Raymundo Arroyave, Texas A&M University; James R. Morris, Oak Ridge National Laboratory; Mikko Haataja, Princeton University; Jeff Hoyt, McMaster University; Vidvuds Ozolins, University of California, Los Angeles; Xun-Li Wang, Oak Ridge National Laboratory

David Pope Honorary Symposium on Fundamentals of Deformation and Fracture of Advanced Metallic Materials—E.P. George, Oak Ridge National Laboratory; Haruyuki Inui, Kyoto University; C.T. Liu, The Hong Kong Polytechnic University

Deformation, Damage, and Fracture of Light Metals and Alloys—Qizhen Li, University of Nevada, Reno; Xun-Li Wang, Oak Ridge

National Laboratory; Yanyao Jiang, University of Nevada, Reno

Dynamic Behavior of Materials V—Marc Andre Meyers, University of California, San Diego; Naresh Thadhani, Georgia Institute of Technology; George Thompson Gray, Los Alamos National Laboratory

Electrode Technology for Aluminium Production—Alan D. Tomsett, Rio Tinto Alcan; Ketil A. Rye, Alcoa Mosjøen; Barry A. Sadler, Net Carbon Consulting Pty. Ltd.

Electrometallurgy Fundamentals and Applications—Michael L. Free, University of Utah

Fatigue and Corrosion Damage in Metallic Materials: Fundamentals, Modeling and Prevention—Tongguang Zhai, University of Kentucky; Zhengdong Long, Kaiser Aluminum; Peter Liaw, University of Tennessee

Federal Funding Opportunities—Jud Ready, Georgia Institute of Technology; Robert D. Shull, National Institute of Standards and Technology

Friction Stir Welding and Processing VI—Rajiv S. Mishra, Missouri University of Science and Technology; Murray W. Mahoney, Retired, Rockwell Scientific; Yutaka S. Sato, Tohoku University; Yuri Hovanski, Pacific Northwest National Laboratory; Ravi Verma, General Motors Corporation

Frontiers in Solidification Science—Jeffrey J. Hoyt, McMaster University; Daniel Lewis, Rensselaer Polytechnic Institute

Furnace Efficiency—Energy and Throughput—Thomas Niehoff, Linde Gas; Cynthia K. Belt, Superior Industries International; Russell J. Hewertson, Air Products and Chemicals Inc; Robert Voyer, Hatch

Geek Speak on the Hill—Jud Ready, Georgia Institute of Technology

Hume-Rothery Symposium Thermodynamics and Diffusion Coupling in Alloys—Application Driven Science—Zi-Kui Liu, The Pennsylvania State University; Larry Kaufman, CALPHAD, Inc.; Annika Borgenstam, Royal Institute of Technology; Carelyn Campbell, National Institute of Standards and Technology

Hydrogen Storage in Materials: Theory and Experiment—Louis Gerard Heeter, Jr., GM R&D Center

Hydrometallurgy Fundamentals and Applications—Michael L. Free, University of Utah

ICME: Overcoming Barriers and

Streamlining the Transition of Advanced Technologies to Engineering Practice—Paul K. Mason, Thermo-Cale Software Inc.; Mei Li, Ford Motor Company; James A. Warren, National Institute of Standards and Technology; Jeff Simmons, AFRL

Incorporating Integrated Computational Materials Science and Engineering (ICME) in the Graduate and Undergraduate Curricula—Laura M. Bartolo, Kent State University; Mark Asta, University of California, Davis

Magnesium Technology 2011—Wim Sillekens, TNO Science and Industry; Sean R. Agnew, University of Virginia; Suveen N. Mathaudhu, U.S. Army Research Laboratory; Neale R. Neelameggham, US Magnesium LLC

Magnetic Materials for Energy Applications—Victorino Franco, Sevilla University; Oliver Gutfleisch, IFW Dresden; Kazuhiro Hono, National Institute for Materials Science; Paul R. Ohodnicki, National Energy Technology Laboratory

Massively Parallel Simulations of Materials Response—Diana Farkas, Virginia Tech; Susan Sinnott, University of Florida

Material Science Advances Using Test Reactor Facilities—Todd R. Allen, University of Wisconsin—Madison

Materials for the Nuclear Renaissance II—Raul B. Rebak, GE Global Research; Brian Vern Cokeram, Bechtel-Bettis; Peter Chou, Electric Power Research Institute

Materials in Clean Power Systems VI: Clean Coal-, Hydrogen Based-Technologies, and Fuel Cells—Xingbo Liu, West Virginia University; Zhenguo “Gary” Yang, Pacific Northwest National Laboratory; Jeffrey Hawk, U.S. Department of Energy; Teruhisa Horita, AIST; Zi-Kui Liu, The Pennsylvania State University

Materials Processing Fundamentals—Prince N. Anyalebechi, Grand Valley State University; Srikanth Bontha, Temple University

Microstructural Processes in Irradiated Materials—Gary S. Was, University of Michigan; Thak Sang Byun, Oak Ridge National Laboratory; Yasuyoshi Nagai, Tohoku University; Christophe Domain, EDF

Neutron and X-Ray Studies of Advanced Materials IV—Rozaliya Barabash, Oak Ridge National Laboratory; Xun-Li Wang, Oak Ridge National Laboratory; Jaimie Tiley, U.S. Air Force Research Laboratory; Peter Liaw, The University of Tennessee; Erica

Lilleodden, GKSS Research Center; Brent Fultz, California Institute of Technology; Y.-D. Wang, Northeastern University

Pb-Free Solders and Other Materials for Emerging Interconnect and Packaging Technologies—Indranath Dutta, Washington State University; Darrel Frear, Freescale Semiconductor; Sung Kang, IBM; Eric Cotts, State University of New York Binghamton; Laura Turbini, Research in Motion; Rajen Sidhu, Intel Corporation; John Osenbach, LSI Corporation; Albert Wu, National Central University, Taiwan

Phase Stability, Phase Transformations, and Reactive Phase Formation in Electronic Materials X—Chih-Ming Chen, National Chung Hsing University; Hans Flandorfer, University of Vienna; Sinn-Wen Chen, National Tsing Hua University; Jae-ho Lee, Hongik University; Yee-Wen Yen, National Taiwan University of Science & Technology; Clemens Schmetterer, TU Bergakademie Freiberg; Ikuo Ohnuma, Tohoku University; Chao-Hong Wang, National Chung Cheng University

Physical and Mechanical Metallurgy of Shape Memory Alloys for Actuator Applications—S.V. Raj, NASA Glenn Research Center; Raj Vaidyanathan, University of Central Florida; Ibrahim Karaman, Texas A&M University; Ronald D. Noebe, NASA Glenn Research Center; Frederick T. Calkins, The Boeing Company; Shuichi Miyazaki, Institute of Materials Science, University of Tsukuba

Polycrystal Modelling with Experimental Integration: A Symposium Honoring Carlos Tome—Ricardo Lebensohn, Los Alamos National Laboratory; Sean Agnew, University of Virginia; Mark Daymond, Queens's University

Practical Methods of Characterization for Understanding Shaping and Forming Processes—Mark R. Stoudt, National Institute of Standards and Technology; Michael Miles, Brigham Young University

Processing and Properties of Powder-Based Materials—K. Morsi, San Diego State University; Ahmed El-Desouky, San Diego State University

Properties, Processing, and Performance of Steels and Ni-Based Alloys for Advanced Steam Conditions—Peter Tortorelli, Oak Ridge National Laboratory; Bruce Pint, Oak Ridge National Laboratory; Paul Jablonski, National Energy Technology Laboratory; Xingbo Liu, West Virginia University

Recent Developments in the Processing, Characterization, Properties and Perfor-



Politics Derail COMPETES Act:

At our press time, the House had just voted to return the COMPETES Act to the Science and Technology Committee. This action does not necessarily kill the bill, whose authorization expires at the end of this year, but it significantly threatens its key provisions which have been supported consistently by science and technology societies including

the Federation of Materials Societies (FMS) and TMS as well as large trade associations such as the U.S. Chamber of Commerce, the National Association of Manufacturers, and the Council on Competitiveness. Republicans succeeded in passing a set of amendments to cut the authorization for the bill to three years from the five approved by the committee. Those amendments, in effect, reduced authorized funding for the National Science Foundation (NSF), Office of Science in the Department of Energy, and the laboratory programs of the National Institute for Standards and Technology to FY 2010 levels, and cut some provisions such as the Energy Department's ARPA-E program. In addition to these cuts, which committee Chairman Bart Gordon (D-TN) said would "gut" the bill, the tipping points appeared to be a requirement that all NSF employees caught watching pornography on their government computers be fired, and that all universities receiving federal funding for research and development be required to admit military recruiters to campus. The two-day debate was ugly to watch, and the science and technology community will be trying to regain the previous bipartisan support for COMPETES.

Politics Factors into Climate Bill, Too: A 987-page bill, six committees with jurisdiction, a mammoth oil spill to consider, no bipartisan support, and a crowded Senate schedule complicated by election campaigns all combine to work against swift passage of the American Power Act introduced by Senators John Kerry (D-MA) and Joe Lieberman (I-CT). The legislation allows offshore oil drilling while giving states a right to prohibit drilling closer than 75 miles from their coast. Even so, one senator called the provision a "non-starter." The most popular title of the bill appears to be the one on manufacturing. It delays national pollution reduction requirements to 2016 for industrial sources. Also, it calls for an authorization of \$20 billion for "critical programs" including an immediate \$6 billion for industrial efficiency and clean technology manufacturing, more than \$7 billion for clean vehicle manufacturing, and more than \$7 billion for research and development of new efficiency and competitiveness for domestic manufacturers.

Report Highlights Impact of Research Funding: A report by the U.S. Congress Joint Economic Committee (JEC) highlights the role of government investment in research and development. The report, titled "The Pivotal Role of Government Investment in Basic Research," concludes that the United States needs to identify and support the next generation of innovations that will create new industries, spur job creation, and fuel economic growth. Because basic research plays a critical role in sparking innovation, it may be prudent for the government to increase its expenditures towards basic research now. The JEC report findings include:

- If research and development were to rely on the private sector alone for funding, many socially beneficial research projects would not be undertaken. This is especially true for basic research projects.
- Federal support for basic research is particularly crucial because the lack of direct commercial applications from basic research projects can deter businesses from performing basic research.
- From 1958 to 2008, total expenditures on R&D as a share of gross domestic product (GDP) have generally hovered around 2.5 percent. However, overall spending on basic research has been substantially smaller, reaching 0.3 percent of GDP in 2008.

"Investments in basic research expand our scientific knowledge, but just as significantly, they promote our economic competitiveness and contribute to our economic growth," said Congresswoman Carolyn B. Maloney, Chair of the JEC. "Standing here today, we do not know what the next round of innovations will be, but the federal government must continue to provide funding for projects that improve our lives and help keep America competitive." Senator Charles E. Schumer, Vice Chair of the JEC, said, "Investments in basic research are a down payment on future job creation and economic growth. Shortchanging these types of investments is a penny wise and pound foolish, because over time, they pay for themselves."

mance of Metal Matrix Composites—Martin I. Pech-Canul, Centro de Investigacion y de Estudios Avanzados del Instituto Politecnico Nacional; Zariff Chaudhury, Arkansas State University; Golam Newaz, Wayne State University

Recycling General Session—Joseph Pomykala, Argonne National Laboratory

Refractory Metals 2011—Omer Dogan, National Energy Technology Laboratory; Jim Ciulik, University of Texas, Austin

Sensors, Sampling, and Simulation for Process Control—Brian G. Thomas, University of Illinois at Urbana-Champaign; Andrew P. Campbell, WorleyParsons; Srinath Viswanathan, University of Alabama; Lifeng Zhang, Missouri University of Science and Technology; James A. Yurko, 22Ti LLC; Thomas Battle, Midrex Technologies

Silicon Production, Purification and Recycling for Photovoltaic Cells—Anne Kvithyld, SINTEF; Gregory J. Hildeman, Solar Power Industries; Gabriella Tranell, Norwegian University of Science and Technology (NTNU); Arjan Ciftja, SINTEF

Size Effects in Mechanical Behavior—Erica T. Lilleodden, GKSS Research Center; Amit Misra, Los Alamos National Laboratory; Thomas

Buchheit, Sandia National Laboratories; Andrew M. Minor, Lawrence Berkeley National Laboratory

Surfaces and Heterostructures at Nano- or Micro-Scale and Their Characterization, Properties, and Applications—Nitin Chopra, The University of Alabama; Ramana G. Reddy, The University of Alabama; Jiyoung Kim, University of Texas; Arvind Agarwal, Florida International University; Sandip P. Harimkar, Oklahoma State University

Thermally Activated Processes in Plastic Deformation—Christopher F. Woodward, U.S. Air Force Research Laboratory

Ultrasonic Welding for Lightweight Components—Frank Balle, University of Kaiserslautern, Institute of Materials Science and Engineering

Waste Heat Recovery—Cynthia K. Belt, Superior Industries International; Mark Jolly, University of Birmingham; Susanne Opalka, United Technologies; Xingbo Liu, West Virginia University

Please Note: General abstract sessions sponsored by the Electronic, Magnetic & Photonic Materials Division; Extraction & Processing Division; Light Metals Division; Materials Processing & Manufacturing Division; and Structural Materials Division are currently being planned. Check the TMS 2011 website regularly for details and updates.



Instruments & Testing Services

Thermal Analysis

- High Temperature & Classical DSC, DTA, TGA, DSC-TGA
- High Accuracy Specific Heat
- Coupling to FTIR & MS

Conductivity & Flash Diffusivity

- -125 to +2000°C
- New Guarded Hot Plate

Dilatometers

- CTE & Sintering to +2800°C

Contract Testing Services

NETZSCH Instruments
37 North Ave.

Burlington, MA 01803

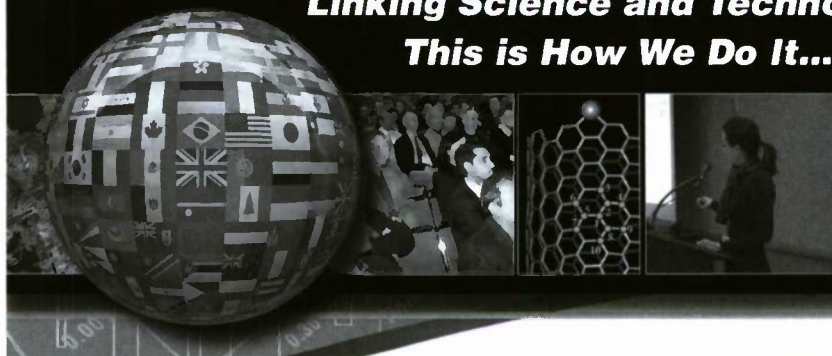
Call (781) 272-5353

Fax (781) 272-5225

e-mail: NIB-Sales@Netzsch.com

www.e-Thermal.com

**Linking Science and Technology for Global Solutions...
This is How We Do It...**



TMS2011
140th Annual Meeting & Exhibition

February 27 to March 3, 2011
San Diego Convention Center
San Diego, California USA

**The Premier Gathering of the World's Leading
Materials Science & Engineering Professionals**

Technical Program Themes

- Aluminum and Magnesium
- Advanced Characterization, Modeling, and Materials Performance
- High Performance Materials
- Materials and Society: Energy and Sustainable Production
- Materials Processing and Production
- Nanoscale and Amorphous Materials
- Professional Development

**Submit Your
Abstract NOW
through July 15!**

Visit:
www.tms.org/tms2011

The Structural Materials Division: Adding Strength to TMS and Its Membership Since 1988

Eric M. Taleff



Among the most important benefits of TMS membership are opportunities for the exchange of technical information, the exchange of ideas, and professional networking. Realizing these benefits requires only that you make contact with fellow members who share your professional interests and responsibilities. Let us explore how this can be accomplished. But first, a bit of history.

The Minerals, Metals & Materials Society (TMS) was born in 1957 of the American Institute of Mining, Metallurgical, and Petroleum Engineers (AIME), itself founded in 1871 as the Metallurgical Society of AIME. TMS siblings under AIME include the Society for Mining, Metallurgy and Exploration (SME); the Association for Iron and Steel Technology (AIST); and the Society of Petroleum Engineers (SPE). Through this relationship, TMS can trace its origin back to one of the first national engineering societies in the United States. Following many years of growth under AIME, TMS was separately incorporated in 1984. TMS is now the professional society of choice for thousands of materials professionals with interests across the entire range of materials science and engineering.

The materials professionals comprising TMS membership took on responsibility for a greatly increased array of specialized technical topics in the years after the society was founded. To address this increase in technical specializations, five technical divisions were created within TMS. These were

announced in the June 1988 *Journal of Metals*, forerunner of *JOM*, by Bob Bartlett, TMS vice president at the time. One of these divisions, the topic of this article, is the Structural Materials Division (SMD). As is evident in its name, the SMD exists to serve the needs of materials professionals concerned with structural materials. A structural material is simply any material applied to the purpose of bearing a load. If you are concerned with such materials, then read on to learn how the SMD might serve you. If your interests and responsibilities include other materials issues, then please investigate the companion TMS technical divisions: the Extraction & Processing Division (EPD); the Light Metals Division (LMD); the Electronic, Magnetic & Photonic Materials Division (EMPMD); and the Materials Processing & Manufacturing Division (MPMD).

The first step toward making contact with TMS members who share your professional interests and responsibilities in structural materials is through the SMD technical committees. The SMD encompasses 11 committees, each devoted to a particular type or aspect of structural materials. Realizing the full benefits available to you as a TMS member is simply a matter of your participation in one or more of these committees. The technical committees of the SMD are:

- Advanced Characterization, Testing, and Simulation Committee
- Alloy Phases Committee
- Biomaterials Committee
- Chemistry and Physics of Materials Committee
- Composite Materials Committee

- Corrosion and Environmental Effects Committee
- High Temperature Alloys Committee
- Mechanical Behavior of Materials Committee
- Nuclear Materials Committee
- Refractory Metals Committee
- Titanium Committee

These committees hold regular meetings at the TMS Annual Meeting, and some also meet during the Materials Science & Technology fall meetings. Technical committee meetings are open to all TMS members, and attending these meetings is an important step toward deriving the full value of your TMS membership. These committees offer opportunities for networking, participation in technical program organization, and other important professional interactions. The "Committee Home Pages" on the TMS website provide an invaluable guide to the technical committees of TMS, and all that is needed for access is your TMS membership. You will find there contacts for technical committee and division officers, which makes additional information on committee or division activities only a short e-mail or telephone call away. Participation in the technical committees will not only serve your professional goals, it will build the greatest strength of TMS as a member-driven society, members serving members. When you next attend the TMS Annual Meeting, please consider which technical committee meetings you will attend. Then, ask your fellow members which they will attend.

Eric M. Taleff, Past Chair of the SMD, is with the Mechanical Engineering Department of the University of Texas at Austin.

JOM READER POLL

To vote, go to www.tms.org/jomsurvey.html.

Last month's question:

President Barack Obama recently announced plans to scrap NASA's Constellation moon-landing project and to redirect funding toward programs that will, among other things, lay the groundwork for a 2030 Mars expedition. Some critics have called the decision a crippling blow to the U.S. space program; others see it as an opportunity to refocus funding into more relevant areas. This month JOM asks, what is the impact of the new priorities for NASA?

Last month's answers:

The United States will lose its status as a worldwide leader of human spaceflight **40%**

Scientific advancement will be stalled as R&D funding is redirected **20%**

Commercial space launch services will be stimulated to fill the void left by NASA's new priorities **0%**

The U.S. space program will ultimately be better positioned for deep space exploration **40%**

None of the above (please elaborate in the comments field) **0%**

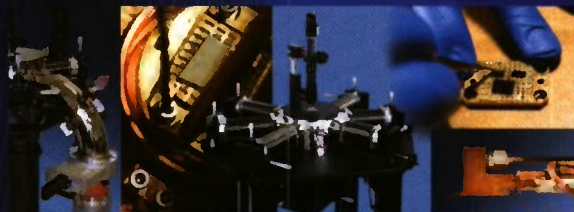
This month's question:

It's time to plan for the TMS 2011 Annual Meeting! This month JOM asks which program theme interests you most:

This month's answers:

- | | |
|---|---|
| <input type="checkbox"/> Advanced Characterization, Modeling, and Materials Performance | <input type="checkbox"/> Materials and Society: Energy and Sustainable Production |
| <input type="checkbox"/> Aluminum and Magnesium | <input type="checkbox"/> Materials Processing and Production |
| <input type="checkbox"/> High Performance Materials | <input type="checkbox"/> Nanoscale and Amorphous Materials |
| | <input type="checkbox"/> Professional Development |

LAKE SHORE CRYOGENIC PROBE STATIONS



Temperatures from 1.5 K – 475 K

Measurements from DC to 67 GHz

Probe up to 4-inch wafers

Up to 6 micro-manipulated probe arms

Vertical or horizontal field magnets

Cryogen-free ■ Load-lock ■ High vacuum



LakeShore

575 McCorkle Boulevard Westerville OH 43082

Phone: (614) 891-2244 Fax: (614) 818-1600

info@lakeshore.com www.lakeshore.com

8th World Trade Fair & Conference
14 – 16 September 2010
Exhibition Centre Essen, Germany

ALUMINIUM 2010

between innovation and environment



The material aluminium is stable, light and corrosion resistant. It can be processed precisely, is conductive and stands for great aesthetic. These excellent characteristics of aluminium allow an innovative development and a visionary product design – and help us to protect the environment.

At ALUMINIUM 2010 you can experience the variety of application possibilities of the future-oriented material aluminium and its unique position between innovation and environment.

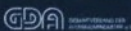
Visitors – Register online now!
Additional information contact: Dan McAuley 203.840.5402

www.aluminium-messe.com

Organiser:



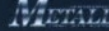
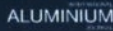
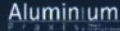
Institutional Patron:



Partner:



Official International Media Partner:



International Media Sponsor:



www.efmd.com

Flexible Film Systems: Current Understanding and Future Prospects

Megan J. Cordill

The electrical and mechanical properties of metal films on polymer substrates are of interest for use in flexible electronic devices and sensors. In these systems, film deformation mechanisms are comparable to those from free-standing films but the influence of the substrate and the interface on the film properties is yet to be fully understood. This understanding is critical to further design improvements and advanced in situ characterization holds the promise of making this possible. With the aid of such techniques direct observation of failure and deformation mechanisms has become possible.

INTRODUCTION

Because of applications in flexible electronics, metal and ceramic films on polymers have become an important area of study. Applications include flexible displays, printed memory, smart textiles, flexible batteries, radio-frequency identifications, organic light emitting diodes for lighting as well as organic sensors and photovoltaics.¹ The devices can range in size from a few square centimeters for sensors, to paper size for flexible displays or lighting, to even larger wearable smart textiles (Figure 1). These applications depend on the technologic parameters of high charge carrier mobility and electrical performance, resolution of the processing conditions, barrier properties and environmental stability, the flexibility and bending radius, and the yield.¹ Flexible electronics need to be robust and reliable, while stretching and compressing without failing mechanically or electrically. This is often referred to as the "stretchability" of the device/film-substrate system.² The current understanding is that for flexible devices to have a high stretchability range a high fracture

strain and good adhesion are needed.² Electrically speaking, it is desirable to have a high charge carrier mobility at high strains.

In the case of flexible electronics and sensor technologies, it is important to examine the behavior of the film and substrate together.³⁻⁵ This provides a more complete system allowing for interfacial properties to be examined and films on polymer substrates are easier to handle than the fragile silicon-based free-standing films. Nanoindentation is a common technique to measure the mechanical behavior of thin films on rigid substrates. In recent years, nanoindentation has been combined with

focused ion beam (FIB) milling to create compression pillars.⁶⁻⁹ The basic yield stress results from this technique find that smaller is stronger due to the dimensional constriction enforced by the pillar.⁶ However, these experiments are not suitable for films on compliant polymer substrates.

One area of flexible electronics research has been focused on creating material systems that have a large stretchability range,² whereby the metal and polymer can both stretch and compress without mechanical or electrical failure. Currently, this is achieved by depositing stiff islands, commonly made of silicon-nitride, where active cells (thin film transistors) are fabricated and connected by metal lines.¹⁰⁻¹⁴ When the whole structure is stretched, strains are small in the islands and large where the polymer substrate is exposed or covered by metal interconnect lines. Mechanically, the fracture strain of the films are relatively small compared to bulk values but the films have high strengths^{10,14} due to the lack of localized deformation that is suppressed while the film remains bonded to the polymer substrate.

Other topics of interest are developing cheap, fast, and easy techniques to manufacture the devices. Popular processing techniques are inkjet printing,¹⁵⁻¹⁸ stamping,^{19,20} and roll-to-roll (reel-to-reel)¹⁹⁻²¹ which are cost-effective and can produce high quality electrical structures on polymer substrates with good electrical properties. Conventional thin film deposition techniques such as sputtering or evaporation are also being employed to create flexible electronics, however, mostly for research applications. The type of processing used will affect the material microstructures which then dictate the mechanical and electrical behavior.

How would you...

...describe the overall significance of this paper?

This article summarizes some of the advancements that flexible electronics have made in recent years. Also discussed are the techniques used to measure mechanical and electrical properties required for these devices.

...describe this work to a materials science and engineering professional with no experience in your technical specialty?

In order to create reliable flexible electronics, the charge carrying metal and ceramic films must adhere well to polymer substrates as well as have good electrical conductivity during flexing and stretching. Techniques to measure the properties and advances in the field are discussed.

...describe this work to a layperson?

Paper-like displays and bendable sensors are made of metal, ceramic, and plastic materials that must stick and stretch together without breaking. The right combination of all of the materials can be used to create electronics that can be folded to fit into a pocket.

FLEXIBLE MATERIALS

The move toward flexible electronic devices has come from the need to have cheaper, lighter, and flexible devices that can be made using various roll-on-roll processing or inkjet printing. The materials used need to be carefully chosen because the process conditions are very different from conventional electronic fabrication routes and the interplay between the other layers is quite important for device performance. The devices available today use a combination of solution-based and evaporation techniques in the manufacturing process.¹ The materials used to create flexible electronic devices have some similarities to traditional thin film transistors (TFTs) and microprocessors. These materials can be separated into two categories: flexible polymer substrates and the charge carrying films (both metal and ceramic).

The polymer substrate basic function is to support the devices and provide large areas to be processed. This reduces manufacturing costs and increases the device yield. Commonly used substrates include polyesters (PE), polyethyleneterephthalate (PET), polyethylenenaphthalate (PEN), polycarbonate (PC),

polyimide (PI), polyetherimide (PEI) and polyvinyl fluoride (PVF). PET, PEN, and PC can be easily modified to create the desired physical and surface properties. These polymers are widely used because the properties can be fine-tuned and they serve as good all-around substrates. Polyimide, PEI, and PVF are higher priced and have specific advantages such as stability against heat and weather.¹ The thickness of the substrates normally ranges between approximately 50 μm and 200 μm depending on the application and the amount of flexibility required. Another polymer substrate gaining interest within the research circles is polydimethyl siloxane (PDMS) because it can be used to pre-strain films to increase stretchability.^{11-14,22,23} Polymer overcoatings have also been found to aid in increasing the environmental protection and failure strain by suppressing fracture of the ceramic islands.^{24,25} For example, a 200 nm polymer overcoating increases the survival rate from 20% to 100% for indium tin oxide (ITO) islands by reducing the intensity of stresses at the island edges and suppressing delamination,²⁵ while encapsulating metal lines with another polymer film does not greatly affect the electrical behavior

during straining.²⁴

Charge-carrying films can be separated into TFT materials and connecting materials. Commonly used ceramics are semiconductors like SiN or silicon. These materials are brittle and fracture at low strains; therefore, they are used sparingly as islands to distribute the strains and increase reliability. Other materials being considered are amorphous silicon, carbon nanotubes, and hybrid materials as well as different device architectures to optimize performance of the TFTs.¹ Copper and gold are good materials to use to connect the ceramic islands because of their ductility and excellent conductive properties. Much is known about depositing these films on rigid substrates using evaporation and sputtering techniques and the electrical properties are also desirable for flexible devices. Other materials used as conducting lines include silver inks that can be printed or ITO films as well as conducting polymers such as Poly(3,4-ethylenedioxythiophene) poly(styrenesulfonate) (PEDOT:PSS).¹ ITO and PEDOT:PSS are transparent conductors and can be used in optical devices.

The use of the mentioned materials alone can provide devices with a large stretchability range, especially when film thickness and grain sizes are considered. Lu et al.^{26,27} have shown that 3 μm thick copper films with large grains can withstand up to 50% tensile strain before electrical failure. However, through the use of pre-strained polymer substrates (i.e., PDMS) or patterned films, the stretchability range can be improved further. Lacour et al.¹¹⁻¹⁴ and Rodgers et al.^{22,23} have used pre-strained PDMS to create wavy gold lines and free-standing silicon nanoribbons which can be strained in tension up to 25%. Gold lines have a built-in compressive residual stress that not only allows for more tensile strain but also some compressive strain. The silicon nanoribbons can be strained in tension, but fail in compression due to the brittle nature of silicon.²² Other wavy silicon structures have been created such as stretchable two-dimensional (2-D) nanomembranes and noncoplanar mesh designs.²³ These designs can accommodate more strain and with a serpentine line layout also provide for more compression of the system out of the plane of the

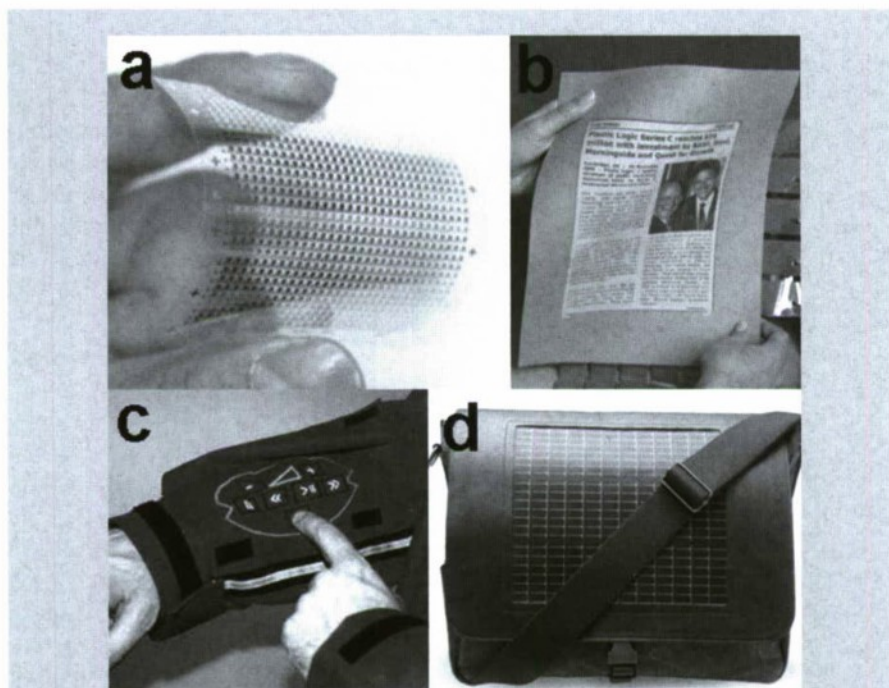


Figure 1. Examples of flexible electronic devices. (a) Sensors courtesy of Gearlog (www.gearlog.com/2009/12/university_of_tokyo_unveils_fl.php); (b) flexible paper displays courtesy of Electronics Weekly (www.electronicweekly.com/Articles/2005/12/15/37190/Largest-flexible-organic-display.htm); (c) wearable electronic clothes by WRONZ/Peratech that activate music and phones; and (d) accessories from Noon Solar (www.noonsolar.com) that recharge small devices (cell phone or iPod) with flexible solar panels.

substrate. A review of such stretchable silicon nanostructures can be found in Reference 23. Another way to increase stretchability is the strategic patterning of the metal lines. Patterning films and lines with holes can also increase the stretchability of devices. Tucker and Li²⁸ have shown with theoretical modeling that a film patterned with holes in a triangle lattice performed better than films patterned with holes in a square lattice. The increased strain accommodation comes from the geometric effect that creates strain deconcentration rather than strain concentration at the edges of the holes because the lattice of holes allows for out of plane elongation.²⁸ Similarly, Lacour et al.²⁹ have shown that tri-branched microcracks in gold films have the same out of plane elongation effect. These techniques for increasing stretchability are being studied and used in laboratory devices. More time and research is needed before they can be implemented for industrial applications.

PROPERTIES OF POLYMER SUPPORTED FILMS

Mechanical properties of thin films can be measured without (free-standing) or with the substrate. With current silicon interconnect fabrication processes, free-standing films can be generated for bulge testing^{30,31} and cantilever bending experiments³²⁻³⁴ to access the mechanical behavior and the processing-structure-property relations of thin films without substrate effects. Bulge testing

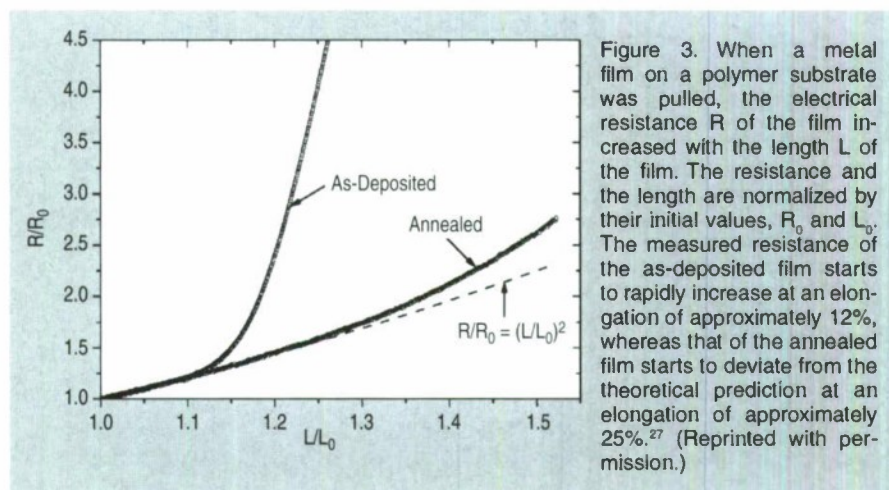


Figure 3. When a metal film on a polymer substrate was pulled, the electrical resistance R of the film increased with the length L of the film. The resistance and the length are normalized by their initial values, R_0 and L_0 . The measured resistance of the as-deposited film starts to rapidly increase at an elongation of approximately 12%, whereas that of the annealed film starts to deviate from the theoretical prediction at an elongation of approximately 25%.²⁷ (Reprinted with permission.)

pressurizes windows of free-standing films while the elastic modulus and stress-strain response is measured with an interferometer from the fringe spacing (Figure 2a). Another nanoindentation based technique is microcantilever bending experiments. With this technique the nanoindenter is used to bend free-standing beams while recording the load and displacement response (Figure 2b). Experiments on gold and aluminum^{32,33} have shown an increased yield stress with decreasing film thickness. Son et al.³² examined the grain size of the films as a function of film thickness using gold and aluminum films. They found that an increased yield stress can be attributed to a Hall-Petch effect for the gold films while the increased strength of aluminum films is also due to the native oxide that forms with the removal of the silicon substrate. At this length scale the native oxide becomes

an important part of the analysis. From the above work and others with bending of free-standing films, it has been found that the dominant length scale is the grain size which is dictating the mechanical properties.

For flexible systems it is better to measure the mechanical properties with the substrate because the polymer substrate influences the properties more than the films. As previously mentioned, thin films supported by polymer substrates are easier to handle than free-standing films which makes traditional mechanical testing techniques possible. In the laboratory, uniaxial tensile straining and nanoindentation are commonly used to determine the mechanical response and 4 point probe experiments are used to measure the electrical response. Uniaxial tensile straining is the technique of choice for mechanical response due to the fact that it is easier to implement and to separate the film and substrate properties than with nanoindentation. The technique also provides the desired properties of elastic modulus, yield stress, and stress-strain response. Performing the experiments in situ with scanning electron microscopy (SEM) or x-ray diffraction (XRD) permits the fracture strains to be easily determined. Performing uniaxial straining in situ with 4 point probe one can measure resistance as a function of strain; this is the typical route to determining both the mechanical and electrical properties. It is an easy experiment to compare film thickness, grain size, and structure/patterning effects. An equation to relate the electrical resistance of the film to its elongation is formed by assuming that the film remains rectangular during straining and the resistivity of the film

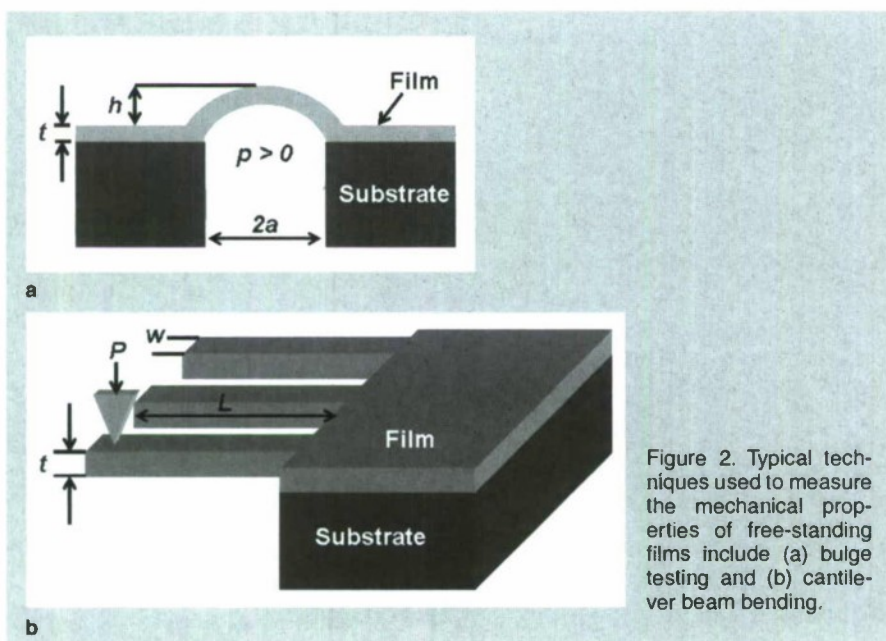


Figure 2. Typical techniques used to measure the mechanical properties of free-standing films include (a) bulge testing and (b) cantilever beam bending.

also remains unchanged.²⁶ The ratio of the resistance of the strained film to the unstrained film is

$$R/R_0 = (L/L_0)^2 \quad (1)$$

In this equation, R is the resistance, L is the strained length, and R_0 and L_0 are the initial values of resistance and length before straining. An example of resistance measurements is shown in Figure 3 from the work of Lu et al.²⁷ Here, the resistance for an annealed copper film is lower than an unannealed copper film, indicating the importance grain size has on the mechanical and electrical response.

When ductile films on polymers are strained in tensile the substrate can suppress the catastrophic failure that allows for the use in flexible electronics and sensors. Theoretical modeling work of ductile films on polymer substrates^{35,36} suggests that the fracture strain can be increased if the adhesion between film and substrate is increased. Metal films that are well adhered to polymer substrates can sustain much larger strains than poorly adhered films because the polymer substrate will constrain plasticity and fracture. During tensile straining, a free-standing metal film will form a neck that leads to failure (Figure 4a), while in a well-bonded film localized necking is mitigated because the substrate suppresses the strain localization that leads to failure (Figure 4b). However,

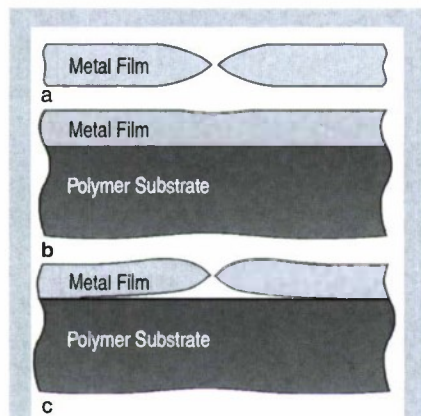


Figure 4. The rupture of a metal film is caused by strain localization. Local thinning leads to local elongation. (a) A free-standing metal film accommodates the local elongation as the ruptured halves move apart. (b) When the film is well bonded to a substrate, the local elongation in the film may be suppressed by the substrate. (c) Debonding of the metal film assists rupture.³⁶ (Reprinted with permission.)

er, when the film is poorly bonded to the substrate strain localization is not suppressed and, once the film delaminates from the substrate, it can be considered free-standing, necking and failing (Figure 4c).^{35,36} Examples of strained ductile films, even those with small grain sizes, have shown that these films can withstand straining without electrical failure up to 20% or more.^{10,26,27} This is because the films locally thin and form void like cracks during straining (Figure 5a) due to the constraining influence of the polymer substrate which allows for current to still flow.^{28,37,38} As shown by several researchers,^{39–47} brittle films will fracture almost immediately when strained in tension and the polymer substrate does little to prevent failure. An example of brittle film fracture in Figure 5b shows a strained chromium film that has not only cracked but also delaminated from the polyimide substrate by forming buckles between the cracks parallel to the straining direction.

In order to improve the stretchability further, adhesion of the metal-polymer interface should be increased. The most common route to increasing the adhesion energy of a film-substrate system is to add an interlayer film between the film and substrate that has better adhesion properties. To increase the adhesion energy of ductile copper or gold films, 10–30 nm of brittle Cr, W, Ti, or Ta are used. Even though these films are ultra thin, they can increase the adhesion and failure strain dramatically and thus the stretchability.^{26,27} The brittle interlayer will fail at strains less than 1% while the current carrying copper or gold film will fail at much higher strains. However, even though the adhesion layer fails first, it does suspend necking even though parts of the film are unsupported by the adhesion layer. Other novel materials such as shape memory alloys³⁷ and metallic glasses³⁸ are also being considered for flexible electronic applications, along with other deposition routes like inkjet printing^{15–18} and stamping processes.^{1,19,20}

VISUALIZING FAILURE WITH IN SITU METHODS

In situ methods are needed to observe fracture and deformation, and measure strains and resistance. Optical microscopy methods have been used to record

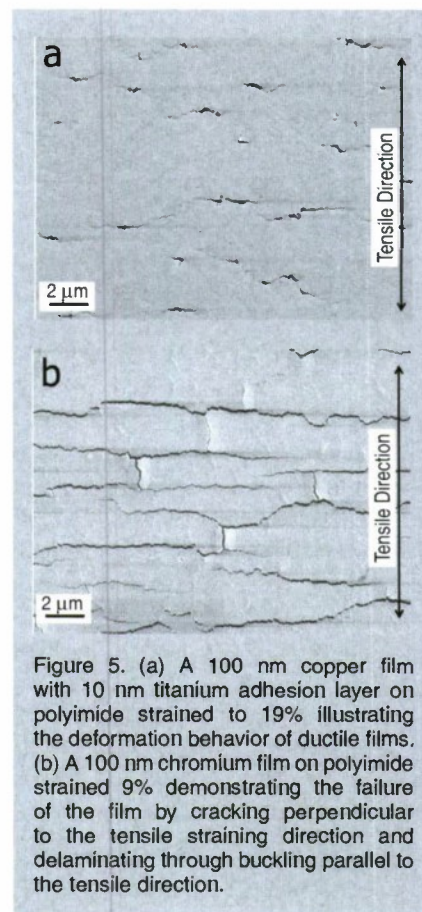


Figure 5. (a) A 100 nm copper film with 10 nm titanium adhesion layer on polyimide strained to 19% illustrating the deformation behavior of ductile films. (b) A 100 nm chromium film on polyimide strained 9% demonstrating the failure of the film by cracking perpendicular to the tensile straining direction and delaminating through buckling parallel to the tensile direction.

the evolution of cracks forming in ceramic gas barrier coatings of SiO_x and SiN_x on various polymer substrates.^{42–46} Through this work three stages of brittle film fragmentation have been observed. An example of an in situ SEM straining experiment of a 70 nm chromium film on PET can be found in Figure 6. The first stage is crack initiation perpendicular to the straining direction (Figure 6 a, b) followed by further cracking (Figure 6 c–e) until a plateau is reached and cracks have stopped forming (stage 2). Once the cracks have stopped forming (Figure 6 f–h), delamination in the form of buckles between the cracks occurs parallel to the straining direction (stage 3). Figure 6i is the corresponding crack density evolution versus the percent strain of the entire experiment with the three fragmentation stages illustrated. Using a shear lag approach⁴⁸ the interfacial shear stress can be calculated from the average crack spacing once the plateau has been reached and the observed fracture strain. Similar approaches have been made with in situ SEM straining of chromium on PI⁴⁰ and with in situ XRD straining of tantalum films on PI.⁴⁷ The buckling that arises in stage 3 is now being used to measure the adhesion energy

of the metal-polymer interface^{47,49} and methodology is still being further developed. Adhesion of films to polymer substrates is not the weakest link in the development of flexible electronics, but it has been shown to increase the flexibility of the device. The important factor is the combination of good adhesion for more flexibility and mechanical reliability with a large charge carrier mobility for successful devices.

Other in situ techniques have been used to measure the stresses and strains in the films during straining. The ability to measure the strain in situ is important to capture certain deformation events that occur in the film. Hommel and Kraft⁵ have shown that thin copper films strained on PI also have an increased yield stress compared to bulk copper when strain is measured ex situ with XRD. Similar experiments by the Spaepen group^{3,4} also measure the strain in situ with an optical diffraction tech-

nique. Initially, XRD techniques were used to measure residual stresses in thin films as well as thermal and electromigration induced strains.^{50,51} More recently, XRD techniques have been used to measure stresses and strains of films and lines strained by a uniaxial tensile device in situ.^{34,47,52,53} This technique allows one to follow several grains during the deformation and study the strains as well as the texture that evolves. For example, Gruber et al.³⁴ found that copper films as thin as 40 nm have an increased flow stress when passivation layers are present and that the film thickness and grain size are important parameters to consider. Frank et al.⁴⁸ measured the stress-strain development of tantalum films on polyimide in both the tensile and compressive directions. The fracture and buckling strains could be accurately measured and used to calculate adhesion of the interface. Another outcome of this work was the reason behind the

buckle formation. Buckles form because initially the film fractures perpendicular to the loading direction. A compressive stress arises between crack fragments which causes the buckling to occur.⁴⁷ Results such as these are important for the development of models to explain deformation as well as to improve current flexible device designs.

In situ experiments with SEM and transmission electron microscopy (TEM) allow for the study the microstructural changes during the deformation, find where deformation is being localized during straining, and allow for the examination of how the microstructure influences failure, both mechanically and electrically. Example in situ TEM experiments have been performed on thermally cycled copper and aluminum single and polycrystalline films.^{54,55} With such a technique, deformation mechanisms can be identified and correlated to the microstructure, stress and

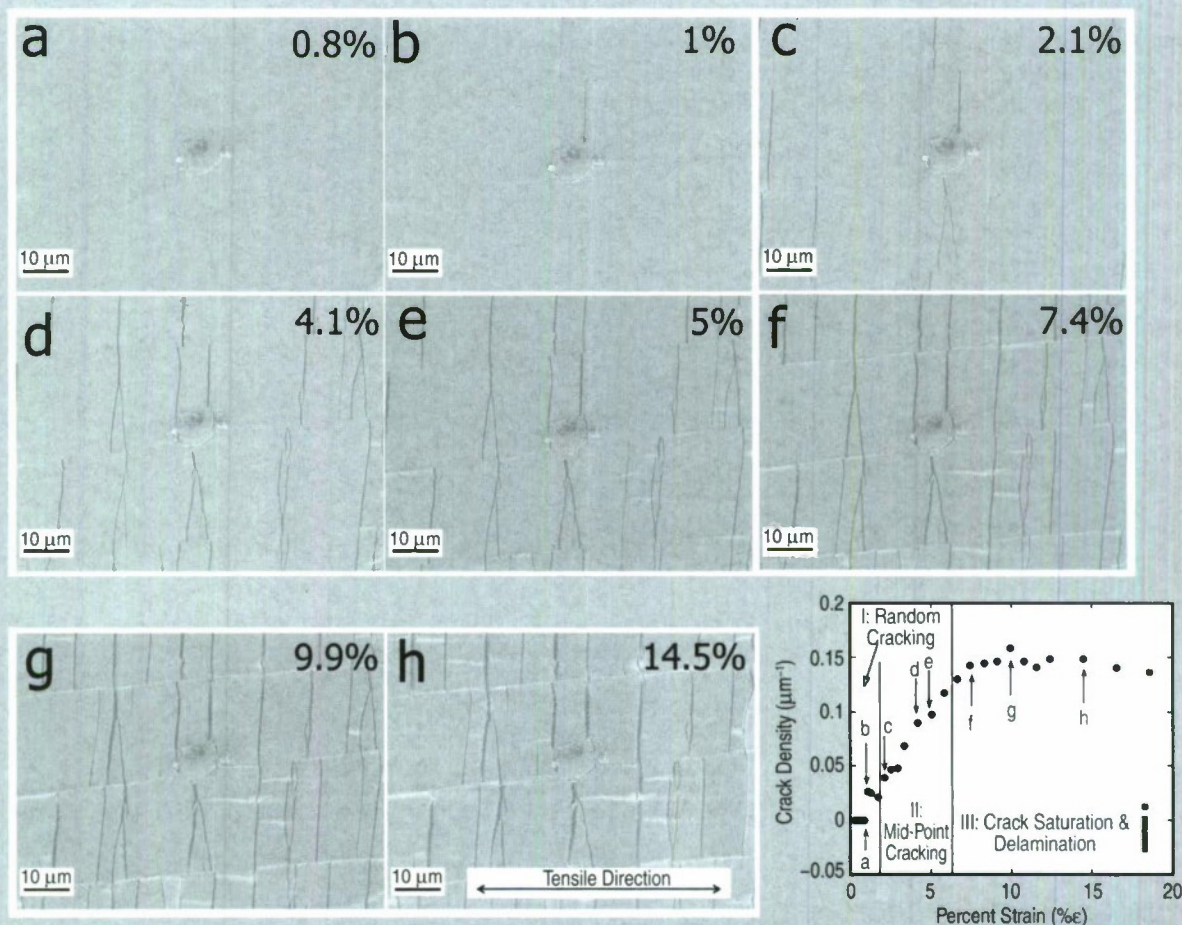


Figure 6. An in situ SEM straining experiment with 70 nm chromium film on PET where the tensile straining direction is horizontal (left to right). (a) Before fracture strain (0.8%) and (b) at fracture strain (1%). The pre-existing cracks in (a) are residual cracks caused by the deposition. In (c)–(h), further cracking occurs until a plateau is reached followed by delamination (buckling) at higher strains. (i) The corresponding evolution of crack density as a function of percent strain for the entire experiment. The three stages of fragmentation are indicated.

temperature. The use of high quality in situ mechanical straining techniques with TEM would allow for dislocation motion and grain boundary deformation mechanisms to be observed in real time. The results from such in situ experiments would aid in the development of computational modeling of plastic events, confirming or refuting existing models.

CONCLUSION

To improve mechanical and electrical properties of these complex material systems, more work at characterizing the processing-structure-property relationships should be performed. Straining experiments on free-standing films emphasize the effects of grain size, film thickness, and film texture. Conversely, studies of strained films on polymer substrates emphasize the electrical properties and thickness effects more than the film microstructure. For example, there is a wealth of information on the mechanical and electrical behavior of copper and gold films and devices deposited with sputtering or evaporation techniques. However, for the lines and devices deposited with inkjet printing or stamping, much is known about the electrical capabilities but little is known about the mechanical response or the resulting microstructure. The microstructure of the film not only determines the mechanical behavior but also the electrical behavior and could be optimized if studied.

Further research should also examine small thicknesses (less than 50 nm) and grain sizes which require the use of TEM. Preparing TEM samples from thin films can be challenging, especially with a polymer substrate that can react poorly under an electron beam. To properly examine the microstructure of thin films and line structures on polymers, one must employ novel sample preparation routes. Recently some advances with novel TEM sample preparation techniques have emerged for films on polymers.⁵⁶ And as shown with in situ TEM straining experiments,^{57,58} a PI substrate was used to support a film during the straining of a dog-bone sample geometry with viewing window. The sample was created using FIB and the window allowed the observation the dislocation activity during the straining.^{57,57} In this

case, the polymer substrate was necessary to support and protect the film. The TEM can also be used to examine the metal-polymer interfaces through high resolution imaging and chemical analysis. Studies in these areas would elucidate more the role of adhesion for these material systems.

Currently the flexible electronics industry is focusing more on the major challenges holding back device development for the open market. Those challenges are accurate and repeatable processing, increasing charge carrier mobility and electrical conductivity and the design of the circuits.¹ All of the industry challenges are intertwined and depend on one another. On the other hand, research institutions are focusing on the how and why of material behavior. This is the reason behind the introduction and use of in situ mechanical and electrical experiments as well as the novel stretchable structures like wavy gold and silicon nanoribbons. Major breakthroughs are needed in the processing and microstructure characterization of flexible devices and will come from the research into the how and why.

References

1. OE-A Roadmap for Organic and Printed Electronics, 3rd edition (Frankfurt: Organic Electronics Association, OE-A, 2009).
2. T. Li et al., *Applied Physics Letters*, 85 (2004), pp. 3435–3437.
3. H. Huang and F. Spaepen, *Acta Materialia*, 48 (2000), pp. 3261–3269.
4. D.Y.W. Yu and F. Spaepen, *J. Applied Physics*, 95 (2004), pp. 2991–2997.
5. M. Hommel and O. Kraft, *Acta Materialia*, 49 (2001), pp. 3935–3947.
6. C.A. Volkert and E.T. Lilleodden, *Philosophical Magazine*, 86 (2006), pp. 5567–5579.
7. M.D. Uchic et al., *Science*, 305 (2004), pp. 986–989.
8. J.R. Greer, W.C. Oliver, and W.D. Nix, *Acta Materialia*, 53 (2005), pp. 1821–1830; erratum *Acta Materialia*, 54 (2005), p. 1705.
9. D. Kiener, C. Motz, and G. Dehm, *J. Materials Science*, 43 (2008), pp. 2503–2506.
10. S.P. Lacour et al., *Applied Physics Letters*, 82 (2003), pp. 2404–2406.
11. S. Wagner et al., *Physica E*, 25 (2004), pp. 326–334.
12. S.P. Lacour et al., *J. Applied Physics*, 100 (2006), pp. 14913–1.
13. S.P. Lacour et al., *Proceedings of the IEEE*, 93 (2005), pp. 1459–1467.
14. S.P. Lacour, C. Tsay, and S. Wagner, *IEEE Electron Device Letters*, 25 (2004), pp. 792–794.
15. G. Eda et al., *Nature Nanotechnology*, 3 (2008), pp. 270–274.
16. S.H. Ko et al., *Nanotechnology*, 18 (2007), 345202.
17. E. Manard et al., *Applied Physics Letters*, 84 (2004), pp. 5398–5400.
18. R.A. Street et al., *Materials Today*, 9 (2006), pp. 32–37.
19. S.R. Forrest, *Nature*, 428 (2004), pp. 977–918.
20. J.A. Rogers et al., *PNAS*, 98 (2001), pp. 4835–4840.

21. Z. Bao, *Advanced Materials*, 12 (2000), pp. 227–230.
22. H. Jiang et al., *Int. J. Solids Struct.*, 45 (2000) pp. 2014–2023.
23. J. Song et al., *J. Vac. Sci. Technol. A*, 27 (2009), pp. 1107–1125.
24. C. Tsay et al., *Mater. Res. Soc. Symp. Proc.*, 875 (2005), pp. 05.5.1.
25. J. Yoon et al., *Applied Physics Letters*, 90 (2007), 211912.
26. N. Lu et al., *Applied Physics Letters*, 91 (2007), 221909.
27. N. Lu et al., *J. Materials Research*, 24 (2) (2009), pp. 379–385.
28. M.B. Tucker and T. Li, *Int'l. J. Applied Mechanics*, 1 (2009), pp. 557–568.
29. S.P. Lacour et al., *Applied Physics Letters*, 88 (2006), 204103.
30. Y. Xiang, T.Y. Tsui, and J.J. Vlassak, *J. Materials Research*, 21 (2006), pp. 1607–1618.
31. R.P. Vinci and J.J. Vlassak, *Annual Review of Materials Science*, 26 (1996), pp. 431–462.
32. D. Son, J. Jeong, and D. Kwon, *Thin Solid Films*, 437 (2003), pp. 182–187.
33. H.D. Espinosa, B.C. Prorok, and M. Fischer, *J. Mechanics and Physics of Solids*, 51 (2003), pp. 47–67.
34. P.A. Gruber et al., *Acta Materialia*, 56 (2008), pp. 2318–2335.
35. T. Li et al., *Mechanics of Materials*, 37 (2005), pp. 261–273.
36. Y. Xiang et al., *Applied Physics Letters*, 87 (2005), pp. 161910–1–3.
37. A. Ishida and M. Sato, *Thin Solid Films*, 516 (2008), pp. 7836–7839.
38. F. Zeng et al., *J. Alloys and Compounds*, 477 (2009), pp. 239–242.
39. J.D. Yeager et al., *J. Neuroscience Methods*, 173 (2008), pp. 279–285.
40. M.J. Cordill et al., *Metallurgical and Materials Transactions A*, 41 (2009) pp. 870–875.
41. G. Rochat et al., *Thin Solid Films*, 437 (2003), pp. 204–210.
42. N.E. Jansson, Y. Leterrier, and J.A.E. Manson, *Engineering Fracture Mechanics*, 37 (2006), pp. 2614–2626.
43. N.E. Jansson et al., *Thin Solid Films*, 515 (2006), pp. 2097–2105.
44. J. Andersons et al., *Mechanics of Materials*, 39 (2007), pp. 834–844.
45. J. Andersons, S. Tarasovs, and Y. Leterrier, *Thin Solid Films*, 517 (2009), pp. 2007–2011.
46. Y. Leterrier, *Progress in Materials Science*, 48 (2003), pp. 1–55.
47. S. Frank et al., *Acta Materialia*, 57 (2009), pp. 1442–1453.
48. A. Kelly and W.R. Tyson, *J. Mechanics and Physics of Solids*, 13 (1965), pp. 329–350.
49. M.J. Cordill et al., *Acta Materialia*, (2009) submitted.
50. N. Tamura et al., *J. Synchrotron Radiation*, 10 (2003), pp. 137–143.
51. C.H. Ma, J.H. Huang, and H. Chen, *Thin Solid Films*, 418 (2002), pp. 73–78.
52. K.J. Martinschitz et al., *Thin Solid Films*, 516 (2008), pp. 1972–1976.
53. E. Eiper et al., *Acta Materialia*, 55 (2007), pp. 1941–1946.
54. G. Dehm et al., *Microelectronic Engineering*, 70 (2003), pp. 412–424.
55. T.J. Balk, G. Dehm, and E. Arzt, *Acta Materialia*, 51 (2003), pp. 4471–4485.
56. A. Taylor et al., *unpublished research* (2009).
57. S.H. Oh et al., *Nature Materials*, 8 (2009), pp. 95–100.
58. G. Dehm, M. Legros, and B. Heiland, *J. Materials Science*, 41 (2006), pp. 4484–4489.

Megan J. Cordill is with the Erich Schmid Institute of Materials Science, Austrian Academy of Science, and the Department of Materials Physics, Montanuniversität Leoben, Leoben, Austria; e-mail megan.cordill@oew.ac.at.

Applications of Porous Silicon Thin Films in Solar Cells and Biosensors

Priyanka Singh, Shailesh N. Sharma, and N.M. Ravindra

An overview of the applications of porous silicon (PS) thin films, as antireflection coatings (ARC) in silicon solar cells and transducers in biosensors, is presented. The reflectance spectra of PS films have been compared with other conventional ARCs (such as SiN_x , $\text{TiO}_2/\text{MgF}_2$ and ZnS), and optimal PS ARC with minimum reflectance has been obtained. The implementation of PS into an industrially compatible screen-printed (SP) solar cell by both the electrochemical etching (ECE) and chemical etching (CE) methods are reviewed. Porous silicon films, formed via ECE for short anodization times, on textured n^+ emitter of c-Si solar cell having SP front and back contacts, lead to improvements in the performance of solar cells and demonstrate their viability in industrial applications.

INTRODUCTION

Porous silicon (PS) is a sponge-like structure, composed of silicon skeleton permeated by a network of pores. Porous silicon can be obtained by anodization or etching of silicon in aqueous hydrofluoric (HF) solutions and was first discovered in 1956 by Uhlir at the Bell Laboratories.¹ Etching of silicon substrate generates a thin layer of porous silicon on the silicon substrate with pores as large as ~200 nm in diameter (as shown in Figure 1A), providing a large surface area for light trapping (in solar cell applications) and molecular interaction (in sensor applications) inside the porous layer. A scanning electron micrograph of such a PS film which has been formed on crystalline silicon (c-Si) substrate is shown in Figure 1A. The right side images illustrate the magnified top and cross-sectional view of the PS layer and clearly indicate the formed pores of diameter ~200 nm

in the PS film.² The potential of porous silicon for various technological applications such as optoelectronic devices,³ displays,⁴ photodetectors,⁵ and biosensors⁶ has been extensively investigated. Such devices can be fabricated by either varying the porosity of the PS film itself or by depositing other films on the PS film such as metals, semiconducting

oxides, or polymer films depending on the applications.⁷ The large surface-to-volume ratio of porous silicon gives it the ability to react with biochemical species and sense them readily. Recently, PS has attracted more attention due to its sensing properties and has been utilized in chemical, biological^{2,6,8-10} and gas¹¹⁻¹⁷ sensing applications. The advantages of PS sensors are their low cost, ability to operate at room temperature, and compatibility with traditional silicon device fabrication technology. Furthermore, interest in porous silicon in the solar cell industry has grown over the last decade.¹⁸⁻²³

See the sidebar for a discussion of the formation and morphology of porous silicon.

APPLICATION OF POROUS SILICON AS ARC IN SILICON SOLAR CELLS

As shown in Figure 2A, bare silicon surface reflects more than 30% of the incident sunlight. These reflection losses can be reduced by texturization (it is an important step during solar cell fabrication, which makes silicon surface textured) and by depositing a suitable ARC on the top surface of the solar cell, reflection losses are reduced. This is shown in Figure 2A. The ARC effect relies on destructive interference of waves reflected at the top and bottom of the ARC, as shown in Figure 2B. It can be seen from Figure 2B that PS_1 and PS_2 are two ARCs formed on c-Si solar cell via ECE formation results in a very low reflectance in a certain wavelength range, which for photovoltaic applications must lie between 650 and 700 nm.²⁸

For example, in Figure 2A, PS_2 shows ~5% reflectance in the wavelength range of 650 and 700 nm. For an

How would you...

...describe the overall significance of this paper?

An overview of the applications of porous silicon (PS) thin films as antireflection coatings (ARC) in silicon solar cells and transducers in biosensors is presented. The implementation of PS into an industrially compatible screen-printed solar cell by both the electrochemical etching and chemical etching methods are reviewed.

...describe this work to a materials science and engineering professional with no experience in your technical specialty?

The use of porous silicon in solar cells and biosensors is described. In particular, the study focuses on the utility of porous silicon as anti-reflection coatings in solar cells.

...describe this work to a layperson?

In recent years, there has been a growing interest in renewable energy sources. Solar energy represents a non-polluting, naturally available source of energy. Silicon is abundantly available in nature in the form of silica. Silicon solar cells represent the largest component that facilitates the conversion of sunlight to electricity. However, silicon reflects a fraction of the incident light (~33%) which then gets wasted. Anti-reflection coatings help to minimize reflection losses. In the manuscript, we describe the use of porous silicon as an anti-reflection coating.

optimal ARC on a silicon substrate, the required refractive index and thickness is given by:

$$n_{ARC} = \sqrt{n_{Si} n_{air}} \quad (1)$$

$$d_{ARC} = \frac{\lambda_{min}}{4n_{ARC}} \quad (2)$$

where, n_{Si} is the refractive index of c-Si which depends on wavelength (3.84 at 650 nm, 3.76 at 700 nm), and n_{air} is the refractive index of air. According to Equation 1, the refractive index (n) of an optimized ARC material on silicon should be equal to 1.96 at 650 nm and 1.94 at 700 nm.²⁸ Hence, from Equations 1 and 2, an ARC thickness (d) of 83 nm (90 nm) is required to produce a zero net reflectance at 650 nm (700 nm).

Table 1 summarizes the available ARC materials and their refractive indices.^{29,30} In order to cover a broad range of the solar spectrum, double layer anti reflection coatings (DLARC) have been investigated by several authors.^{31–33} Higher refractive index materials (from 2.2 and 2.6) are preferred as bottom layer films and lower refractive index materials (from 1.3 to 1.6) are generally used as top layer films in DLAR coatings. MgF_2/ZnS , MgF_2/TiO_2 , and SiO_2/SiN , have been reported as DLAR coating materials.³⁴ Canham et al.²⁴ have established that a PS film used as an ARC should be 60% porous to exhibit an optimal n_{ARC} value. The PS refractive index varies from 1.25 to 3;^{24,35} therefore, the additional capability of PS films as single and double layer ARC is evident.

Figure 3 shows the reflectance of PS films along with other ARCs, such as double layer TiO_2/MgF_2 , SiN_x and ZnS .^{20,35–37} In Figure 3A–C, PS films are formed on n^+ emitter of multicrystalline silicon (mc-Si), SP solar cell. In Figure 3D, PS films are formed on n^+ emitter of SP c-Si solar cell. In Figure 3A, PS films are formed via chemical etching³⁵ and in Figure 3B–D, PS films are formed via electrochemical anodization using a two-electrode arrangement.^{20,36,37} The detailed description of these studies has been presented in the literature.^{20,35–37}

Reflectance of Porous Silicon Films

Figure 3A shows the reflectance characteristics of a mc-Si solar cell with (a) PS and (b) double layer (TiO_2/MgF_2) ARC.^{20,35} This study has been performed by a group at Fraunhofer-ISE (ISE) on commercial cells from ASE GmbH.²⁰ The lower reflectance of PS ARC than that of the double layer (TiO_2/MgF_2) ARC, in the wavelength range of ~600–700 nm, clearly exhibits its better anti-reflecting properties for applications in solar cells.³⁵

In a recent study by Kwon et al.,³⁶ the

FORMATION AND MORPHOLOGY OF POROUS SILICON

Formation

The most common method for fabricating porous silicon (PS) is the electrochemical etching (ECE) of silicon in HF based electrolyte. The electrolyte contents used for PS formation may vary substantially. However, the electrolyte is generally a mixture of aqueous HF and ethanol (CH_3CH_2OH). Ethanol is used as a surfactant to facilitate extraction of hydrogen bubbles formed during etching.^{20,24} Electrochemical anodization is usually performed in an especially designed Teflon cell, using a two-electrode arrangement as shown in Figure 1B. The back of the silicon wafer is held strongly in contact with a metallic copper plate which acts as anode. The PS formation process is performed at a constant current density. The platinum electrode acts as cathode which is positioned in the electrolyte above the silicon surface that is to be etched. The PS film fabricated using this method is generally homogenous in both porosity and thickness.²⁴

An alternative method for processing PS is stain or chemical etching (CE) which requires the dipping of silicon substrate in a solution of HF, nitric acid (HNO_3), and water (H_2O). No external bias is used in this process.²⁴ Nevertheless, the PS formed using this method is inhomogeneous in both porosity and thickness due to the fact that hydrogen gas evolved during formation remains on the surface of the wafer.²⁵ However, PS formation by stain-etching is particularly attractive because of its simplicity and is useful to produce very thin PS films.²⁶ Archer²⁶ has revealed that it is possible to create stain films as thin as 25 Å through stain etching with HF- HNO_3 solution.

Figure A shows the morphology of three PS films prepared for HF concentrations of (a) 12.5%, (b) 16.7%, and (c) 25%, in which PS films are prepared by electrochemical etching on p type c-Si wafer. The scanning electron micrograph of the surface of PS film (a), in Figure A, reveals its highly porous nature; film (b) exhibits lower porosity. The top view of the film (c) surface reveals no porous structure even at the largest magnification; on the other hand, many large cracks have been observed. PS films prepared at a current density of 10 mA cm^{-2} and HF concentrations higher than 25% showed surface morphology similar to sample (c).²⁷

Morphology

Porous silicon morphology (i.e., pore size, porosity, and pore depth) depends on the type of silicon wafer, its resistivity, method of PS formation (i.e., ECE or CE) and on process conditions such as current density, HF concentration, HF: C_2H_5OH ratio in ECE and HF: HNO_3 ratio in CE.^{24,27} Figure A shows the morphology of three PS films prepared for HF concentrations of (a) 12.5%, (b) 16.7%, and (c) 25%, in which PS films are prepared by electrochemical etching on p type c-Si wafer. The scanning electron micrograph of the surface of PS film (a), in Figure A, reveals its highly porous nature; film (b) exhibits lower porosity. The top view of the film (c) surface reveals no porous structure even at the largest magnification; on the other hand, many large cracks have been observed. PS films prepared at a current density of 10 mA cm^{-2} and HF concentrations higher than 25% showed surface morphology similar to sample (c).²⁷

Figure A. Top view scanning electron micrographs of three PS films fabricated in etching solutions with different HF concentrations: (a) 12.5%, (b) 16.7%, and (c) 25%. Anodization current is 10 mA cm^{-2} .²⁷

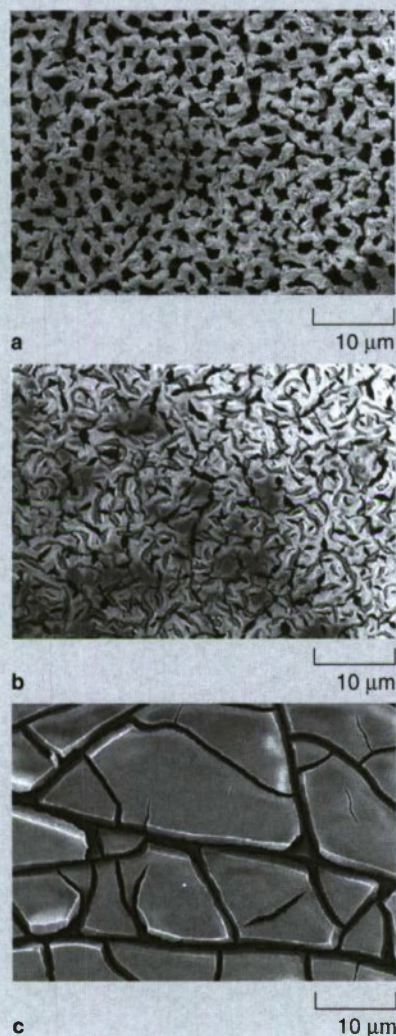


Table I. Refractive Indices (n) for Various Antireflection Coating Materials Corresponding to Wavelength of 650 to 700 nm^{29,30}

Material	Refractive Index (n)
CeO	1.95
CeO ₂	2.30–2.40
Al ₂ O ₃	1.80–1.90
Glass	1.50–1.70
MgF ₂	1.30–1.40
MgO	1.74
Si ₃ N ₄	1.90
SiO	1.80–1.90
SiO ₂	1.46
TiO ₂	2.30
Ta ₂ O ₅	2.10–2.30
ZnS	2.33

reflectance of (a) PS ARC is found to be quite comparable to the reflectance of (c) conventional SiN_x ARC on a (b) textured mc-Si in the wavelength range of ~600–700 nm (Figure 3B). It can be seen that PS ARC shows a minimum reflectance of ~3.1% at 570 nm and SiN_x ARC shows a minimum reflectance of ~2.0% at 730 nm. As a result, PS ARC demonstrates optical performance that is superior to vacuum-deposited SiN_x ARC film. In addition, PS is formed uniformly on the entire area of the mc-Si wafer.³⁶

The reflectance of a solar cell with an optimized (a) PS ARC and (b) with a SiN ARC is shown in Figure 3C. In this work, PS has been formed on mc-Si solar cells with a very large area (100–164 cm²). It is clearly seen that similar reflectance is obtained for PS and for the conventional SiN_x ARC.²⁰ This indicates the advantages of PS as ARC to make solar cells cost effective.

The reflectance spectra of the c-Si solar cells with ARCs (a) PS₁, (b) PS₂, (c) ZnS, and (d) without ARC, in the wavelength range of 360–600 nm are shown in Figure 3D.³⁷ PS₁ and PS₂ are two porous silicon films deposited on n⁺ emitter of c-Si solar cells at different charge densities $Q_1 = 0.06 \text{ C/cm}^2$ and $Q_2 = 0.9 \text{ C/cm}^2$, respectively. It can be seen that, in the entire investigated range of wavelengths, the reflectance of the samples with (a) PS₁, (b) PS₂ ARC is less, compared to (c) ZnS ARC and (d) without ARC. It is clear that, in the wavelength range of 550–600 nm, both PS₁ and PS₂ show significantly less reflectance³⁷ and, hence, PS exhibits good

anti-reflecting properties in solar cell applications.

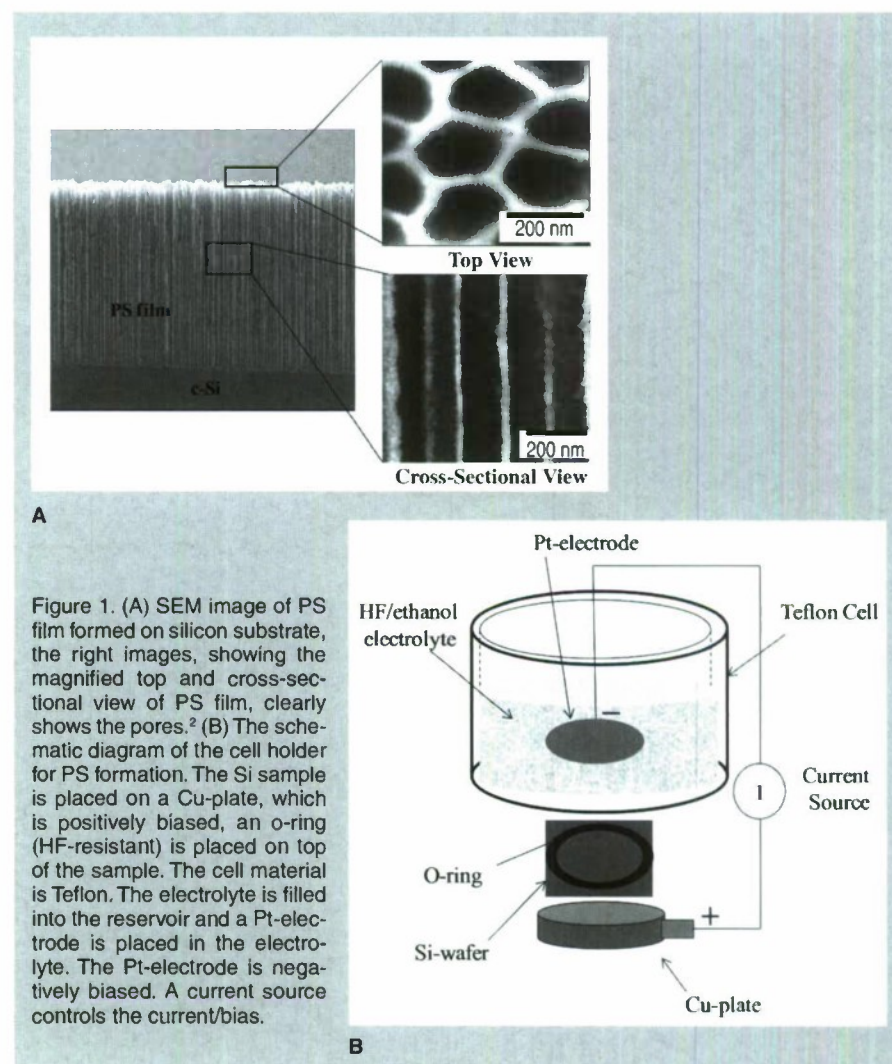
In this work, we have formed PS films via ECE technique in a mixture of HF and C₂H₅OH (1:1 by volume) using Si as the anode and Pt as the counter electrode as shown in Figure 1B. PS has been formed on n⁺ textured emitter of c-Si SP solar cell (area~10 cm²) at varying current density (J-10-40 mA cm⁻²) and time (t-20 s to 60 s). Figure 2A shows the reflectance spectra of two such PS films; PS₁ and PS₂ along with bare and textured silicon surfaces as a function of wavelength in the range 400–1,100 nm. PS₁ corresponds to current density (J) of 10 mAcm⁻² and time (t) of 30 s whereas PS₂ corresponds to J = 20 mAcm⁻² and t = 20 s. It can be seen from Figure 2A that PS₂ ARC shows lower reflectivity values in the most useful part of the solar spectrum ($\lambda_{\text{min}} = 650\text{--}700 \text{ nm}$) as compared to PS₁. Therefore, it is important to note here that an optimal PS can be obtained

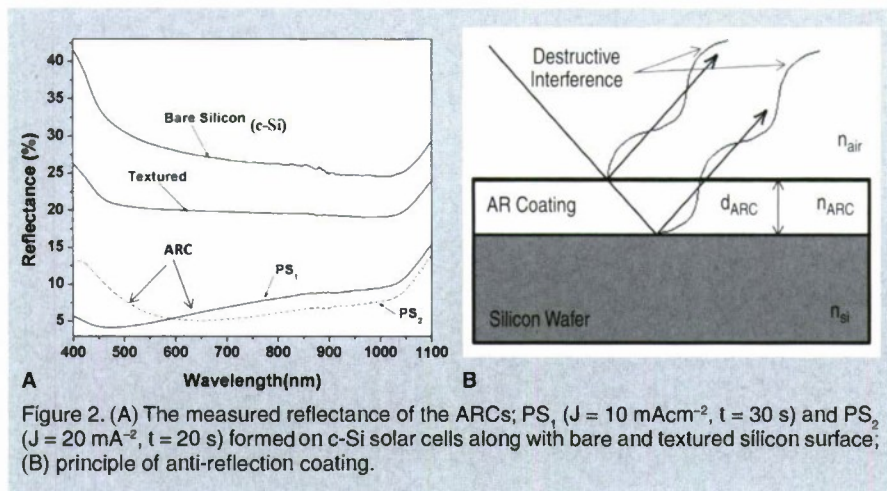
by varying current density and time.

These results clearly indicate that PS can be implemented as ARC in industrial solar cells and can possibly replace other conventional single and double layer ARCs.

Application of Porous Silicon in Industrial Solar Cells

Industrial solar cells are generally fabricated on large area (~100 cm²) Cz c-Si or mc-Si substrates using low-cost processing techniques to obtain a relatively good efficiency at reduced cost. Typical efficiency of commercially produced c-Si solar cells lies in the range of ~13–17%. The efficiency of solar cells depends on processing techniques and influence the production cost at all production stages. Therefore, substantial effort is directed toward efficiency improvement. The industrial solar cell processing steps involve texturization, phosphorous diffusion (to make p-n junction), realization of front and back





contacts using screen printing techniques followed by deposition of antireflection coating. The schematic representation of one such c-Si solar cell by Sun Power is shown in Figure 4,³⁸ where the expected solar cell efficiency is ~29%. However, various losses such as reflection, recombination and resistive losses reduce the cell efficiency to 14.7%. It can be seen from Figure 4 that the total losses account for 14.3%, wherein 1.8% of the reflection losses are due to front metallic grid structure and 0.4% reflection losses are after texturization and ARC deposition. The main attraction of porous silicon in the photovoltaic (PV) industry is to use it as a cost effective ARC for large-scale applications. The main advantage of PS as an ARC (as discussed in the preceding section) is well known; it reduces the reflection losses resulting from the silicon surface. Furthermore, PS has a large active area and is capable of light down-shifting in energy or photon energy down-converter (ultraviolet to visible). The use of PS films in solar cells has led to a reduction in the surface recombination velocity, enhancement of the spectral response in the short-wavelength region, and increase in the photogeneration velocity of charge carriers.^{18–24} Porous silicon can also serve as a wide bandgap absorber in a multiple-junction cell structure, with c-Si as the substrate.²⁴ Attempts have been reported to use two PS films with two different bandgaps in a three-bandgap solar cell on a silicon wafer.³⁹

Porous silicon ARC formed via ECE or CE on finished solar cells has a serious problem of fill factor degradation due to the increase in series resistance (R_s). Screen printed metalized contacts make direct contact with HF solution

during PS formation and therefore degrade the quality of the SP contacts. In order to avoid this degradation problem, the following two approaches can be adopted. In the first approach, ECE can be performed for a short time and this seems to be more convenient for large-scale implementation of PS in finished SP solar cells.²⁰ In the second approach PS formation can be done on the heavily doped n^+ emitter surface prior to the contact metallization step.²⁰ However, it is very difficult to obtain a stable ohmic contact on PS layer because of the large surface state density.⁴⁰ Therefore, ECE on finished solar cells, for short times seems to be a better option to obtain a homogenous PS ARC. Moreover, in ECE by varying the current density and time, it is possible to obtain PS films with varying refractive indices and thicknesses.³⁵ Both the methods have been applied to SP silicon solar cells.^{20,35,36,41,42} The results of PS ARC implementation using chemical and electrochemical methods in industrial mc-Si solar cell processing are presented in these studies.^{20,35,36,41–43} We have formed PS ARC for short anodization times via ECE on finished solar cells. Solar cells have been fabricated on c-Si (p-type) wafer using industrial processing steps as described above and have silver fingers on the front side and Ag-Al contact on back side.

A research group at the Università Roma Tre (RM3)⁴³ and a group from Fraunhofer-ISE (ISE)³⁵ implemented stain-etched PS ARC on screen printed mc-Si solar cell that is currently used in the PV industry. RM3 used the solar cells from Eurosolar S.p.A.⁴³ whereas ISE used commercial cells from ASE GmbH.³⁵ The electrochemical method has been applied by Interuni-

versity Microelectronics Center, Belgium (IMEC) and Centre National de la Recherche Scientifique–Laboratoire de Physique des Solides de Bellevue (CNRS-LPSC).²⁰ The efficiency potential of a PS ARC has been investigated by the Interuniversity Microelectronics Center, Belgium on high-quality FZ Si substrates ($2 \times 2 \text{ cm}^2$).²⁰ Centre National de la Recherche Scientifique–Laboratoire de Physique des Solides de Bellevue focuses on the formation of PS ARC for commercial mc-Si solar cells ($5 \times 5 \text{ cm}^2$) and the PS film is formed at a constant current density of 50 mA cm^{-2} for 3.5 s. The details of solar cell processing and PS formation are described in the following publications.^{20,43} From our recent studies, it is found that the properties of PS formed using screen-printed silver and aluminum as the back contacts are superior as compared to the corresponding films with evaporated back contacts.^{44–46} The PS films formed with screen-printed silver and aluminum-back contacts show better crystalline perfection, higher stability, higher Photoluminescence (PL) efficiency and negligible PL decay compared to that formed with evaporated silver and aluminum as the back contact for the same current density and time of anodization. The results conclusively demonstrate the viability of screen-printing contact technology for the possible application of PS films in Si-solar cells.^{44–46}

Table II summarizes the measured photovoltaic performance parameters; current density (J_{sc}), open circuit voltage (V_{oc}), fill factor (FF) and efficiency (η) under global AM1.5 illumination for chemical and electrochemical etching on mc-Si solar cells before and after PS formation. In chemical etching, the efficiency of ISE solar cells increases after PS formation; however, the fill factor degraded which may be attributed to the increase in R_s , mainly due to the interaction of HF acid with glass-containing silver paste in SP contacts.³⁵ In the RM3 cells, the metallization is protected by a polymeric film which explains the smaller degradation of R_s , and hence the achieved higher FF and efficiency.⁴³ In electrochemical etching, it can be seen from Table II that efficiency of 14.6% and 13.2% has been obtained on the solar cells of IMEC and CNRS-LPSB, respectively. After PS formation, fill

factor does not change in IMEC solar cells, whereas fill factor increases for CNRS-LPSB. The characteristics of the cell ($5 \times 5 \text{ cm}^2$ Polix mc-Si) with the PS film (η -13.2%) are similar to commercial cells.²⁰ Table II also lists the results obtained for optimal PS ARC (PS₂-Figure 2A), implemented on a screen printed c-Si solar cell. It has led to ~20.8% relative improvement in J_{sc} , a significant gain of ~15mV in V_{oc} and a relative increment of about ~3% in FF. This yields a ~26% increase in efficiency. In a study by Kwon et al.,³⁶ the optimization of a PS selective emitter in a screen printed mc-Si ($2 \times 2 \text{ cm}^2$) solar cell results in a 13.2% efficiency with electroplating.³⁶

Thus, PS has immense potential as ARC in commercial solar cell application. Simplicity and low cost of the ECE technique as well as its adaptation to silicon solar cell manufacturing provides a very promising technology in an industrial process.

Characterization of Porous Silicon Films

The surface morphology of PS films has been studied by scanning electron microscope (SEM) and atomic force microscope (AFM). Figure 5A and B

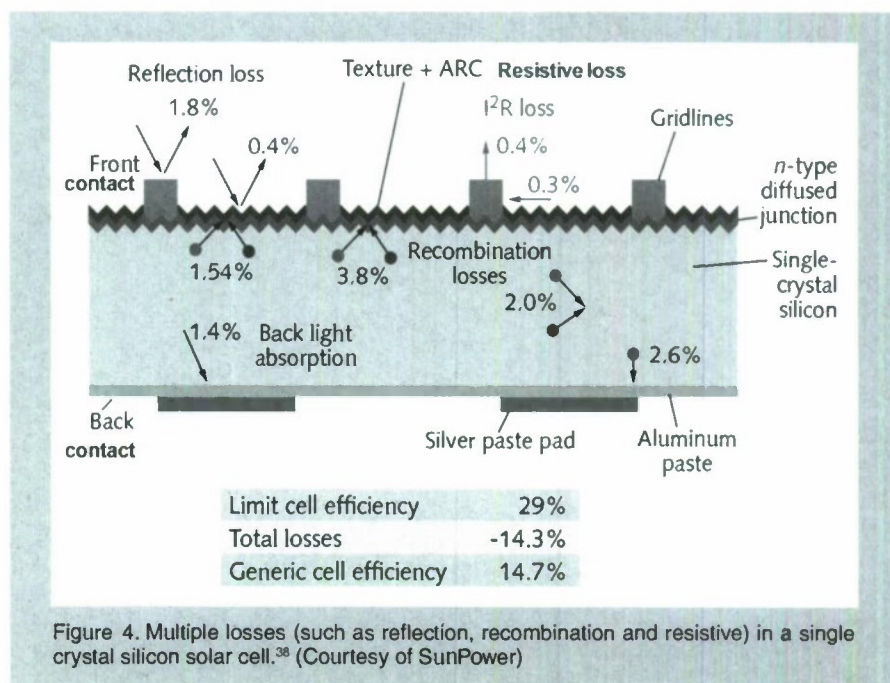


Figure 4. Multiple losses (such as reflection, recombination and resistive) in a single crystal silicon solar cell.³⁶ (Courtesy of SunPower)

shows surface morphology, as seen by SEM and AFM for film PS₂, which has been formed on n⁺ emitter of textured c-Si solar cell. As can be seen from Figure 5A, the textured surface shows uniform large pyramids of sizes varying from 1 to 10 μm approximately. The SEM image indicates that the front screen printed silver finger has not been damaged after PS formation. Figure 5B shows

three-dimensional (3-D) picture of PS layer, which consists of irregular upright surface features with typical size distribution of ~150–500 nm or even smaller, where the maximum pore size is ~500 nm long and ~50 nm wide whereas the minimum pore size is ~150 nm long and ~30 nm wide. Such types of structures are generally observed in PS films.²⁴

Fourier transform infrared (FTIR) analysis is widely used to characterize the bonding properties in PS films. Here, we present FTIR and photoluminescence (PL) spectra on PS films of various thicknesses, formed on p type c-Si wafer via ECE. In this work, PS films of various thicknesses are formed at optimized current density (J) of 20 mA cm^{-2} with time (t) variation from 1 to 20 minutes, respectively.⁴⁵ As current density increases, the thickness of PS film increases.⁴⁴ The PS films of various thicknesses, (a)–(e) in Figure 6A and B, are formed at a constant J of 20 mA cm^{-2} and at time $t = 1 \text{ min.}, 2 \text{ min.}, 5 \text{ min.}, 20 \text{ min.},$ and $30 \text{ min.},$ respectively.⁴⁵ The thickness of PS films, (a) and (b), are ~150 nm and ~200 nm, respectively, as measured by an ellipsometer; for films (c)–(e), the thickness varies from 5 to 20 μm as estimated from gravimetric measurements.¹⁸ Corresponding FTIR and PL spectra are recorded for these PS films (Figure 6A and B).

Figure 6A shows the FTIR spectra of PS films of various thicknesses (a)–(e). During PS formation, a large number

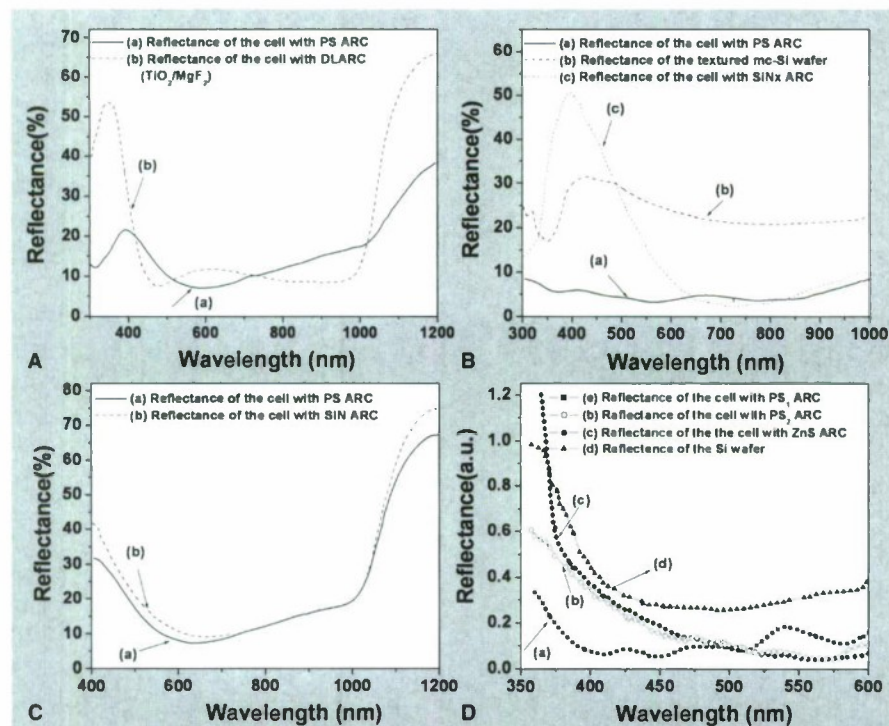
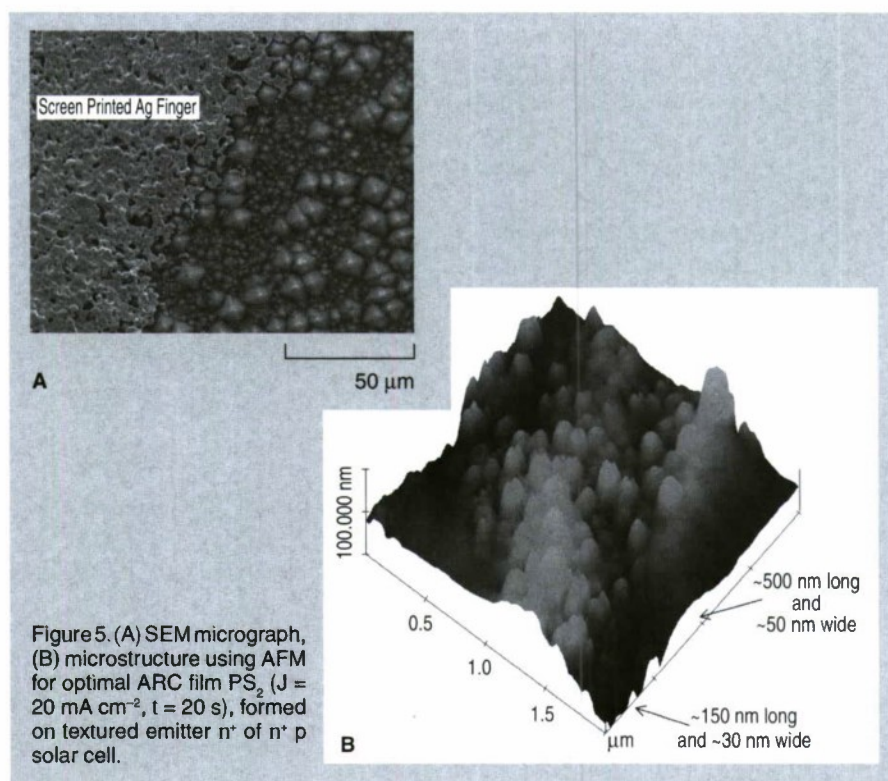


Figure 3. (A) Reflectance characteristics of cells with (a) PS ARC and (b) double film ($\text{TiO}_2/\text{MgF}_2$) ARC;^{20,35} (B) reflectance characteristics of (a) PS ARC (b) alkaline-textured mc-Si wafer, and (c) single-film SiN_x ARC;³⁶ (C) reflectance characteristics of mono-Si cells with (a) PS ARC and (b) with conventional SiN_x ARC;²⁰ (D) reflectance spectra of samples with ARCs (a) PS₁, (b) PS₂, (c) ZnS and (d) without ARC.³⁷

of Si-hydride bonds as well as Si-hydroxide bonds are formed and possibly passivate the Si/PS interface.⁴⁷ It can be seen in Figure 6A that PS films exhibit mainly Si-H related modes at $\sim 2101\text{ cm}^{-1}$ due to Si-H stretching mode, $\sim 910\text{ cm}^{-1}$ due to Si-H₂ scissors or Si-H₃ symmetric or antisymmetric deformation, doublet $\sim 666\text{ cm}^{-1}$ and 627 cm^{-1} due to Si-H₂ and Si-H wagging while Si-O related modes are marked by very weak signatures at $\sim 1,035\text{ cm}^{-1}$ due to a bulk interstitial Si-O-Si asymmetric stretching model.^{18,20,45}

As the thickness of PS films increase (i.e., FTIR spectra from (a)–(e)), a clear increase in both line-width and intensity of these modes can be seen. This indicates the relatively higher hydrogen content in the PS films as thickness increases. However, for very thin PS films, (a), and (b), the FTIR spectra shows only weak signatures of these bands. The distinct presence of Si-H stretching mode at $\sim 2,101\text{ cm}^{-1}$ represents the quality of passivation for PS films (d) and (e). Small peak at $\sim 2,308\text{ cm}^{-1}$ can be related to O back-bonded to Si in Si-H stretching mode.⁴⁸ Similar FTIR results on PS films are also discussed in the Reference 20.

Figure 6B shows the corresponding room temperature PL spectra of these PS films (a)–(e). The thin porous silicon film (a) does not exhibit any PL properties which may be attributed to the weak signals of Si-H bands in the FTIR spectra. However, a weak PL can be seen



for PS films (b) and (c) which may be attributed to the increase in intensity of Si-H and related bands in the FTIR spectra. The absence of PL properties in PS film (a), and weak PL for films (b) and (c) are apparently due to the silicon skeletons not being narrow enough for quantum confinement. The PL intensity increases as PS film thickness increases (from (a)–(e)) as shown in Figure 6B and a sharp peak at $\sim 688\text{ nm}$ has been obtained for the PS films (d) and (e) corresponding to 10 and 30 minutes of PS formation. The increase in the corre-

sponding normalized PL peak intensity is correlated with the increase in the Si-H and Si-H₂ bonds observed in the FTIR spectra. Therefore, it is worthwhile to note here that SEM, AFM, PL and FTIR studies are important characterization techniques to investigate the structural and passivating properties of PS films.

APPLICATIONS OF POROUS SILICON IN BIOSENSORS

Biosensors have emerged as highly promising for rapid diagnosis of bacteria in foods. The general function of a biosensor is to convert a biological recognition event into an electrical or optical signal.^{49,50} Signal transduction has been accomplished with electrochemical,⁵¹ field-effect transistor,⁵² optical absorption, fluorescence and interferometric devices.⁵³ As discussed previously,^{2,6,8–17} a number of theoretical and experimental works, concerning the noteworthy properties of nanostructured porous silicon in chemical and biological sensing, have been reported, showing that, due to its morphological and physical properties, PS is a very versatile sensing platform.^{2,6,8–17}

In our recent studies, we observed that PS films formed on textured substrates show higher PL intensity and higher lifetime values as compared to those formed on polished substrates for the same current density.⁵⁴ Porous sili-

Table II. Measured Photovoltaic Parameters; Current Density (J_{sc}), Open Circuit Voltage (V_{oc}), Fill Factor (FF), and Efficiency (η) under Global AM1.5 Illumination on Solar Cells using Chemical and Electrochemical PS Formation²⁰

PS Process	Cells From	ARC	Area	J_{sc} (cm^2)	V_{oc} (mAcmm^{-2})	FF (mV)	η (%)
Chemical	ASE (ISE)	No ARC	100	22.3	575	0.774	9.9
	ASE (ISE)	PS ARC	100	28.9	574	0.740	12.3
	(Eurosolare)						
	RM3	No ARC	164	22.4	588	0.685	9.0
	RM3	PS ARC	164	27.2	592	0.753	12.1
Electrochemical	(ASE GmbH)						
	IMEC	PS ARC	4	30.4	603	0.78	14.3
		(non-textured)					
	IMEC	PS (textured)	4	31.3	601	0.78	14.6
	CNRS-LPSB	No ARC	25	31.6	595	0.73	13.6
	CNRS-LPSB	PS ARC	25	30.4	583	0.74	13.2
	Present work	No ARC	10	19.7	545	0.67	7.15
	Present work	PS ARC	10	23.8	560	0.68	9.01

con layers and their interfaces have been characterized by recording diffraction curves and measuring lattice mismatch/strain and the radius of curvature due to induced biaxial stress caused by the lattice expansion of PS film due to pores.⁵⁵ The higher range of strain values exhibited by PS films on textured specimens corresponding to a wide range of band gaps compared to that formed on polished specimens indicates that stable and higher porosity PS films can be formed on textured substrates at higher current densities. The larger surface area available for PS films formed on textured substrates enables the even distribution of strain, thus, leading to enhanced stability as compared to the corresponding films formed on polished specimens.⁵⁵ This factor is responsible for PS films formed on textured substrates to withstand higher strain without any elastic relaxation at high current densities and can be used for gas-sensing measurements.⁵⁶ In the case of PS films on polished specimens, the relaxation of the induced strain starts at relatively lower current densities as compared with PS films on textured substrates and thus is not suitable for gas-sensing applications.

The surface of porous silicon needs to be stabilized for biosensing applications and is achieved by means of oxidation, silanization, or hydrosilylation.^{57,58} Even without resorting to the above techniques, PS surface can be stabilized using an appropriate post-anodization treatment. At an optimum current density, passivation of defects by a novel nascent-H treatment resulted in the significant enhancement in the PL efficiency.⁵⁹ The degraded PL intensity in the treated samples upon prolonged oxidation for several months was higher as compared to that for the as anodized samples. Infrared vibrational studies indicated that the enhancement in PL was due to the H-passivation of defects in the Si-pore interface as also elucidated from capacitance-voltage studies.⁵⁹ Furthermore, it has been found that HF-treated PS surfaces are relatively stable against oxidation as compared to untreated PS films.⁶⁰ Upon oxidation of the HF treated PS films, the PL intensity initially increases as a result of reduction in crystallite size to exhibit quantum size effects and then decreases owing to loss of luminescing

structures due to over-oxidation of the silicon columns. It can be inferred that the surface passivation either by hydrogen or oxygen is one of the requisite conditions for obtaining strong PL efficiency in PS.⁶¹ It seems that more than one emission mechanisms are responsible to explain the luminescence properties of PS.⁶⁰

Furthermore, PS biosensor technology has shown great capability in detecting biological molecules with high selectivity, using specific linker agents and probe molecules.⁶¹ For the biomedical applications of PS, biomolecules have to be first immobilized on its surface through functional groups deposited on it. The common approach is to create a covalent bond between the PS surface and the biomolecules which specifically recognize the target analytes.⁶¹ The reliability of a biosensor strongly depends on the functionalization process as well as its rapidity, simplicity, homogeneity, and repeatability.⁶² It is well known that, after anodization, the fresh silicon surface is predominately hydride-terminated which is quite reactive and sensitive to oxidation.⁶² Thus, to increase the

surface stability of PS, there is a need to functionalize the surface of PS by a suitable precursor. In one of our recent works, nanostructured PS surface was biofunctionalized by thermally depositing thin biocompatible films with a large density of amine groups, using 3-aminopropyltriethoxysilane (APTS) on to its surface.⁶³ The aim of the study was to demonstrate the covalent bonding between organic molecules (immunoglobulin) and modified inorganic surface (nanostructure PS) which can be used for the detection of protein signals. In this study, PS films prepared at an optimized $J \sim 50 \text{ mA cm}^{-2}$, having high PL intensity, stable surface bond configurations, mechanically strong structure and hydrogen-passivated surfaces were used for APTS treatment.⁶³ The presence of reactive amino groups on the PS surface along with glutaraldehyde as a linker aids in the covalent binding of the antibody (Human IgG) onto the PS surface.⁶³ Different antigen concentrations can be detected with a good reproducibility with this technique which opens a possibility of using this biofunctionalized material for future biosensors.

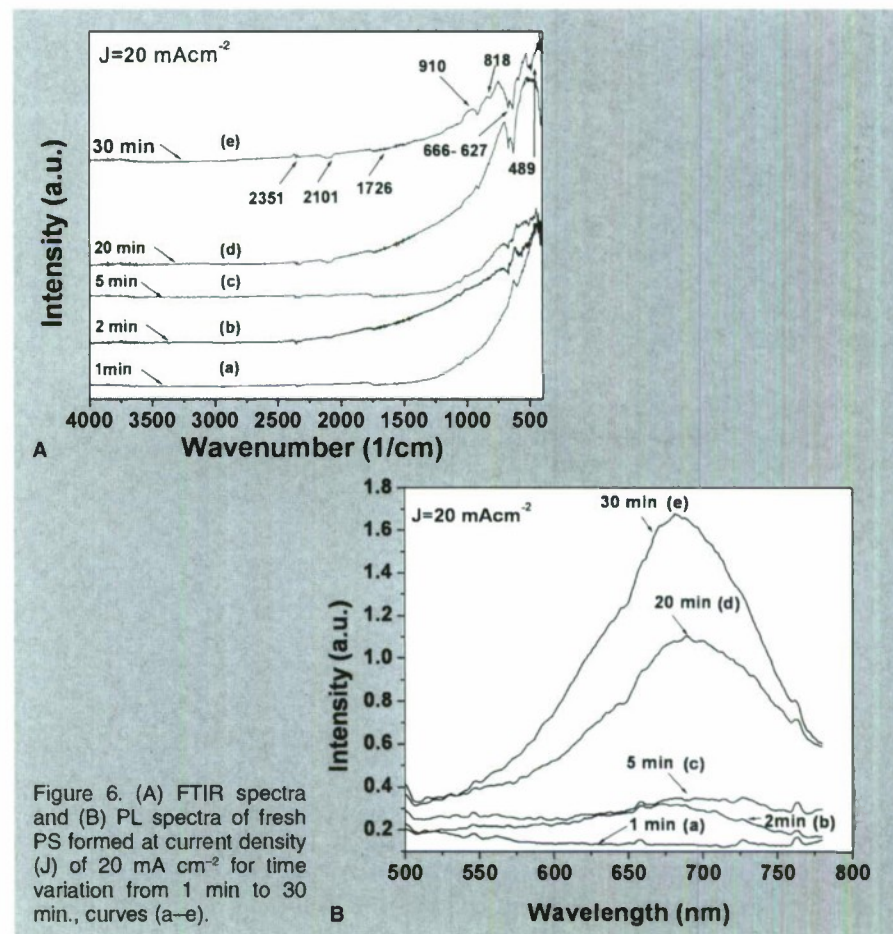


Figure 6. (A) FTIR spectra and (B) PL spectra of fresh PS formed at current density (J) of 20 mA cm^{-2} for time variation from 1 min to 30 min., curves (a–e).

In recent developments, the process of filling the PS pores with metallic, dielectric or semiconducting oxide, enzyme, or molecular receptor films, has resulted in PS sensors that are capable of detecting penicillin, alkali metal ions, humidity, and hydrocarbons.⁶⁴ In a paper by Jane et al.,⁶⁵ numerous PS biosensors are discussed. One category of biosensor belongs to interference effects in PS single and double layers; the second category discusses the photoluminescence-based transduction; third category is based on PS microcavities and fourth category discusses the electrochemical transduction with porous silicon. The PS biosensors of different categories are compared on the basis of their performance, such as: concentration range, sensitivity for analyte and their detection limit.⁶⁵

Silicon Kinetics has introduced nano PS biosensor and chips to monitor biomolecular interactions,⁶⁶ where a nanoporous region has been formed on a c-Si wafer via electrochemical etching. Figure 7A shows the principle of nanoporous biosensor, which is based on the

changes in refractive index in the PS layer, when light reflected from the top of the porous region interferes with light reflected from the bottom of the porous region and creates optical interference patterns. The optical path difference signal (OPD signal) is derived from the interferogram as in Figure 7B and rises proportionately with the amount of bound biomolecules. As can be seen in Figure 7B, the first step is to immobilize the first biomolecule of interest i.e., the target on sensor surface (with the desired surface chemistry) and, then, the solution with the second biomolecule of interest i.e., the analyte is introduced; any net binding of the analyte to the target changes the effective index of refraction in the porous region as biomolecules displace buffer solutions with lower indices of refraction.⁶⁶

The simplest example of optical interferometric PS biosensor is shown in Figure 8A⁶ which monitors changes in the refractive index that occur in PS single- or double-layer films, wherein PS films are made via electrochemical etching of p type c-Si wafer. In this sensor,

binding of molecules induces changes in the refractive index of the porous silicon films.⁶ The biosensor has been demonstrated for small organic molecules (biotin and digoxigenin), 16-nucleotide DNA oligomers, and proteins (streptavidin and antibodies) at pico- and femtomolar analyte concentrations. The sensor is also highly effective for detecting single and multi molecular assemblies.⁶

Another example is a porous silicon biosensor chip, fabricated by Mathew et al.,¹⁰ which detects *Escherichia coli* (*E. coli*) bacterium and is based on the light emitting properties of porous silicon. In this work, PS films are made via electrochemical etching of p type c-Si wafer and the biosensor adapts single-tube chemiluminescence-based assay for detection of *E. coli*.¹⁰ The reaction of β -galactosidase enzyme from *E. coli* with the dioxetane substrate generates light at 530 nm. Figure 8B shows the light emission of a control porous silicon biosensor chip (blank with no *E. coli* culture) as well as that of porous- and planar-silicon biosensor chips tested with an overnight *E. coli* pure culture. As shown in Figure 8B, the porous silicon biosensor chip has higher light emissions compared to the planar silicon biosensor chip due to the higher surface area of the porous chip.¹⁰ Sensitivity of the porous silicon biosensor is determined to be 10^1 – 10^2 colony forming units (CFU) of *E. coli*.

A potentiometric biosensor for the detection of triglycerides for metabolomics has been developed by Setzu et al.⁶⁷ In this study, PS layers are formed on n^+ type c-Si wafer by electrochemical etching. This biosensor immobilizes lipase enzyme in the PS layer and it induces hydrolysis of a triglyceride, which in turn results in a decrease in the pH and hence shifts the open circuit potential. This approach of immobilization of the enzyme within PS layer considerably increases the working life of the sensor as compared to other lipase-based triglyceride-detection methods.

A label-free optical biosensor for the detection of rabbit IgG (rabbit polyclonal antibody) in whole blood using a PS microcavity has been reported by Bonanno et al.⁶⁸ Porous silicon microcavities are formed via ECE into highly doped n-type silicon. Shift in wavelength enables the sensor to detect antibodies in either

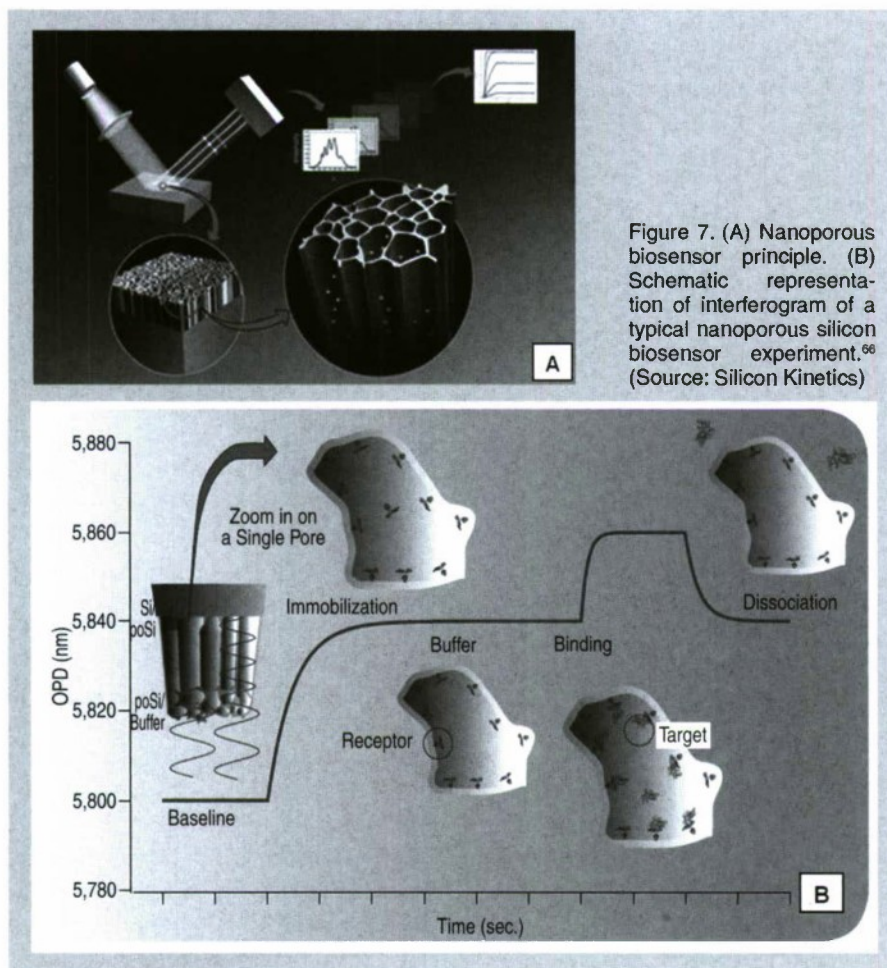


Figure 7. (A) Nanoporous biosensor principle. (B) Schematic representation of interferogram of a typical nanoporous silicon biosensor experiment.⁶⁶ (Source: Silicon Kinetics)

undiluted serum or whole blood.⁶⁸ Immobilization of antibody on PS surface is done by using biotin-streptavidin. The biosensor has exhibited linear detection range of 2–10 mg/mL.

Another example of PS microcavity sensor has been reported by Ouyang et al.,⁶⁹ in which macroporous silicon microcavities were electrochemically synthesized from n-type c-Si wafers. This sensor is operated by analyzing the induced red-shift in the absorbance peak which is caused by the binding of an analyte to an immobilized probe molecule. The device detects an extracellular domain of intimin (intimin-ECB), a protein associated with the pathogenicity of enteropathogenic *Escherichia coli*. Immobilization has been carried out by attaching probe molecules: Tir-IBD, the translocated intimin receptor-intimin binding domain, covalently to the PS surface. Intimin-ECB can be detected in a concentration of 4 μ M after optimizing the concentration of probe molecules.

Rossi et al.⁷⁰ have developed a new method for improving the sensitivity for detection of the bacteriophage virus MS2 using thin films of nanoporous silicon. The PS films are prepared using ECE technique on polished p⁺-c-Si wafer. They have shown that a 100 nm thick PS layer with a covalently immobilized antibody has a sensitivity and dynamic range similar to that of the Luminex liquid array-based assay while outperforming protein micro-array methods.⁷⁰

A porous silicon optical biosensor has been developed for monitoring protein-protein binding, specifically protein A with IgG.⁷¹ Thin film of (5 μ m) PS has been used for immobilization and transducing matrix and the sensor operates by measurement of the Fabry–Perot fringes in the white light reflection spectrum from the PS layer. Analyte binding causes change in effective optical thickness of functionalized porous silicon Fabry–Perot film and thus transduction is achieved. Sensor demonstrates its stability, reversibility and insensitivity to nonspecific interactions.

Recently, a Fourier transformed reflectometric interference spectroscopy (FT-RIFS) PS biosensor has been reported by Shang et al.⁷² In this setup, double layers of porous silicon films have been prepared by ECE on p-type c-Si wafers and used as a sensing element for the

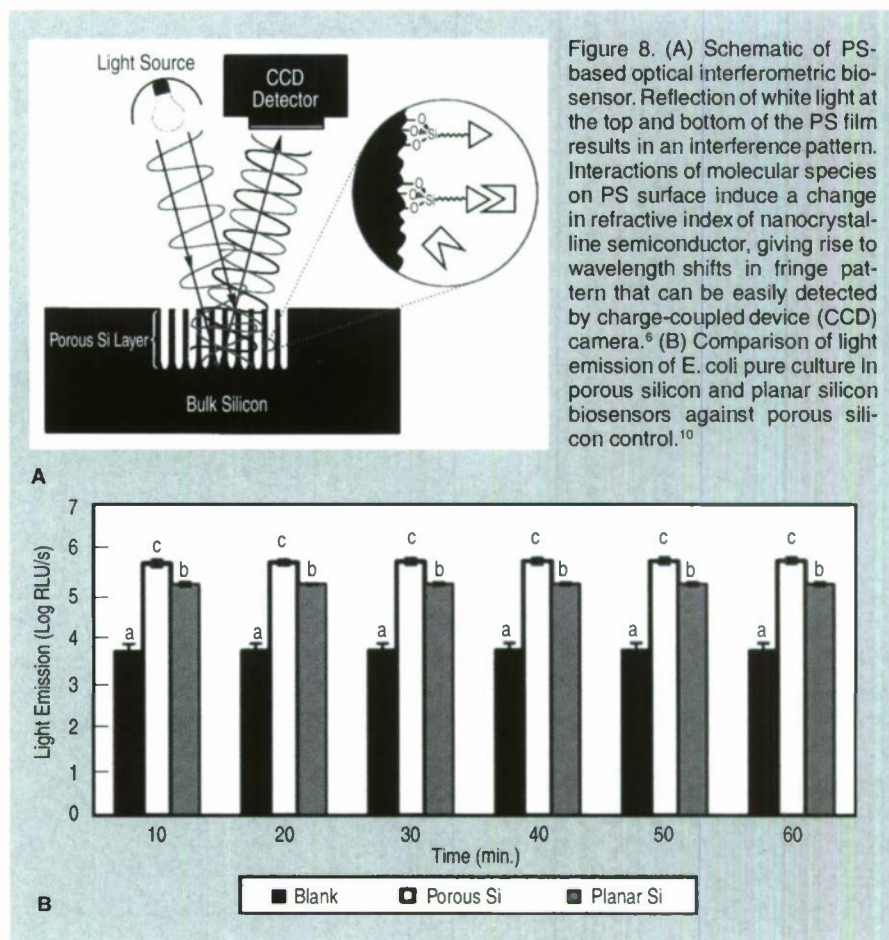


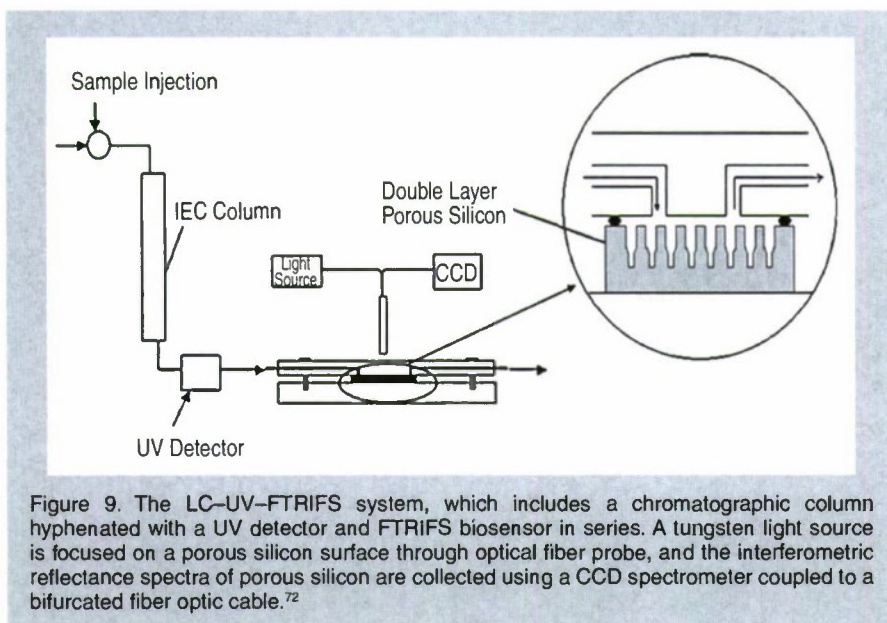
Figure 8. (A) Schematic of PS-based optical interferometric biosensor. Reflection of white light at the top and bottom of the PS film results in an interference pattern. Interactions of molecular species on PS surface induce a change in refractive index of nanocrystalline semiconductor, giving rise to wavelength shifts in fringe pattern that can be easily detected by charge-coupled device (CCD) camera.⁶ (B) Comparison of light emission of *E. coli* pure culture in porous silicon and planar silicon biosensors against porous silicon control.¹⁰

detection of target molecule by FT-RIFS, where trypsin and its inhibitor are used as the model probe-target system. The FT-RIFS biosensor has been combined with a UV detector for screening the target molecule from complex component mixtures separated by a LC (liquid chromatography) column, as shown in Figure 9. The outer PS layer, attached with trypsin by amino-silane and glutaraldehyde, can specifically bind with the trypsin inhibitor and acts as a sample channel, while the bottom layer serves as a reference signal channel. The binding event between trypsin and trypsin inhibitor is simultaneously detected by the FT-RIFS biosensor in real-time by monitoring the change in optical thickness of the porous silicon layer. Optical signals have a linear relationship with the concentration of trypsin inhibitor in the range of 10–200 ng mL⁻¹.⁷²

CONCLUSIONS

Porous silicon has a large potential for applications in photovoltaics. Reflectance of PS film is quite comparable to the reflectance of conventional ARCs (such as SiN_x, double layer TiO₂/MgF₂ and ZnS). The PS film can be easily

implemented as ARC into an industrially screen-printed solar cell by both the electrochemical and chemical etching. PS films, formed via ECE for short anodization times are applied on textured n⁺ emitter of c-Si having SP front and back contacts. Implementation of optimal PS ARC has led to ~20.8% relative improvement in J_{sc}, a significant gain of ~15 mV in V_{oc} and a relative increment of about ~1.3% in FF. This yields a ~26% increase in efficiency. PS films formed on textured c-Si substrates exhibit higher porosity and PL efficiency, negligible PL decay, better mechanical strength, adherence to the substrate, non-fractured surface morphology and lower stress compared to porous silicon formed on polished c-Si substrates at the same current density and demonstrate the viability of possible application of PS films in Si-solar cells. PS surface morphology on textured emitters in solar cells, as seen by SEM, shows that PS formation does not degrade the unprotected front metallic grid pattern. AFM measurements of PS ARC on textured emitters in solar cells reveal that the maximum pore size is ~500 nm long and ~50 nm wide whereas the minimum



pore size is ~150 nm long and ~30 nm wide. Fourier transform infrared and PL spectra are utilized to characterize the PS films of various thicknesses. Fourier transform infrared results show passivating capabilities of PS films and, therefore, allow fabricating solar cells without an additional passivation coating. The study of the optical properties by PL spectra show that the increase in the PL intensity may be attributed to the presence of Si-H and Si-H₂ bonds with increase in PS film thickness.

Porous silicon biosensors based on optical interferometry and light emitting properties are discussed. For an optimized current density, the functionalization of the PS surface has been achieved by silanization method using APTS as a precursor. The presence of reactive amino groups on the PS surface along with glutaraldehyde as the linker aids in the covalent binding of the antibody (Human IgG) onto the PS surface leading to detection of different antigen concentrations with a good reproducibility.

References

1. A. Uhler, *Bell Syst. Tech. J.*, 35 (1956), p. 333.
2. H. Ouyang et al., *Adv. Funct. Mater.*, 15 (2005) p. 1851.
3. B. Hamilton, *Semicond. Sci. Technol.*, 10 (1995), p. 1187.
4. V.V. Doan and M.J. Sailor, *Science*, 256 (1992), p. 1791.
5. M.J. Sailor, J.L. Heinrich, and J.M. Lauerhaas, *Semicond. Nanocrystals*, ed. P.V. Kamat and D. Meisel, (New York: Elsevier, 1996), p. 103.
6. V.S.Y. Lin et al. *Science*, 278 (1997), p. 840.
7. V. Parkhutik, *Solid State Electron.*, 43 (1999), p. 1121.
8. L. De Stefano et al., *Sensors*, 7 (2007) p. 214.
9. S.M. Weiss et al., *Opt. Express*, 13 (2005), p. 1090
10. F.P. Mathew and E.C. Alcolija, *Biosensors Bioelec-*

tron., 20 (2005), p. 1656.

11. F. Besseuile et al., *Biosens. Bioelect.*, 21 (2005), p. 908.
12. C. Pacholski et al., *J. Am. Chem. Soc.*, 127 (2005), p. 11636.
13. K. Watanabe, et al., *Sens. Actuat. B: Chem.*, 33 (1996), p. 194.
14. A. Foucaran et al., *Thin Solid Films*, 297 (1997), p. 317.
15. C. Baratto et al., *Sens. Actuators B: Chem.*, 65 (2000), p. 257.
16. L. Boarino et al., *Mater. Sci. Eng. B*, 69-70 (2000), p. 210.
17. C. Baratto et al., *Sens. Actuators B: Chem.*, 77 (2001), p. 62.
18. A.G. Cullis, L.T. Canham and P.D. Calcott, *J. Appl. Phys.*, 82 (1997), p. 909.
19. S. Bastide et al., *Sol. Eng. Mater. Sol. Cells*, 57 (1999), p. 393.
20. R. R. Bilyalov et al., *Sol. Eng. Mater. Sol. Cells*, 65 (2001), p. 477.
21. A. Krotkus et al., *Sol. Eng. Mater. Sol. Cells*, 45 (1997), p. 267.
22. L. Stalmans et al., *Sol. Eng. Mater. Sol. Cells*, 58 (1999), p. 237.
23. Z. Swiatek et al., *Mater. Sci. Eng. B*, 101 (2003), p. 291.
24. L. Canham, *Properties of Porous Silicon* (London: INSPEC, 1997).
25. K.H. Beckmann, *Surface Science*, 3, (1965) p. 324.
26. R.J. Archer, *J. Phys. Chem. Solids*, 14 (1960), p. 14.
27. J. Dian et al., *App. Surf. Sci.*, 238 (1-4) (2004), p. 169.
28. S. Strehlke et al., *Mat. Sci. Eng. B*, 69-70, (2000), p. 81.
29. B.J. Thompson, *Thin Films for Optical Systems* (New York: Marcel Dekker Inc., 1995), p. 295.
30. M.A. Green, *Solar Cells* (Upper-Saddle River, NJ: Prentice-Hall Inc., 1982), p. 164.
31. J. Zhao and M.A. Green, *IEEE Trans. Elect. Dev.*, 38 (1991), p. 1925.
32. Z. Chen et al., *IEEE Trans. Elect. Dev.*, 40 (1993), p. 1161.
33. G. Zhang, J. Zhao, and M.A. Green, *Sol. Eng. Mater. Sol. Cells*, 51 (1998), p. 393.
34. S.E. Lee, S.W. Choi, and J. Yi, *Thin Solid Films*, 376 (2000), p. 208.
35. R.R. Bilyalov et al., *Proc. 26th IEEE Photovol. Spec. Conf.*, (Piscataway, NJ: IEEE, 1997) p. 147.
36. J.H. Kwon, S.H. Lee, and B.K. Ju, *J. Appl. Phys.*, 101 (2007), 104515.
37. Z.N. Adamian et al., *Sol. Eng. Mat. Sol. Cells*, 64 (2000), p. 347.

38. S. Eglash, *Laser Focus World*, 45 (12) (2009), p. 39.
39. L. Kore and G. Bosman, *Sol. Eng. Mater. Sol. Cells*, 57 (1999), p. 31.
40. D. Deresmes et al., *Thin Solid Films*, 255 (1995), p. 258.
41. M. Schnell, R. Lüdemann, and S. Schaefer, *Proc. 16th Eur. Comm. Photovol. Sol. Eng. Conf.*, ed. James and James (London: Earthscan Publications Ltd., 2000), p. 1482.
42. R.J. Martin-Palma et al., *Semicond. Sci. Technol.*, 16 (2001), p. 657.
43. L. Schirone et al., *Proc. Sec. World Conf. Photovol. Eng. Conv.*, (1998), p. 276.
44. Priyanka Singh, "Fabrication, Characterization and Other Related Studies for Performance Improvement of Crystalline Silicon Solar Cells" (Ph.D. Thesis, National Physical Laboratory and Jamia Millia Islamia, New Delhi, India, 2008).
45. Priyanka Singh et al., *Sol. Eng. Mat. Sol. Cells*, 9 (2007), p. 1510.
46. P. Singh et al., *Adv. Mater. Res.*, 31 (2008), p. 249.
47. K.H. Jung, S. Shih, and D.L. Kwong, *J. Electrochem. Soc.*, 140 (1993), p. 3046.
48. S.N. Sharma, R.K. Sharma, and S.T. Lakshmikumar, *Physica E*, 28 (2005), p. 264.
49. T.M. Cahn, *Biosensors* (London: Chapman & Hall, 1993).
50. N.M. Ravindra et al., *JOM*, 59 (12), (2007) p. 37.
51. J.J. Hickman et al., *Science*, 252 (1991), p. 688.
52. H.M. McConnell et al., *ibid.*, 257 (1992), p. 1906.
53. A. Brecht and G. Gauglitz, *Biosens. Bioelectron.*, 10 (1995), p. 923.
54. S.N. Sharma et al., *Mater. Sci. and Eng. B*, 127 (2006), p. 255.
55. G. Bhagavannarayana et al., *Mater. Chem. and Phys.*, 97 (2-3), (2006), p. 442.
56. S.N. Sharma et al., *Physica E-Low-Dimens. Sys. & Nanostr.*, 36 (1), (2007), p. 65.
57. A. Janshoff et al., *J. Am. Chem. Soc.*, 120 (1998), p. 12108.
58. J.M. Buriak et al., *J. Am. Chem. Soc.*, 121 (1999), p. 11491.
59. S.N. Sharma et al., *Appl. Surf. Sci.*, 182 (2001), p. 333.
60. S.N. Sharma, R. Banerjee, and A.K. Barua, *Curr. App. Phys.*, 3 (2003), p. 269.
61. L. Mongo et al., *Anal. Bioanal. Chem.*, 385 (2006), p. 146.
62. L. De Stefano et al. *J. Opt. A: Pure Appl. Opt.*, 8 (2006), p. S540.
63. S. Singh et al., *J. Mater Sci: Mater. Med.*, 20 (2009), p. 181.
64. M.P. Stewart and J.M. Buriak, *Adv. Mater.*, 12 (2000), p. 859.
65. A. Jane et al., *Trends in Biotech.*, 27 (2009), p. 230.
66. Silicon Kinetics, Inc., 10455 Pacific Center Court, San Diego, CA 92121; www.siliconkinetics.com/.
67. S. Setzu et al., *Phys. Stat. Solidi A: Appl. Res.*, 204 (2007) p. 1434.
68. L.M. Bonanno and L.A. De Louise, *Biosens. Bioelectron.*, 23 (2007), p. 444.
69. H. Ouyang et al., *Anal. Chem.*, 79 (2007), p. 1502.
70. A.M. Rossi et al., *Biosens. Bioelectron.*, 23 (2007), p. 741.
71. K.P.S. Dancil, D.P. Greiner, and M.J. Sailor, *J. Am. Chem. Soc.*, 121 (1999), p. 7925.
72. Y. Shang et al., *Biosens. Bioelectron.*, 25 (2010), p. 1056.

Priyanka Singh, researcher, and Nuggehalli Ravindra, professor and chair, are with the Physics Department, New Jersey Institute of Technology, 161 Warren Street, Newark, NJ 07102; Shailesh N. Sharma, scientist, is with the National Physical Laboratory, Electronic Materials Division, Semiconductor building, Dr. K.S. Krishnan Marg St., New Delhi 110012, India. Dr. Ravindra can be reached at (973) 596-5742; fax (973) 596-5794; e-mail nmravindra@gmail.com.

Effects of Substrate Temperature and RF Power on the Formation of Aligned Nanorods in ZnO Thin Films

Sudhakar Shet, Kwang-Soon Ahn, Ravindra Nuggehalli, Yanfa Yan, John Turner, and Mowafak Al-Jassim

We report on the effects of substrate temperature and RF power on the formation of aligned nanorod-like morphology in ZnO thin films. ZnO thin films were sputter-deposited in mixed Ar and N₂ gas ambient at various substrate temperatures and RF powers. We find that the substrate temperature plays more important role than RF power in the formation of ZnO nanorod-like morphology. At low substrate temperatures (below 300°C), ZnO nanorod-like morphology does not form regardless of RF powers. High RF power helps to promote the formation of aligned ZnO nanorod-like morphology. However, lower RF powers usually lead to ZnO films with better crystallinity at the same substrate temperatures in mixed Ar and N₂ gas ambient and therefore better photoelectrochemical response.

INTRODUCTION

Hydrogen is widely considered as the alternative to fossil fuels for producing and storing energy. The most-promising method of hydrogen production is photoelectrochemical (PEC) water decomposition using a source of renewable energy such as solar energy. The PEC decomposition of water is based on the principle that when two electrodes, at least one of which is a semiconductor, are immersed in an aqueous electrolyte and exposed to light, the absorbed light energy will be converted into electricity. This electricity is then used for water electrolysis.¹ In a typical PEC cell, the photoelectrode is made up of semiconductor material. When a photoelectrode is exposed to light, if the energy of the photons ($h\nu$) is equal to or larger than the bandgap of the semiconductor material, electron-hole pairs will form. These electrons and holes help in water oxidation and hydrogen reduction

to produce oxygen and hydrogen gas, respectively.¹

Photoelectrochemical systems based on transition metal oxides, such as TiO₂, ZnO, and WO₃, have received extensive attention since the discovery of photoinduced decomposition of water on TiO₂ electrodes.^{2–10} TiO₂ has been extensive-

ly studied. ZnO has a similar bandgap (~3.3 eV) and band-edge positions as compared to TiO₂. Furthermore, ZnO has a direct bandgap and higher electron mobility than TiO₂.⁹ Thus ZnO could also be a potential candidate for PEC splitting of water for H₂ production.¹⁰

To increase photocurrent, a photoelectrode should have a high contact area with the electrolyte to provide more interfacial reaction sites. Therefore, the morphological features of the thin films, such as grain size, grain shape, and surface area would have profound influence on the performance of thin film electrodes for PEC applications. It has been expected that electrodes with nanostructures would exhibit improved PEC performance as compared to those without nanostructures. Recently, ZnO electrodes with different nanostructures have been studied because of their potential applications in optoelectronic nanoscale devices. It has been reported that ZnO nanorods were synthesized using catalyst, and recently, catalyst-free ZnO nanorods have been synthesized by various chemical and physical techniques such as metal-organic vapor-phase epitaxy, plasma-enhanced chemical vapor deposition and pulsed laser deposition.^{11–14} In our earlier studies,¹⁵ we have found that aligned single crystal ZnO nanorods along the c-axis can be synthesized by radio frequency (RF) sputter-deposition in mixed Ar and N₂ ambient, and ZnO films with aligned nanorods exhibited improved performance as compared to ZnO films without nanorods. So far, RF sputtering is much less considered than other methods for the growth of ZnO nanorods. In RF sputtering, RF power, ambient gas, flow rate, and deposition temperature play a critical role in sputtering yield, which in turn determines the Zn/O ra-

How would you...

...describe the overall significance of this paper?

To date, the technologies for hydrogen generation using sources of renewable energy are in the incubation stage. However, there is a growing interest in developing hydrogen technologies that rely on renewable energy. The most-promising method of hydrogen production is photoelectrochemical water decomposition using renewable energy such as solar.

...describe this work to a materials science and engineering professional with no experience in your technical specialty?

Hydrogen is widely considered as the alternative to fossil fuels for producing and storing energy. Our current global economy depends heavily on fossil fuels, which are integral to agriculture, industry, transportation, and day-to-day life. Consequently, there has been intense effort to develop technologies based on the applications of hydrogen as a fuel, instead of fossil fuels.

...describe this work to a layperson?

Hydrogen is widely considered to be the fuel of the future. It has potential applications for nonpolluting vehicles, domestic heating, and aviation. The use of fuel cells powered by hydrogen generated by solar energy will reduce harmful emissions to nearly zero. Recently, hydrogen production through direct water splitting has become an important research area.

tio, and consequently growth rate. Variation in size and aspect ratio will result in nanostructures. Detailed examination on the deposition condition for ZnO nanorod growth and study of the ZnO nanorod-like morphology for PEC applications is needed.

In this paper, we report on effects of substrate temperatures and RF powers on the formation of aligned nanorod-like morphology in ZnO thin films. In

our study, ZnO nanorod-like nanostructures were grown by vapor growth. The growth of ZnO preferentially oriented nanorod-like nanostructures is most likely determined by the surface energies. Surfaces with high energies grow much slower than surfaces with low energies. The presence of nitrogen in the growth ambient can act as a reducing agent and change the surface energy, which in turn affects the morphology

of the nanostructures. The growth rate, which is related to the RF power applied to Zn target, can also affect the surface energies and consequently the morphology of the nanostructures. Fluorinated tin oxide (fluorinated doped tin oxide) substrates may affect the nucleation density, but may not play a critical role in influencing the morphology. ZnO thin films were sputter-deposited in mixed Ar and N₂ gas ambient at various substrate temperatures and RF powers. We find that the substrate temperature plays a more important role than RF power in the formation of ZnO nanorod-like morphology. At low substrate temperatures (below 300°C), ZnO nanorod-like morphology does not form regardless of RF powers. Above 300°C, aligned ZnO nanorod-like morphology starts to form with RF power of 200 and 300 W. With RF power of 100 W, aligned nanorods start to form at substrate temperatures above 400°C. In mixed Ar and N₂ gas ambient, lower RF powers usually result in higher crystallinity and therefore better PEC response.

See the sidebar for experimental procedures.

RESULTS AND DISCUSSION

Film Characterization

We first present the results of ZnO thin films grown at 100 W RF power and different temperatures (from 100 to 500°C). The x-ray diffraction (XRD) curves obtained from these films are shown in Figure 1a. No clear preferred orientation was observed for samples deposited at temperatures below 400°C, indicating no obvious formation of aligned nanorod-like morphology at these temperatures when 100 W RF power was applied. However, for samples deposited above 400°C, some degree of preferred orientation is observed. When the RF power was increased to 200 W, clear preferred orientation was observed at substrate temperatures of 400 and 500°C as shown in Figure 1b. Figure 1c shows XRD curves for the ZnO(Ar: N₂) (300 W) films deposited at 300 W RF power. The preferred orientation is also very clear for samples deposited at 400°C and 500°C. The measured full width at half maximum (FWHM) values of (002) peaks of these samples are shown in Figure 2a. The FWHM values are

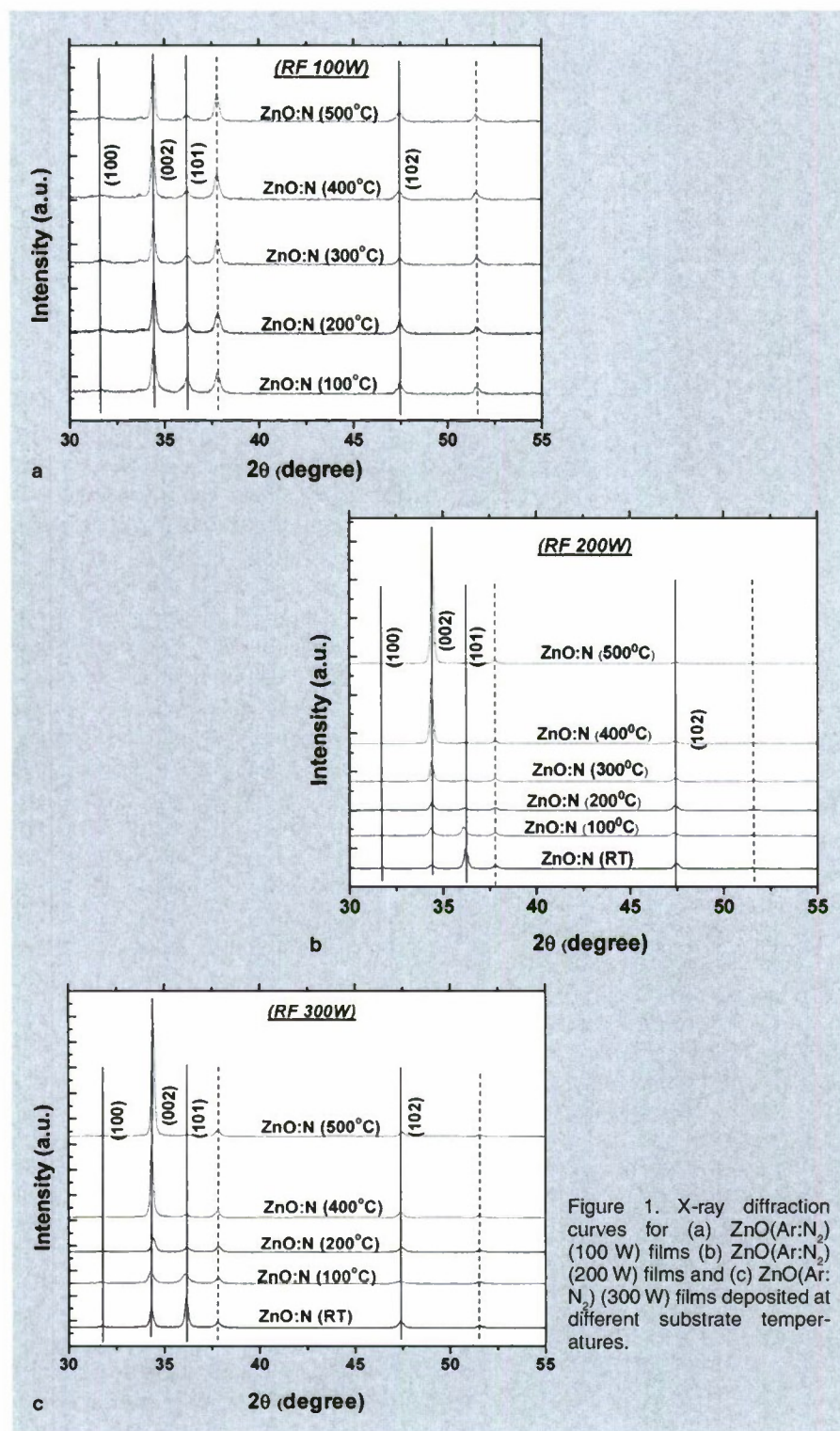


Figure 1. X-ray diffraction curves for (a) ZnO(Ar:N₂) (100 W) films (b) ZnO(Ar:N₂) (200 W) films and (c) ZnO(Ar: N₂) (300 W) films deposited at different substrate temperatures.

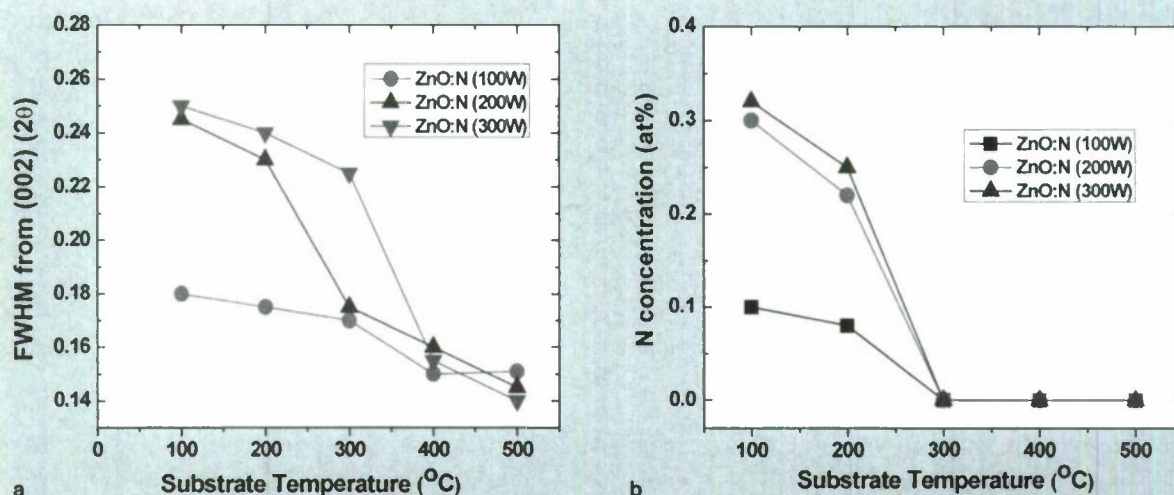


Figure 2. (a) FWHM values estimated from (0002) peaks for the ZnO(Ar:N₂) films. (b) Measured N concentrations for the ZnO(Ar:N₂) films as a function of the substrate temperature.

larger for ZnO(Ar:N₂) films deposited at temperatures below 300°C than that grown above 300°C with the same RF powers. It is also seen that at the substrate temperatures below 300°C, the higher RF powers lead to larger FWHM values. This is because N can be incorporated at substrate temperatures below 300°C and the incorporation of N leads to reduced crystallinity. Higher RF power leads to more N-incorporation and therefore larger FWHM values. At substrate temperature above 300°C, no clear N was incorporated. The crystallite size is increased from around 32 nm for 100°C deposition temperature to

around 68 nm for 100°C deposition temperature. In these cases, the crystallinity is independent of the RF power. The N concentrations (at.%) for the ZnO(Ar:N₂) films measured by XPS are shown in Figure 2b. With the increase in substrate temperature, the N concentration decreased rapidly and disappeared at temperatures above 300°C.

The preferred orientation observed from XRD gives an indication of the formation of nanorod-like morphology. The aligned growth of grains leads to rough surface and extension of grains showed a nanorod-like morphology. Atomic force microscopy (AFM) and

scanning electron microscopy (SEM) surface imaging were carried out to verify the formation of nanorod-like morphology. As an example, Figure 3 shows AFM surface morphology (5×5 μm²) of ZnO(Ar:N₂)(200W) films deposited at various substrate temperatures. It shows clearly that the ZnO(Ar:N₂) deposited at 100°C has a random orientation. As substrate temperature increases, aligned nanorod-like morphology along the c-axis were promoted to form. At 500°C, the ZnO(Ar:N₂) film reveals growth of hexagonal-like nanorod-like morphology. AFM images reveal that the significantly increased (002) peak in the

EXPERIMENTAL PROCEDURES

The ZnO(Ar:N₂) films were deposited by reactive RF sputtering a ZnO target using an Ar/Ni gas mixture. Transparent conducting F-doped SnO₂ (FTO) coated glass (20–23 Ω/□) were used as the substrate to allow photoelectrochemical (PEC) measurements. The detailed growth conditions can be found in our earlier publications. ZnO films were deposited at RF power of 100 W to 300 W and substrate temperature 100°C to 500°C. All the deposited samples were controlled to have similar film thickness of 0.5±0.05 μm for 100 W and 1±0.05 μm for 200 W and 300 W as measured by stylus profilometry.

The structural and crystallinity characterizations were performed by x-ray diffraction (XRD) measurements, using an x-ray diffractometer (XGEN-4000, SCINTAG Inc.), operated with a Cu Kα radiation source at 45 kV and 37 mA. The N concentration in the ZnO(Ar:N₂) films was evaluated by x-ray photoelectron spectroscopy (XPS). Monochromatic Al Kα radiation was used for all data sets, and the analyzer was set to 59 eV pass energy. Argon ion sputtering (3 keV, 0.8 μAmm⁻², 120 s) was used to clean samples prior to analysis.

The surface morphology was examined by atomic force microscopy conducted in the tapping mode with a silicon tip, and field emission scanning electron microscopy. The UV-Vis absorption spectra of the samples were measured by an n&k analyzer 1280 (n&k Technology, Inc.) to investigate the optical properties.

Photoelectrochemical measurements were performed in a three-electrode cell with a flat quartz-glass window to facilitate illumination to the photoelectrode surface.^{16–20} The sputter-deposited films were used as the working electrodes. Pt plate and an Ag/AgCl electrode were used as counter and reference electrodes, respectively. A 0.5-M Na₂SO₄ mild aqueous solution was used as the electrolyte for the stability of the ZnO.^{16–21} Photoelectrochemical response was measured using a fiber optic illuminator (150 W tungsten-halogen lamps) with an ultraviolet/infrared (UV/IR) filter. Light intensity was measured by a photodiode power meter, in which total light intensity with the UV/IR filter was fixed to 125 mW/cm².

Because the films were deposited on conducting substrates, measurements of electrical property by the Hall Effect were not possible. Instead, the electrical properties were measured by Mott-Schottky plots, which were obtained by alternating current (AC) impedance measurements. AC impedance measurements were carried out with a Solartron 1,255 frequency response analyzer using the above three-electrode cells. Measurements were performed under dark conditions with an AC amplitude of 10 mV and frequency of 5,000 Hz were used for the measurements taken under dark condition and the AC impedances were measured in the potential range of –0.7 V to 1.25 V (vs. Ag/AgCl reference). The series capacitor-resistor circuit model was used for Mott-Schottky plots.^{22,23}

XRD curve obtained in ZnO(Ar:N₂) at various RF powers is largely due to the formation of aligned nanorod-like morphology along the c-axis.

Figure 4 shows representative finite element-SEM top-view images of ZnO nanorod-like morphology deposited with varying RF powers. Figure 4a shows a SEM image of ZnO film deposited at 400°C with RF power of 100 W. It shows the formation of mixed pyramid-like ZnO and nanorod-like morphology ZnO, indicating that 400°C is the critical substrate temperature for the formation of ZnO nanorod-like morphology. Figures 4b and c show SEM images of ZnO thin films deposited at

500°C with RF powers of 200 W and 300 W, respectively. Vertically aligned, single crystal hexagonal-like nanorod-like morphology with flat (0002) surfaces are clearly seen in these ZnO(Ar:N₂) films. Thus, our results suggest that substrate temperature plays a more important role than RF power in the formation of aligned ZnO nanorod-like morphology. However, high RF power helps the formation of ZnO nanorod-like morphology. No metal clusters were found at the end of the nanorods, indicating that the growth mechanism is not the catalyst-assisted vapor-liquid-solid (VLS) growth.¹¹⁻¹³ The nanorod structures provide high surface areas

and superior carrier transport (or conductivity) along the c-axis, which may lead to increased interfacial reaction sites and the reduced recombination rate.^{24,25}

Photoelectrochemical Response

The PEC response for the ZnO(Ar:N₂) thin films deposited at various substrate temperatures and RF powers was also investigated. We found that ZnO samples with aligned nanorod-like morphology indeed exhibited higher photo-currents. For example, Figures 5a and b show photocurrent-voltage curves of the ZnO(Ar:N₂) films deposited at 200°C and 500°C, at 300W,

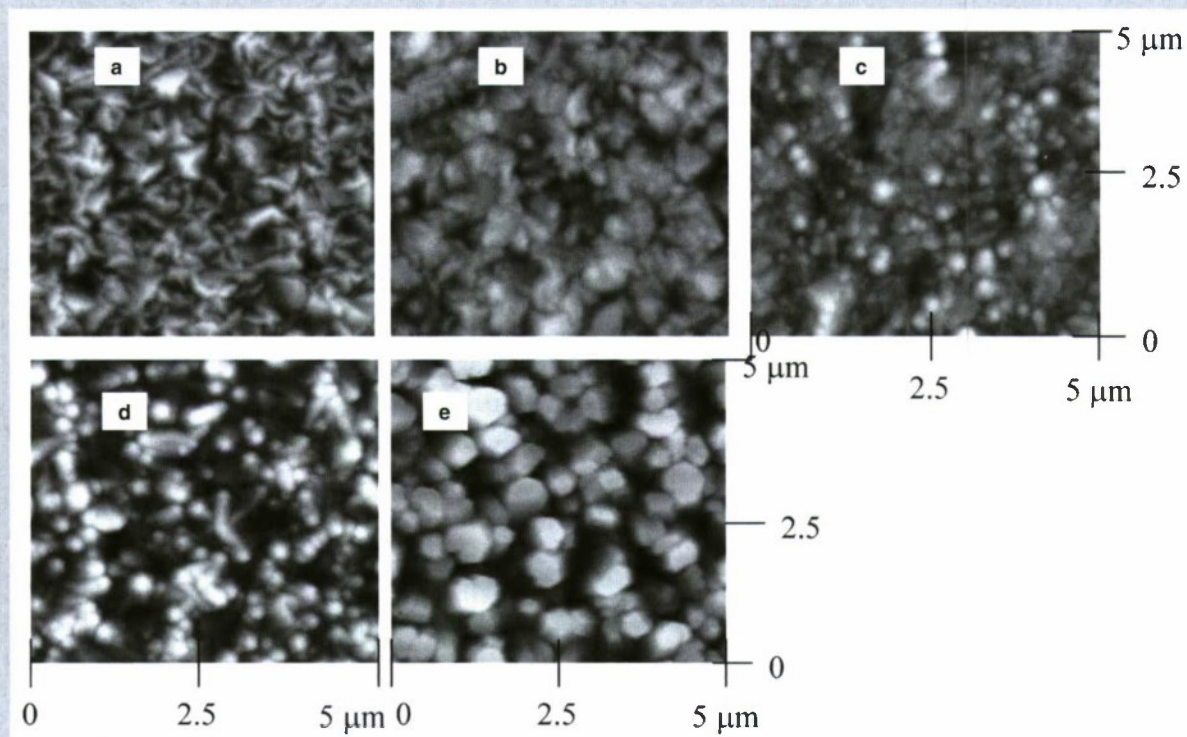


Figure 3. AFM surface morphology (5×5 μm²) of (a–e) the ZnO(Ar:N₂) (200 W) films deposited at the substrate temperatures of 100, 200, 300, 400, and 500°C, respectively.

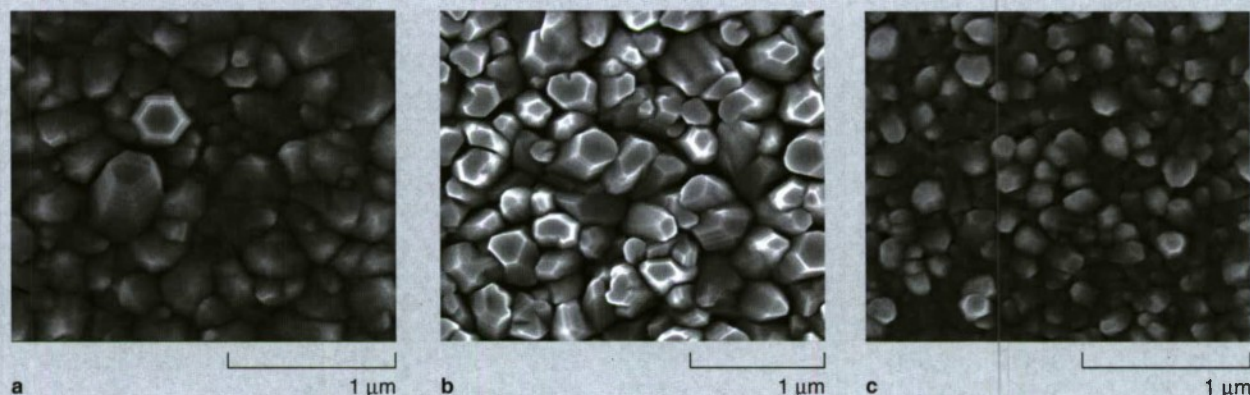


Figure 4. FE-SEM top-views of (a) ZnO(Ar:N₂) (100 W) deposited at 400°C, (b) ZnO(Ar:N₂) (200 W) deposited at 500°C, (c) ZnO(Ar:N₂) (300 W) deposited at 500°C.

respectively, under continuous illumination (curve 2), dark condition (curve 1), with an UV/IR filter. Both ZnO(Ar:N₂) films show very small dark currents up to potential of 1.25 V. It is seen that the ZnO(Ar/N₂) films deposited at 500°C (with nanorod-like morphology) exhibited much higher photocurrents than the films deposited at 200°C (without nanorod-like morphology).

To see the effects of substrate temperature and RF power on PEC response, we measured photocurrents at 1.2 V potential for ZnO(Ar:N₂) films under continuous illumination with UV/IR filter. Figure 6 shows the measured photocurrents as a function of the deposition temperature for the ZnO(Ar:N₂) films at various substrate temperatures and RF powers. It is seen that the substrate temperature plays an important role in determining the photo-current. For a given RF power, higher substrate temperatures lead to improved photocurrents. ZnO(Ar:N₂) films deposited at 400°C for 100 W and 500°C for 200 and 300 W exhibits the best photoelectrochemical response. This is because of the improved crystallinity and formation of aligned nanorod-like morphology at high substrate temperatures. The ZnO(Ar:N₂) films deposited at 400°C with RF power of 100 W shows slightly better photo-currents than the films deposited at 500°C with RF power of 200 W and 300 W. This is attributed to the better crystallinity of films deposited at 400°C, as indicated in Figure 2b. Thus, the rapid enhancement in PEC response of the ZnO(Ar:N₂) films is consistent with the XRD results indicating either increased crystallinity or formation of nanorod-like morphology along the c-axis.

Figure 7a shows XRD curves obtained from samples prepared at deposition temperature of 100°C with RF powers from 100 to 500W ZnO(Ar:N₂) films. The crystallinity of ZnO films decreases gradually with the increase in RF power. The measured FWHM values of the (002) peaks are shown in Figure 7b. Figure 7c shows the measured N concentrations (at.%) for these ZnO(Ar:N₂) films. The FWHM values correlate very well with the N concentration and RF power, i.e., when RF power increases, FWHM value and

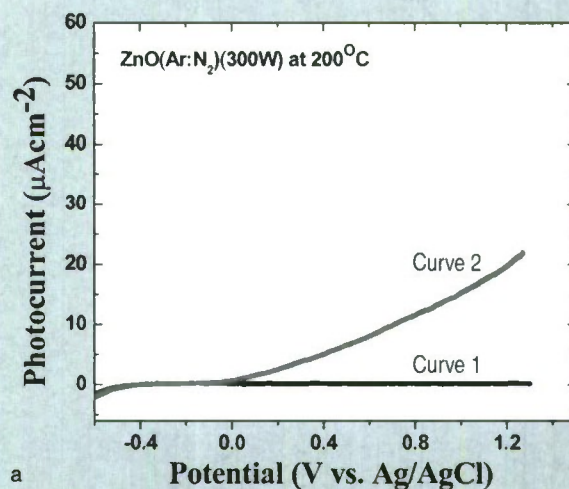
N concentration also increase. This is a clear evidence of the fact that higher RF power would enhance the incorporation of N at low substrate temperature.

Figure 8 shows the measured photocurrents as a function of the RF power for the ZnO(Ar:N₂) films deposited at a substrate temperature of 100°C. It is seen that the photocurrent decreases as the RF power increases from 100 to 500W. This trend can be attributed to the decrease of film crystallinity. Therefore,

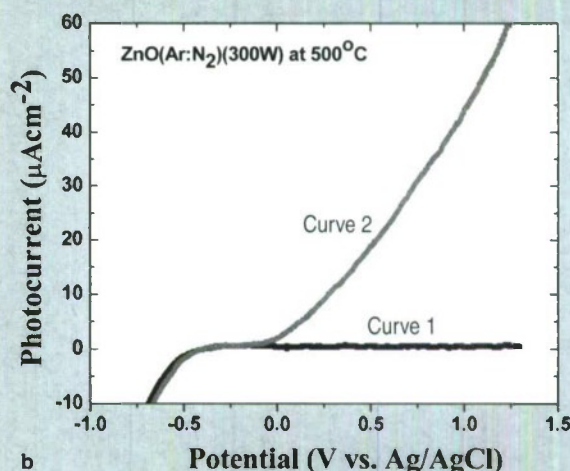
high RF power is not favorable for crystallinity of ZnO films when N is available in the growth chamber.

CONCLUSIONS

We have synthesized and characterized ZnO thin films deposited at various substrate temperatures and different RF powers in mixed Ar and N₂ gas ambient. We found that high substrate temperature and high RF powers help to promote the formation



a



b

Figure 5. Photocurrent-voltage curves of (a) ZnO(Ar:N₂)(300W) deposited at 200°C and (b) ZnO(Ar:N₂)(300W) deposited at 500°C under continuous illumination (curve 2), and dark condition (curve 1), with an UV/IR filter. Electrolyte and scan rate were 0.5 M Na₂SO₄ mild aqueous solution and 5 mV/s, respectively.

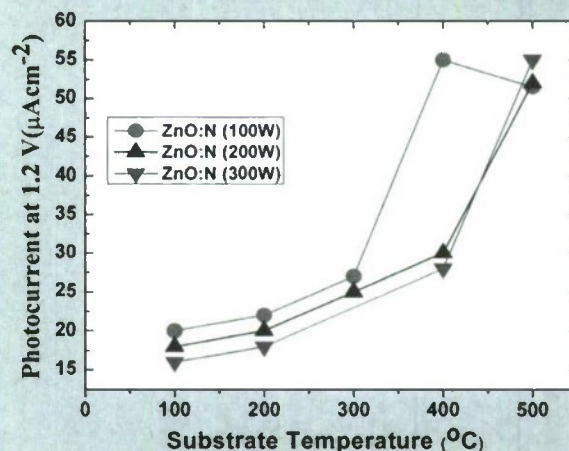


Figure 6. Photocurrents measured at 1.2 V as a function of the substrate temperature for the ZnO(Ar:N₂) films deposited at various RF powers.

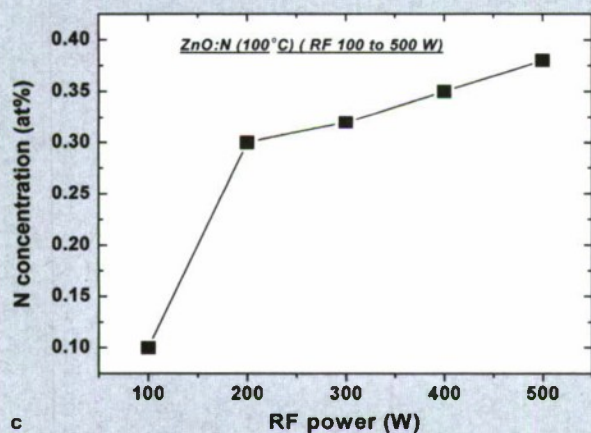
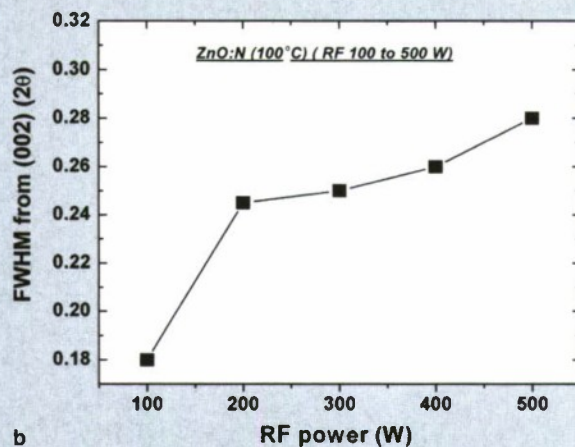
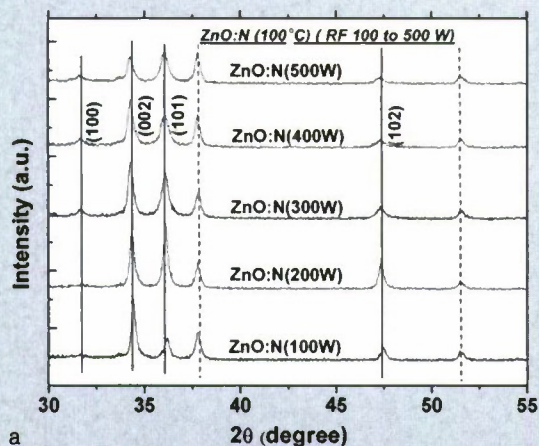


Figure 7, (a) X-ray diffraction curves for ZnO(Ar: N₂)(100°C) at RF powers from 100 W to 500 W. (b) FWHM values estimated from the (0002) peaks for ZnO(Ar: N₂)(100°C) films at RF power from 100 W to 500 W. (c) N concentrations for ZnO(Ar: N₂)(100°C) films deposited at RF power from 100 W to 500 W.

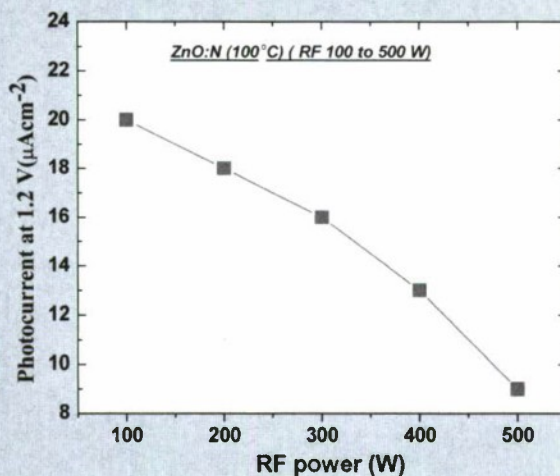


Figure 8. Photocurrents measured at 1.2 V as a function of RF power for ZnO(Ar: N₂) films deposited at substrate temperature of 100°C.

of aligned nanorod-like morphology of ZnO thin films grown in mixed Ar and N₂ gas ambient, resulting in the significantly enhanced PEC response. However, substrate temperature plays a more important role than RF power in the formation of ZnO nanorod-like morphology. Our results suggest that the formation of aligned nanorod-like morphology can be optimized by tuning the growth conditions, such as substrate temperatures and RF powers.

ACKNOWLEDGEMENTS

We thank Kim Jones for FE-SEM and Glenn Teeter for XPS experiments. This work was supported by the U.S. Department of Energy EERE Hydrogen Program under contract #DE-AC36-99-GO10337.

References

1. T. Bak et al., *Int'l. J. Solar Energy*, 27 (2002), p. 991.
2. A. Fujishima and K. Honda, *Nature (London)*, 238 (1972), p. 37.
3. R. Asahi et al., *Science*, 293 (2001), p. 269.
4. O. Khaselev and J.A. Turner, *Science*, 280 (1998), p. 425.
5. V.M. Aroutiounian, V.M. Arakelyan, and G.E. Shahnazaryan, *Solar Energy*, 78 (2005), p. 581.
6. J. Yuan, M. Chen, J. Shi, and W. Shangquan, *Int'l. J. Hydrogen Energy*, 31 (2006), p. 1326.
7. G.K. Mor et al., *Nano Lett.*, 5, (2005), p. 191.
8. B. O'Regan and M. Grätzel, *Nature*, 353 (1991), p. 737.
9. K. Kakiuchi, E. Hosono, and S. Fujihara, *J. Photochem. & Photobiol. A: Chem.*, 179, (2006), p. 81.
10. T.F. Jaramillo et al., *Macromol. Rapid Comm.*, 25 (2004), p. 297.
11. X. Liu et al., *J. Appl. Phys.*, 95 (2004), p. 3141.
12. W.I. Park et al., *Appl. Phys. Lett.*, 80 (2002), p. 4232.
13. S. Choopun, H. Tabata, and T. Kawai, *J. Cryst. Growth*, 274 (2005), p. 167.
14. F. Xu et al., *Nanotech.*, 17 (2006), p. 588.
15. K.-S. Ahn et al., *J. Power Source*, 176 (2008), p. 387.
16. S. Shet et al., *J. Appl. Phys.*, 103 (2008), 073504.
17. S. Shet et al., *J. Mater. Research*, 25 (2010), p. 69; Doi: 10.1557/JMR.2010.0017.
18. K.-S. Ahn et al., *Appl. Phys. Lett.*, 91 (2007) 231909.
19. K.-S. Ahn et al., *Appl. Phys. Lett.*, 95 (2009) 022116.
20. K.-S. Ahn et al., *Appl. Phys. Lett.*, 93 (2008) 163117.
21. K.-S. Ahn et al., *J. Electrochem. Soc.*, 154 (2007), p. B956.
22. S.-H. Kang et al., *J. Phys. Chem. C*, 111 (2007), p. 9614.
23. J. Akikusa and S.U.M. Khan, *Int. J. Hydrogen Energy*, 27 (2002), p. 863.
24. C.M. López and K.S. Choi, *Chem. Commun.* (2005), p. 3328.
25. M. Law et al., *Nature Mater.*, 4 (2005), p. 455.

Sudhakar Shet, Yanfa Yan, John Turner, and Mowafak Al-Jassim are with the National Renewable Energy Laboratory, Golden, CO 80401 USA; Kwang-Soon Ahn is with the School of Display and Chemical Engineering, Yeungnam University, Gyeonbuk 712-749, Korea; Shet and Ravindra Nuggehalli are with the New Jersey Institute of Technology, Newark, NJ 07102 USA. Dr. Shet can be reached at (303) 384-7621; e-mail Sudhakar.Shet@nrel.gov.

Corrosion as a Nanostructure Synthesis Strategy

M.P. Brady



In the most general sense corrosion reactions involve the conversion of one material form, structure, and/or arrangement into another. The connotation of corrosion is almost always in a negative sense (i.e., degradation of materials resulting in loss of properties and performance). However, because corrosion reactions involve energetically favorable product formation (oxidation in the chemical sense), they are potentially one of the most rapid, inexpensive, and technologically relevant methods of self-constructing new materials and structures.¹ They can result in the formation of a myriad of phase arrangements, ranging from nanoscale clusters, dispersions, and phases (including fibers, tubes, whiskers, and pores) to external layers, varying from nanometers to hundreds of micrometers thick.¹

The use of corrosion reactions as a synthesis approach goes back decades. One of the best known examples from the engineered materials field is the Lanxide process developed in the 1980s,² which used accelerated oxidation processing of molten metals to manufacture ceramic and metal matrix composites. Another well-known commercial example of corrosion-based synthesis routes to bulk composite materials is internal oxidation, which is used, for example, in Glidcop® Cu to form nanoscale dispersions of alumina to achieve strength while minimizing the impact on electrical properties.³ The most technologically important example of corrosion-based synthesis

is thermal oxidation of silicon to form silicon dioxide for semiconductor industry applications.⁴

In recent years there has been an explosion of interest in nanoscale materials. Although often not recognized as such, corrosion reactions are at the forefront of many nanosynthesis techniques. This is because even though the results of corrosion reactions are evident on a bulk macro scale, their mechanistic basis can be traced to atomic and nanoscale processes (e.g., Reference 5). Reports of nanoscale oxide whisker and fiber formation during oxidation (particularly when water vapor species are present) go back at least 50 years.⁶ Metal dusting phenomena, whereby severe corrosion of alloys can occur in high carbon activity gaseous environments, results in the formation of carbon nanotube and related nanostructured carbon species and potentially offers a low-cost synthesis route to these materials.^{7,8} High-temperature chlorination reactions of transition metal carbides are of great recent interest for energy storage applications due to the potential to controllably form nanoporous carbon structures, the carbide-derived carbon class of materials.⁹ Aqueous and electrochemical corrosion phenomena are also widely used to form nanostructured materials (particularly templates) by processes such as dealloying, anodization, and other forms of passive film manipulation.^{10–12} In all cases, the more widespread recognition of the basis of these synthesis routes in corrosion phenomena may accrue significant benefit and insight from the decades of studies available in the corrosion literature.

This topic highlights recent examples of the use of corrosion reactions

to synthesize nanoscale materials. In the following papers, a diverse range of both low- and high-temperature corrosion processes have been exploited to successfully synthesize unique nanoscale structures of scientific and technical interest. A common theme among these papers is that the basis to achieve a high degree of synthesis control of desired nanoscale features is grounded in the fundamental understanding of the corrosion processes employed.

ACKNOWLEDGEMENTS

Editorial work was sponsored by the U.S. Department of Energy, Office of Energy Efficiency and Renewable Energy, Fuel Cell Technologies Program.

References

1. M.P. Brady and P.F. Tortorelli, *Intermetallics*, 12 (7-9) (2004), pp. 779–789.
2. A.W. Urquhart, *Materials Science and Engineering A*, 144 (1991), pp. 75–82.
3. T.S. Srivatsan, S. Anand, and J.D. Troxell, *Materials Letters*, 14 (1) (1992), pp. 11–16.
4. M.L. Green et al., *J. Applied Physics*, 90 (5) (2001), pp. 2057–2121.
5. J. Erlebacher et al., *Nature*, 410 (6827) (2001), pp. 450–453.
6. P. Kofstad, *High Temperature Corrosion* (New York: Elsevier Applied Science Publishers LTD., 1988), pp. 154–157.
7. H.Y. Tsai, J.K. Chang, and W.T. Tsai, *Diamond and Related Materials*, 18 (2-3) (2009), pp. 324–327.
8. Z. Zeng and K. Natesan, *Chemistry of Materials*, 17 (14) (2005), pp. 3794–3801.
9. Y. Gogotsi et al., *Nature Materials*, 2 (9) (2003), pp. 591–594.
10. J.W. Schultze and M.M. Lohrengel, *Electrochimica Acta*, 45 (15-16) (2000), pp. 2499–2513.
11. C.R. Martin, *Science*, 266 (5193) (1994), pp. 1961–1966.
12. D. Routkevitch et al., *IEEE Transactions on Electron Devices*, 43 (10) (1996), pp. 1646–1658.

Michael P. Brady, senior R&D staff member with the Materials Science and Technology Division, Oak Ridge National Laboratory, Oak Ridge, TN, is the advisor to JOM from the Corrosion and Environmental Effects Committee of the Structural Materials Division of TMS.

Materials "Alchemy": Shape-Preserving Chemical Transformation of Micro-to-Macroscopic 3-D Structures

Kenneth H. Sandhage

Enhanced for the Web

This article appears on the JOM web site (www.tms.org/jom.html) in html format and includes links to additional on-line resources.

The scalable fabrication of nanostructured materials with complex morphologies and tailorable chemistries remains a significant challenge. One strategy for such synthesis consists of the generation of a solid structure with a desired morphology (a "preform"), followed by reactive conversion of the preform into a new chemistry. Several gas/solid and liquid/solid reaction processes that are capable of such chemical conversion into new micro-to-nanostructured materials, while preserving the macroscopic-to-microscopic preform morphologies, are described in this overview. Such shape-preserving chemical transformation of one material into another could be considered a modern type of materials "alchemy."

INTRODUCTION

Sealable fabrication protocols for the syntheses of structures with functional chemistries and complex morphologies that can be tailored over various length scales (even down to the nanoscale) may have a significant impact in a variety of current or potential applications. One paradigm for such fabrication involves separation of the processes for structure formation and for chemical tailoring; that is, a solid structure (a "preform") of a given chemistry may first be fabricated with desired macro-to-nanoscale morphological features, and then converted into a new chemistry via morphology-preserving gas/solid or liquid/solid reaction(s). The extensive literature available on the ki-

How would you...

...describe the overall significance of this paper?

Scalable processes are needed for fabricating complex three-dimensional (3-D) nanostructured components with tailored chemistries for numerous applications. This paper describes how 3-D micro-to-macroscopic preforms, generated by scalable biological or synthetic methods, may be converted into new nanostructured materials with desired chemistries and properties via shape-preserving reactions.

...describe this work to a materials science and engineering professional with no experience in your technical specialty?

Reactive gases and liquids can be used to transform complex 3-D metal- or ceramic-rich preforms into new ceramics, metals, or ceramic/(inter)metallic composites, while retaining the preform shapes and dimensions. Displacement reactions (oxidation-reduction or metathetic) and oxidation reactions are described for generating near net-shaped nanostructured materials for chemical, electrical, optical, structural, and thermal applications.

...describe this work to a layperson?

The medieval "art of transmuting metals" (alchemy) was aimed at converting common materials into precious ones. This paper describes how certain materials, formed into complex shapes by common biological or synthetic methods, can be transformed by chemical reactions into new materials with attractive properties, while retaining the starting shapes. Such a modern type of materials alchemy can yield a variety of advanced components, such as microscopic gas sensors, efficient filters for purifying water, and erosion-resistant rocket nozzles.

neties and phase evolution associated with such reactions in the field of high temperature oxidation/corrosion provides a rich source of mechanistic information that can be utilized for such materials "alchemy."

The purpose of this overview is to provide examples of the following three reaction-based approaches for the chemical conversion of shaped solid preforms: gas/solid displacement reactions, liquid/solid displacement reactions, and gas/solid oxidation reactions. Under appropriate conditions, each of these reaction-based approaches can be used to transform solid preforms into new nanostructured materials while preserving the preform morphology (note: a "nanostructured material" refers herein to a material with one or more physical features, such as a phase size, crystal size, and/or pore size, with a dimension below one micrometer). The syntheses of two types of shaped, nanostructured materials will be discussed here: microscopic structures with nanoscale features (generated via the application of gas/solid displacement reactions to solid microscopic preforms), and macroscopic structures with nanoscale phase and/or crystal sizes (generated via the application of liquid/solid displacement reactions, or gas/solid oxidation reactions, to solid macroscopic preforms).

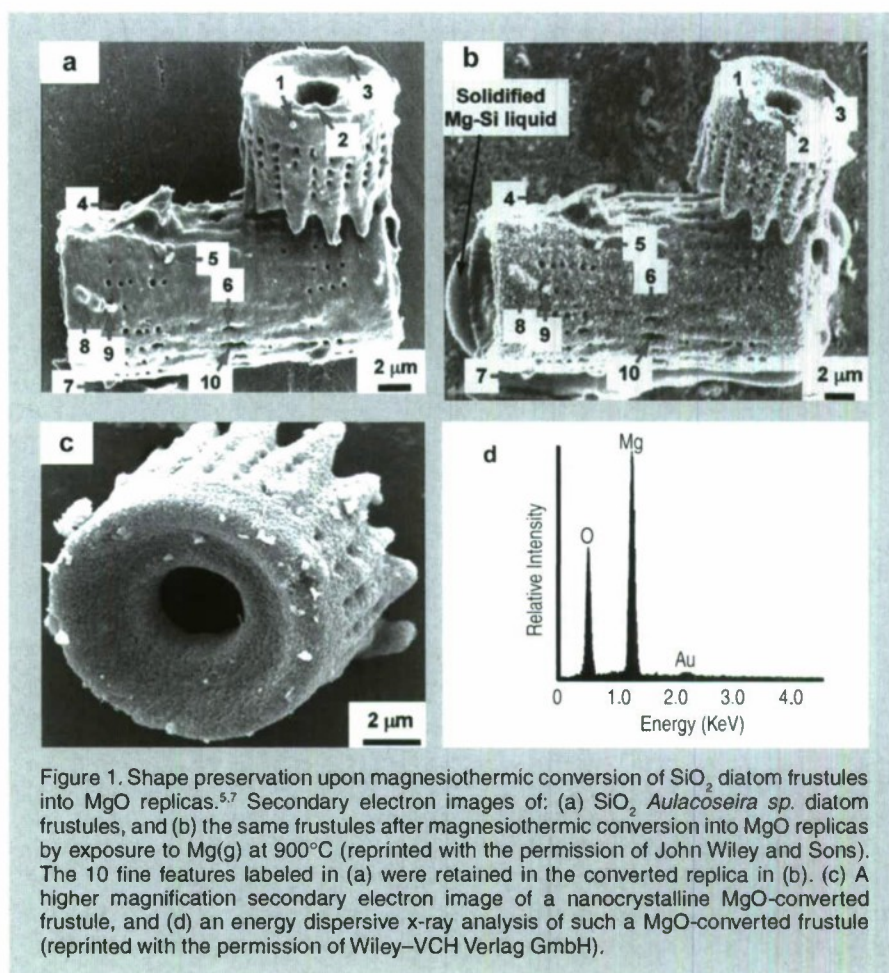
CONVERSION OF MICROSCOPIC PREFORMS BY GAS/SOLID REACTIONS

Given the capability of gases to readily migrate through fine-scale pores or to penetrate into narrow cavities of high aspect ratio, gas/solid displacement reactions can be effective means of introducing new chemistries to complex-

shaped, nanostructured, three-dimensional (3-D) oxide-based templates. Such displacement reactions have been used to convert intricate microscopic synthetic or biologically derived oxide preforms into a variety of other functional oxide, metal, or oxide/metal composite materials while retaining the morphology and nanoscale features of these starting preforms.

Biologically Replicable, 3-D, Microscale, Nanostructured Preforms: Diatom Frustules

Among the most complex-shaped, three-dimensional (3-D) nanostructured oxide templates available for the application and evaluation of shape-preserving gas/solid displacement reactions are the silica-based microshells (frustules) generated by diatoms. Diatoms are single-celled algae that populate a wide variety of aquatic environments.^{1,2} Each diatom species generates an amorphous silica frustule with a particular 3-D shape and patterned nanoscale features (e.g., pores, channels, protuberances of 10^1 – 10^2 nm size), which suggests a strong degree of genetic control over the silica formation process.^{1,3} Such species specificity (genetic control) of the diatom frustule morphology enables enormous numbers of similarly shaped frustules to be generated via sustained culturing (repeated doubling) of a single diatom species⁴ (e.g., 80 reproduction cycles from a single parent diatom cell can yield 2^{80} , or more than one trillion trillion, daughter cells with frustules of similar morphology). Furthermore, the 10^4 – 10^5 extant diatom species possess frustules with a spectacular variety of intricate 3-D morphologies.¹ Future genetic engineering of diatoms may allow for a wide range of tailored 3-D shapes.³ The precise (down to nanoscale), hierarchical (nano-to-microscale), complex (3-D), reproducible (genetically-controlled), and scalable (massively-parallel reproduction) nature of diatom microshell assembly under ambient conditions, coupled with the wide variety of selectable (and, in the future, perhaps tailorable) morphologies among extant diatom species, make diatom frustules unique and highly attractive as templates for synthetic chemical conversion into



microscale nanostructures for potential devices applications (with a future potential for “Genetically Engineered Microdevices”).^{5–9}

Oxide, Oxide/Metal, and Metal Replicas via Oxidation-reduction Displacement Reactions

The first demonstration of the use of a gas/solid displacement reaction to convert a nanostructured 3-D oxide microparticle (i.e., a silica diatom frustule) into an entirely new oxide composition, while retaining the microparticle morphology, was reported in 2002.⁷ Diatom frustules were exposed to magnesium vapor (generated by heating solid magnesium granules) at 900°C for 4 h to allow for a net magnesiothermic displacement reaction (Reaction 1), where {Si} refers to Si dissolved within a Mg-Si alloy liquid. (Note that all reactions are given in Table I.) Because the Mg: SiO_2 reactant ratio was maintained at a value well above the 2:1 molar ratio required by the stoichiometry of Reaction 1, the

excess magnesium vapor continued to react with the silicon product to generate a magnesium-silicon liquid (note: the eutectic temperature for magnesium-rich compositions in the Mg-Si system is only 638°C ¹⁰). This Mg-Si alloy liquid poured out of the reacted frustules to yield MgO-based structures that retained the 3-D frustule morphology and patterned pores (Figure 1).^{5,7} This magnesiothermic process has also been used to convert “biosculpted” silica structures into magnesia replicas.¹¹ The exposure of a silica-precipitating peptide, derived from the sitaffin-1A protein of the diatom *Cylindrotheca fusiformis*, to a tetramethylorthosilicate precursor solution under a linear shear flow condition resulted in the formation of interwoven microfilamentary silica fibrils. Upon reaction with magnesium gas at 900°C , the silica microfilaments were converted into nanocrystalline magnesium oxide replicas that retained the microfilamentary shape and fine (submicrometer) features.¹¹ Nanocrystalline magnesia in the form of such intricate porous 3-D micropar-

Table I. Chemical Conversion Reactions

$2\text{Mg(g)} + \text{SiO}_2\text{(s)} \Rightarrow 2\text{MgO(s)} + \text{(Si)}$	(1)
$2\text{Mg(g)} + \text{SiO}_2\text{(s)} \Rightarrow 2\text{MgO(s)} + \text{Si(s)}$	(2)
$2\text{TiF}_4\text{(g)} + \text{SiO}_2\text{(s)} \Rightarrow 2\text{TiOF}_2\text{(s)} + \text{SiF}_4\text{(g)}$	(3)
$3\text{SiF}_4\text{(g)} + \text{SiO}_2\text{(s)} \Rightarrow 2\text{Si}_2\text{OF}_6\text{(g)}$	(4)
$2\text{TiOF}_2\text{(s)} + 2(1-\text{a})\text{H}_2\text{O(s)} \Rightarrow 2\text{TiO}_{2-\text{a}}\text{F}_{2\text{a}}\text{(s)} + 4(1-\text{a})\text{HF(g)}$	(5a)
$2\text{TiOF}_2\text{(s)} + (1-\text{a})\text{O}_2\text{(s)} \Rightarrow 2\text{TiO}_{2-\text{a}}\text{F}_{2\text{a}}\text{(s)} + 2(1-\text{a})\text{F}_2\text{(g)}$	(5b)
$4\text{Al(l)} + 3\text{SiO}_2\text{(s)} \Rightarrow 2\text{Al}_2\text{O}_3\text{(s)} + 3\text{(Si)}$	(6)
$13\text{(Al)} + 3\text{TiO}_2\text{(s)} \Rightarrow 2\text{Al}_2\text{O}_3\text{(s)} + 3\text{TiAl}_3\text{(s)}$	(7a)
$7\text{(Al)} + 3\text{TiO}_2\text{(s)} \Rightarrow 2\text{Al}_2\text{O}_3\text{(s)} + 3\text{TiAl(s)}$	(7b)
$3\text{(Mg)} + \text{Al}_2\text{O}_3\text{(s)} \Rightarrow 3\text{MgO(s)} + 2\text{(Al)}$	(8)
$\text{(Zr)} + \text{WC(s)} \Rightarrow \text{ZrC(s)} + \text{W(s)}$	(9)

ticles (available in a wide variety of shapes as diatom frustules) or 2-D microfilamentary structures can be attractive for use in environmental (e.g., for heavy metal precipitation from, or neutralization of, acidic wastewater streams; for $\text{SO}_2\text{(g)}$ removal from gaseous emissions), chemical/petrochemical (e.g., as an acid acceptor, filler, or thickening catalyst in the production of plastics), pharmaceutical (e.g., in cosmetics and ointments), or agricultural (e.g., in fertilizers, as a carrier for pesticides, in livestock feed) applications.^{12–16}

The gas/solid magnesiothermic reaction of an oxide template may also be used to generate a nanocrystalline elemental replica of the template. By lowering the magnesiothermic reaction temperature to 650°C , and by reducing the molar $\text{Mg}:\text{SiO}_2$ reactant ratio to a value just above that required by the stoichiometry of Reaction 1, the formation of an Mg_2Si compound and the Mg-Si alloy liquid were suppressed, so that nanocrystalline MgO/Si composite replicas of diatom frustules were formed, as indicated by Reaction 2.^{17–21} The products of this reaction correspond to a co-continuous, nanocrystalline mixture of MgO (65.1 vol.%) and Si (34.9 vol.%). Owing to the continuity of the Si phase, porous Si replicas of the diatom frustules have been produced by selective acid

dissolution of the interconnected MgO network.²¹ As revealed in Figure 2, the 3-D frustule morphology and features as small several tens of nanometers were well-preserved in the resulting nanocrystalline Si replicas. The Si frustule replicas possessed a much higher specific surface area ($>500\text{ m}^2/\text{g}$) than the starting SiO_2 frustules, and contained a high population of nanoscale ($<2\text{ nm}$ diameter) pores.²¹ Such a single porous silicon frustule replica was found to act as a rapid, sensitive, low-voltage, and minimally invasive gas sensor (Figures 2g and h).²¹ This now-patented^{8,9,22,23} shape-preserving magnesiothermic reduction process has also recently been used to convert synthetic mesoporous silica films and colloidal silica assemblies into porous silicon replicas.^{24–26} Such nanocrystalline porous silicon replica structures, generated from biosilica or synthetic silica templates, can be attractive for a number of chemical, biochemical, electrical, and optical applications (e.g., for sensing, biocatalysis, batteries, and photovoltaics).^{21,24–29} Szczech and Jin³⁰ have subsequently reported that Mg_2Si -bearing diatom frustule replicas generated by this magnesiothermic conversion process may be useful for thermoelectric applications (note: the formation of such solid Mg_2Si , relative to solid Si or Mg-Si liquid products, may be controlled by

adjustment of the $\text{Mg}:\text{SiO}_2$ reactant ratio at modest temperatures^{20,21}).

Oxide Replicas via Metathetic (Halide) Displacement Reactions

Metathetic gas/solid displacement reactions, involving halide gases, have also been utilized for the shape-preserving conversion of intricate 3-D silica microparticles, ordered porous silica films, and silica microspheres into nanocrystalline replicas comprised of other oxides.^{31–36} For example, the exposure of diatom SiO_2 frustules to TiF_4 gas, generated by the vaporization of solid TiF_4 , has been used to transform the frustules into titanium oxyfluoride, $\text{TiOF}_2\text{(s)}$, according to a metathetic displacement reaction (Reaction 3).^{31,32} Initial experiments conducted at $500\text{--}700^\circ\text{C}$ with molar $\text{TiF}_4:\text{SiO}_2$ reactant ratios $>4.9:1$ resulted in reactive evaporation and disintegration of the silica frustules (Figures 3a–c).^{31,32} Such reactive silica evaporation (a type of active corrosion^{37,38}) at such modest temperatures indicated that a volatile Si-O -bearing gas species had formed. Hexafluorodisiloxane gas, $\text{Si}_2\text{OF}_6\text{(g)}$, is one such likely species that can form by Reaction 4. The apparent formation of $\text{Si}_2\text{OF}_6\text{(g)}$, and the associated vaporization of the SiO_2 template, was avoided by conducting the metathetic reactive conversion at lower temperatures (i.e., $180\text{--}350^\circ\text{C}$) and at lower molar $\text{TiF}_4:\text{SiO}_2$ reactant ratios ($\leq 2.4:1$).^{31–34} Under these conditions, the SiO_2 reactive evaporation was suppressed and the TiOF_2 product formed on the SiO_2 frustule surfaces (i.e., analogous to a transition from active to passive corrosion^{37,38}). Complete reaction then yielded nanocrystalline TiOF_2 structures that retained the SiO_2 frustule shape and fine features.^{31–33} Such TiOF_2 replicas were then converted into nanocrystalline anatase TiO_2 -based replicas (Figures 3d and e) via reaction with humid oxygen at $\leq 600^\circ\text{C}$ as shown in Reactions 5a and 5b,^{32,33} where $\text{TiO}_{2-\text{a}}\text{F}_{2\text{a}}\text{(s)}$ refers to fluorine-doped anatase titania. The open nanocrystalline nature of these anatase microparticles, along with the retention of a controlled amount of fluorine (via tailoring of the humid oxygen treatment), enabled these doped titania replicas to act as effective agents for the rapid hydrolytic

destruction of pesticides (methyl paraxon and methyl parathion) in water without the need for UV light.³³ This patented shape-preserving metathetic reaction process^{8,9,22} has also been used to convert opalescent 3-D porous silica preforms into nanocrystalline titania structures that retained the general morphology and structural features of the preforms.³⁵ Given the chemical, biochemical, optical, and electrical properties of titania, the ability to convert 3-D silica microparticles, ordered opalescent films, microspheres, or other silica-derived morphologies into nanocrystalline titania replicas can be quite attractive for generating sensitive, minimally-invasive gas detectors (e.g., for CO(g) or H₂(g)), efficient photocatalysts (e.g., for the reaction of detergents or dyes in water), index-tailored waveguides (e.g., for visible or near IR wavelengths), controlled-shape pigment particles (e.g., for paints, paper, plastics, ink, and cosmetics), nano-

structured medical implants (e.g., as biocompatible coatings for bone implants), efficient antimicrobial agents (e.g., for killing *E. coli* bacteria), and highly-porous electrodes (e.g., for dye-sensitized solar cells).³⁹⁻⁴⁴

Further Chemical Modification of Replicas via Coating and/or Additive Reactions

The new oxide chemistries of replica structures generated by gas/solid displacement reactions can enable the coating of these replicas with additional functional oxides (i.e., so as to yield multilayered and/or multicomponent replicas). Consider, for example, the syntheses of BaTiO₃-based coatings on shaped microtemplates (e.g., intricate microparticles, porous inverse opals, or patterned films). Such templated BaTiO₃-based structures can be attractive for electronic (e.g., capacitor, varistor), electrochemical (e.g., gas sensing), thermal (e.g., temperature sensing), or

optical (e.g., phosphor) applications.⁴⁵⁻⁴⁷ However, BaTiO₃ is not thermochemically compatible with SiO₂; that is, the deposition of a Ba-Ti-O-bearing coating on a SiO₂ template, followed by thermal treatment to allow for conversion of the coating into crystalline BaTiO₃, tends to result in the formation of undesired silicate compounds (e.g., BaTiSiO₅, BaTiSi₂O₇, BaTiSi₃O₉).⁴⁸ Fortunately, MgO replicas of SiO₂ templates are chemically compatible with BaTiO₃.⁴⁹ Furthermore, because nanocrystalline magnesia surfaces can be readily hydroxylated, magnesia templates are attractive for reaction with, and binding of, alkoxide precursors used in sol-gel deposition processes. Weatherspoon et al.⁵⁰⁻⁵² have demonstrated the efficacy of such a combined magnesiothermic reaction and sol-gel coating approach by generating BaTiO₃ coatings on MgO diatom frustule replicas. After magnesiothermic conversion of silica frustules at 900°C for 1.5 h,

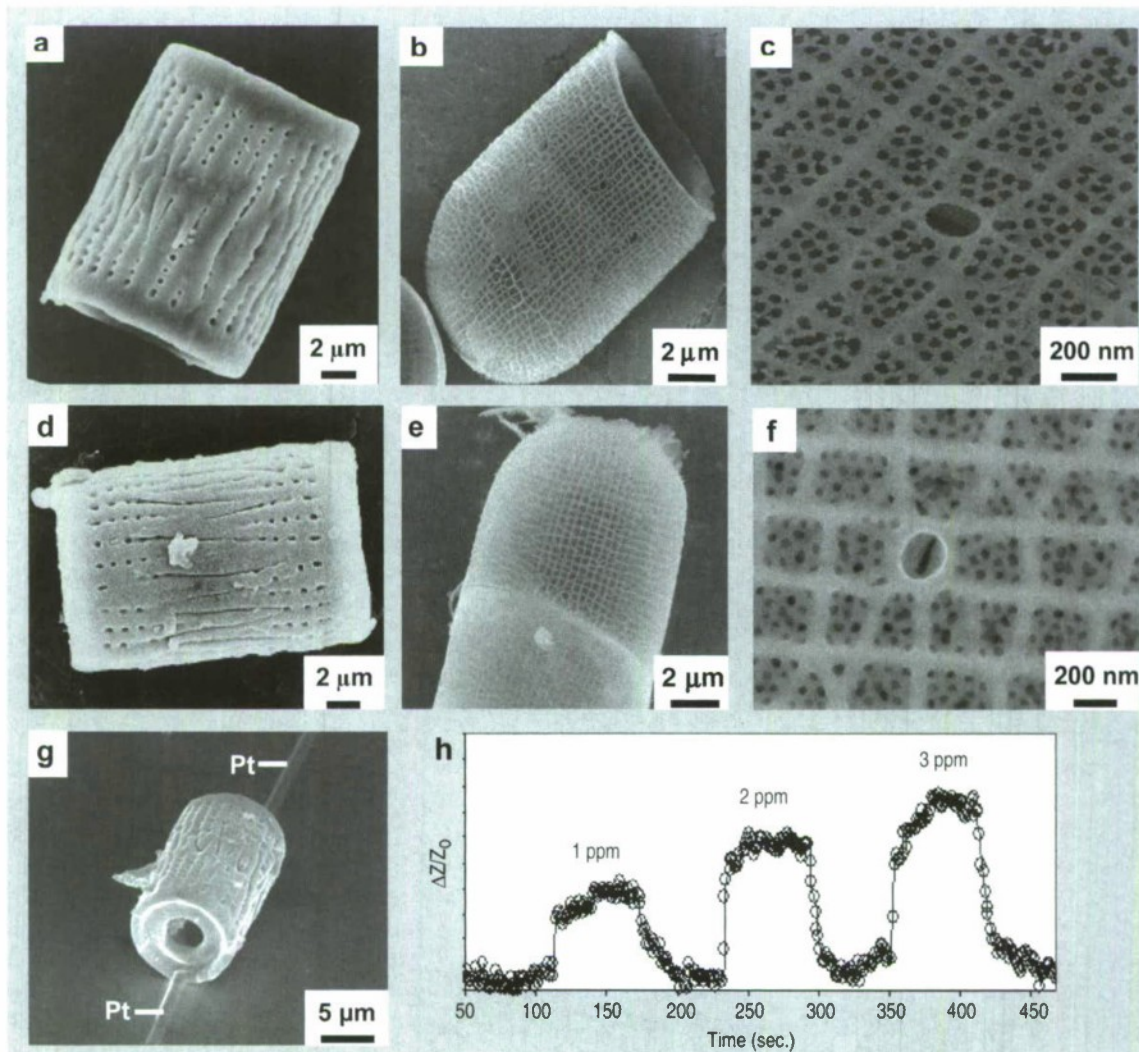
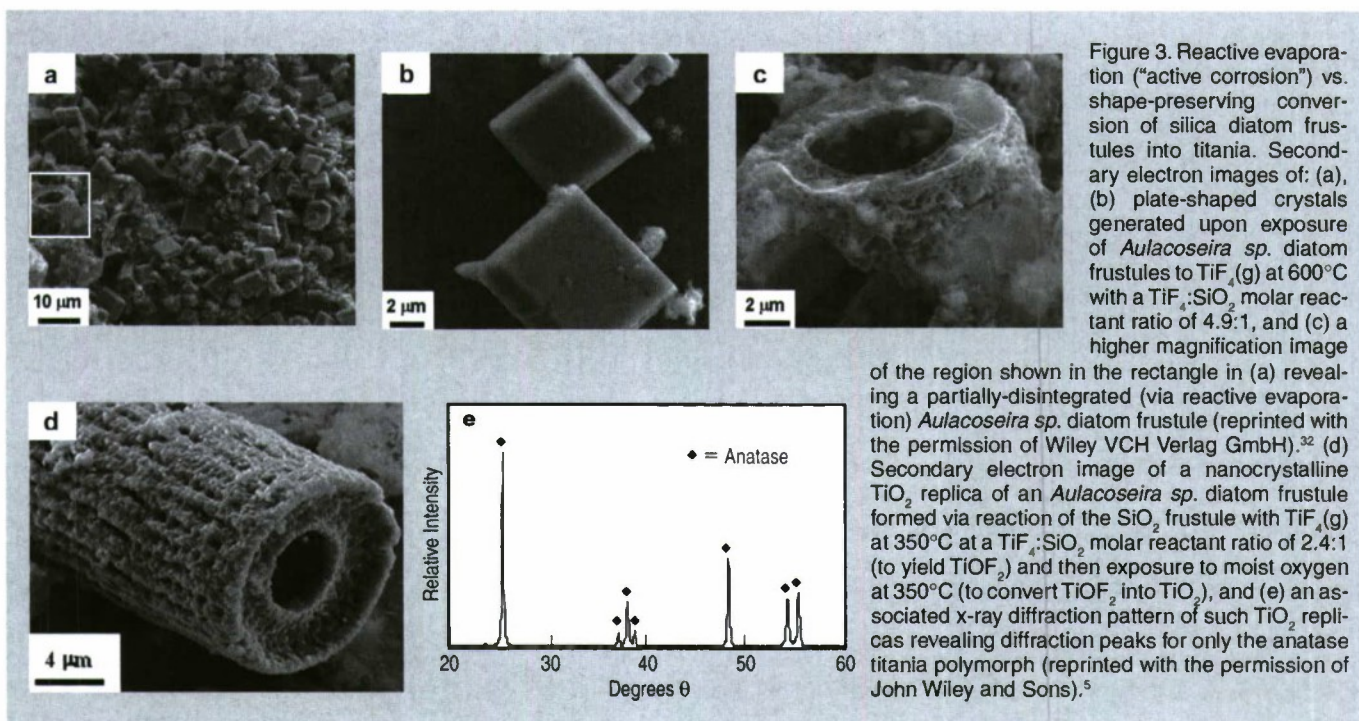


Figure 2. Shape-preserving magnesiothermic conversion of SiO₂ diatom frustules into porous, nanocrystalline Si replicas.²¹ Secondary electron images of: (a) an *Aulacoseira* sp. diatom frustule (obtained as diatomaceous earth); (b), (c) a cultured *Melosira nummuloides* diatom frustule; (d) a porous Si replica of an *Aulacoseira* sp. diatom frustule; (e), (f) a Si replica of a *M. nummuloides* diatom frustule. (g) A single Si frustule replica gas sensor. (h) Relative impedance change of the sensor in (g) upon exposure to flowing NO gas (1, 2, or 3 ppm NO in an Ar carrier).



the magnesia frustule replicas were immersed in a heated aqueous NaOH solution. The resulting hydroxylated magnesia replicas were then exposed to a refluxed solution of barium titanium ethylhexanoisopropoxide in ethanol at 70°C . After evaporation of the volatile components of the solution at 56°C , the coated frustules were heated in air to 700°C for 1.5 h to allow for organic pyrolysis and crystallization of the coating. The resulting frustules contained a thin (150 nm), continuous, and conformal coating of nanocrystalline BaTiO_3 (average crystal size of 20 nm). Indeed, the coating was sufficiently continuous as to yield freestanding BaTiO_3 frustule replicas upon selective dissolution of the underlying MgO template.⁵² A similar react-and-coat process has also been used by these authors to synthesize photoluminescent Eu-doped BaTiO_3 -bearing frustule replicas.⁵¹

Nanostructured elemental replicas of shaped oxide templates, generated through a magnesiothermic reduction (displacement reaction) process, may also be used as templates for subsequent electroless deposition of other functional elements. The coating of relatively noble metals (Au, Ag, Pd) on porous nanostructured templates can be attractive for a number of catalytic (e.g., for $\text{CO}(\text{g})$ oxidation, fuel cell catalysts), electrochemical (e.g., sensors), electronic (e.g., electrodes), thermal

(e.g., cryogenic heat exchangers), and other applications.^{53–55} While the direct electroless deposition of noble metal coatings on silica templates is inhibited by the insulating nature of this oxide, porous silicon replicas possess appropriate electronic and chemical (reducing) characteristics for such deposition. Bao et al.⁵⁶ have recently synthesized nanocrystalline noble metal replicas of 3-D silica microparticle templates (diatom frustules) by first converting the silica into porous silicon (via magnesiothermic reduction), and then applying metal coatings onto/within the porous silicon via subsequent electroless deposition. Subsequent selective dissolution of the Si in an aqueous NaOH solution then yielded freestanding porous Ag, Au, or Pd structures that retained the 3-D morphology of the starting silicon frustule replicas (Figure 4).⁵⁶ The frustule-shaped silver, gold, and palladium microparticles possessed average crystal sizes of only 14, 50, and 43 nm, respectively.

Oxide replicas of patterned templates, generated via metathetic gas/solid displacement reactions, can also be used as reactive templates for the generation of functional multicomponent oxides. For example, nanocrystalline titania replicas produced by the reaction of silica templates with titanium tetrafluoride gas (using Reactions 3, 5a, and 5b) have been converted into barium tita-

nate (BaTiO_3) replicas through hydrothermal reaction by Ernst, et al.^{52,57} The titania replicas were sealed, along with barium hydroxide octahydrate and water, inside a Teflon chamber and then heated to 100°C for 48 h to allow for hydrothermal conversion into barium titanate. The resulting frustule-shaped particles were found to be comprised of nanocrystalline BaTiO_3 with an average crystal size of only 63 nm.^{52,57}

CONVERSION OF MACROSCOPIC PREFORMS BY LIQUID/SOLID REACTIONS

Several liquid/solid displacement reaction-based approaches have been developed to allow for the conversion of shaped, macroscopic, ceramic-bearing preforms into composites comprised of new ceramic and metallic or intermetallic products that retain the shapes and dimensions (to within 1%) of the starting preforms. Under appropriate conditions, these approaches have yielded composites with micrometer-to-submicrometer phase and/or crystal sizes. Two general categories of such liquid/solid displacement reaction-based processes are reactive metal penetration and reactive casting. Reactive metal penetration refers to the conversion of a dense, shaped ceramic-bearing preform into a dense product, comprised of new ceramic and metallic or intermetallic

phases, via the inward migration of a liquid/solid reaction front through the dense preform.^{58–69} Reactive casting refers to the conversion of a porous, shaped ceramic-bearing preform into a dense ceramic/metallic or ceramic/intermetallic composite via the infiltration (with or without the assistance of an applied pressure) of a metallic liquid through the porous preform and reaction of this liquid with one or more solid phases in the preform.^{70–85}

Reactive Metal Penetration

A common displacement reaction used in reactive metal penetration is shown in Reaction 6,^{58–60} where {Si} refers to silicon dissolved within an aluminum-silicon melt. With this process, dense amorphous SiO_2 preforms, which may be readily fabricated into complicated shapes through conventional glass forming methods, are immersed in a bath of molten Al at $\geq 1,000^\circ\text{C}$. The reaction of a silica preform with molten

aluminum (Reaction 6) proceeds by the formation of an Al_2O_3 -bearing reaction zone that migrates through the preform at a linear rate (on the order of 1–5 mm/h) at 1,000–1,200°C.⁵⁹ The volume of 2 moles of $\text{Al}_2\text{O}_3(\text{s})$ is substantially less than the volume of 3 moles of $\text{SiO}_2(\text{s})$. Hence, this reaction-induced volume reduction generates space that is accommodated by the molten metal. The silicon product of this displacement reaction can dissolve into the molten metal and then diffuse into the excess surrounding aluminum bath at $\geq 1,000^\circ\text{C}$.⁵⁹ Upon cool down, the resulting composites are comprised of a fine mixture of interpenetrating Al_2O_3 and Al-rich phases (Figures 5a and b). (Note: owing to the continuity of both phases, this reactive metal penetration process has also been referred to as the co-continuous ceramic composite, or C^4 , process by Breslin, Dachs, and colleagues, who pioneered this approach.^{58–61}) An interesting microstruc-

tural characteristic of such composites is the growth texture of the alumina product phase; that is, the c-axis of the $\alpha\text{-Al}_2\text{O}_3$ phase is strongly aligned with the direction of migration of the reaction front.⁶¹ This reactive metal penetration process yields co-continuous $\text{Al}_2\text{O}_3/\text{Al}$ -rich composites that retain the shape and dimensions (to within 1%) of the starting dense SiO_2 preforms (Figure 5c).^{58–61} Reactive metal penetration has also been used to convert dense aluminosilicate (e.g., mullite, $\text{Al}_6\text{Si}_2\text{O}_{13}$; sillimanite, Al_2SiO_5) preforms into dense, near net-shape, co-continuous composites of Al_2O_3 and Al-rich alloy (or Al-rich alloy + Si).^{62–64} The values of specific modulus (62–86 $\text{GPa}\cdot\text{cm}^3/\text{g}$), hardness (8–12 GPa), toughness (5–10 $\text{MPa}\cdot\text{m}^{1/2}$), and thermal conductivity (80 $\text{WK}^{-1}\cdot\text{m}^{-1}$), and the wear behavior reported for these lightweight (3.4–3.7 g/cm^3) $\text{Al}_2\text{O}_3/\text{Al}$ -bearing composites make such reaction-formed materials attractive for applications such as

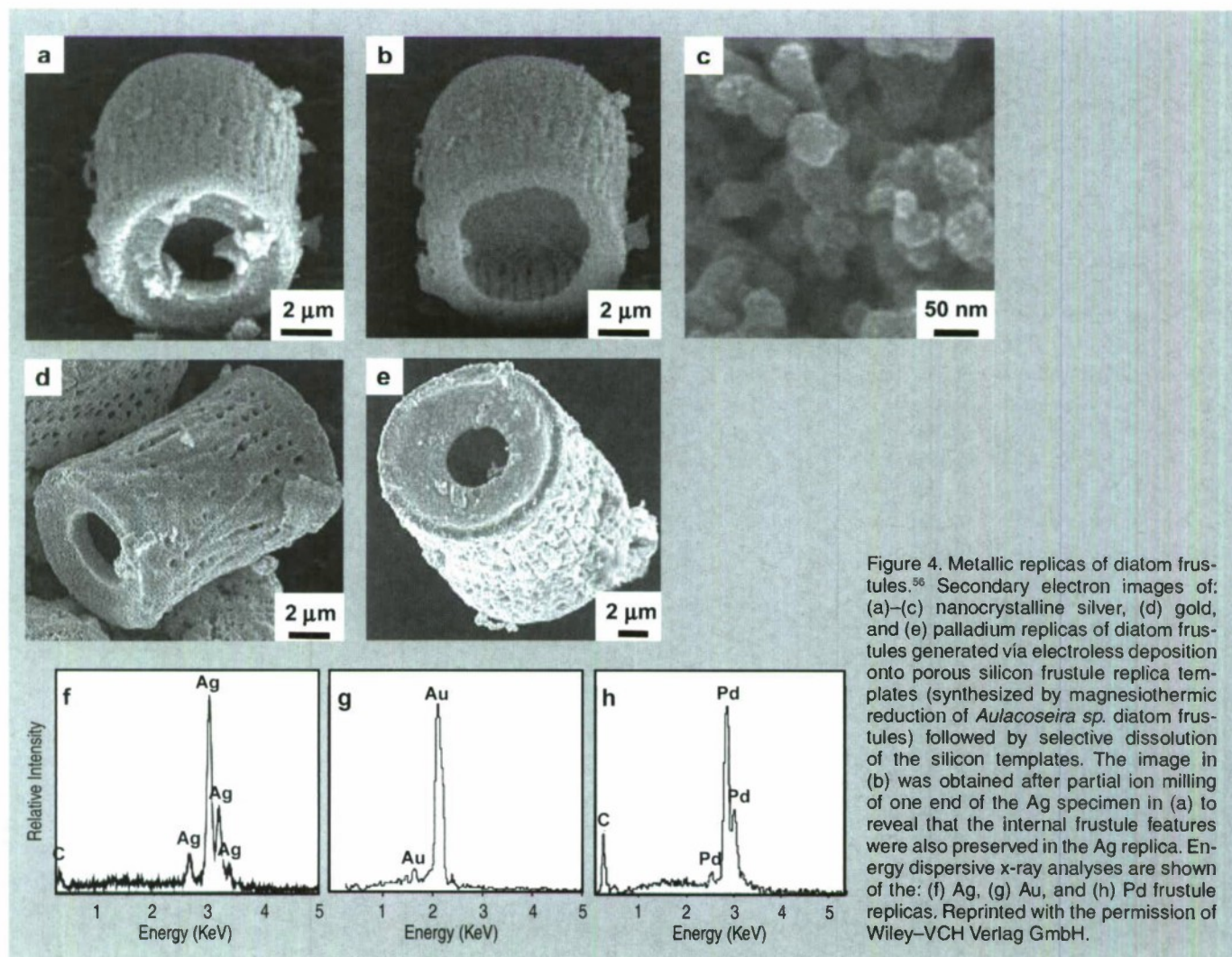


Figure 4. Metallic replicas of diatom frustules.⁵⁶ Secondary electron images of: (a)–(c) nanocrystalline silver, (d) gold, and (e) palladium replicas of diatom frustules generated via electroless deposition onto porous silicon frustule replica templates (synthesized by magnesiothermic reduction of *Aulacoseira* sp. diatom frustules) followed by selective dissolution of the silicon templates. The image in (b) was obtained after partial ion milling of one end of the Ag specimen in (a) to reveal that the internal frustule features were also preserved in the Ag replica. Energy dispersive x-ray analyses are shown of the: (f) Ag, (g) Au, and (h) Pd frustule replicas. Reprinted with the permission of Wiley-VCH Verlag GmbH.

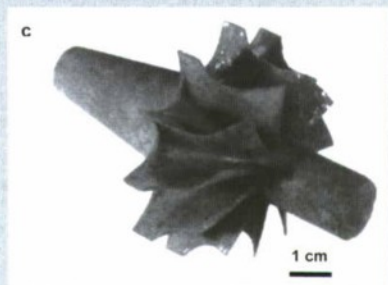
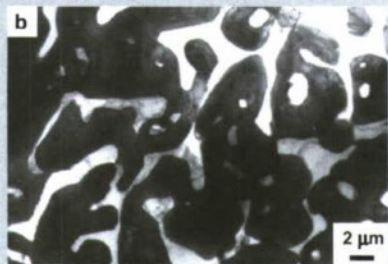


Figure 5. Dense, near net-shape $\text{Al}_2\text{O}_3/\text{Al}$ composites produced by reactive metal penetration. (a) Secondary electron and (b) transmission electron images of interpenetrating $\text{Al}_2\text{O}_3/\text{Al}$ -based composites fabricated by the reactive metal penetration (or co-continuous ceramic composite, C^4) process.⁵⁹ (c) An optical image of a near net-shape $\text{Al}_2\text{O}_3/\text{Al}$ turbocompression wheel fabricated by reactive metal penetration.⁵⁹ Images provided by G.S. Daehn (The Ohio State University).

automotive disk brake rotors and calipers, internal combustion engine piston crowns, turbine compressors, and cylinder liners.^{58–62,65} The thermal and mechanical performance of such co-continuous composites have been further tailored through modifications of the preform and melt chemistries. For example, the reaction of shaped preforms comprised of mixtures of SiC and SiO_2 with an Al-Si alloy melt has yielded SiC/ Al_2O_3 /Al-based composites with enhanced thermal conductivity, thermal shock resistance, and wear resistance.^{60,65} The continuous metallic phase has also been modified by immersing shaped $\text{Al}_2\text{O}_3/\text{Al}$ -bearing composites in a second bath of another metal alloy to allow for chemical alteration via liquid phase diffusion and exchange. For example, such a liquid

exchange process has been used to generate composites with continuous Cu-Al-Fe, Fe-Al, or Ni-Al phases for higher temperature applications.^{60,61,66}

The average size of the oxide and metal colonies within co-continuous alumina/aluminum-bearing composites formed by reactive metal penetration of silica-bearing or mullite-bearing preforms at 1,000–1,200°C is typically several micrometers, although a significant population of submicrometer sized ligaments has also been observed.^{59,64,67} The oxide and metal colony size can be appreciably reduced, however, through alloying additions to the molten aluminum. For example, Strange and Breslin⁶⁸, and Evarts⁶⁹ have reported that the introduction of copper into the aluminum melt has a dramatic impact on the scale of the microstructure of composites formed by reactive metal penetration. These authors immersed dense amorphous SiO_2 preforms into Cu-Al melts comprised of 30–63 at.% (50–80 wt.%) Cu at 1,100–1,150°C. The rates of linear penetration for these copper-aluminum alloy melts into the silica preforms were lower than for pure molten aluminum. Dramatic reductions in the colony sizes of the co-continuous oxide and intermetallic (AlCu , Al_2Cu) phases were observed for melts with ≥ 50 at.% Cu (Figures 6a–d). The nanostructured $\text{Al}_2\text{O}_3/\text{AlCu}/\text{Al}_2\text{Cu}$ composites were also found to exhibit substantially higher values of hardness than microstructured $\text{Al}_2\text{O}_3/\text{AlCu}/\text{Al}_2\text{Cu}$ composites.⁶⁹ Yoshikawa et al.⁶⁶ have reported that the reactive metal penetration of molten Fe-Al alloys into dense amorphous SiO_2 rods at 1,200–1,300°C yielded co-continuous, nanocrystalline $\text{Al}_2\text{O}_3/\text{Fe}_x\text{Al}_y$ composites.⁶⁶ With increasing iron content in the melt (from 5–30 at.% Fe), the rate of reactive metal penetration into the silica preform decreased and composites with iron-aluminum intermetallic phases of higher iron content were generated (i.e., predominantly Al_3Fe for a 20 at.% Fe melt vs. predominantly Al_5Fe_2 for a 30 at.% Fe melt).⁶⁶

Reactive Casting

Reactive casting of molten metals or alloys into porous ceramic-bearing preforms has also been used to generate near net-shaped composites comprised

of new ceramic (e.g., Al_2O_3 , MgO, MgAl_2O_4 , ZrC, HfC) and metallic (e.g., Al, Mg-Al, Fe-Ni-Al, Fe-Ni-Cr, Fe-Cr-Al, Ni-Co-Cr-Al, W) or intermetallic (e.g., NbAl_3 , Nb_2Al , TiAl_3 , $\text{Ti}(\text{Al},\text{Si})_3$, NiAl, Ni_3Al , FeAl) phases.^{58,60,70–85} Prior to such reactive casting, a reactant-bearing powder or powder mixture, containing appropriate ceramic or ceramic and metal constituents, is first shaped into a rigid preform of desired morphology and porosity. Preforms of

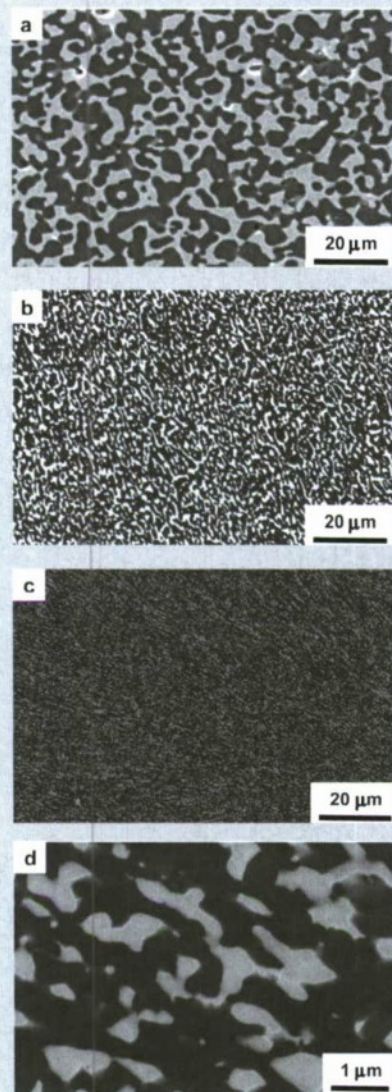


Figure 6. Influence of the composition of the reactive melt on the domain sizes of the oxide and metal/intermetallic products produced by reactive metal penetration. Secondary electron images of co-continuous composites of Al_2O_3 (dark phase) and: (a) Al, or (b)–(d) AlCu and Al_2Cu .⁶⁹ These composites were generated by the immersion of dense amorphous silica in a molten aluminum-bearing bath containing (a) no Cu, (b) 50 at.% (70 wt.%) Cu, and (c), (d) 63 at.% (80 wt.%) Cu at 1,150°C. Reprinted with the permission of J.S. Evarts.

complex morphology have been prepared by a variety of methods, including slip or gel casting, green machining, powder injection molding, or rapid prototyping approaches.^{79,80,85} Some firing of the preform is typically conducted prior to pressureless reactive infiltration to allow for some particle necking in the preform (for sufficient rigidity to avoid shape distortion during reactive casting) and to obtain a desired level of preform porosity. Indeed, the final phase content of composites generated by reactive casting may be tailored by adjusting the porosity, as well as the phase content, of the shaped rigid preform. Consider, for example, the net liquid/solid displacement Reactions 7a, 7b, 8, and 9,^{70–80} where {Al}, {Mg}, and {Zr} refer to aluminum, magnesium, and zirconium present within a melt. Like for Reaction 6, displacement Reactions 7a and 7b generate oxide products that possess a smaller volume than the oxide reactant (e.g., the volume of 2 moles of $\alpha\text{-Al}_2\text{O}_3$ is 9.3% smaller than the volume of 3 moles of rutile TiO_2 ⁸⁶). Such a reaction-induced reduction in the internal solid oxide volume, coupled with the starting open pore volume of the rigid preform, provides the space required to accommodate the formation of the solid titanium aluminide product (via the reactive casting approach known as the infiltration alumina aluminide alloy, or i-3A, process^{70–72}). By tailoring the starting preform porosity, the aluminum content of the aluminide phase (e.g., TiAl_3 vs. TiAl) and the relative amount of aluminide in the final dense composite may be adjusted.^{70–72} Displacement Reactions 8 and 9, on the other hand, generate more ceramic volume than is consumed (e.g., the volume of 3 moles of MgO is 32% larger than the volume of 1 mole of $\alpha\text{-Al}_2\text{O}_3$). Such a reaction-induced increase in the internal solid volume within a reacting, rigid preform can be used to generate ceramic/metal or ceramic/intermetallic composites with relatively high ceramic contents (via the reactive casting approach known as the displacive compensation of porosity, or DCP, process^{73–80}). Indeed, electrically-insulating $\text{MgO}/\text{Mg-Al}$ composites comprised of ≥ 83 vol.% MgO have been produced by such a reactive casting process; that

is, sufficient metallic liquid was extruded out of the rigid specimen during reactive conversion of Al_2O_3 into MgO (Reaction 8) that the remaining entrapped metallic (Al-Mg) phase was discontinuous.⁷³ Because the partially sintered (necked) preforms remain rigid during such reactive infiltration, porous preforms of complex shape, fabricated by gel casting,⁷⁹ green machining,⁸⁰ or three-dimensional printing,⁸⁰ have been converted into dense ceramic-rich products that retain the shapes and dimensions (to within 1%) of the starting porous preforms (Figure 7a–c).

The sizes of ceramic and metal or intermetallic phases generated within reactively cast composites can be appreciably refined through the use of fine-scale reactant phases in the starting porous preforms, rapid molten metal infiltration at a modest temperature, and modest post-infiltration heat treatment.^{71,72,82} For example, $\text{Al}_2\text{O}_3/\text{Ti}(\text{Al},\text{Si})_3$ -based composites with phase sizes of a few micrometers to submicrometers have been produced by: i) attrition milling of a mixture of fine Al_2O_3 (1.2 μm ave. size) and TiO_2 (0.5 μm ave. size) powders, ii) compacting and sintering the powder mixture for 0.5 h at 1,150°C (to generate a rigid preform with a porosity of 49 vol.%), iii) rapid squeeze casting (within a few seconds) of a molten Al-Si alloy at 700°C into the porous preform, and then iv) annealing of the resulting infiltrated preform for 3 h at 800°C.^{72,82} While the as-cast specimen contained unreacted TiO_2 , Al, and Si phases and no apparent $\text{Ti}(\text{Al},\text{Si})_3$ product (as determined from x-ray diffraction analysis), the subsequent 800°C/3 h thermal treatment resulted in complete conversion of the as-cast specimen into an intimate mixture of Al_2O_3 and $\text{Ti}(\text{Al},\text{Si})_3$. Such fine-scale, reactively cast, near net-shape $\text{Al}_2\text{O}_3/\text{Ti}(\text{Al},\text{Si})_3$ composites possessed fracture strengths (4 point bending) of 490–540 MPa, fracture toughness (by indentation) values of 5.0–8.6 $\text{MPa}\cdot\text{m}^{1/2}$, and hardness values of 5.7–7.4 GPa.^{72,82} A similar approach (milling of fine oxide/metal powders, partial sintering, rapid squeeze casting, and modest annealing after casting) has been used to fabricate near net-shaped metal matrix composites (Fe-Ni-Cr-based or Ni-Co-Cr-Al-based) rein-

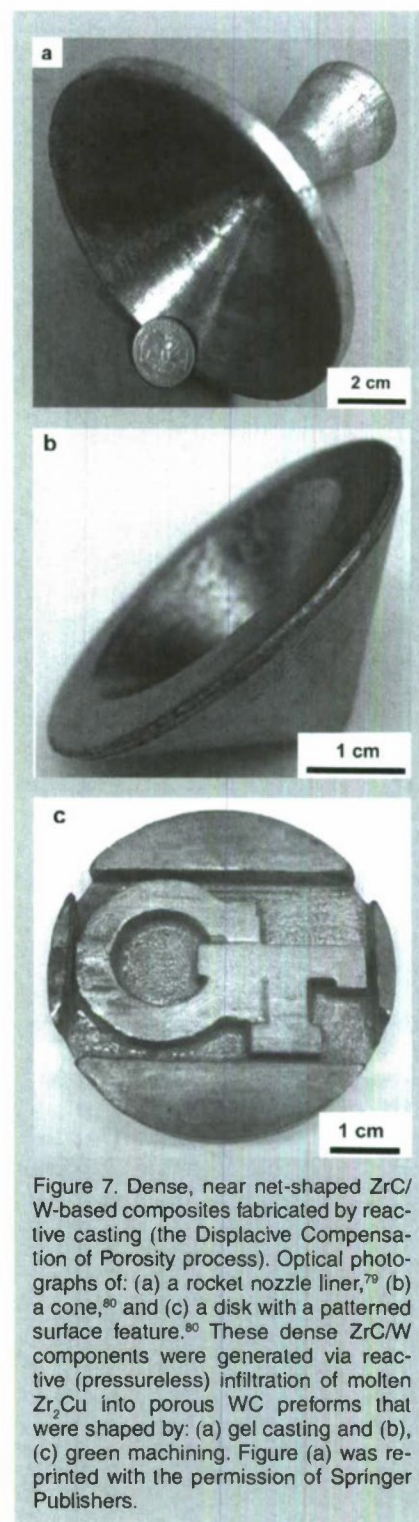


Figure 7. Dense, near net-shaped ZrC/W-based composites fabricated by reactive casting (the Displacive Compensation of Porosity process). Optical photographs of: (a) a rocket nozzle liner,⁷⁹ (b) a cone,⁸⁰ and (c) a disk with a patterned surface feature.⁸⁰ These dense ZrC/W components were generated via reactive (pressureless) infiltration of molten Zr_2Cu into porous WC preforms that were shaped by: (a) gel casting and (b), (c) green machining. Figure (a) was reprinted with the permission of Springer Publishers.

forced with nanoscale Al_2O_3 filaments (via the reactive casting approach known as the infiltration Metal Matrix Composite process^{81–85}). The fracture strengths of reactively cast Fe-Ni-Cr-based alloy composites reinforced with nanoscale Al_2O_3 at 550°C and 900°C were found to be almost twice the values of a similar reference metal alloy lacking the alumina phase.⁸³ A derivative of such reactive casting (“in-situ”

Table II. The Pilling Bedworth Ratio (PBR) and Melting Points (T_m) of Several Elements*

Element (T_m)	Oxide	PBR	Element (T_m)	Oxide	PBR
Al (660°C) \Rightarrow	$Al_2O_3^a$	1.28	Mg (650°C) \Rightarrow	MgO	0.803
Zr (1855°C) \Rightarrow	ZrO_2^b	1.51	Ba (727°C) \Rightarrow	BaO	0.670
Ni (1455°C) \Rightarrow	NiO	1.67	Ca (842°C) \Rightarrow	CaO	0.638
Ti (1670°C) \Rightarrow	TiO_2^c	1.77	Sr (769°C) \Rightarrow	SrO	0.611
Si (1414°C) \Rightarrow	SiO_2^d	1.88	Li (181°C) \Rightarrow	Li_2O	0.567
Cr (1863°C) \Rightarrow	Cr_2O_3	2.01	Na (97.8°C) \Rightarrow	Na_2O	0.541
Nb (2469°C) \Rightarrow	Nb_2O_5	2.70	K (63.7°C) \Rightarrow	K_2O	0.474

* $PBR = V_{N_2O_x} / [xV_N] = [M_{N_2O_x} \rho_{N_2O_x}] / [xM_N \rho_N]$ where $V_{N_2O_x}$ refers to the molar volume of an oxide, N_2O_x ; V_N refers to the molar volume of an element N; $M_{N_2O_x}$ refers to the molecular mass of N_2O_x ; M_N refers to the atomic mass of N; and $\rho_{N_2O_x}$ and ρ_N refer to the densities of N_2O_x and N, respectively).

^afor Al_2O_3 as corundum; ^bfor monoclinic ZrO_2 ; ^cfor TiO_2 as rutile; ^dfor SiO_2 as low quartz

or “short-distance” infiltration^{82,85,87,88}, involving local aluminum melting and brief reaction within attrition-milled oxide/metal mixtures under an applied pressure, has also been used to synthesize dense metal alloy matrix composites reinforced with interconnected Al_2O_3 filaments of a few hundred nanometers thickness. Such Fe-Cr-Ni alloy/nanofilamentary Al_2O_3 composites have exhibited fracture strength and fracture toughness values of 1,100 MPa and 18 MPa·m^{1/2}, respectively, in three-point bending.⁸⁸

CONVERSION OF MACROSCOPIC PREFORMS BY GAS/SOLID REACTIONS

Two general oxidation-based approaches that are capable of converting shaped, macroscopic, freestanding, solid metal-bearing preforms into oxide products that retain the preform shape with relatively little or no change in dimensions (Figure 8) are the reaction bonded metal oxide (RBMO) process, and the volume identical metal oxidation (VIMOX) process. (Note: while the reaction bonded metal oxide, RBMO, process is often referred to as the reaction bonded aluminum oxide, or RBAO, process, in light of the pioneering work of Claussen, et al.,^{89,93–100} the RBMO label is used herein, as this process may be used to generate a variety of metal oxides.)

Use of Oxidation-induced Volume Changes for Near Net-Shape Processing

For both of the patented RBMO⁸⁹ and VIMOX processes,^{90,91} the volume change(s) associated with oxidation are used to partially or fully offset op-

posing volume changes resulting from other phenomena. Consider the oxide-to-metal volume ratios for several elements, often referred to as the Pilling Bedworth Ratio (PBR), presented in Table II.⁹² For the elements in the left half of Table II, the PBR values are well in excess of unity (as is true for most elements). For a solid, porous preform containing one or more of these elements (as well as perhaps other constituents that exhibit an increase in solid volume upon oxidation, such as silicon carbide), the oxidation-induced increase in solid volume may be offset by the sintering-induced shrinkage during post-oxidation annealing. Hence, a shaped porous preform containing tailored amounts of metal, ceramic, and porosity may be converted, with appropriate oxidation and sintering treatments, into a dense all-oxide body that preserves the preform shape with relatively little or no net shrinkage. For example, porous green-machined bodies of Al, Al_2O_3 , SiC, and ZrO_2 have been converted into dense composites of $Al_6Si_2O_{13}$ (mullite) and ZrO_2 that retain the preform shape and dimensions (to within 1%).⁹³ This is the basic premise for near net-shape processing by the RBMO method. The RBMO approach has been extensively utilized to generate low-shrinkage Al_2O_3 -based (e.g., Al_2O_3 , Al_2O_3 - ZrO_2 , Al_2O_3 - ZrO_2 - Nb_2O_5) or $Al_6Si_2O_{13}$ (mullite)-based ($Al_6Si_2O_{13}$, $Al_6Si_2O_{13}$ - ZrO_2 , $Al_6Si_2O_{13}$ -SiC, $Al_6Si_2O_{13}$ -SiC- ZrO_2) materials for applications requiring high stiffness, strength, wear resistance, and modest weight (e.g., gears, dies, punches, or dental implants).^{94–101}

For the alkali and alkaline earth elements shown in the right half of Table

II, the PBR values are well below unity. Such oxidation-induced reductions in solid volume may be used to accommodate volume expansions resulting from the oxidation of other elements and/or the formation of oxide compounds. Hence, a shaped dense preform containing tailored amounts of alkali or alkaline earth elements and other metallic and/or ceramic phases may be converted, by appropriate oxidation and post-oxidation annealing treatments, into a dense all-oxide body that retains the shape and dimensions of the preform. For example, a compacted green body of Ba, Sr, Al, Al_2O_3 , and SiO_2 has been converted into a (Ba,Sr) $Al_2Si_2O_8$ (celsian) body that retained the preform shape and dimensions (to within 1%).^{102,103} This is the basic premise for near net-shape processing by the VIMOX approach. The VIMOX approach has yielded a variety of near net-shaped, functional, alkaline earth oxide-bearing components (e.g., ferroelectric BaTiO₃, PTCR (Ba,Pb)TiO₃, proton-conducting BaCeO₃, ferrimagnetic BaFe₁₂O₁₉, bio-compatible Ca₆(PO₄)₁₀(OH)₂, and refractory MgAl₂O₄, BaAl₂O₄, and BaAl₂Si₂O₈).^{102–115}

Fabrication of Shaped, Metal-bearing Preforms

The fabrication of solid RBMO and VIMOX preforms typically involves the preparation of a powder mixture comprised of desired metal and ceramic phases, and then compaction and forming of the powder mixture into a green body of desired shape, porosity, and strength. For both approaches, preforms comprised of fine, intimate mixtures of metal and ceramic phases are required in order to obtain desired oxidation and reaction kinetics. High-energy ball milling can be an effective means of preparing such fine, reactive mixtures, although proper care needs to be taken during such milling to avoid undesired reactions (e.g., excessive oxidation and hydration of metallic constituents, formation of brittle intermetallic compounds) and excessive incorporation of wear debris from the milling media and milling vessel into the powder mixture. Proper optimization of milling intensity (e.g., rotation speed during attrition milling), ball-to-charge ratio, starting oxide particle size, mill-

ing time, and milling fluid is required to obtain metal/ceramic mixtures of desired composition, phase content, and phase size for subsequent compaction, forming, and oxidation/reaction treatments.^{94–98,100,103,105,107,116,117} A sufficient amount of ductile metal in the milled powder mixture is required to allow for uniform compaction and forming into a green body of relatively high strength, and to achieve the desired oxidation-induced volume change(s) for shape and dimension preservation. Compacted RBMO and VIMOX powder mixtures with ≥ 30 vol.% ductile metal can readily be machined, using conventional steel tooling, into intricately-shaped green bodies.^{93,96,100,103,112,114,118} Metal-rich alkaline-earth-bearing precursors (e.g., with ≥ 60 vol.% metal) have also been rolled into thin (down to 25 μm) tapes or drawn into multifilamentary (down to 250 nm diameter filaments) wires.^{103,104,107,108,111,119,120}

Oxidation Processing

The conversion of metal-bearing RBMO and VIMOX green bodies into shape-preserved, oxide-based bodies of desired phase content and microstructure requires the use of controlled oxidation and post-oxidation annealing treatments. Particular concerns associated with the oxidation treatment include: the generation of appreciable metallic liquid due to incomplete oxidation at subsolidus temperatures, and thermal runaway (ignition) associated with the exothermic nature of the oxidation reactions.^{100,104,105,121,122} Excessive metallic liquid formation (with or without ignition) can lead to undesired agglomeration and phase coarsening, an uncontrolled change in preform composition or porosity (due to the loss of a nonwetting metallic liquid from the preform), and/or a distortion in the preform shape.^{100,104,108,111} Ignition can lead to the extensive formation of defects (cracks, pores) and geometric distortions due to thermal stresses associated with steep temperature gradients and chemical stresses associated with sharp compositional gradients.^{121,122} In the RBMO process, the oxidation treatment is typically conducted with a prolonged heat treatment (involving a slow heating rate and/or an extended isothermal anneal) below the melting

point of aluminum to allow for extensive subsolidus oxidation.^{96–98,117} The time required for such subsolidus aluminum oxidation in the RBMO process has been reported to depend upon the amount of aluminum, the aluminum particle size and the preform porosity (which are affected by the milling and compaction conditions), as well as the preform size.^{98,117,121} In order to dramatically shorten the required oxidation time while avoiding ignition, particularly for green bodies with relatively large characteristic dimensions, feedback control firing (using the rate of specimen weight gain to control heating), has successfully been applied to RBAO green bodies.¹²² With PBR values less than unity, porous (non-protective) oxide scales tend to form on alkaline earth metals (Mg, Ca, Sr, Ba) during oxidation at modest temperatures (e.g., at 300–500°C), so that

the oxidation of VIMOX preforms can occur at a relatively rapid rate at subsolidus temperatures, even for green bodies of low initial porosity.^{92,102–115} However, the thermally-insulating nature of the resulting porous alkaline earth oxides requires that a modest rate of heating be used during subsolidus oxidation to avoid ignition and the associated thermal and chemical stresses and defects/distortions.^{92,103,105,111,114}

Post-oxidation Annealing

The subsolidus oxidation of VIMOX preforms can yield fine nanocrystalline oxide-bearing mixtures that, in turn, can react with other metal or oxide constituents in the preforms to generate binary oxide compounds at low temperatures. For example, the oxidation of barium in air or oxygen at 300°C yields a fine-grained peroxide, BaO_2 , that reacts rapidly at modest tempera-

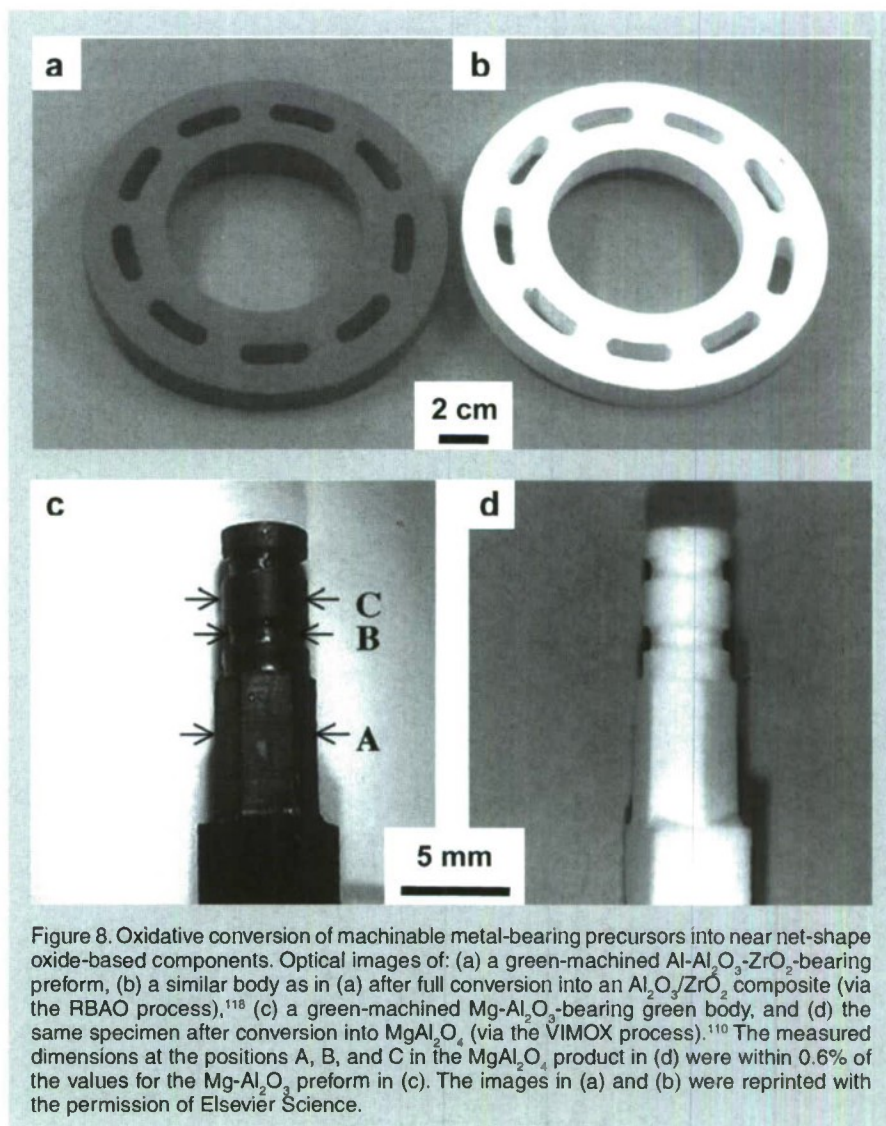


Figure 8. Oxidative conversion of machinable metal-bearing precursors into near net-shape oxide-based components. Optical images of: (a) a green-machined $\text{Al-Al}_2\text{O}_3\text{-ZrO}_2$ -bearing preform, (b) a similar body as in (a) after full conversion into an $\text{Al}_2\text{O}_3/\text{ZrO}_2$ composite (via the RBAO process),¹¹⁸ (c) a green-machined $\text{Mg-Al}_2\text{O}_3$ -bearing green body, and (d) the same specimen after conversion into MgAl_2O_4 (via the VIMOX process).¹¹⁰ The measured dimensions at the positions A, B, and C in the MgAl_2O_4 product in (d) were within 0.6% of the values for the $\text{Mg-Al}_2\text{O}_3$ preform in (c). The images in (a) and (b) were reprinted with the permission of Elsevier Science.

tures with other metallic constituents to yield binary oxide compounds (e.g., the reaction of BaO_2 with Al, Si, and Ti has yielded BaAl_2O_4 , Ba_2SiO_4 , and Ba_2TiO_4 , respectively, at 300–550°C—well below the melting points of Al, Si, and Ti).^{103,105,106,109,113,124,125} Continued firing and reaction of such oxidized VIMOX preforms has yielded a variety of fully-reacted, functional multicomponent oxides at modest temperatures. For example, dense tapes of the superconductor, $\text{Bi}_2\text{Sr}_2\text{Ca}_1\text{Cu}_2\text{O}_{8+x}$, and of the proton conductor, $\text{Ba}(\text{Ce},\text{Nd})\text{O}_3$, have been produced from oxidized metal-rich precursor tapes after firing at peak temperatures of only 860°C and 900°C, respectively.^{103,126} Dense composites comprised of alternating layers enriched in fine (submicrometer thick) platelets of superconducting $\text{YBa}_2\text{Cu}_3\text{O}_{7-y}$ and in Ag have been generated via an oscillating internal oxidation treatment of Y-Ba-Cu-Ag metallic precursor tapes at 400–600°C followed by firing at a peak temperature of 900°C.¹²⁷ Intentionally porous tapes of nanocrystalline doped $(\text{Ba},\text{Pb})\text{TiO}_3$ (a thermistor material with a relatively high Curie temperature) and ferrimagnetic $\text{BaFe}_{12}\text{O}_{19}$ have been generated at 750°C and 900–1,080°C, respectively.^{103,108,111}

RBMO preforms have also been converted into dense, nanocrystalline oxide-based materials. With proper use of high-energy milling to obtain a finely-divided, well-intermixed assemblage of reactive metallic and ceramic phases, with appropriate conditions of compaction and oxidation, and with the use of fine second phases to inhibit grain growth during post-oxidation sintering, dense RBMO composites have been synthesized with submicrometer grain sizes. For example, Claussen et al.⁹⁷ have reported the syntheses of reaction bonded composites comprised of 55 vol.% mullite, 10 vol.% silicon carbide, 21 vol.% alumina, and 14 vol.% zirconia with phase sizes well below 1 μm . The introduction of fine (0.2 μm dia.) $\alpha\text{-Al}_2\text{O}_3$ seeds to preform mixtures to enhance the conversion of $\gamma\text{-Al}_2\text{O}_3$ (a metastable alumina polymorph formed during low-temperature aluminum oxidation) into $\alpha\text{-Al}_2\text{O}_3$, and to further refine the grain size of sintered reaction-bonded alumina, has been suggested by Suvaci and Messing.¹²⁸ Mullite crystal

seeding to reduce the mullite grain size in reaction-bonded mullite has also been proposed by She et al.¹²⁹ Fine-grained reaction-bonded alumina has been reported to exhibit superplastic-like behavior at 1,250–1,500°C, which may be utilized to generate dense, shaped, nanocrystalline components, via sinter forming or sinter forging, at appreciably lower temperatures than for pressureless sintering.^{97,101} Bourz et al.¹³⁰ have generated sinter-forged nanocrystalline (0.63 μm ave. alumina grain size) reaction-bonded alumina-zirconia composites of >95% of theoretical density at only 1,300°C. Such nanocrystalline, reaction-bonded alumina-zirconia composites have exhibited room temperature fracture strengths (in biaxial bending) of 1.1 GPa.¹³⁰ Dense, fine-grained, reaction-bonded alumina-zirconia composites prepared by pressureless sintering at 1,550°C have also exhibited respectable room temperature fracture strength and fracture toughness values (in 4-point bending) of ≥ 700 MPa and 3.5 $\text{MPa}\cdot\text{m}^{1/2}$.^{96,100} Dense, fine-grained, reaction-bonded mullite-silicon carbide-alumina-zirconia composites (with 49–55 vol.% mullite) prepared by pressureless sintering at 1,550°C have exhibited room temperature fracture strength and fracture toughness values (in 4-point bending) of 490–610 MPa and 4.1–4.9 $\text{MPa}\cdot\text{m}^{1/2}$.^{97,99}

CONCLUSIONS

As demonstrated in this overview, nanostructured materials with complex macroscopic-to-microscopic shapes and with tailorable chemistries may be fabricated by first generating a preform with a desired morphology and then chemically transforming the shaped preform into a new material that retains the preform morphology (a type of materials “alchemy”). This fabrication paradigm enables materials that can be readily generated with complex shapes (e.g., formable metal-rich compositions for macroscale components or biologically formed inorganic microscale structures) to be used in the preform fabrication step prior to chemical transformation into the desired material. Under appropriate conditions, gas/solid and liquid/solid reactions can then be used for the shape-preserving conversion of such macroscopic-to-mi-

croscopic solid preforms into chemically tailored nanostructures with desired properties. The identification of reaction conditions that allow for such shape-preserving conversion into new nanostructured materials has been significantly aided by utilizing well-known concepts and phenomena from the field of high temperature corrosion (e.g., the Pilling–Bedworth Ratio, active vs. passive corrosion, ignition, internal oxidation). Indeed, by taking the perspective that fluid/solid reactions are a type of “chemical processing”, as opposed to a type of “corrosion”, this author is confident that scholars who are well-versed in the prior mechanistic knowledge established in the field of high temperature corrosion will continue to develop attractive reaction-based approaches for synthesizing advanced nanostructured materials with tailored morphologies, chemistries, and properties.

ACKNOWLEDGEMENTS

K.H.S. acknowledges the financial support of the Air Force Office of Scientific Research (Dr. Charles Lee, Dr. Hugh DeLong, and Dr. Joan Fuller, program managers) and the U.S. Department of Energy (Dr. Michael Markowitz, program manager).

References

1. E.E. Round, R.M. Crawford, and D.G. Mann, *The Diatoms. Biology and Morphology of the Genera* (New York: Cambridge University Press, 1990).
2. D.G. Mann, *Phycologia*, 38 (6) (1999), pp. 437–495.
3. M. Hildebrand, *Chem. Rev.*, 108 (2008), pp. 4855–4874.
4. V. Martin-Jezequel, M. Hildebrand, and M.A. Brzezinski, *J. Phycol.*, 36 (2000), pp. 821–840.
5. K.H. Sandhage et al., *Int. J. Appl. Ceram. Technol.*, 2 (4) (2005), pp. 317–326.
6. R. Gordon, F.A.S. Sterrenburg, and K.H. Sandhage, *J. Nanosci. Nanotechnol.*, 5 (1) (2005), pp. 1–4.
7. K.H. Sandhage et al., *Adv. Mater.*, 14 (6) (2002), pp. 429–433.
8. K.H. Sandhage, U.S. patent 7,067,104 (27 June 2006).
9. K.H. Sandhage, U.S. patent 7,204,971 (17 April 2007).
10. A.A. Nayeib-Hashemi and J.B. Clark, *Bull. Alloy Phase Diagr.*, 5 (6) (1984), pp. 584–592.
11. M.B. Dickerson et al., *J. Nanosci. Nanotech.*, 5 (1) (2005), pp. 63–67.
12. M.T. Frost et al., *Trans. Inst. Mining Metall.*, 99 (1990), pp. C117–C124.
13. R. Kon and M. Miyazaki, *Fragrance J.*, 31 (8) (2003), pp. 63–68.
14. J.J. Mortvedt and J.J. Kelsoe, *Fert. Res.*, 15 (2) (1988) pp. 155–161.
15. Z. Xin, W.B. Tucker, and R.W. Hemken, *J. Dairy Sci.*, 72 (2) (1989), pp. 462–470.
16. S. Spychaj and F.J. Balta Calleja, *J. Mater. Sci. Lett.*, 12 (16) (1993), pp. 1255–1257.
17. Y. Cai et al., *J. Am. Ceram. Soc.*, 88 (7) (2005), pp.

- 2005–2010.
18. M.S. Haluska et al., *Powder Diff.*, 20 (4) (2005), pp. 306–310.
19. M.S. Haluska et al., *Rev. Sci. Instr.*, 76 (2005), pp. 126101-1–126101-4.
20. S.M. Allan et al., *Ceram. Eng. Sci. Proc.*, 26 (3) (2005), pp. 289–296.
21. Z. Bao et al., *Nature*, 446 (3) (2007), pp. 172–175.
22. K.H. Sandhage, U.S. patent 7,393,517 (1 July 2008).
23. K.H. Sandhage and Z. Bao, U.S. patent 7,615,206 (10 November 2009).
24. E.K. Richman et al., *Nano Lett.*, 8 (9) (2008), pp. 3075–3079.
25. R.F. Shepherd et al., *Adv. Mater.*, 20 (24) (2008), pp. 4734–4739.
26. M. Ibisate, D. Golmayo, and C. Lopez, *Adv. Mater.*, 21 (28) (2009), pp. 2899–2902.
27. M. Bengtsson et al., *Phys. Status Solidi A*, 182 (2000), pp. 495–504.
28. H.-C. Shin et al., *J. Power Sources*, 139 (2005), pp. 314–320.
29. V. Pacebutas, K. Grigoros, and A. Krotkus, *Phys. Scripta*, T69 (1997), pp. 255–258.
30. J.R. Szczech and S. Jin, *J. Solid State Chem.*, 181 (7) (2008), pp. 1565–1570.
31. R.R. Unocic et al., *Chem. Comm.*, 7 (2004), pp. 795–796.
32. K.H. Sandhage et al., *Handbook of Biomineralization*, ed. P. Behrens and E. Bauerlein (Weinheim, Germany: Wiley-VCH Verlag GmbH, 2007), pp. 235–253.
33. S.-J. Lee et al., *J. Am. Ceram. Soc.*, 90 (5) (2007), pp. 1632–1636.
34. S. Shian and K.H. Sandhage, *Rev. Sci. Instr.*, 80 (2009), pp. 115108/1–115108/7.
35. J.C. Lyle et al., *Chem. Mater.*, 16 (20) (2004), pp. 3829–3837.
36. S. Shian et al., *J. Am. Ceram. Soc.*, 89 (2) (2006), pp. 694–698.
37. C. Wagner, *J. Appl. Phys.*, 29 (9) (1958), pp. 1295–1298.
38. S.Y. Ip, M.J. McNallan, and D.S. Park, *J. Am. Ceram. Soc.*, 75 (7) (1992), pp. 1942–1048.
39. T. Hyodo et al., *Chem. Sensors* 18 (2002), pp. 178–180.
40. M. Lanata et al., *Opt. Mater.*, 17 (2001), pp. 11–14.
41. C.J. Barbe et al., *J. Am. Ceram. Soc.*, 80 (1997), pp. 3157–3171.
42. M. Manso et al., *Biomater.*, 23 (2002), pp. 349–356.
43. G. Fu, P.S. Vary, and C.-T. Lin, *J. Phys. Chem. B*, 109 (18) (2005), pp. 8889–8898.
44. J.H. Braun, *J. Coatings Technol.*, 69 (868) (1997), pp. 59–72.
45. A.B. Alles, V.R.W. Amarakoon, and V.L. Burdick, *J. Am. Ceram. Soc.*, 72 (1) (1989), pp. 148–151.
46. M. Viviani et al., *J. Euro. Ceram. Soc.*, 21 (10-11) (2001), pp. 1981–1984.
47. M.A.R.C. Alencar et al., *Appl. Phys. Lett.*, 84 (23) (2004), pp. 4753–4755.
48. D.E. Rase and R. Roy, *J. Am. Ceram. Soc.*, 38 (11) (1955), pp. 389–395.
49. R.S. Roth et al., *J. Solid State Chem.*, 104 (1) (1993), pp. 99–118.
50. M.R. Weatherspoon et al., *Chem. Commun.*, (5) (2005), pp. 651–653.
51. M.R. Weatherspoon et al., *J. Electrochem. Soc.*, 153 (2) (2006), pp. H34–H37.
52. Y. Cai et al., *Ceram. Eng. Sci. Proc.*, 27 (8) (2007), pp. 49–56.
53. R. Zeis et al., *J. Power Sources* 165 (1) (2007), pp. 65–72.
54. D. Ding and Z. Chen, *Adv. Mater.*, 19 (15) (2007), pp. 1996–1999.
55. R.W. Ertenberg, B. Andraka, and Y. Takano, *Phys. B*, 284-288 (2000), pp. 2022–2023.
56. Z. Bao et al., *Adv. Mater.*, 21 (4) (2009), pp. 474–478.
57. E.M. Ernst et al., *J. Mater. Res.*, 22 (5) (2007), pp. 1121–1127.
58. M.C. Breslin, U.S. patent 5,214,011 (25 May 1993).
59. M.C. Breslin et al., *Mater. Sci. Eng.*, A195 (1995), pp. 113–119.
60. G.S. Daehn and M.C. Breslin, *JOM*, 58 (11) (2006), pp. 87–91.
61. E. del Rio et al., *Mater. Sci. Eng. A*, 463 (2007), pp. 115–121.
62. R.E. Loehman, K. Ewsuk, and A.P. Tomsia, *J. Am. Ceram. Soc.*, 79 (1) (1996), pp. 27–32.
63. W.G. Fahrenholtz et al., *J. Am. Ceram. Soc.*, 79 (9) (1996), pp. 2497–2499.
64. Y. Gao et al., *J. Mater. Sci.*, 31 (1996), pp. 4025–4032.
65. M.Y. Chen and M.C. Breslin, *Wear*, 249 (10-11) (2001), pp. 868–876.
66. N. Yoshikawa, A. Hattori, and S. Taniguchi, *Mater. Sci. Eng.*, A342 (2003), pp. 51–57.
67. V.S.R. Murthy et al., *J. Am. Ceram. Soc.*, 88 (10) (2005), pp. 2902–2907.
68. A.C. Strange and M.C. Breslin, U.S. patent 5,728,638 (17 March 1998).
69. J.S. Everts, M.S. Thesis, The Ohio State University (2008).
70. C. Scheu et al., *Phys. Stat. Sol. A*, 166 (1998), pp. 241–255.
71. F. Wagner et al., *J. Euro. Ceram. Soc.*, 19 (1999), pp. 2449–2453.
72. P. Beyer, R. Janssen, and N. Claussen, *Adv. Eng. Mater.*, 2 (11) (2000), pp. 734–737.
73. P. Kumar and K.H. Sandhage, *J. Mater. Sci.* 34 (23) (1999), pp. 5757–5769.
74. K.A. Rogers et al., *J. Am. Ceram. Soc.*, 82 (3) (1999), pp. 757–760.
75. K.H. Sandhage and P. Kumar, U.S. patent 6,407,022 (18 June 2002).
76. M.B. Dickerson, R.L. Snyder, and K.H. Sandhage, *J. Am. Ceram. Soc.*, 85 (3) (2002), pp. 730–732.
77. K.H. Sandhage et al., U.S. patent 6,598,656 (29 July 2003).
78. K.H. Sandhage and P. Kumar, U.S. patent 6,833,337 (21 December 2004).
79. M.B. Dickerson et al., *J. Mater. Sci.*, 39 (19) (2004), pp. 6005–6015.
80. D.W. Lipky et al., *J. Euro. Ceram. Soc.*, accepted, in press.
81. N. Claussen et al., European patent 1,252,349, German patent 10,047,384 (9 August 2001).
82. P. Kumar et al., *Scripta Mater.*, 44 (2001), pp. 751–757.
83. T. Selchert, R. Janssen, and N. Claussen, *Ceram. Eng. Sci. Proc.*, 24 (4) (2003), pp. 175–180.
84. T. Selchert, R. Janssen, and N. Claussen, *Ceram. Eng. Sci. Proc.*, 25 (1-3) (2004), pp. 459–464.
85. R. Janssen, S. Schepokat, and N. Claussen, *J. Euro. Ceram. Soc.*, 28 (2008), pp. 1369–1379.
86. JCPDS International Center for Diffraction Data File 43-1484 for Al_2O_3 , 21-1276 for TiO_2 , 45-946 for MgO , 35-0784 for ZrO_2 , 25-1047 for WC , 4-0806 for W (JCPDS International Center for Diffraction Data, Newtown Square, PA, 2007).
87. N. Travitsky et al., *Adv. Eng. Mater.*, 5 (4) (2003), pp. 256–259.
88. N. Travitsky et al., *Mater. Sci. Eng.*, A344 (2003), pp. 245–252.
89. N. Claussen, U.S. patent 5,607,630 (4 March 1997).
90. K.H. Sandhage, U.S. patent 5,318,725 (7 June 1994).
91. K.H. Sandhage, U.S. patent 5,447,291 (5 September 1995).
92. N.B. Pilling and R.E. Bedworth, *J. Inst. Met.*, 29 (1923), pp. 529–591.
93. D. Holz et al., *J. Euro. Ceram. Soc.*, 16 (1996), pp. 255–260.
94. N. Claussen, T. Le, and S. Wu, *J. Euro. Ceram. Soc.*, 5 (1989), pp. 29–35.
95. N. Claussen, N.A. Travitsky, and S. Wu, *Ceram. Eng. Sci. Proc.*, 11 (1990), pp. 806–820.
96. S. Wu, D. Holz, and N. Claussen, *J. Am. Ceram. Soc.*, 76 (4) (1993), pp. 970–980.
97. N. Claussen, S. Wu, and D. Holz, *J. Euro. Ceram. Soc.*, 15 (1994), pp. 97–109.
98. D. Holz et al., *J. Am. Ceram. Soc.*, 77 (10) (1994), pp. 2509–2517.
99. S. Wu and N. Claussen, *J. Am. Ceram. Soc.*, 77 (11) (1994), pp. 2898–2904.
100. R. Janssen and N. Claussen, *Ceram. Eng. Sci. Proc.*, 22 (3) (2001), pp. 51–58.
101. M. Reiterer, T. Kraft, and H. Riedel, *J. Euro. Ceram. Soc.*, 24 (2004), pp. 239–246.
102. S.M. Allameh and K.H. Sandhage, *J. Mater. Res.*, 13 (5) (1998), pp. 1271–1285.
103. K.H. Sandhage et al., *Mater. & Manuf. Proc.*, 15 (1) (2000), pp. 1–28.
104. M.M. Antony and K.H. Sandhage, *J. Mater. Res.*, 8 (11) (1993), pp. 2968–2977.
105. H.J. Schmutzler, M.M. Antony, and K.H. Sandhage, *J. Am. Ceram. Soc.*, 77 (3) (1994), pp. 721–729.
106. H.J. Schmutzler and K.H. Sandhage, *Metall. Trans. B*, 26B (1995), pp. 135–148.
107. H.J. Schmutzler, K.H. Sandhage, and J.C. Nava, *J. Am. Ceram. Soc.*, 79 (6) (1996), pp. 1575–1584.
108. G.A. Ward and K.H. Sandhage, *J. Am. Ceram. Soc.*, 80 (6) (1997), pp. 1508–1516.
109. S.M. Allameh and K.H. Sandhage, *J. Am. Ceram. Soc.*, 80 (12) (1997), pp. 3109–3126.
110. P. Kumar and K.H. Sandhage, *J. Mater. Res.*, 13 (12) (1998), pp. 3423–3435.
111. S.M. Allameh and K.H. Sandhage, *J. Mater. Res.*, 14 (11) (1999), pp. 4319–4328.
112. D.H. Viers and K.H. Sandhage, *J. Am. Ceram. Soc.*, 82 (1) (1999), pp. 249–252.
113. R. Citak, K.A. Rogers, and K.H. Sandhage, *J. Am. Ceram. Soc.*, 82 (1) (1999), pp. 237–240.
114. E. Saw et al., *J. Am. Ceram. Soc.*, 83 (4) (2000), pp. 998–1000.
115. E. Saw et al., *Mater. & Manuf. Proc.*, 15 (1) (2000), pp. 29–46.
116. M.J. Watson et al., *J. Am. Ceram. Soc.*, 81 (8) (1998), pp. 2053–2060.
117. E. Suvaci and G.L. Messing, *J. Mater. Sci.*, 34 (13) (1999), pp. 3249–3261.
118. K.H. Sandhage and N. Claussen, *The Encyclopedia of Materials Science and Technology*, Volume 9, ed. K.H.J. Buschow et al. (New York: Elsevier Science Publishers, 2001), pp. 8035–8040.
119. L.J. Masur et al., *JOM*, 46 (12) (1994), pp. 28–30.
120. K.H. Sandhage et al., *J. Am. Ceram. Soc.*, 79 (7) (1996), pp. 1839–1850.
121. S. Gaus et al., *J. Am. Ceram. Soc.*, 82 (4) (1999), pp. 909–915.
122. M.J. Watson et al., *Acta Mater.*, 49 (6) (2001), pp. 1095–1103.
123. M.J. Watson et al., *J. Am. Ceram. Soc.*, 88 (12) (2005), pp. 3380–3387.
124. X.-D. Zhang, K.H. Sandhage, and H.L. Fraser, *J. Am. Ceram. Soc.*, 81 (11) (1998), pp. 2983–2997.
125. X.D. Zhang, K.H. Sandhage, and H.L. Fraser, *J. Mater. Res.*, 13 (11) (1998), pp. 3122–3134.
126. T.J. Detrie and K.H. Sandhage, *J. Mater. Res.*, 15 (2) (2000), pp. 306–316.
127. K.H. Sandhage, *J. Electrochem. Soc.*, 139 (6) (1992), pp. 1661–1671.
128. E. Suvaci and G.L. Messing, *J. Am. Ceram. Soc.*, 84 (3) (2001), pp. 657–659.
129. J. She et al., *J. Euro. Ceram. Soc.*, 22 (2002), pp. 323–328.
130. M.M.R. Boutz et al., *Mater. Sci. Eng. A*, A233 (1997), pp. 155–166.

Kenneth H. Sandhage is the B. Mifflin Hood Professor in the School of Materials Science and Engineering, and Adjunct Professor in the School of Chemistry and Biochemistry, at the Georgia Institute of Technology, 771 Ferst Drive, Atlanta, GA 30332; (404) 894-6882; e-mail: ken.sandhage@mse.gatech.edu.

Processing of Porous Carbon with Tunable Pore Structure by the Carbide-derived Carbon Method

Nadejda Popovska and Martina Kormann

Biomorphic TiC ceramics were covered with highly porous carbon, so-called carbide-derived carbon (CDC), by selective etching of Ti with chlorine in a temperature range between 400°C and 1,200°C. Microporous carbon with narrow pore size distribution was obtained at temperature ranging from 400°C to 800°C. Chlorination at higher temperatures leads to formation of mesopores because of increased degree of order of the obtained CDC. A higher etching rate as well as higher degree of order at lower reaction temperature was observed if a catalytically active metal like Fe or Ru was presented during the chlorination process. This is associated with an increased amount of mesopores and with a decrease in specific surface area. Therefore, the CDC processing in the presence of a catalyst offers another way to produce ordered carbon structures at lower temperatures.

INTRODUCTION

Carbide-derived carbon (CDC) is a new class of microporous materials. It is defined as carbon produced by selective extraction of metal atoms from the carbide crystal lattice by halogens, supercritical water, oxygen at low partial pressure, or other etching agents.¹ CDC is a promising candidate for applications as a supercapacitor, catalyst support, or adsorbent for gases. As described in the literature, the CDC structure depends on the initial carbide precursor as well as on the process parameters like temperature and etching agent.^{1,2} Most investigations on CDC are based on metal carbides in powder form. In previous works^{3,4} we reported about the preparation of porous carbons by CDC approach using TiC and TiC/TiO₂ structures produced

from paper preforms by the chemical vapor infiltration and reaction (CVI-R) technique. Based on these results we extended our study to include CDC from biomorphic SiC ceramic. A comparative study of both carbide precursors was performed regarding reaction kinetics, the influence of hydrogen as well as microstructure of the resulting carbon.² SiC shows lower reactivity than TiC. Temperatures below 650°C are not sufficient to remove Si from SiC. The addition of hydrogen to the reactive gas inhibits the chlorination reaction.

This work summarizes the results of studying the chlorination process of biomorphic TiC ceramic and the microstructure of the resulting carbon. The effect of the presence of a transition metal catalyst in the form of salts or oxides during the chlorination process

was also investigated. A post-treatment of CDC in CO₂ was used to enhance its porosity. CDC from biomorphic ceramics can be produced in different shaped structures with high mechanical stability, offering the advantage of easy separation from a reaction mixture compared to CDC in powder form.

See the sidebar for experimental procedures.

RESULTS AND DISCUSSION

Biomorphic TiC ceramics derived from paper preforms show high shape stability and very good mechanical performances. The cross section of the sample after chlorination (Figure 1) consists of a core of the initial carbon biotemplate (C_b), surrounded by a not converted carbide precursor, followed by a layer of highly porous carbon (CDC).

The surface morphology of TiC ceramics before and after chlorination was investigated by scanning electron microscopy (SEM) and is presented in Figure 2. The original fiber structure of the carbon biotemplate was maintained over all process steps. The EDX analysis shows that after the etching process no titanium could be detected on the fiber surface.

Generally, it is well known that the addition of hydrogen to chlorine leads to reduced reaction rate, but almost no details about the effect of hydrogen/chlorine ratio on the etching process are given in the literature. Our investigations show a linear decrease of etching rate with increasing hydrogen/chlorine ratio independent of the carbide precursor used. A critical hydrogen/chlorine ratio, where no etching takes place, was estimated to be 0.72 for TiC-CDC and 0.66 for SiC-CDC.²

The specific surface area (SSA)

How would you...

...describe the overall significance of this paper?

For the first time, biomorphic ceramic structures are used to produce carbide-derived carbon (CDC) with high specific surface area and controlled pore structure, which is easier to handle compared to CDC in powder form.

...describe this work to a materials science and engineering professional with no experience in your technical specialty?

Porous carbon with tunable microstructure is produced from metal carbides by high-temperature treatment in halogen containing atmosphere.

...describe this work to a layperson?

This work deals with the processing of high porous carbon materials derived from paper preforms.

of the CDC as a function of the reaction temperature at different chlorine concentrations is presented in Figure 3. The curves show similar run with a maximum SSA at 800°C. The decline in SSA at higher temperatures is associated with a starting graphitization. This assumption was confirmed by further investigations with Raman spectroscopy.

The pore structure of the CDC was investigated by low temperature nitrogen sorption. As described in an earlier publication,⁴ the TiC-CDC shows very narrow pore size distribution with pore size less than 1 nm. An increase of etching temperature leads to a broadening of the distribution curve. In the temperature range 400–800°C mainly microporous carbon was obtained, whereas at 1,000–1,200°C also mesopores ($d > 2$ nm) were generated.

Nitrogen sorption isotherms recorded for TiC-CDC obtained after chlorination at different temperatures are shown in Figure 4. The TiC samples chlorinated at 400° and 800°C show a typical type I isotherm according to International Union of Pure and Applied Chemistry (IUPAC) classification, which is characteristic for microporous materials with pores less than 2 nm. The CDC sample obtained at 1,000°C shows a hysteresis which is attended by mesopores. However, the largest hysteresis loop was observed with TiC-CDC at 1,200°C associated with the largest mesopore volume.

Presence of Transition Metal Catalyst during Chlorination⁶

The presence of a catalyst enhances the etching of titanium by chlorine resulting in a 12–30% higher etching rate depending on the type of the catalyst. The temperature dependence of SSA for TiC-CDC obtained without and with catalyst is presented in Figure 5.

All curves have similar run with maximum SSA at 800°C. This tendency of showing maximum SSA at intermediate reaction temperatures was already described in Figure 3. CDC samples produced at low temperature have an amorphous structure and contain pores that are probably too small to be accessible to nitrogen molecules.¹ With increasing reaction temperature better ordered domains such as multi-

EXPERIMENTAL PROCEDURE

Processing of Biomorphic TiC Ceramic by Chemical Vapor Infiltration and Reaction (CVI-R)

Biomorphic TiC ceramic was produced by the CVI-R technique in a two-step process using carbonized paper preform as template. Paper consisting mainly of cellulose fibers was converted first into carbon biotemplate (C_b) by pyrolysis in inert atmosphere at 850°C, followed by chemical vapor infiltration at 1,100°C and atmospheric pressure with $TiCl_4/CH_4/H_2$ as precursor system according to Equation 1.⁵ $TiCl_4$ is vaporized in a bubbler and carried into the reactor by a carrier gas H_2 or He. The gaseous precursors diffuse into the pores of the carbon biotemplate, where reductive decomposition of $TiCl_4$ in excess of hydrogen and chemical reaction to TiC takes place simultaneously.

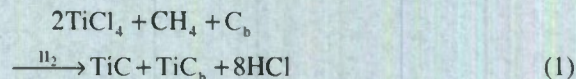


Figure A presents the flow chart of processing of biomorphic TiC ceramic.

Loading of Biomorphic TiC Ceramics with Fe or Ru Catalysts by Dip Coating

A dip coating method was used to prepare biomorphic TiC ceramic structures loaded with iron and ruthenium catalysts.⁶ The samples were dipped into saturated solutions of $Fe(II)Cl_2 \cdot 4H_2O$, $Fe(III)(NO_3)_3 \cdot 9H_2O$ and $Ru(III)Cl_3 \cdot H_2O$ in ethanol and dried. This procedure was repeated until the desired catalyst loading was achieved. The ceramics with $Fe(NO_3)_3 \cdot 9H_2O$ were calcinated at 200°C for 5 hours to form iron (III) oxide Fe_2O_3 . In the following the catalysts are named as Fe(II), Fe(III) and Ru(III).

To prepare Fe/Ru bimetallic catalyst the TiC samples were first dipped into the Fe(III) solution, dried and subsequently dipped into ruthenium solution. The amount of iron or ruthenium was calculated from the mass increase and verified by inductively coupled plasma optical emission spectrometry (ICP/OES). A constant catalyst concentration of 0.5 wt.% Ru(III) and 0.5 wt.% Fe(III) was used for the investigations with bimetallic catalyst. For all other experiments a typical catalyst concentration of 0.5 wt.% iron or ruthenium was used. The catalyst concentration is calculated as catalytically active metal.

Etching of Biomorphic TiC Ceramic with Chlorine

The biomorphic TiC ceramic was covered with porous carbon by selective etching of the metal in chlorine or hydrogen/chlorine atmosphere in a range of temperatures between 400 and 1,200°C as presented schematically in Figure B. The gas mixtures consisted of helium with 0.020 or 0.026 mol/h Cl_2 without or with addition of H_2 .

The carbide samples were placed in a horizontal tubular flow reactor operated at atmospheric pressure and heated up to the reaction temperature under helium. Once the desired temperature was reached, chlorine or hydrogen/chlorine gas mixture was passed through the reactor tube. After chlorination, the furnace was cooled down to room temperature under helium/hydrogen flow to remove the residual chlorine and the reaction by-products from the pores of the samples. A detailed description of the chlorination apparatus and the applied procedure used in this study can be found elsewhere.^{2,4}

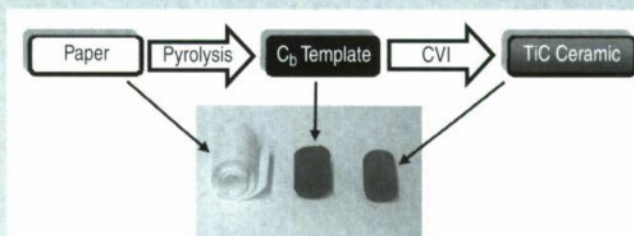


Figure A. Processing schema of biomorphic TiC ceramic derived from paper preforms by CVI-R technique.

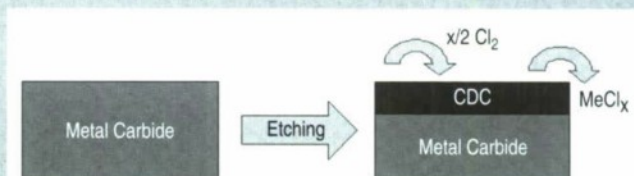


Figure B. Processing of CDC.¹

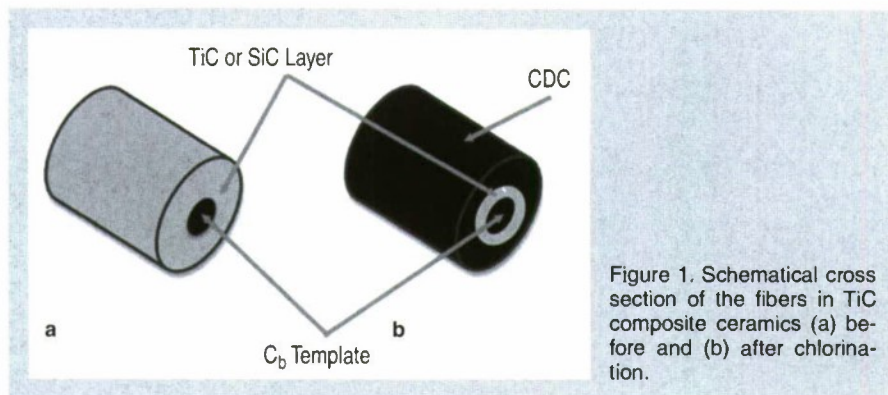


Figure 1. Schematic cross section of the fibers in TiC composite ceramics (a) before and (b) after chlorination.

walled graphitic structures start forming within the CDC structure. The small areas in between these walls are generally not accessible to N_2 and therefore the amount of improved organized multiwalled graphite ribbons could decrease the SSA. Despite the higher etching rate in the presence of a catalyst, the corresponding curves are shifted to lower SSA values which may be caused by a higher degree of order of the resulting CDC. The strongest influence of a catalyst on the SSA was found in the case of Ru(III).

Sorption isotherms (Figure 6) for samples chlorinated in the presence of a catalyst show a similar behavior as described in previous work for TiC-CDC.² Figure 6 shows the isotherms

measured by nitrogen sorption experiments on samples chlorinated at 800 and 1,200°C without and with the addition of a bimetallic catalyst. Isotherms of type I according to the IUPAC classification⁷ were found indicating that CDC obtained at 800°C is microporous. Additionally some mesoporosity is also present because of the weak slope of the isotherm for relative pressure > 0.1 which does not show a real horizontal plateau. This is associated with the filling of mesopores. The sample obtained in the presence of a catalyst exhibits a hysteresis loop of type H4 because of capillary condensation and mesoporosity. Type 4 hysteresis arises due to large mesopores embedded in the ma-

trix of smaller pores.⁸ As described in previous publications^{2,3} the pore size of CDC derived from biomorphic carbide precursors is influenced by the etching temperature. At temperatures up to 1,000°C microporous CDC is formed. But in the case of TiC loaded with bimetallic Ru(III)/Fe(III) catalyst before chlorination a hysteresis can already be seen at reaction temperature of 800°C. The hysteresis loop is more pronounced at increased etching temperature which suggests higher amount of mesopores. The carbides chlorinated at 1,200°C show an isotherm with better pronounced hysteresis but still the isotherm escalates at relative pressures < 0.1 . Therefore, the produced CDC is mainly mesoporous but also some micropores can be found.

CDC obtained at 800°C is mainly microporous with a micropore fraction of about 80%. Increasing reaction temperature and the presence of a catalyst promote the formation of mesopores by reducing micropore volume. The pore size of micropores is below 1 nm as shown in previous publications.^{2,4} Higher temperature favors the formation of mesopores maintaining the average size of the micropores. The

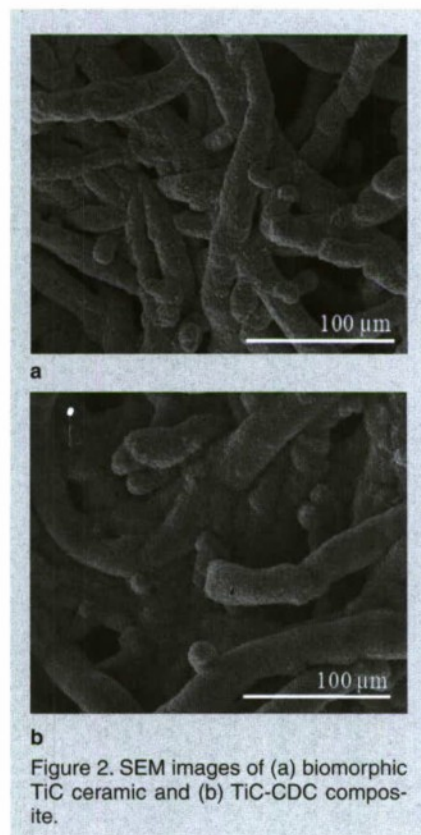


Figure 2. SEM images of (a) biomorphic TiC ceramic and (b) TiC-CDC composite.

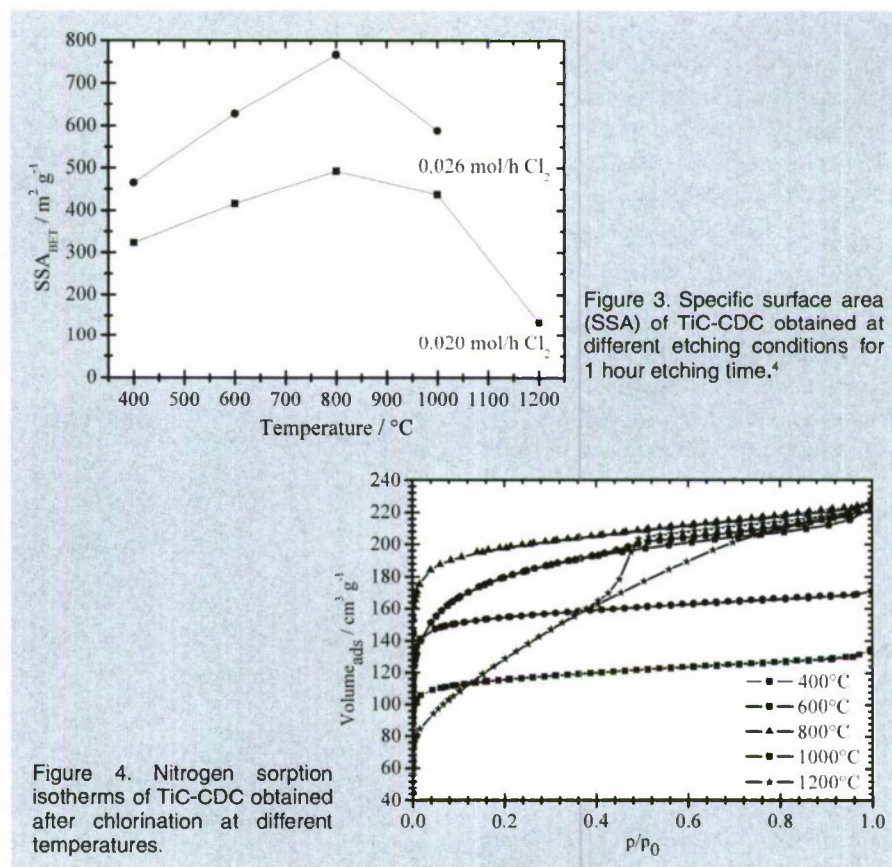


Figure 4. Nitrogen sorption isotherms of TiC-CDC obtained after chlorination at different temperatures.

produced mesopores are in the range of 3–5 nm. The amount of micropores diminishes at higher reaction temperatures.

Raman spectroscopy is a suitable method to determine the degree of order of carbon materials. The two characteristic peaks in Raman spectra around 1,330–1,342 cm^{-1} (D-band) and 1,585–1,600 cm^{-1} (G-band) in Figure 7 confirm the conversion of TiC to carbon after chlorination.

To estimate the degree of order and graphite crystallinity of carbon materials the area ratio between D- and G-band (A_D/A_G) was determined. A much higher intensity of the D-band compared to the G-band is evident in the whole range of chlorination temperature indicating a disordered structure of CDC independent of the presence of a catalyst. However, an increase in reaction temperature leads to a decrease of the area ratio of both bands suggesting an increased degree of order (Figure 8). This conclusion is more strongly pronounced for chlorination in the presence of Ru(III) catalyst. Further evidence for the development of higher degree of order of the carbon structures is indicated by the appearance and the shape of the second order Raman peaks at 2,700 cm^{-1} (2D) and 2,940 cm^{-1} (D''). The G' -band which suggests an enhanced carbon ordering is pronounced for TiC-CDC obtained only at elevated temperature such as 1,200°C. Catalyst added to the precursor carbide seems to enhance the graphitization expressed by clearly visible G' -band even at temperatures as low as 1,000°C.

Similar to the results of SSA analysis it can clearly be seen that the presence of catalyst lowers the area ratio of D- and G-band suggesting an ordering of carbon structure mainly in the temperature range 600–1,000°C since changes in the peak ratio are usually related to amorphization or graphitization.¹⁰ At 1,200°C without and with catalyst the same area ratio were obtained indicating that at temperature as high as 1,200°C no catalyst is necessary to enhance the microstructural order of resulting CDC. For TiC-CDC a sequence to higher ordered microstructure can be estimated as follows:

no catalyst < Fe < Ru < Ru/Fe

The dependence of the degree of or-

der of CDC on the etching temperature and the presence of a catalyst during the chlorination was additionally ex-

amined by HRTEM. Higher ordered carbon structures such as onion-like or graphite ribbons have been observed at

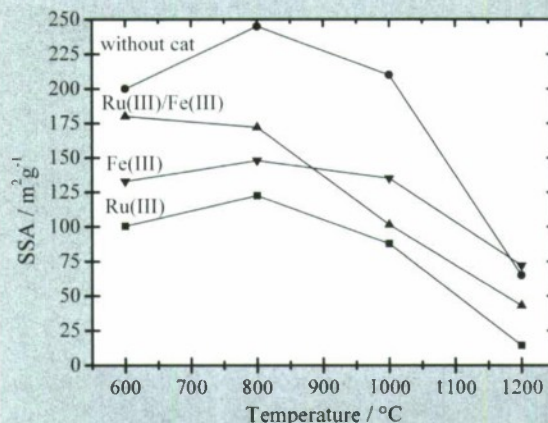


Figure 5. SSA of TiC-CDC obtained at different temperatures without and with catalyst (0.5 wt.%).⁶

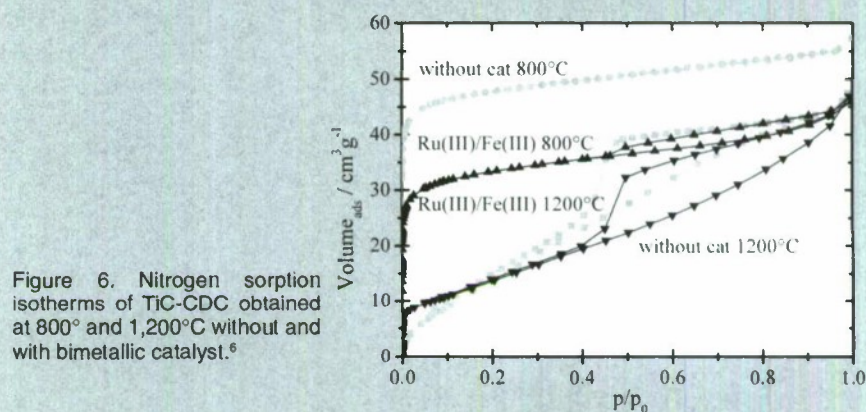


Figure 6. Nitrogen sorption isotherms of TiC-CDC obtained at 800°C and 1,200°C without and with bimetallic catalyst.⁶

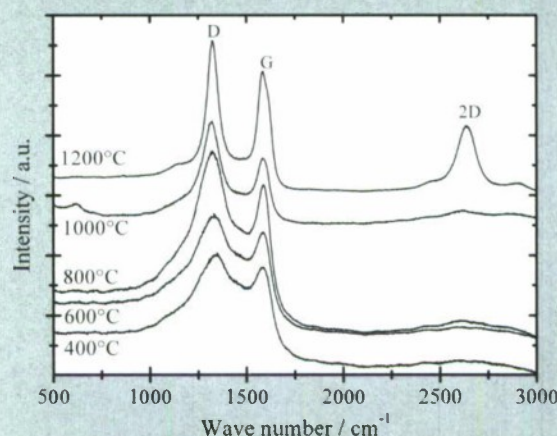


Figure 7. Raman spectra of TiC-CDC obtained at different chlorination temperatures without catalyst.

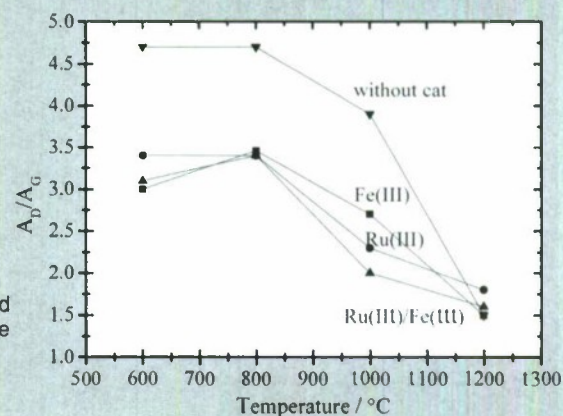


Figure 8. Area ratio of D- and G-bands as a function of the chlorination temperature.⁶

higher chlorination temperatures (Figure 9). Reaction temperature of 800°C (Figure 10a) results in predominantly amorphous carbon structure, whereas at 1,200°C (Figure 10b) large areas of carbon with improved degree of order can be found in TiC/Ru(III). The dark octagon in the micrographs (Figure 10a and b) is assigned to the catalyst RuCl_3 which was confirmed by analytical electron microscopy using EDS in the TEM. Obviously in the surrounding area close to the catalyst nanoparticles a higher degree of order of carbon occurs.

The mechanism for the formation of carbon with enhanced degree of order

in the vicinity of the catalyst nanoparticles was not object of this work. It is well known that transition metals such as Fe, Ni or Co, can interact with carbonaceous materials.¹¹ Carbon species may diffuse and dissolve into the metal particle. This leads to supersaturation resulting in precipitation of carbon from the solid solution as graphitic carbon surrounding the catalyst nanoparticle. Analogies from literature to the carbon formation by the CDC process in the presence of a catalyst could be expected.

CDC with Enhanced Porosity by Activation with Carbon Dioxide

The post-treatment of the produced CDC samples was done by high temperature activation in carbon dioxide. The partial oxidation is a method to enhance the porosity of carbon materials.¹² TiC-CDC was activated for different treatment times at 850°C in CO_2 atmosphere. More information about the activation process is given in Reference 13. The nitrogen sorption analysis shows that the activation process clearly enhances the adsorption capacity of CDC. The SSA for TiC-CDC without post-treatment is around $1,000 \text{ m}^2 \text{ g}^{-1}$. It can be doubled within 9 h activation time. Shorter activation times maintain the microporous character of CDC whereas longer reaction times lead to a widening of micropores and formation of mesopores. The values of the SSA and the pore volume for the activated CDC samples are given in Table I.

Therefore activation of CDC in CO_2 is an effective and easy way to enhance the SSA as well as the micropore volume of CDC materials if the treatment time is adjusted.

CONCLUSIONS

Biomorphic TiC ceramics derived from paper preforms by chemical vapor infiltration were covered with high porous carbon by selective etching in chlorine or hydrogen/chlorine mixture in a temperature range of 400–1,200°C. Addition of hydrogen to the reactive gas inhibits the chlorination reaction. A linear decrease of etching rate with increasing hydrogen/chlorine ratio was observed. A critical ratio, where no appreciable etching takes place was esti-

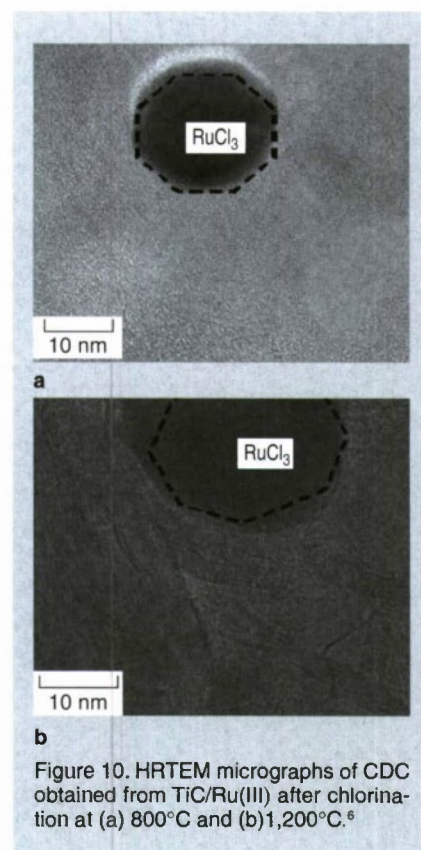


Figure 10. HRTEM micrographs of CDC obtained from TiC/Ru(III) after chlorination at (a) 800°C and (b) 1,200°C.⁶

mated to be 0.72.

The specific surface area of CDC is strongly dependent on the reaction temperature reaching a maximum value at 800°C. After that SSA decreased because of starting graphitization as shown by Raman spectroscopy. Carbons produced from biomorphic TiC showed narrow pore size distribution with pore sizes below 1 nm which broadens with increasing etching temperature. At 1,200°C noticeable mesopores are generated in mainly microporous material.

The presence of catalytically active transition metals such as Ru(III), Fe(III) and their mixture Ru(III)/Fe(III) during the chlorination enhances the etching rate but no significant effect of the catalyst type could be found. Additionally, the presence of a catalyst improved the degree of order of the resulting CDC at reaction temperatures as high as 600°C. At chlorination temperature of 1,200°C its degree of order was not influenced by the presence of a catalyst. The effect of the catalyst type on increasing the degree of order of the resulting CDC was found to be as follows:

no catalyst < Fe < Ru < Ru/Fe
Addition of the transition metal

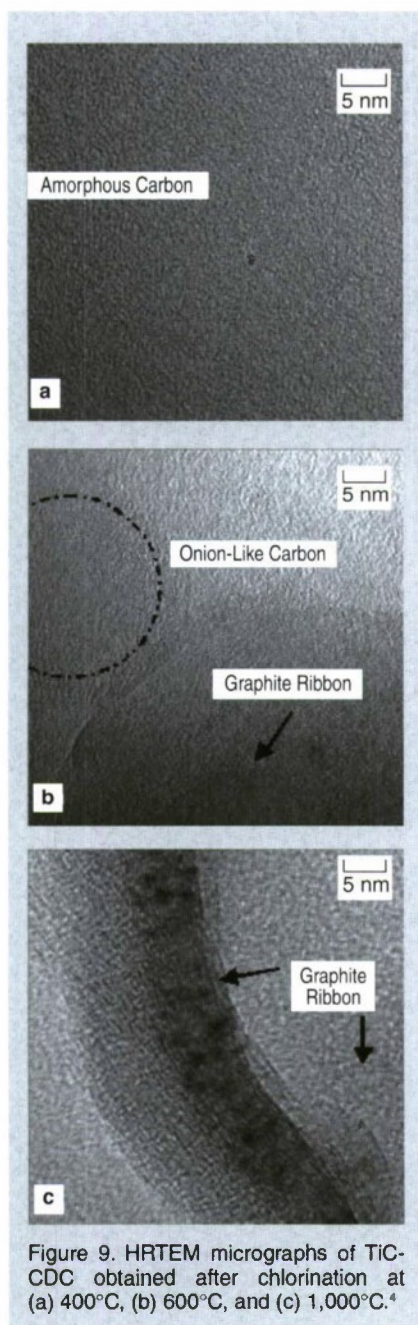


Figure 9. HRTEM micrographs of TiC-CDC obtained after chlorination at (a) 400°C, (b) 600°C, and (c) 1,000°C.⁴

Table I. Pore Analysis of CDC Activated with CO₂¹³

t _{BET} (h)	Burn-off (%)	SSA _{BET} (m ² g ⁻¹)	V _{tot} (cm ³ g ⁻¹)	V _{tot,DFT} (cm ³ g ⁻¹)	V _{mic,DFT} (cm ³ g ⁻¹)	V _{mic} /V _{tot,DFT} (%)
—	—	977.0	0.41	0.38	0.37	96.9
6	36.0	1810.5	0.80	0.75	0.68	90.7
9	49.9	2240.3	1.11	1.05	0.77	73.8

catalyst to the carbide precursor led to CDC with higher degree of order at lower temperatures which is associated with an increased mesopore volume and decrease in the SSA.

Specific surface area up to 2,300 m²g⁻¹ and pore volume of about 1.3 cm³g⁻¹ have been achieved by high temperature activation of CDC with carbon dioxide. The microporous character of the CDC samples can be maintained by using moderate activation times.

It can be concluded that the biomorphic carbides could be converted into high porous carbon with tunable pore structure and degree of order varying the reaction temperature and adding a catalytic active metal during the chlorination process. These materials possess shape stability and very good me-

chanical performances. Possible applications are adsorbents, gas storage or catalyst support because of their easy separation from the reaction mixture.

References

1. G. Yushin, A. Nikitin, and Y. Gogotsi, "Carbide-derived Carbon," *Nanomaterials Handbook*, ed. Y. Gogotsi (Boca Raton, FL: CRC Press, 2006), pp. 239–282.
2. M. Kormann, H. Gerhard, and N. Popovska, "Comparative Study of Carbide-derived Carbons Obtained from Biomorphic TiC and SiC Structures," *Carbon*, 47 (2009), pp. 242–250.
3. H. Ghanem et al., "Processing of Biomorphic Porous TiO₂ Ceramics by Chemical Vapor Infiltration and Reaction (CVI-R) Technique," *Journal of the European Ceramic Society*, 27 (2007), pp. 3433–3438.
4. M. Kormann et al., "Processing of Carbide-derived Carbon (CDC) using Biomorphic Porous Titanium Carbide Ceramics," *Journal of the European Ceramic Society*, 28 (2008), pp. 1297–1303.
5. N. Popovska et al., "Paper Derived Biomorphic Porous Titanium Carbide and Titanium Oxide Ceramics Produced by Chemical Vapor Infiltration

and Reaction (CVI-R)," *Journal of the European Ceramic Society*, 25 (2005), pp. 829–836.

6. M. Kormann et al., "Effect of Transition Metal Catalysts on the Microstructure of Carbide-derived Carbon," *Carbon*, 47 (2009), pp. 2344–2351.

7. K.S.W. Sing et al., "Reporting Physisorption Data for Gas/Solid Systems," *Pure Applied Chemistry*, 57 (1985), pp. 603–619.

8. M. Kruk and M. Jaroniec, "Gas Adsorption Characterization of Ordered Organic-inorganic Nanocomposite Material," *Chemistry of Materials*, 13 (2001), pp. 3169–3183.

9. C. Beny-Bassez and J.N. Rouzaud, "Characterization of Carbonaceous Materials by Correlated Electron and Optical Microscopy and Raman Microspectroscopy," *Scanning Electron Microscopy*, 1 (1985), pp. 119–132.

10. A.C. Ferrari and J. Robertson, "Interpretation of Raman Spectra of Disordered and Amorphous Carbon," *Physical Review B*, 61 (2000), pp. 14095–14107.

11. W. Lian et al., "The Transformation of Acetylene Black into Onion-like Hollow Carbon Nanoparticles at 1,000°C using an Iron Catalyst," *Carbon*, 46 (2008), pp. 525–530.

12. R.C. Bansal, J.B. Donnet, and H.F. Stoeckli, *Active Carbon* (New York: Marcel Dekker, 1988).

13. M. Kormann and N. Popovska, "Processing of Carbide-derived Carbons with Enhanced Porosity by Activation with Carbon Dioxide," *Microporous and Mesoporous Materials*, 130 (2010) pp. 167–173.

Nadejda Popovska, head of the research group, and Martina Kormann, research associate, are with the Department of Chemical Reaction Engineering, University Erlangen-Nuremberg, Germany. Prof. Popovska can be reached at n.popovska@rzmail.uni-erlangen.de.

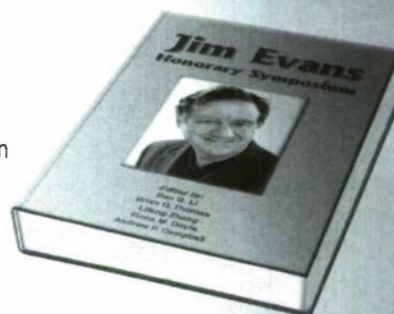
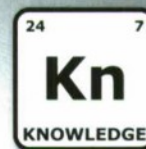
Jim Evans Honorary Symposium

B. Li, B. Thomas, L. Zhang, F. Doyle, A. Campbell, editors

This symposium represents Jim Evans, Professor of Metallurgy Emeritus and the P. Malozemoff Professor Emeritus in the Department of Materials Science and Engineering, University of California, Berkeley, which he joined in 1972. His research deals with rate phenomena governing the productivity of processes for producing metals and other materials. This has involved investigations of wide ranging technologies such as aluminum reduction cells, electromagnetic casters, chemical vapor deposition, fluidized bed electrodes and batteries.

Topics covered included:

- Materials production
- Fluid flow in materials production
- Mass transport in materials production
- Modeling of materials production
- Electrochemical phenomena in materials production
- Electromagnetic phenomena in materials production
- Sensors and measurement of physical parameters in high temperature and hostile environments
- Control of environmental impact of materials production
- Novel cells for aqueous electrolysis
- Novel cells for molten salt electrolysis
- Mathematical modeling in light metals production
- Novel batteries
- Novel leaching reactors



TMS Member price: 109.00 • Non-member price: 154.00 • TMS Student Member price: 84.00

Structure/Processing Relationships in the Fabrication of Nanoporous Gold

F. Kertis, J. Snyder, Lata Govada, Sahir Khurshid, N. Chayen, and J. Erlebacher

Nanoporous gold made by dealloying silver/gold alloys is a relatively new material finding application in catalysis, sensing, and other areas. Here we discuss the metallurgical processing required to make patterned foils of nanoporous gold with large, flat grains, with which we are exploring an application as substrates for the heterogeneous nucleation of protein crystals.

INTRODUCTION

Figure 1 shows a scanning electron microscope (SEM) micrograph of a remarkable and beautiful material—nanoporous gold (NPG). Nanoporous gold can be a mesoporous or macroporous material, depending on whether we find its pore size in the 2–50 nm range (meso) or greater than 50 nm range (macro), following International Union of Pure and Applied Chemistry nomenclature.^{1,2} It is being explored for a wide variety of applications that leverage its chemical inertness, ease of fabrication, high surface area, electrical conductivity, and flexible form factor. Such applications naturally include catalysis^{3–5} and sensing,⁶ but more unusual applications have been imagined. Perhaps NPG can be used as a support for enzymatic solar cells,⁷ or as a substrate for the heterogeneous nucleation of macromolecule crystals (proteins) under milder supersaturation conditions than usually required.⁸ The metallurgical development of NPG for the last of these applications motivates this article, and is discussed in more detail later.

The increase in research activity in NPG or dealloying (the electrochemical method used to make NPG), from ten papers in 2000 to 163 in 2009,⁹ has been driven by two factors. First, NPG is an example of a bulk nanostructured

material. That is, the pores in NPG can be as small as 5 nm, but samples of NPG are themselves macroscopic. Having nanoscale features, NPG exhibits unusual optical and mechanical properties not associated with non-porous, bulk gold. For instance, it is brittle and very strong. It is not even gold colored, but instead can range in color from a deep reddish copper to nearly black (black gold!). The visceral nature of the material in the context of the explosion of interest in nanotechnology in the last decade should not be underestimated.

Second, the cultural history of NPG is fascinating. In the 20th century, deal-

loying and NPG were studied in the context of corrosion, as it is considered perhaps a model system for stress-corrosion cracking; that is, the focus was on how dealloying leads to materials degradation. A re-branding of dealloying as a useful materials processing tool has occurred over the last decade, but this is historically circular. Pre-Columbian artisans used dealloying to create so-called Tumbaga artworks, which used dealloying (aka “depletion gilding” to the art community) to create a golden skin over a base-metal enriched cast interior (see Figure 2),¹⁰ and observations of the stability of gold alloys in various environments have been made periodically throughout the ages, such as Cennino Cennini’s admonition in the very first “how-to” book of art, dating from the early 15th century, that one should never use gold/silver alloy leaf outside, because it will turn black.¹¹

The technique of dealloying to make nanoporous gold refers to the selective chemical or electrochemical dissolution of one alloy component from a multi-component metal.¹² Consider, for instance, the silver/gold alloy system. These components are completely miscible across the entire composition spectrum, a nearly ideal solution. However, if you immerse an Ag₇₀Au₃₀ ingot into concentrated nitric acid, the silver will dissolve out, leaving behind NPG with a pore size of ~15 nm. This porous structure is much finer than the grain size of the original ingot, and the temptation would be to interpret the porosity as an excavated structure. This is not the case. Any number of diffraction tools would show a buried porous gold structure within the polycrystalline ingot, but none do. Rather, porosity forms dynamically during the dissolution of silver. As the silver atoms are

How would you...

...describe the overall significance of this paper?

Nanoporous gold has been receiving attention as a new bulk nanostructured material. Here we remedy the lack of processing information in the literature with a detailed review, and a discussion of the challenges found when tailoring the material to be a substrate for crystal growth from solution.

...describe this work to a materials science and engineering professional with no experience in your technical specialty?

We find that important bulk metallurgical principles must be applied to the fabrication, coarsening, and application of nanoporous gold, even though the feature size of the pores in this material is small compared to any grain size.

...describe this work to a layperson?

This paper describes how to make visible amounts of a nanostructured material, specifically, a porous metal whose feature sizes have nearly atomic dimensions.

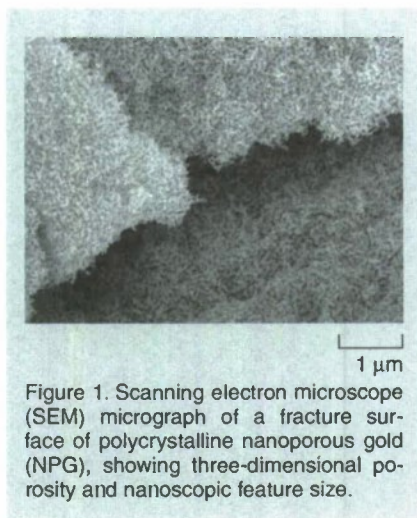


Figure 1. Scanning electron microscope (SEM) micrograph of a fracture surface of polycrystalline nanoporous gold (NPG), showing three-dimensional porosity and nanoscopic feature size.

being dissolved into the solution, the gold atoms that remain diffuse along the metal/electrolyte interface and reform into the porous structure.^{2,13} What is particularly intriguing here is that the original lattice orientation of each grain is maintained. That is, the gold atoms are surface diffusing on the lattice of the underlying crystal and maintain the lattice. So, if one has a grain of Ag/Au 1 cm wide, it can be dealloyed to form a grain of NPG 1 cm wide. On the scale of porosity, grain boundaries are essentially absent.

The kinetics of dissolution and surface diffusion that are the elements of the choreography leading to porosity evolution have been discussed in a number of locations, and a working model has been developed that captures the essential aspects of the physics and chemistry of dealloying.¹ With the idea of a two-component random solid solution as the base alloy (e.g., silver/gold), the kinetics of dealloying are controlled mostly by the electrochemical potential placed on the alloy. Commonly, this potential is positive enough (on the hydrogen scale) that one component is oxidized to a soluble species, but the other is not.

Independent of materials, the characteristics of dealloying include an alloy parting limit,¹² a composition-dependent critical potential,¹⁴ and a change in surface composition and morphology from planar to porous with increasing dissolution potential.¹² The parting limit refers to the sharp threshold in composition (% remaining component) above which dealloying cannot occur regardless of the applied potential. We

now understand the parting limit to be related to the geometry of percolation within the lattice, the central idea being that continuous chains of silver atoms of a certain width must exist if dissolution is to proceed into the bulk.^{15,16} The critical potential E_c is that electrochemical potential required to actually dissolve silver from the lattice. Usually E_c is greater than the potential required to dissolve a pure material; for silver in silver/gold, the critical potential may rise hundreds of millivolts above the equilibrium potential of Ag/Ag⁺. We now understand the critical potential to be thermodynamic in origin, and is found by a free energy balance between the energy gained by dissolving silver into the solution, and the energy penalty associated with creating a new alloy/electrolyte interface.¹⁷

It is not surprising that the critical potential is often associated with the kinetic balance of silver dissolution rate and gold surface diffusivity, the latter being driven by capillary forces and tending to both smooth out and passivate the surface. Clearly, if gold diffusion is very fast compared to dissolution, then the surface will not corrode very deeply, behavior consistent



Figure 2. Columbian "tumbaga" sculpture ("Bell with Feline Deity") dated between 900–1500 A.D. Tumbaga refers to the gold/copper alloy used to make the artifact, which was then "depletion gilded" (i.e., surface dealloyed) to produce an object that looked like pure gold. Image permission of the Walters Art Gallery, Baltimore, Maryland.

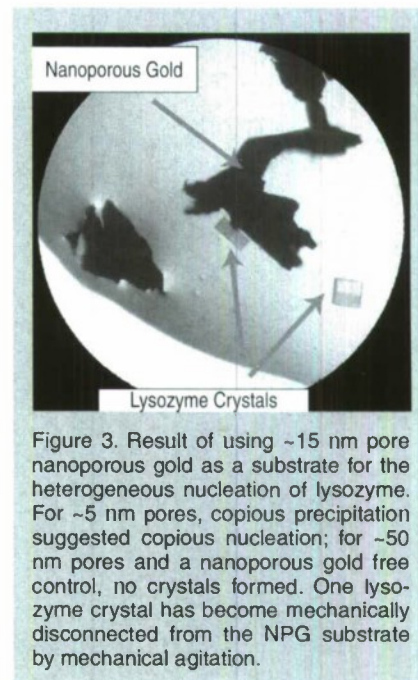


Figure 3. Result of using ~15 nm pore nanoporous gold as a substrate for the heterogeneous nucleation of lysozyme. For ~5 nm pores, copious precipitation suggested copious nucleation; for ~50 nm pores and a nanoporous gold free control, no crystals formed. One lysozyme crystal has become mechanically disconnected from the NPG substrate by mechanical agitation.

with dissolution at potentials below E_c . However, in practice, one must dealloy at a rate sufficiently high in order to grow nicely uniform, porous microstructures. This is an aspect of the distinction between an "intrinsic critical potential," that potential above which corrosion will occur, perhaps slowly and perhaps without porosity evolution, and the "empirical critical potential," which we would prefer be formally associated with porosity evolution.^{17,18}

In this paper, we discuss some practical aspects of NPG fabrication. Our technology driver has been the formation of patterned, uniform and flat, highly porous surfaces with variable pore size with application as substrates for the nucleation and growth of macromolecules (proteins). The motivation for this project was an interesting observation that on porous substrates, with pore size of order the protein diameter, crystal nucleation occurred at milder supersaturations than typically required, leading to higher quality crystals (see Figure 3).⁸ The increased nucleation rate with a porous substrate could be likened to homogeneous vs. heterogeneous nucleation during solidification, but with important differences. Primarily, the free energy of crystallization of a macromolecule is dominated by the change in entropy of the molecule as it changes from the fluid, random three-dimensional (3-D) phase, to a rigid, crystalline phase.¹⁹

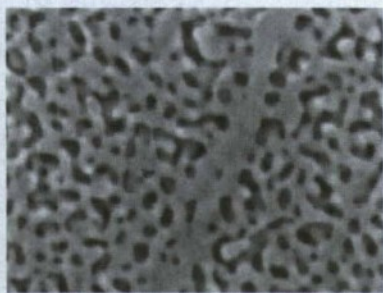


Figure 4. During recrystallization of NPG leaf, gold has segregated to grain boundaries to a high-enough concentration that they do not dealloy. This effect helps "zip" the grain boundary, as shown in the micrograph, and leads to good mechanical integrity.

and not by any enthalpic interaction with a substrate (indeed, a too-high interaction energy between proteins and surfaces tends to simply denature them). Our hypothesis has been that a random, porous substrate, allows the macromolecule to sample a quasi-random 3-D distribution of orientations near the surface, alleviating the entropic hit associated with nucleation.

The use of nanoporous gold for this application is natural, as the pore size is easily varied by annealing, and the surface chemistry of gold is easily modified by the use of adsorbing organic monolayers.²⁰ However, there are some important materials design constraints that needed to be overcome. The experiment called for small droplets of protein solution to be deposited on round patches of porous gold patterned on a foil of undealloyed material in the so-called "sitting drop" configuration. Macroscopic flatness (larger than the size of any protein or pore size) is not important here, but, as discussed below, we encountered unexpected metallurgical relationships between the grain size, rolling history and pore quality, and obstacles in patterning the substrates. Our experiences here may inform the utilization of NPG in other applications.

METALLURGICAL PROCESSING OF NPG

Initial Ingot Formation

Alloy compositions from 20–40 at.% Au are suitable for dealloying to make NPG. More gold, and the parting

limit is passed; less gold and the material falls apart into a suspension of gold nanoparticles. Silver and gold form a homogenous solid solution across their entire composition range with a shallow two-phase region between the liquidus and solidus.²¹ Silver and gold are both easily melted even in air, but one must be careful with silver-rich alloys as their melts possess high oxygen solubility and they tend to "volcano" when solidified. In the work presented here, alloys were melted in an induction furnace in a horizontal Bridgman-like configuration. The crucibles used were made of high purity graphite or a machinable alumina ceramic, with an ingot dimension of 0.25" × 0.25" × 1.5". The packed crucible was placed in a quartz tube purged with flowing argon. The hot zone of the furnace coils was ~0.25" to 0.5" wide, depending on the RF power set on the induction furnace. The quartz tube was placed on two rollers. This configuration allowed translation of the crucible through the hot zone, a kind of crude hand-operated directional solidification.

Melting brings a race amount of

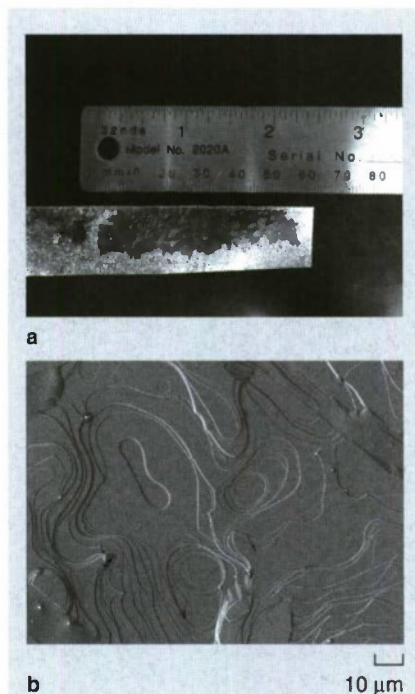


Figure 5. (a) An example of a large grain (~5 cm wide) embedded in a silver/gold foil formed by the rolling annealing cycles described in the text. (b) SEM micrograph of the surface of the large grains showing wide flat terraces. Pinned step edges can be further minimized using the cleaning protocols described in the text.

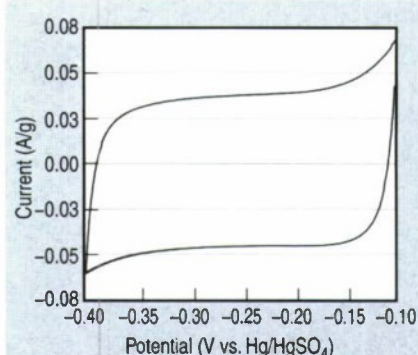


Figure 6. Electrochemical double layer capacitance measurement of clean, oxide-free NPG. Scan rate 5 mV/s, 0.1 M H_2SO_4 .

buried oxide or carbide to the surface, which could be pulled off to the side and ground off after solidification. These impurities impeded grain growth (see below), and were important to remove completely. They exist even with high purity (greater than 99.99% pure) starting materials. Often, a dozen or more solidification/cleaning cycles were required to get a clean melt. Homogenization of the solidified ingots was performed at temperatures between 850 and 900°C for periods greater than 24 h.

After solidification, ceramic dust from the furnace impeded the formation of clear step trains and flat terraces on the surface of the crystals. A cleaning protocol of 5 minutes in an oxygen plasma cleaner followed by immersion in saturated NaOH solution at 200°C removed carbide or carbon impurities, and the NaOH solution alone dissolved surface oxide impurities.

Fabrication of Large Grain Silver/Gold Alloy Foil

Under the right processing conditions, NPG, or more generally nanoporous metals made by dealloying, retain the same polycrystalline microstructure as their parent alloy. The surface diffusion mass transport leading to porosity evolution in principle occurs only on the lattice of the grains, so if one started with a grain size of 10 μm, then one would be left with NPG with 10 μm grains, even though the pore size may be only 10 nm. This characteristic has led to NPG being processed in many different forms. A survey of these forms include bulk samples of order a few millimeters wide,²² nanowires,²³

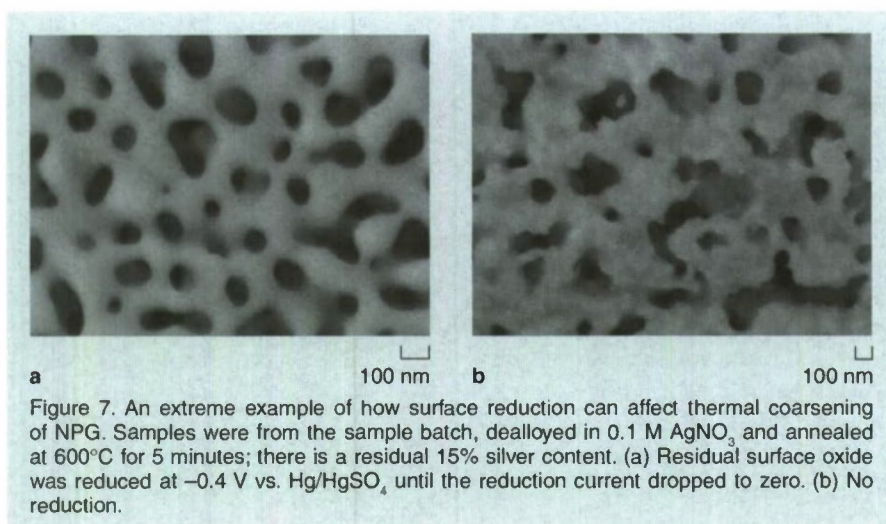


Figure 7. An extreme example of how surface reduction can affect thermal coarsening of NPG. Samples were from the sample batch, dealloyed in 0.1 M AgNO_3 and annealed at 600°C for 5 minutes; there is a residual 15% silver content. (a) Residual surface oxide was reduced at -0.4 V vs. Hg/HgSO_4 until the reduction current dropped to zero. (b) No reduction.

vapor-deposited and micromachined thin films,^{24,25} rolled foils,²⁶ and even free-standing hammered ultra-thin foils commonly called “leaf.”²⁷

It was in the context of studying gold leaf that some metallurgical relationships between the grain structure and NPG quality became clear. Previously, it has been noticed in the context of studies of stress-corrosion cracking that in an ingot of silver/gold that was solidified and then homogenized, silver tended to segregate to the grain boundaries.²⁸ Upon dealloying, this led

to some grain boundary cracking, an effect that needed to be deconvoluted from the mechanical properties of NPG itself. In extreme cases, such segregation and cracking has been used to facilitate the formation of films of NPG “prisms.”²⁹ (As an aside, the mechanical properties of NPG is an interesting sub-field, focused on the mechanics of nanoscale truss systems whose characteristic lengths are smaller than any dislocation cell size.³⁰ Nanoporous gold with pore sizes less than ~ 50 nm are inherently brittle,³¹ even though gold is

ductile, for reasons that are unclear but whose elucidation may have important ramifications for understanding stress corrosion cracking of engineering alloys).

When NPG leaf (original alloy composition $\text{Ag}_{65}\text{Au}_{35}$) was examined, it was noticed that although the hammered foil was only 100–150 nm thick, that lateral grain size often exceeded $10\text{ }\mu\text{m}$.²⁷ As there is no annealing step in the fabrication of leaf, this observation strongly suggested room-temperature recrystallization had occurred. But equally interesting, Scanning electron microscopy (SEM) observation of the grain boundaries in the dealloyed microstructure showed they were gold-rich (Figure 4). The observation suggested that recrystallization leads to segregation and enrichment of gold at grain boundaries, which tends to “zip up” the microstructure upon dealloying.^{26,27}

In our application as substrates for crystal growth, minimization of grain boundary cracking is obviously important. Ideally, as well, the grain size would be larger than the droplet of solution from which the proteins precipitate (3 nm). While the observations

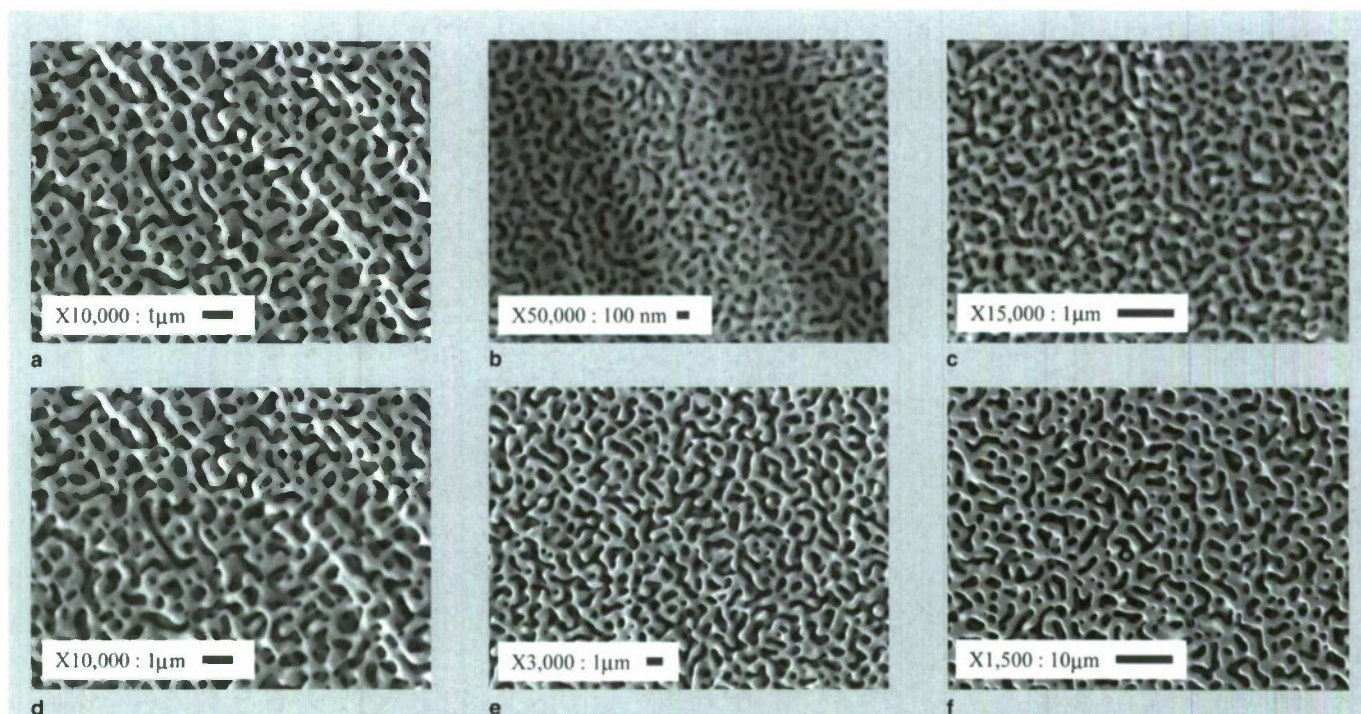


Figure 8. Scanning electron microscopy micrographs of samples of NPG annealed at various times and temperatures. Note the striking self-similar aspect to the coarsening, the topographic features of the precursor alloy surface (e.g., the ridges in the 300°C sample), and how the crystallographic orientation of the grains are manifested in the porous structure (e.g., local two-fold symmetry in the (001) 600°C sample, and local three-fold symmetry in the 900°C sample). (a) As-dealloyed in concentrated nitric acid; (b) 300°C , 15 min.; (c) 400°C , 15 min.; (d) 600°C , 5 min. (note scale change); (e) 800°C , 10 min.; (f) 900°C , 30 min.

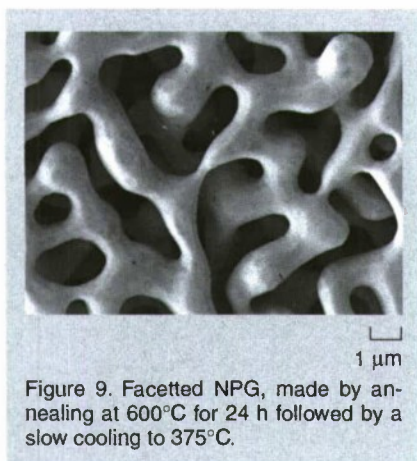


Figure 9. Faceted NPG, made by annealing at 600°C for 24 h followed by a slow cooling to 375°C.

of gold segregation to grain boundaries in leaf was suggestive, 10 μm was too small. Vapor-deposited films were unsuitable for this application because the grain size tended to be small compared to the length scale of porosity, and thin film deposition stresses tend to lead to cracking and delamination upon dealloying.²⁴ It was decided that a useful substrate form factor would be rolled foils, and a rolling and annealing protocol was developed to generate the required large grains; the grain size sometimes exceeded 2 cm laterally. The method is a variation on the technique sometimes referred to as critical strain annealing.

Critical strain annealing (CSA) is premised on the notion there is a critical strain which must be surpassed before which a sample will recrystallize upon annealing.³² Furthermore, the more one strains above the critical strain, the more grains will appear upon recrystallization. Usually, this is explained by a nucleation argument—the more plastic strain induced in the sample, the more nucleation of stress-free grains upon recrystallization. Central to the argument is the unstated notion that the stress drives not only nucleation, but also grain growth. For silver/gold alloys, we find the CSA to be $\sim 1\%$; however, even with highly pure samples, there is still copious nucleation, and the typical lateral grain size of as-rolled and recrystallized samples is less than 100 μm .

In foils rolled to a thickness less than 100 μm , many of the recrystallized grains are columnar, and some of them even have the low-energy (111) surface orientations (which is neither the rolling nor the recrystallization

texture). We have found that if foils less than 100 μm are rolled to strains less than the CSA, and then annealed again, grain growth occurs without recrystallization. Serendipitously, the (111) oriented grains grow fastest. Furthermore, this process can be repeated to get large grains; order cm lateral dimension grains are shown in Figure 5. Microscopically, these grains have extremely flat surfaces, with wide terraces often exceeding 100 μm ,³³ and the slight gold segregation to grain boundaries that keeps the samples “zipped” during dealloying. Interestingly, this grain growth requires rolling, and we have not been able to induce grain growth by tension. The working hypothesis here is that the columnar grain boundaries need to be put in shear in order to de-pin them, as suggested by Cahn.³⁴

The details of the processing used to grow large, flat grains in rolled thin foils are as follows. A clean, homogenized ingot of silver/gold is rolled to a thickness less than 100 μm . The foil is cut into sheets and stacked between machinable alumina plates, and annealed for 24 hours at 900°C. Stacking of the foils between ceramic plates is important to keep a high vapor pressure atmosphere of silver around the sample; otherwise the surface tends to lose silver due to evaporation and drops in composition below the parting limit. The first anneal leads to recrystallization. After the first anneal, the foils are lightly rolled either between

smooth tungsten foil or between sheets of smooth acrylic, but only so that there is a slight smoothening of the surface. Then, samples are re-annealed at 900°C, again stacked between ceramic plates. This light rolling/annealing cycle is repeated (usually 5–6 times) until the desired grain size is achieved.

Dealloying Silver/Gold to Make NPG

In dealloying (i.e., the actual formation of porosity), two concerns are paramount: pore/ligament size (morphology) and residual silver fraction (composition). During the initial dissolution process, the pore size can be controlled a bit by the initial alloy composition. Alloys with lower gold fraction tend to have larger pores, and alloys with gold fractions nearer to the parting limit composition tend to have smaller pores, although there have been no systematic studies.

The most common method to dealloy silver from silver/gold alloys is by immersion in concentrated nitric acid, in which silver is highly soluble. This condition is called “free corrosion.” While surface diffusion of gold is required to form the porous structure, the nature of the surface species that participates in surface diffusion is highly dependent on the anion in the electrolyte, because each kind of anion forms a complex with diffusing gold atoms that has a different binding energy. This is an important point, and leads to the observation that the chemical

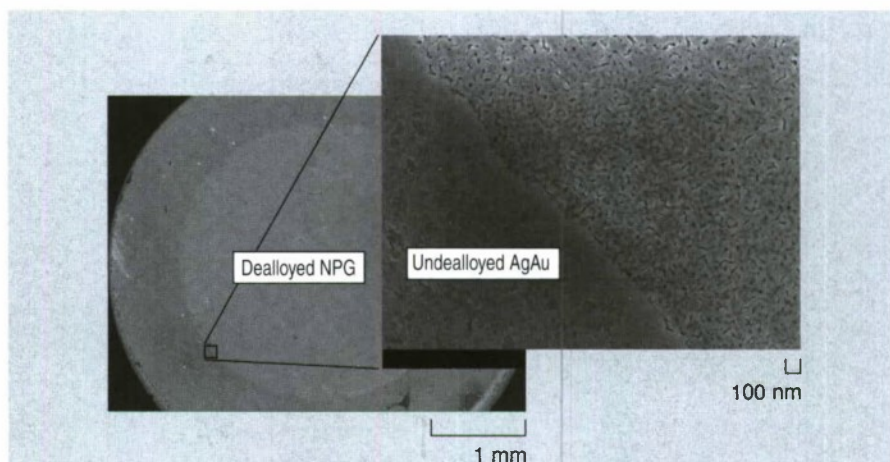


Figure 10. Scanning electron microscopy images of a single crystal grain in a Ag/Au foil with a 2 mm diameter patterned region of NPG made with a PDMS mask. Dealloying was performed in 0.1 M AgNO_3 at 0.563 V vs. Hg/HgSO_4 for 10 minutes, then the sample was reduced in 0.1 M H_2SO_4 at -0.1 V vs. Hg/HgSO_4 , and annealed at 400°C for 30 minutes to accentuate the porous region at lower magnifications.

composition of the electrolyte leads to different gold surface diffusion rates. Most anions that complex Ag^+ into a soluble species lead to orders-of-magnitude increases in the surface diffusivity of gold compared to vacuum or aqueous conditions without any ionic species.³⁵

At room temperature, anions such as nitrate lead to pore sizes in the 10–15 nm range during the initial stages of dealloying, but if the sample is left in nitric for periods of about 24 hours, this pore size coarsens to ~30 nm.²⁷ Smaller pore sizes in nitric can be made if the nitric acid is cooled to -20°C .³⁶ The addition of chloride, bromide, or iodide to the dealloying electrolyte leads to large increases in the surface diffusivity of gold, and consequently porosity with larger feature sizes.³⁷ One must be careful with the use of these anions, however—a too-high concentration of chloride leads to the formation of insoluble silver chloride species on the surface, and all of these anions are difficult to fully desorb.

For better control of the pore size during dealloying, a potentiostat in a three electrode configuration is used. The advantage here is that milder acids can be used, and there is better control over pore morphology. (The nature of the reference electrode is important and chloride from common Ag/AgCl reference electrodes can contaminate the electrolyte; use a salt bridge, or, preferably, a Hg/HgSO_4 reference.) The higher the dealloying potential (above the critical potential), the faster silver dissolution proceeds compared to gold surface diffusion, and the finer the porosity. Here, the concern is that at high potentials surface oxide species can form. The nature of these surface species have not been fully clarified, although there are reports of gold oxide formation.³⁸

An especially benign and easy method to make highly porous NPG is to dealloy in neutral silver nitrate, e.g., 0.1 AgNO_3 at high potential. As discussed in Reference 39, the use of a neutral solution is non-intuitive because the Pourbaix (potential/pH/phase) diagram suggests that at high anodic potentials silver will form insoluble oxides. However, once the instability initiates, there is an accumulation of protons right at

the etch front, creating a pH depression at the etch front. This situation is analogous to mechanisms of pitting or crevice corrosion. What's convenient is that immediately behind the etch front, the pH rises, leading to the formation of a morphology-stabilizing surface oxide. In this way, pore sizes as small as 5 nm are easily formed at room temperature. The flipside to the morphological stabilization is a significant amount of residual silver remains in the final sample of NPG, which can be as high as 15%. This silver can be removed, however, by repeated reduction/dissolution cycles.³⁹

We find that regardless of electrolyte and dealloying potential, significant amounts of residual surface oxide species of some sort always remain. These can be reduced in dilute sulfuric acid, and such reduction is important for clean surface electrochemistry, or for reproducible thermal anneals. Figure 6 shows cyclic voltammograms in the double layer region of a sample of NPG dealloyed in silver nitrate. The square, symmetric character of the voltammograms is a good check on the quality of the material, and will not be found on samples with any degree of surface oxide (the slight vertical offset disappears in deaerated electrolyte). It is interesting to note that for these samples we measure a specific capacitance of 11 F/g. On a mass basis, this is low, but on an atom basis the capacitance is ~2,100 F/mol, approximately the same as carbon nanotubes.⁴⁰

Annealing of NPG

The pore size of NPG can be further processed by thermal annealing, in order to grow the pore/ligament size to scales upwards of 10 μm . Here, it is quite important to thoroughly clean any electrolyte off the sample, and start with a fully reduced surface. Figure 7 shows an example of annealed NPG with and without residual surface oxide. The bumpy, sharp features of the sample annealed without reduction have clearly inhibited coarsening and led to a more random, bumpy, and finer scale material. Examples of porous gold with such features are commonly found in the literature,⁴¹ and coarsening results from such samples should be viewed with caution.⁴²

Figure 8 shows examples of clean NPG annealed at various temperatures and times. The pores in the bottom right of Figure 8, annealed at 900°C for 30 minutes, are large enough to be seen with optical microscopy. For many of these samples, the crystallographic orientation of the underlying grain is readily apparent in the quasi-random periodicity or symmetry of the final material. The three-fold symmetry of the (111) oriented grains are apparent in the 120 degree angles (Figure 8, bottom right), and on (001) oriented grains (Figure 8, bottom left) cubic symmetry is apparent. High resolution transmission electron microscopy (TEM) confirms the single-crystal nature of this material, if it wasn't obvious from the grain observations.²⁷ In microscopy, however, one must be careful about sample preparation. Ion milling for sample thinning or focused ion beam milling tends to break up the ligaments into polycrystalline aggregates; although the resultant materials are porous, they are not indicative of the native microstructure. This has been a point of confusion for some groups in the recent literature,^{41,43,44} but hopefully a recent x-ray diffraction and orientational imaging microscopy study have now resolved single crystal nature of NPG once and for all.⁴⁴

An interesting morphological characteristic of the annealed samples in Figure 8 is that there is a pronounced lack of facets. This observation is a result of processing and surface thermodynamics. Scanning electron microscopy of small gold particles⁴⁵ has shown that the equilibrium, or Wulff shape of gold crystallites is not fully faceted at high temperatures. At $1,000^\circ\text{C}$, most of the surface area of the equilibrium shape is actually completely round, with only small (111) facets. We hypothesize that an analogous situation is the case for all of the samples in Figure 8, which have been quenched quickly by taking small samples out of hot furnaces. In Figure 9, a sample placed in a hot 600°C furnace, and then slowly cooled to $<400^\circ\text{C}$ is shown, and here the length scale and kinetics have led to nicely faceted ligaments.

To reiterate an earlier point, the nice, extended porous microstructure in annealed NPG is only apparent because

the grain size is always bigger than the pore size by at least an order of magnitude. Materials with small grain sizes can also be dealloyed, but if both the pore and grain size is of the order of nanometers, the final product tends to be a porous sintered agglomeration of nanoparticles, and not NPG. This is an important distinction here because the properties of the sintered agglomerate are dominated by grain boundaries. These properties include the mechanical properties, but also thermal stability. In well-prepared NPG, there are no grain boundaries, and thus no grain boundary grooving. Grain boundaries are unstable to thermal grooving, and such materials tend to coarsen driven by chemical potential gradients associated with the local (positive) spherical curvature of the grains (as in models of grain growth or Ostwald ripening). In contrast, ligaments in NPG are morphological saddle points, with both positive and negative curvature. The inclusion of the negative curvature term in the chemical potential given by the Gibbs-Thomson equation alleviates the chemical potential gradient, leading to greater morphological stability.⁴⁶

Patterning NPG

The particular goal we have been concerned with here is the production of clearly delineated circles of NPG on silver/gold foil with as large grains as possible/convenient. For this purpose a mask is required, and the common polydimethylsiloxane (PDMS) elastomer used in so-called "soft lithography" works well for this purpose. Polydimethylsiloxane, however, is not very stable in strong acids, which also tend to seep into the elastomer/metal interface, and thus dealloying in concentrated nitric acid under free corrosion is not an option. With these observations in mind, we have found our best patterning results by using a PDMS mask that is not fully cured, and silver nitrate as a dealloying electrolyte. Figure 10 shows an example of our success—a circular patterned region of NPG.

CONCLUSIONS

The history of NPG began by studying it as a prototypical material for corrosion—a materials degradation process with negative connotation. Over the last decade, the material has been considered as useful and applicable in its own right. And more generally, dealloying is being considered a flexible and important processing tool to make bulk amounts of nanostructured materials. The authors are continually surprised by the further observation that classical metallurgy involving problems such as grain growth, recrystallization, texture development, surface orientation, Wulff shape, etc., plays such a central role in the fabrication of high quality material.

ACKNOWLEDGEMENTS

The authors are grateful to the U.S. National Science Foundation (NSF) and the U.K. Engineering and Physical Sciences Research Council via a Materials World Network program funded under grants DMR-0804187 (NSF) and the EP/G027005 (EPSRC).

References

1. J. Erlebacher and R. Seshadri, *MRS Bulletin*, 34 (2009), pp. 561–566.
2. J. Erlebacher et al., *Nature*, 410 (2001), pp. 450–453.
3. Y. Ding and M.W. Chen, *MRS Bulletin*, 34 (2009), pp. 569–576.
4. C. Xu et al., *J. Am. Chem. Soc.*, 129 (2007), pp. 42–43.
5. R. Zeis et al., *J. Catalysis*, 253 (2008), pp. 132–138.
6. F. Yu et al., *Anal. Chem.*, 78 (2006), pp. 7346–7350.
7. P.N. Ciesielski et al., *ACS Nano*, 2 (2008), pp. 2465–2472.
8. N.E. Chayen et al., *J. Mol. Biol.*, 312 (2001), pp. 591–595.
9. ISI Web of Science, <http://apps.isiknowledge.com>.
10. A.J. Forty, *Nature*, 282 (1979), pp. 597–598.
11. C. Cennini, *The Craftsman's Handbook: The Italian "Il libro dell'arte"*, translated by Daniel V. Thompson, (New York: Dover Publications, 1960).
12. H.W. Pickering and C. Wagner, *J. Electrochem. Soc.*, 114 (1967), pp. 698–706.
13. J. Erlebacher, *J. Electrochem. Soc.*, 151 (2004), pp. C614–C626.
14. K. Sieradzki et al., *J. Electrochem. Soc.*, 149 (2002), pp. B370–B377.
15. K. Sieradzki et al., *Phil. Mag. A*, 59 (1989), pp. 713–746.
16. D.M. Artymowicz et al., *Phil. Mag.*, 89 (2009), pp.

1663–1693.

17. J. Rugolo et al., *Nature Materials*, 5 (2006), pp. 946–949.
18. A. Dursun et al., *Electrochem. and Solid State Lett.*, 6 (2003), pp. B32–B34.
19. P.G. Vekilov et al., *Acta Cryst.*, D58 (2002), pp. 1611–1616.
20. S. Ahl et al., *Plasmonics*, 3 (2008), pp. 13–20.
21. W.T. Zheng et al., *ASM Alloy Phase Diagrams Center*, editor-in-chief, P. Villars; section editors, H. Okamoto and K. Cenual (Materials Park, OH: ASM International, 2006), www.asminternational.org/AsmEnterprise/APD.
22. Y. Sun and T.J. Balk, *Scripta Mat.*, 58 (2008), pp. 727–730.
23. C. Ji and P.C. Searson, *Appl. Phys. Lett.*, 81 (2002) pp. 4437–4439.
24. E. Seker et al., *Acta Mat.*, 56 (2008), pp. 324–332.
25. D. Lee et al., *Scripta Mat.*, 56 (2007), pp. 437–440.
26. N.A. Senior and R.C. Newman, *Nanotechnology*, 17 (2006), pp. 2311–2316.
27. Y. Ding et al., *Adv. Mat.*, 16 (2004), pp. 1897–1900.
28. F. Friedersdorf, "Stress-corrosion Cracking of Binary Noble Metal Alloys (Ph.D. thesis, Johns Hopkins University, 1994).
29. M. Hakamada and M. Mabuchi, *Nano Lett.* 6 (2006), pp. 882–885.
30. J. Weissmuller et al., *MRS Bulletin*, 34 (2009), pp. 577–586.
31. K. Sieradzki and R. Li, *Phys. Rev. Lett.*, 68 (1992), pp. 1168–1171.
32. D.J. Bailey and E.G. Brewer, *Metallurgical and Materials Trans. A*, 6 (1975), pp. 403–408.
33. J. Snyder and J. Erlebacher, *Langmuir*, 25 (2009), pp. 9596–9604.
34. J.W. Cahn et al., *Acta Mat.*, 54 (2006), pp. 4953–4975.
35. J.G. Velasco, *Chem. Phys. Lett.*, 313 (1999), pp. 7–13.
36. L.H. Qian and M.W. Chen, *Appl. Phys. Lett.*, 91 (2007), 083105.
37. A. Dursun et al., *J. Electrochem. Soc.* 150 (2003), pp. B355–B360.
38. P. Durkin and A.J. Forty, *Phil. Mag. A*, 45 (1982), pp. 95–105.
39. J. Snyder et al., *J. Electrochem. Soc.* 155 (2008), pp. C464–C473.
40. J. Snyder et al., *Advanced Materials*, 20 (2008), pp. 4883–4886.
41. A.M. Hodge et al., *Adv. Eng. Mat.*, 8 (2006), pp. 853–857.
42. M. Hakamada and M. Mabuchi, *J. Mater. Res.*, 24 (2009), pp. 301–304.
43. J. Beiner et al., *J. Appl. Phys.* 97 (2005), 024301.
44. S. Van Petegem et al., *Nano Lett.*, 9 (2009), pp. 1158–1163.
45. J.C. Heyraud and J.J. Metois, *Acta Met.*, 28 (1980), pp. 1789–1797.
46. C. Herring, *The Physics of Power Metallurgy*, ed. W.E. Kingston (New York: McGraw-Hill, 1951), pp. 143–179.

F. Kertis and J. Snyder are graduate students at Johns Hopkins University. L. Govada and S. Khurshid are in Prof. N. Chayen's group at Imperial College, London, U.K. J. Erlebacher, Professor of Materials Science and Engineering, and Chemical and Biomolecular Engineering at Johns Hopkins University, 3400 N. Charles St., Baltimore, MD 21218. Dr. Erlebacher can be reached at Jonah.Erlebacher@jhu.edu.

The Anodization of Aluminum for Nanotechnology Applications

Woo Lee

In light of the ever-increasing demand for the development of an effective, inexpensive and technologically simple method, a naturally occurring self-organization of oxide nanopores during the anodization of aluminum has recently attracted a vast amount of research attention in the field of nanotechnology. This article gives a brief overview on some of the recent advances in the anodization of aluminum, focusing on the fabrication of highly ordered nanoporous anodic aluminum oxide. Conventional anodization, newly developed hard anodization, pulse anodization process, and generic approaches for the fabrication of three-dimensional pore structures with periodically modulated diameters are discussed.

INTRODUCTION

Anodization is an electrochemical oxidation process employed to increase the thickness of the native oxide layer on the surface of metals (e.g., Al, Ti, Hf, W, Nb, Sn, Zr, etc.) or semiconductors (e.g., Si, InP, GaAs, etc.) (Figure 1a).¹⁻³ Among anodizable materials, aluminum has been of particular interest due to its many profitable engineering properties. In general, anodization of aluminum can result in two different types of anodic oxide depending on the nature of an electrolyte used; a compact and non-porous barrier-type oxide from neutral electrolytes and a porous-type oxide from acidic electrolytes (Figure 1b).³ Over the last several decades, the process, particularly porous-type anodization, has raised substantial technological interest in the industry.^{4,5} Many desirable properties such as higher thickness, hardness, good corrosion resistance, higher abrasive and wear resistance over the native

oxide can be imparted to the aluminum or its alloys by subjecting the metal

How would you...

...describe the overall significance of this paper?

This article conveys some of the latest advances in anodization of aluminum, which has long been an indispensable process in the surface finishing industry, but now becomes one of the most important processes in nanotechnology for developing advanced nanodevices.

...describe this work to a materials science and engineering professional with no experience in your technical specialty?

This article is an introduction to anodization of aluminum, which is a subject of electrochemistry. Anodization of aluminum under a controlled electrochemical condition yields ordered porous alumina with a close-packed hexagonal array of cylindrical nanochannels. The diameter, density, and aspect ratio of pores can be tightly controlled by varying the anodization condition, which makes the porous anodic alumina an important platform in nanotechnology for developing various functional nanostructures.

...describe this work to a layperson?

Anodization of aluminum, an electrochemical oxidation of aluminum, can produce a honeycomb-like nanoporous oxide film. The process was developed for the protection of seaplane parts from corrosive seawater in 1923. The products of the process can be found everywhere around us, for example in cookware, architectural items, vehicles, and machine parts. Now nanotechnology scientists are paying attention to this nearly century-old process for developing various functional nanostructures. This article gives a brief overview on the recent progress in the anodization of aluminum.

to anodic oxidation. The anodic process also provides a suitable surface or base for subsequent electroplating, painting and decorative coloration by incorporation of pigments followed by sealing of the anodized materials.

This electrochemical process has recently drawn a renewed attention in academic research, especially in the field of nanotechnology. An idealized structure of nanoporous anodic aluminum oxide (AAO) is schematically shown in Figure 1c. Anodic aluminum oxide formed by porous-type anodization under a controlled electrochemical condition is characterized by a large number of non-interconnecting parallel pores extending through the film to the oxide/metal interfaces, where each cylindrical nanopore is closed by a thin barrier oxide layer with hemispherical geometry. Each pore and the region surrounding it comprise a hexagonal cell. These cells are self-organized in the form of a hexagonally close-packed structure, like a honeycomb.⁶ Based on the recent development, self-ordered nanoporous AAOs with a uniform pore diameter in the range of 20–400 nm and with a pore density in the range of 10^8 – 10^{10} pores/cm² can conveniently be prepared by anodization of aluminum. The depth of straight nanopores can easily be controlled in the range of a few tens of nanometers to more than several hundred micrometers by varying the anodization time. Due to the unique structural feature of nanoporous AAO and also to the tailoring capability of its structural parameters, the anodization process has attracted scientific attention in the use of the resulting AAO not only as template for fabricating structurally well-defined nanostructures (e.g., arrays of nanodots, nanotubes, and nanowires) in a large quantity,⁷⁻¹² but

as a starting material for developing high-performance sensor, biomedical, photonic, energy harvesting, and memory devices.¹³⁻¹⁷

MILD ANODIZATION

Over the past several decades, studies on aluminum anodization have been driven by the aluminum industry, and thus mostly devoted to the improvement of technical quality of the anodic films for various commercial applications and also to the production at an efficient rate and cost. Although a wide variety of anodization processes and proprietaries have continued to be developed in industry, the spatial ordering and the uniformity of pores in anodic oxide films have not been a matter of concern. Anodic oxide films produced by a typical industrial process, which is represented by hard anodization (HA), are characterized by non-uniform pore structures with numerous micrometer-sized cracks. Thus, they are not suitable for nanotechnology applications.

In 1995, Masuda and Fukuda

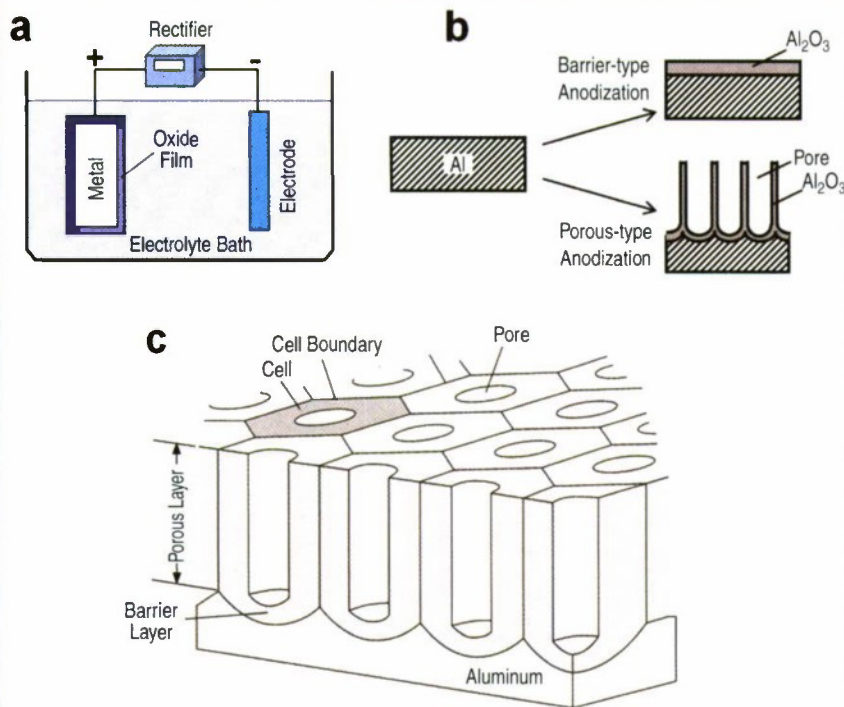


Figure 1. Schematic illustrations showing (a) a simplified anodization setup, (b) two different types of aluminum anodization, and (c) an idealized structure of anodic aluminum oxide (AAO) produced by a porous-type anodization.

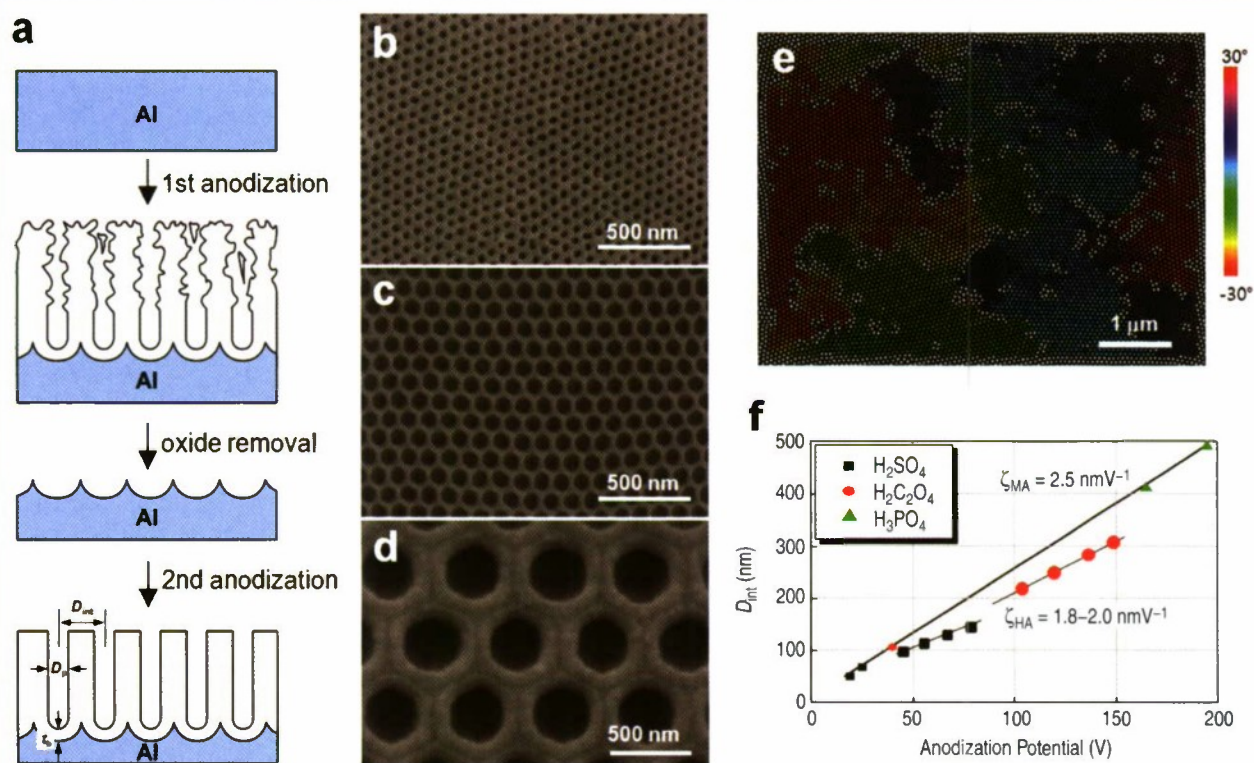


Figure 2. (a) A schematic procedure of a conventional two-step mild anodization (MA) for self-ordered anodic aluminum oxide (AAO). (b-d) Representative SEM micrographs of self-ordered AAOs produced by MA using (b) 0.3 M H_2SO_4 at 25 V, (c) 0.3 M $H_2C_2O_4$ at 40 V, and (d) 1 wt.% H_3PO_4 at 195 V. (e) A color-coded SEM image of AAO formed by two-step MA using 0.3M H_2SO_4 at 25 V, showing a poly-domain structure (Reprinted with permission from Reference 44 © 2008 American Chemical Society). An area with the same color consists of a domain. Pores that have no apparent hexagonal coordination (i.e., defect pores) are marked white. (f) Summary of self-ordering potentials and the corresponding interpore distance (D_m) in mild anodization (MA) and hard anodization (HA).

found that AAO formed by long-term anodization ($t \sim 160$ h) under a potentiostatic condition ($U = 40$ V) using 0.3 M oxalic acid exhibits a self-ordered cell configuration at the bottom part of AAO as a consequence of gradual rearrangement of the cells initially in a random configuration.¹⁸ They reported that the size of the defect-free domain, in which pores are almost ideally arranged forming a honeycomb structure, increases with the anodization time but is limited to several micrometers.¹⁸ This experimental observation led to the development of the 'two-step anodization' process, by which nanoporous AAO with highly ordered arrangement of uniform nanopores can be obtained (Figure 2a).¹⁹ Since then, anodization of aluminum has drawn renewed attention, particularly in the field of nanotechnology research for the application of highly ordered AAO to the development of various functional nanostructures. Many studies have been carried out in an attempt to improve the regularity of the pore arrangement, to control the size and position of the pores, and to understand the development of nanopores and their self-organizing process during anodization of aluminum. Much research effort has focused on the exploration of optimum ordering conditions for the electrolyte systems (i.e., sulfuric, oxalic, phosphoric, and chromic acid) that were investigated by Keller et al. in the early 1950s.⁶

Ordered AAOs that are suitable for nanotechnology applications have been fabricated by mild anodization (MA) of aluminum in a limited processing window, known as 'self-ordering regime,' under which self-organized growth of ordered nanopores occurs (Figure 2b–d): (i) sulfuric acid (H_2SO_4) at 25 V for an interpore distance (D_{int}) = 63 nm,^{20,21} (ii) oxalic acid ($\text{H}_2\text{C}_2\text{O}_4$) at 40 V for $D_{\text{int}} = 100$ nm,^{18,20,21} and (iii) phosphoric acid (H_3PO_4) at 195 V for $D_{\text{int}} = 500$ nm.²³ Many morphological investigations revealed that structural parameters (e.g., the pore diameter (D_p), interpore distance (D_{int}), barrier layer thickness (t_b)) of AAOs formed under self-ordering regimes depend primarily on anodization potential (U),^{21,24,25} which is in line with the earlier reports.^{6,26–29} The interpore distance (D_{int}) and the barrier layer thickness (t_b) are linearly

dependent on the applied potential (U) with proportionality constants $\zeta = 2.5$ nmV⁻¹ for D_{int} and $\eta = 1.2$ nmV⁻¹ for t_b (Figure 2f).^{6,21,24,28} Pore diameter (D_p) has also been known to increase at a rate of ca. 1.3 nmV⁻¹.²⁶ But the potential dependence of D_p is not as sensitive as the interplay between the current density and the temperature, concentration and nature of the electrolyte used.^{30–32} For the self-ordered AAO formed under MA conditions, Nielsch et al. proposed an empirical rule that self-ordering of porous alumina requires a porosity (P) of about 10% irrespective of the anodizing potential and composition of electrolyte and anodization conditions; $P(\%) = \text{the surface area ratio of pores to the whole oxide film} = (\pi/2\sqrt{3})(D_p/D_{\text{int}})^2 \times 100$.²⁴ But there are some reports that self-ordered AAOs can be attained at other porosity (P) values ranging from 10% to 30% depending on MA conditions.^{31,33}

Anodization of aluminum has been extensively studied over the last several decades. But there is still much work to do in order to fully understand the

self-organized formation of oxide nanopores. For self-organized growth of AAOs, mechanical stress at the metal/oxide interface that is associated with volume expansion during oxidation of aluminum was proposed as a main driving force for the close-packed hexagonal arrangement of oxide nanopores.^{21,34} It is generally accepted for steady-state film growth that oxide nanopores are generated as results of a dynamic equilibrium between the rate of field-assisted oxide dissolution at the electrolyte/oxide (e/o) interface and the rate of oxide formation at the metal/oxide (m/o) interface, which keeps the thickness of the barrier layer constant.^{22,26,30,35,36} However, this dissolution-based pore formation mechanism has been disputed many experiments. Oxygen isotope (¹⁸O) studies indicated that the pore formation does not take place through a simple oxide dissolution process, and suggested that pore formation consists of some kind of oxide decomposition through the direct ejection of Al^{3+} into the solution and the oxide formation

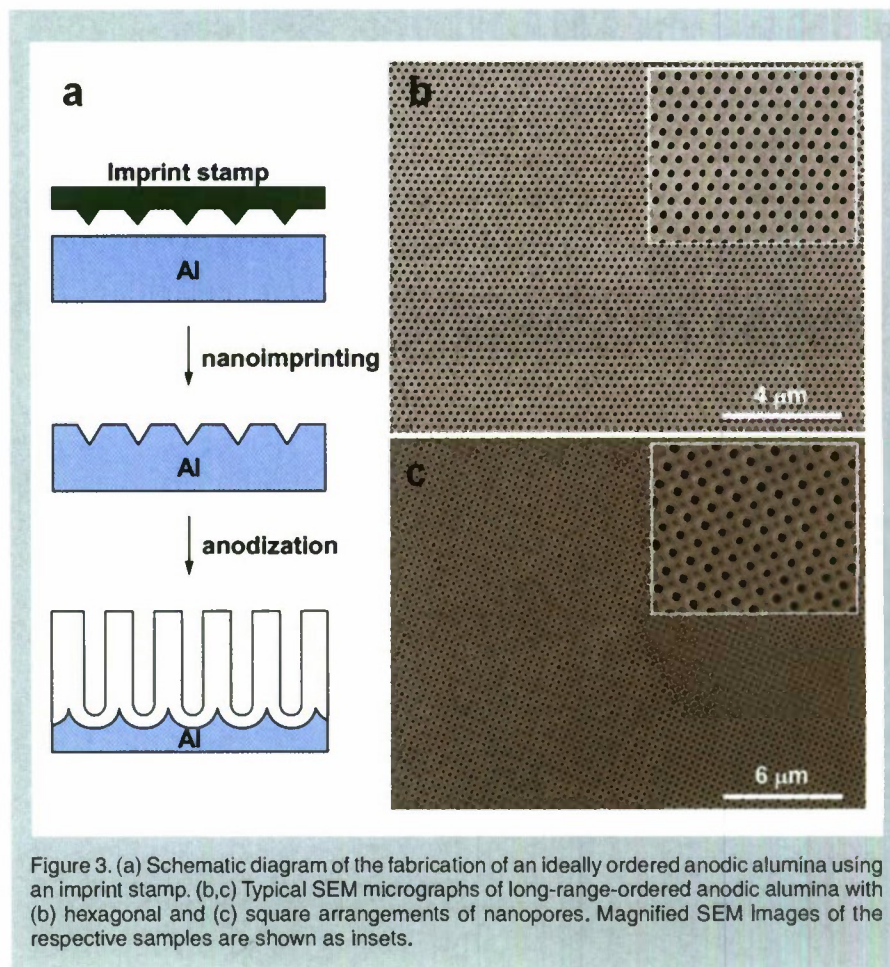


Figure 3. (a) Schematic diagram of the fabrication of an ideally ordered anodic alumina using an imprint stamp. (b,c) Typical SEM micrographs of long-range-ordered anodic alumina with (b) hexagonal and (c) square arrangements of nanopores. Magnified SEM images of the respective samples are shown as insets.

at the *m/o* interface through oxygen transport.^{37,38} Other experiments revealed that the field-assisted oxide dissolution at the pore base is virtually negligible.^{39,40} In line with these results, recent tungsten tracer studies indicate that flow of oxide materials has a major role in forming pores, contrary to expectations of a dissolution model of pore development.^{41,42} The flow of the oxide was suggested to arise from the field-assisted plastic flow of oxide materials from pore base toward the cell boundary and the generation of stress due to electrostriction and the oxidation of aluminum. This flow-based pore formation mechanism has been further supported by theoretical study.⁴³

Anodic aluminum oxide formed by two-step anodization under the self-ordering regimes exhibit a poly-domain structure, in which each domain with an ideally ordered array of nanopores is separated with neighboring domains by a boundary along which defect pores and imperfections in pore arrangement are present.^{18,44} For certain nanotechnology applications, it is highly desirable to utilize long-range ordered AAOs without any defects. Fabrication of ideally ordered AAO with a single-domain configuration over a few mm² area was first demonstrated by Masuda et al. by anodizing a pre-patterned aluminum.⁴⁵ The process involves pre-texturing of the aluminum surface by nanoindentation using an appropriate stamp prior to anodization (see Figure 3). Each indent formed on the aluminum substrate by nanoindentation initiates pore nucleation and leads to a long-range ordered pore arrangement within the stamped area. This method was further extended to fabricate a hole array architecture with square- or triangle-shaped openings in a close-packed square or hexagonal arrangement.⁴⁶ Several groups have achieved pre-patterning of aluminum by employing a focused ion beam (FIB) technique,⁴⁷ holographic lithography,⁴⁸ and microsphere lithography,⁴⁹ and demonstrated fabrication of single-domain AAOs with an arbitrary interpore distance (D_{int}). An economic approach to the fabrication of single-domain AAOs in a wafer-scale is also currently available.⁵⁰

Nanoimprint-assisted anodization

of aluminum provides an effective way to fabricate single-domain AAOs. However, the major limitation of the process is that the attainable maximum aspect ratio or depth of nanochannels maintaining the initial hole configuration depends critically on anodization conditions.¹⁷ High aspect ratio of uniform nanopores can be obtained only under a narrow processing window (i.e., self-ordering regime), which practically limits the range of selection over the interpore distance (i.e., D_{int} = 63 nm, 100 nm, 500 nm for 25 V-H₂SO₄, 40 V-H₂CO₄, and 195 V-H₃PO₄ anodization, respectively). When anodization is conducted outside the self-ordering condition, the initial degree of the spatial ordering defined by nanoindentation decreases drastically. These process limitations reduce the potential applications of nanoporous alumina. Substantial efforts have been made to explore a new self-ordering regime in a wider range of D_{int} .^{51–53} The research activity to date includes extending the voltage range by

appropriately tuning of the three well-known acid electrolytes (i.e., H₂SO₄, H₂CO₄, and H₃PO₄) and searching new electrolyte systems. However, applied voltages higher than the optimum value required to maintain stable anodization in a given electrolyte always result in “breakdown” or “burning” of the oxide film caused by catastrophic flow of electric current coupled with a large amount of reaction heat.⁵⁴

HARD ANODIZATION

Recently, Lee et al. showed that the self-ordering regimes can be extended by implementing hard anodization (HA) of aluminum.⁵⁵ The HA process was originally developed in the surface finishing industry in the early 1960s, and has been widely used for various industrial applications by taking advantage of the high-speed oxide growth (50–100 $\mu\text{m h}^{-1}$).^{56,57} However, the process has not been employed in current nanotechnology research due to the difficulties involved in controlling important structural parameters, such as pore size (D_p), interpore distance (D_{int}), and the aspect ratio of the nanopores of the resulting anodic alumina. By introducing a thin protective oxide layer on aluminum prior to performing HA process and carefully controlling the reaction heat during HA, Lee et al. could suppress the burning event and grow self-ordered AAOs using oxalic acid at anodization potentials $U > 100$ V, establishing a new self-ordering regime with a widely tuneable interpore distance (D_{int} = 200–300 nm) (Figure 2f). The rate of oxide growth in HA was found to be 25 to 35 times faster than that in MA. The newly developed method turned out to be applicable to other electrolyte systems.^{8,59}

The HA process is characterized by a high current density (j) that is typically one or two orders of magnitude higher than that of the ordinary MA. The current in anodization of aluminum is related to the passage of ionic species through the barrier layer. Under high field condition, the ionic current density (j) can be related to the electric field strength (E); $j = j_0 \exp(\beta E) = j_0 \exp(\beta \Delta U / t_b)$, where j_0 and β are the material-dependent constants and $\Delta U / t_b$ is the effective electric field strength (E) across the barrier layer of thickness t_b .

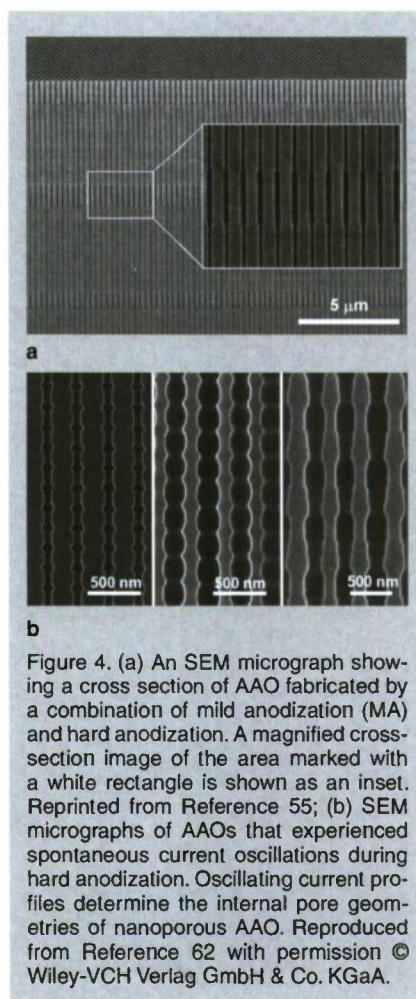


Figure 4. (a) An SEM micrograph showing a cross section of AAO fabricated by a combination of mild anodization (MA) and hard anodization. A magnified cross-section image of the area marked with a white rectangle is shown as an inset. Reprinted from Reference 55; (b) SEM micrographs of AAOs that experienced spontaneous current oscillations during hard anodization. Oscillating current profiles determine the internal pore geometries of nanoporous AAO. Reproduced from Reference 62 with permission © Wiley-VCH Verlag GmbH & Co. KGaA.

Investigation of HA processes revealed that the current density (i.e., the electric field strength E across the barrier layer) is a key parameter governing the self-organization of oxide nanopores in a given anodization potential (U). The barrier layer thickness for HA increases at a rate of $t_b^{MA} = 0.6\text{--}1.0\text{ nmV}^{-1}$,^{55,60} which is smaller than $t_b^{MA} \sim 1.2\text{ nmV}^{-1}$ for MA processes.^{6,28} HA-AAOs exhibit a reduced voltage dependence of the interpore distance (D_{int}) with a proportionality constant $\zeta_{HA} = 1.8\text{--}2.0\text{ nmV}^{-1}$,^{55,58,59} compared to MA-AAOs (i.e., $\zeta_{MA} = 2.5\text{ nmV}^{-1}$).^{21,24} Similar lines of experimental results have also been reported by other researchers.^{52,61} For oxalic acid-based HA, the porosity (P_{HA}) of HA-AAO turned out to be $P_{HA} = 3.3\text{--}3.4\%$, which is about one-third of the porosity value ($P_{MA} \sim 10\%$) that was proposed as a requirement for self-ordered AAO under MA conditions.²⁴ On the basis of the newly found self-ordering behavior in HA, Lee et al. realized the fabrication of AAO membranes with periodically modulated diameter of nanopores along the pore axes by combining MA and HA process, in which each modulation step required the exchange of the electrolyte solution in order to satisfy both MA and HA processing conditions (Figure 4a).⁵⁵ Quite recently, they further showed that AAOs experienced spontaneous current oscillations (amplitude $\sim 0.8\text{ Acm}^{-2}$) during a potentiostatic HA can have modulated pore structures, in which the modulation contrast is proportional to the amplitude of current oscillation, and suggested that one may achieve structural engineering of nanoporous AAO by deliberately manipulating the current during anodization of Al (Figure 4b).⁶³

The fabricated AAOs with modulated pore structure could be starting materials for developing three-dimensional (3-D) porous architectures that may offer potential for photonic applications, and also model systems for investigating separations of particles and adsorption characteristics of molecules. In addition, it is expected that these AAOs can be readily utilized as template materials for fabricating novel nanowires or nanotubes, whose diameters are periodically modulated along their axes, and thus, enable one to study the various physical properties

that originated from the surface topography.

PULSE ANODIZATION

As mentioned in the previous section, combination of conventional MA and the newly developed HA could offer a new degree of freedom for tailoring the pore structure of AAOs by combining properties from the two anodization processes. Based on this

The fabricated AAOs with modulated pore structure could be starting materials for developing three-dimensional porous architectures that may offer potential for photonic applications, and also model systems for investigating separations of particles and adsorption characteristics of molecules.

concept, Lee et al. developed a generic approach for continuous structural engineering of nanoporous AAO based on pulse anodization (PA) of aluminum under a potentiostatic condition using H_2SO_4 or $\text{H}_2\text{C}_2\text{O}_4$.⁶³ In a typical PA process, periodic pulses consisting of a low-potential pulse (U_{MA}) followed by a high potential pulse (U_{HA}) are applied to continuously achieve MA and HA conditions, respectively (Figure 5a). During PA in a given electrolyte, anodization current changes periodically to a value corresponding to each pulsed potential (i.e., j_{MA} for U_{MA} and j_{HA} for U_{HA} ; $j_{MA} < j_{HA}$), and thus the pore structure of the resulting AAO is periodically modulated (Figure 5b). Nanoporous AAO formed by a PA process exhibits a layered structure of MA-AAOs with a smaller pore diameter and HA-AAOs with a larger pore diameter, in which the thickness of

each anodized segment is determined by the pulse durations (τ_{MA} and τ_{HA}) at given anodization potentials (U_{MA} and U_{HA}) (Figure 5c).

An interesting finding from the case of sulfuric acid-based PA is that an oxide segment (HA-AAO) formed by a high potential pulse (U_{HA}) contains a higher level of anionic impurity from the electrolyte than an oxide segment (MA-AAO) formed by a low potential pulse (U_{MA}). Therefore, PA in sulfuric acid solution results in a periodic compositional modulation along the pore axes of AAO. HA-AAO segments with a higher impurity content exhibit a poor chemical stability against an etchant (e.g., 5 wt.% H_3PO_4). This enables one to completely delaminate a single as-prepared anodic film into a stack of well-defined AAO membranes sheets by an extended etching of HA-AAO segments (Figure 5d). Accordingly, PA followed by selective etching of HA-AAO segments by an appropriate etchant provides a simple, continuous, and economic way for the mass production of nanoporous AAO membranes.

PA can also be conducted under a galvanostatic condition to tailor the internal pore structure of AAO. In this case periodic current pulses are applied to achieve MA and HA conditions, and anodization potential changes periodically to a value corresponding to each pulsed current. Recently, Lee et al. reported a convenient method for the preparation of structurally well-defined alumina nanotubes with controllable lengths.⁶⁴ The approach is based on the fact that H_2SO_4 -AAO formed under a high electric field strength (E) exhibits a weakened junction strength between cells. They employed galvanic pulses to selectively combine MA and HA conditions, where the pulse duration (τ_{HA}) for HA determines the length of nanotubes. By taking advantage of the weak junction strength between cells and of the modulated pore structures along the pore axis, individual alumina nanotubes could be separated from an as-prepared AAO.

The reaction involved in anodic oxidation of aluminum is exothermic. The dissolution of the resulting oxide by acid electrolyte is endothermic. The main contribution to heat generation in

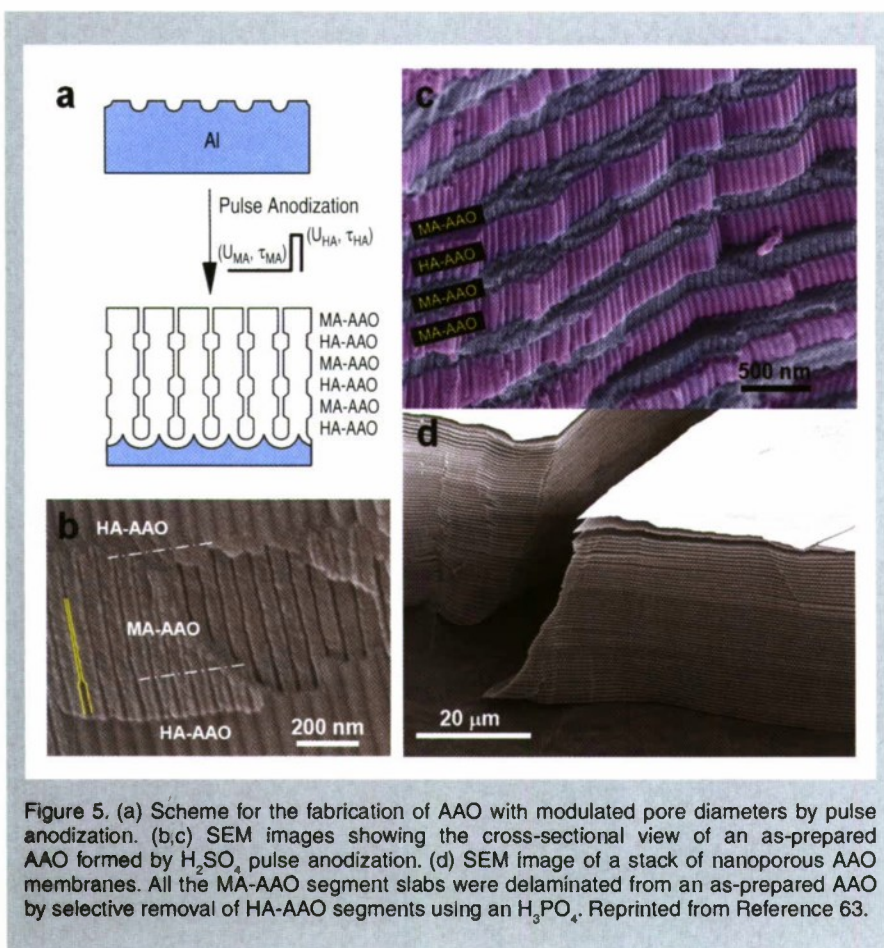


Figure 5. (a) Scheme for the fabrication of AAO with modulated pore diameters by pulse anodization. (b,c) SEM images showing the cross-sectional view of an as-prepared AAO formed by H_2SO_4 pulse anodization. (d) SEM image of a stack of nanoporous AAO membranes. All the MA-AAO segment slabs were delaminated from an as-prepared AAO by selective removal of HA-AAO segments using an H_3PO_4 . Reprinted from Reference 63.

anodization of aluminum is related to current flow through the barrier oxide layer. The production of Joule's heat (Q) is proportional to the square of the current density (j) according to $Q = Ujt = R_b j^2 t$, where R_b and t are the resistance of the barrier layer and the reaction time, respectively. HA is accompanied by a large evolution of heat due to the high anodic current (j) associated with the high electric field (E) at the barrier oxide. Since current density (j_{HA}) in HA is about one or two orders of magnitude higher than that (j_{MA}) in MA, heat production during HA could be roughly two to four orders of magnitude larger. The excessive heat does not only trigger breakdown of an anodic film but promotes undesired acidic dissolution of oxide membrane by the electrolyte. PA promises effective dissipation of reaction heat, which is one of the major causes of burning of an anodic film during anodization of aluminum under high current density (j). The accumulated Joule's heat during an HA-pulse of a high current density can be efficiently dispersed during the subsequent MA-pulse of a low current density, overcoming "burning" of an anodic film.

CONCLUSION

Self-ordered porous alumina formed by anodization of aluminum has increasingly become a popular template system in the development of functional nanostructures. Anodization of aluminum can be categorized into two main groups; mild anodization and hard anodization. The former method produces self-ordered and straight pore structures, but it is slow and only works for a narrow range of processing conditions. The latter method, which is widely used in the industry, is faster, but it produces anodic films with disordered and non-uniform pore structures. In these respects, the newly developed hard anodization process offers substantial advantages over the processes established previously. The process allows 25–35 times faster oxide growth with an improved ordering of the nanopores, compared to the conventional mild anodization. It establishes a new self-ordering regime over a wide range of interpore distance. On the other hand, pulse anodization enables selective combination of the advantages of mild anodization and the new hard an-

odization process. This generic process allows continuous tailoring of the internal pore structure as well as the composition of the anodic oxide by deliberately designing the pulse sequences. Therefore it provides a new degree of freedom in template-based synthesis of functional nanostructures that can be used for developing advanced devices as well as for investigating a diverse range of research problems in chemistry and physics.

In spite of some recent advances in anodization of aluminum, there is still much work to do. Exploration of new electrolytes systems and novel porous architectures will continue to expand the field of applications of anodic alumina. In addition, engineering the properties (e.g., wear or plasma resistance) of anodic films formed by the new processes is an interesting subject of research for the commercial applications. As mentioned in the present overview, there are still many open questions regarding the mechanism responsible for the pore formation and self-organization. Understanding the electrochemical process during the anodization of aluminum could provide a solid foundation for developing ordered porous structures from other valve metals, such as Hf, Ti, W, Zr, Nb, Ta, Sn, etc., which is currently an active area of research.

ACKNOWLEDGEMENTS

This article is dedicated to the memory of the late Prof. Ulrich Gösele. Financial support in part from the Korea Research Council of Fundamental Science and Technology through the "Development of Advanced Industrial Metrology" project is gratefully acknowledged.

References

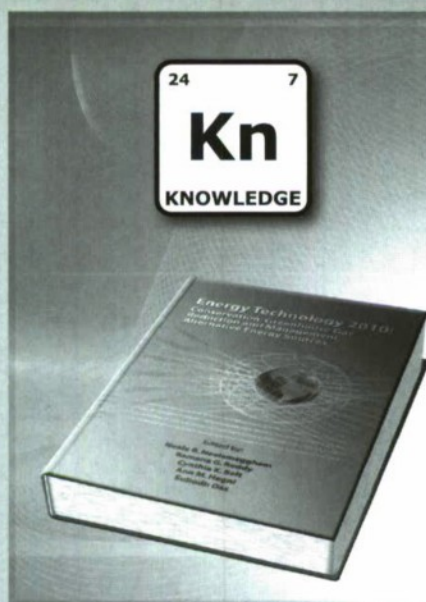
1. M.M. Lohrengel, *Mater. Sci. Eng. R*, 11 (1993), pp. 243–294.
2. H. Föll et al., *Mater. Sci. Eng. R*, 39 (2002), pp. 93–141.
3. J.W. Diggle, T.C. Downie, and C.W. Goulding, *Chem. Rev.*, 69 (1969), pp. 365–405.
4. P.G. Sheasby and R. Pinner, *The Surface Treatment and Finishing of Aluminum and Its Alloys* (Materials Park, OH and Stevenage, U.K.: ASM International and Finishing Publications Ltd., 2001).
5. G.D. Bengough and J.M. Stuart, U.K. patent 223,994 (1923).
6. F. Keller, M.S. Hunter, and D.L. Robinson, *J. Electrochem. Soc.*, 100 (1953), pp. 411–419.
7. S.R. Nicewarner-Peña et al., *Science*, 294 (2001), pp. 137–141.

8. W. Lee et al., *Angew. Chem. Int. Ed.*, 44 (2005), pp. 6050–6054.
9. W. Lee et al., *Chem. Mater.*, 17 (2005), pp. 3325–3327.
10. W. Lee et al., *Nature Nanotech.*, 3 (2008), pp. 402–407.
11. Z. Huang et al., *Nano Lett.*, 8 (2008), pp. 3046–3051.
12. L. Liu et al., *Angew. Chem. Int. Ed.*, 47 (2008), pp. 7004–7008.
13. Z. Huang et al., *J. Med. Devices*, 1 (2007), pp. 79–83.
14. D. Ding et al., *Sens. Actuators B*, 124 (2007), pp. 12–17.
15. D. Gong et al., *Biomed. Microdevices*, 5 (2003), pp. 75–80.
16. Z. Fan et al., *Nature Mater.*, 8 (2009), pp. 648–653.
17. H. Asoh et al., *J. Electrochem. Soc.*, 148 (2001), pp. B152–B156.
18. H. Masuda and K. Fukuda, *Science*, 268 (1995), pp. 1466–1468.
19. H. Masuda and M. Satoh, *Jpn. J. Appl. Phys.*, 35 (1996), pp. L126–L129.
20. H. Masuda, E. Hasegawa, and S. Ono, *J. Electrochem. Soc.*, 144 (1997), pp. L127–L130.
21. A.P. Li et al., *J. Appl. Phys.*, 84 (1998), pp. 6023–6026.
22. F. Li, L. Zhang, and R.M. Metzger, *Chem. Mater.*, 10 (1998), pp. 2470–2480.
23. H. Masuda, K. Yada, and A. Osaka, *Jpn. J. Appl. Phys.*, 37 (1998), pp. L1340–L1342.
24. K. Nielsch et al., *Nano Lett.*, 2 (2002), pp. 677–680.
25. I. Vrublevsky et al., *Appl. Surf. Sci.*, 227 (2004), pp. 282–292.
26. J.P. O'Sullivan and G.C. Wood, *Proc. Roy. Soc. Lond. A*, 317 (1970), pp. 511–543.
27. K. Ebihara, H. Takahashi, and M. Nagayama, *J. Met. Finish. Soc.*, 34 (1983), pp. 548–553.
28. M.S. Hunter and P. Fowle, *J. Electrochem. Soc.*, 101 (1954), pp. 481–485.
29. M.S. Hunter and P. Fowle, *J. Electrochem. Soc.*, 101 (1954), pp. 514–519.
30. V.P. Parkhutik and V.I. Shershusky, *J. Phys. D: Appl. Phys.*, 25 (1992), pp. 1258–1263.
31. G.D. Sulka and K.G. Parkola, *Electrochim. Acta*, 52 (2007), pp. 1880–1888.
32. G. Paolini et al., *J. Electrochem. Soc.*, 112 (1965), pp. 32–38.
33. S. Ono et al., *J. Electrochem. Soc.*, 151 (2004), pp. B473–B478.
34. O. Jessensky, F. Müller, and U. Gösele, *Appl. Phys. Lett.*, 72 (1998), pp. 1173–1175.
35. T.P. Hoar and N.F. Mott, *J. Phys. Chem. Solids*, 9 (1959), pp. 97–99.
36. Z. Su and W. Zhou, *Adv. Mater.*, 20 (2008), pp. 3663–3667.
37. C. Cherki and J. Siejka, *J. Electrochem. Soc.*, 120 (1972), pp. 784–791.
38. J. Siejka and C. Ortega, *J. Electrochem. Soc.*, 124 (1977), pp. 883–891.
39. G.E. Thompson, *Thin Solid Films*, 297 (1997), pp. 192–201.
40. Z. Wu, C. Richter, and L. Menon, *J. Electrochem. Soc.*, 154 (2007), pp. E8–E12.
41. P. Skeldon et al., *Electrochem. Solid-State Lett.*, 9 (2006), pp. B47–B51.
42. S.J. Garcia-Vergara et al., *Electrochim. Acta*, 52 (2006), pp. 681–687.
43. J.E. Houser and K.R. Hebert, *Nature Mater.*, 8 (2009), pp. 415–420.
44. R. Hillebrand et al., *ACS Nano*, 2 (2008), pp. 913–920.
45. H. Masuda et al., *Appl. Phys. Lett.*, 71 (1997), pp. 2770–2772.
46. H. Masuda et al., *Adv. Mater.*, 13 (2001), pp. 189–192.
47. C.Y. Liu, A. Datta, and Y.L. Wang, *Appl. Phys. Lett.*, 78 (2001), pp. 120–122.
48. Z. Sun and H.K. Kim, *Appl. Phys. Lett.*, 81 (2002), pp. 3458–3460.
49. S. Fournier-Bidoz et al., *Adv. Mater.*, 16 (2004), pp. 2193–2196.
50. W. Lee et al., *Small*, 2 (2006), pp. 978–982.
51. S. Shingubara et al., *Electrochem. Solid-State Lett.*, 7 (2004), pp. E15–E17.
52. S.-Z. Chu et al., *Adv. Mater.*, 17 (2005), pp. 2115–2119.
53. S. Ono, M. Saito, and H. Asoh, *Electrochim. Acta*, 51 (2005), pp. 827–833.
54. N. Sato, *Electrochim. Acta*, 16 (1971), pp. 1683–1692.
55. W. Lee et al., *Nature Mater.*, 5 (2006), pp. 741–747.
56. E. Lichtenberger-Bajza, A. Domony, and P. Csokán, *Werkstoffe. Korros.*, 11 (1960), pp. 701–707.
57. P. Csokán, *Metallüberfläche*, 15 (1961), pp. B49–B53.
58. W. Lee, K. Nielsch, and U. Gösele, *Nanotechnology*, 18 (2007), 475713.
59. K. Schwirn et al., *ACS Nano*, 2 (2008), pp. 302–310.
60. K. Schwirn, "Harte Anodisation von Aluminium mit Verdünnter Schwefeläure" (Ph.D. Dissertation, Martin-Luther-Universität Halle-Wittenberg, 2008).
61. Y. Li et al., *Nanotechnology*, 17 (2006), pp. 5101–5105.
62. W. Lee, J.-C. Kim, and U. Gösele, *Adv. Funct. Mater.*, 20 (2010), pp. 21–27.
63. W. Lee et al., *Nature Nanotech.*, 3 (2008), pp. 234–239.
64. W. Lee, R. Scholz, and U. Gösele, *Nano Lett.*, 8 (2008), pp. 2155–2160.

Woo Lee is principal researcher with the Center for Nanometrology, Korea Research Institute of Standards and Science (KRISS), Yuseong, 305-340 Daejeon (Korea) and is also an associate professor with the Department of Nano Science, University of Science and Technology, 305-333 Daejeon (Korea). Prof. Lee can be reached at +82-42-868-5397; email woolee@kriiss.re.kr.

Energy Technology 2010: Conservation, Carbon Dioxide Reduction and Production from Alternative Sources

N. Neelameggham, R. Reddy, C. Belt, A. Hagni, S. Das, editors



This book covers energy conservation and new technologies needed within the materials field for today's climate of high energy costs and environmental consequences of greenhouse gas emissions. Also included in this book are papers from the second symposium on carbon dioxide reduction metallurgy.

This title includes approaches on carbon dioxide (CO₂) emission reduction in metal production by improved energy efficiency in life cycle fuel use, reductions in carbonate-based flux/raw material usage, as well as finding thermodynamically feasible reactions leading to lower emissions. Also covered are energy saving techniques for extraction and processing of ferrous and nonferrous metals and other materials.

TMS Member price: 104.00 • Non-member price: 144.00 • TMS Student Member price: 79.00

Surface Engineering for Amorphous-, Nanocrystalline-, and Bio-materials

Sandip P. Harimkar, Arvind Agarwal, Sudipta Seal, and Narendra B. Dahotre

Recent developments in the understanding of amorphous and nanostructured materials have established that the disordered atomic arrangement and microstructural features at the nano-scale can play an important role in enhancing the structural and functional properties of materials. While significant progress has been made in the processing of these advanced materials in bulk shapes, there are major issues related to crystallization, undesirable phase transformations, and grain growth during bulk processing of these materials. On the other hand, these materials can be good candidates for engineered surfaces. Surface engineering is rapidly gaining acceptance for synthesizing surfaces (in the form of coatings and modified surfaces) of amorphous-, nanocrystalline-, and bio-materials with outstanding properties. The forefront of this area continues to evolve with exploration of new concepts and methodologies, novel surface processing routes, microstructure analysis, property evaluations, and simulation/modeling. To discuss the developments and opportunities in this area, a symposium titled "Surface Engineering for Amorphous-, Nanocrystalline-, and Bio-materials" was held at the TMS 2010 Annual Meeting. The symposium was comprised of around 40 technical presentations, including eight invited presentations by leading researchers in this field of surface engineering. The symposium also featured an invited presentation by Dr. Clark Cooper, Director of the Materials and Surface Engineering program at National Science Foundation (NSF). His presentation provided the NSF perspective on the needs and opportunities in surface engineering research/education. The surface engineering topic in this *JOM* issue is intended to follow up the discussions at the TMS

2010 Annual Meeting and provide a representative spectrum of current research efforts in the rapidly evolving field of surface engineering. Five papers that represent this spectrum are presented in this issue.

The first paper, "Spark Plasma Sintering for Multi-scale Surface Engineering of Materials" by M. Mulukutla et al., presents an overview of their ongoing efforts on using novel spark plasma sintering (SPS) process for producing engineered coatings of amorphous and nanostructured materials for various applications, including structural, tribological, and biomedical applications. The SPS route is explored for processing coatings of iron-based bulk metallic glasses, nanocrystalline hydroxyapatite, and nanocrystalline alumina.

The second paper, "Electrophoretic Deposition of Hyaluronic Acid and Composite Films for Biomedical Applications" by R. Ma et al. presents detailed investigations of a new electrochemical approach for development of composite coatings containing bioceramics, bioglass, heparin, and salicylate drugs, and bovine serum albumin protein in the hyaluronic acid matrix. The paper highlights the potential applications of electrophoretic deposition for the surface modification of biomedical implants and fabrication of biosensors.

The third paper, "Laser Process Effects on Physical Texture and Wetting in Implantable Ti-Alloys" by S.R. Paital et al. presents an overview of surface engineering techniques based on laser processing of implantable titanium alloys for improved wettability and cell compatibility. The paper discusses three different laser processing techniques, laser interference patterning, continuous wave laser direct melting, and pulsed la-

ser direct melting.

The fourth paper, "Characteristics of Hemocompatible TiO_2 Nano-films Produced by the Sol-gel and Anodic Oxidation Techniques" by C.E. Schvezov et al. presents an overview of two simple techniques for producing TiO_2 nano-films for implants where hemocompatibility properties are required as well as good mechanical and tribological behavior.

The fifth paper, "Effect of Current Density on the Pulsed Co-electrodeposition of Nanocrystalline Nickel-copper Alloys" by M. Agarwal et al. presents an in-depth investigation of the electrochemical synthesis of nanocrystalline Ni-Cu films from citrate baths. Various strategies for controlling the composition and properties of the films are presented.

We would like to thank the participants of our symposium in 2010 for making it a success. We also thank the authors for making excellent contributions to this surface engineering topic. We hope the articles presented here will help the researchers working in the field of surface engineering and possibly trigger thoughts for new developments.

Sandip P. Harimkar, Assistant Professor, is with the School of Mechanical and Aerospace Engineering, Oklahoma State University, Stillwater. He is also the Vice Chair of the Surface Engineering Committee of the TMS Materials Processing & Manufacturing Division (MPMD). Arvind Agarwal, Associate Professor, is with the Mechanical and Materials Engineering department, Florida International University, Miami. He is also the Chair of the Surface Engineering Committee. Sudipta Seal, Professor, is with the Department of Mechanical, Materials, and Aerospace Engineering, Director of Advanced Materials Processing Analysis Center and Nanoscience Technology Center, University of Central Florida, Orlando. Narendra Dahotre, Professor and Chair, is with the Department of Materials Science and Engineering, University of North Texas, Denton. Drs. Harimkar, Agarwal, Seal, and Dahotre are the *JOM* advisors for the Surface Engineering Committee.

Spark Plasma Sintering for Multi-scale Surface Engineering of Materials

Mrinalini Mulukutla, Ashish Singh, and Sandip P. Harimkar

Recently, significant progress has been made in understanding the effect of multi-scale microstructural features, including nano-, micro-, and macro-features, on the properties of materials. Controlling the length scale of microstructural features provides tremendous opportunities for enhancing the properties of materials, including extraordinary strength and hardness, unprecedented damage from tribological contacts, and improvements in a number of functional properties of the materials. Spark plasma sintering (SPS) process which combines the effects of uniaxial pressure and pulsed direct current is becoming increasingly important for the processing of bulk shapes of amorphous and nanostructured materials. These materials can also be good candidates for high-performance coatings. This article presents a review of our ongoing efforts to use SPS to produce engineered coatings of amorphous and nanostructured materials for various applications, including structural, tribological, and biomedical applications.

INTRODUCTION

Recent developments in the understanding of amorphous and nanostructured materials have established that the disordered atomic arrangement and microstructural features at the nanoscale can play an important role in enhancing the structural and functional properties of materials.¹⁻³ One of the challenges facing the current industry is the preparation of such high performance amorphous and nanocrystalline materials for advanced technology. To obtain such high performance materials with the desired phase and/or controlled grain/feature size, one must have accurate control over the processing parameters

used in preparing them. Significant efforts have recently been focused on synthesizing nanostructured materials in bulk useful shapes from starting

amorphous- or nano-powders. Most of the thermal processing approaches such as solidification processing and powder metallurgical techniques (such as hot pressing) tend to induce crystallization in bulk amorphous materials or grain growth of the starting nano-grained material.⁴⁻⁷ On the other hand, these amorphous and nanostructured materials can also be good candidates for high performance coatings.

Various coating technologies, including laser processing,⁸ thermal spraying,⁹ electrodeposition,¹⁰ physical/chemical vapor deposition,¹¹ and cold spraying,¹² have traditionally been used for engineering microstructure and composition at the surfaces of various materials. Many of these technologies have successfully demonstrated improvements in structural and functional properties, including wear resistance, corrosion resistance, biocompatibility, electrical conductivity, etc. While each technology offers some advantages over the other, they are also associated with some distinct disadvantages. Depending on the combination of coating and substrate materials, major disadvantages of the various coating technologies include slow deposition rates, non-uniform coating, weak interfacial bonding (delamination), undesirable phase transformations, porosity, and cracking.¹³ In view of the recent developments in the area of amorphous and nanostructured materials, significant efforts have been made to explore the possibilities of using traditional coating processes for producing surfaces on these advanced materials. While traditional surface engineering techniques have been extensively used for tailoring surface microstructure and composition of conventional materials, the efficient fabrication of fully amor-

How would you...

...describe the overall significance of this paper?

The paper introduces a novel spark plasma sintering technique for surface engineering of amorphous and nanostructured materials for various applications, including structural, tribological, and biomedical applications. The spark plasma sintering offers much better control over the phase and feature size in the coatings compared to conventional surface engineering techniques.

...describe this work to a materials science and engineering professional with no experience in your technical specialty?

The disordered atomic arrangement and microstructural features at nanoscale or the surface play an important role in enhancing the structural and functional properties of materials. However, retention of such features at the surface during conventional surface engineering is difficult due to thermally activated phase transformations and grain growth. The spark plasma sintering introduced in this paper allows the synthesis of such multi-scale coatings by combining the effects of pulse electric current and uniaxial pressure.

...describe this work to a layperson?

Amorphous and nanocrystalline materials are new materials with outstanding properties compared to conventional materials, which are mostly micro-crystalline. In this paper, we present a novel method to fabricate these materials in the form of coatings to achieve desired properties for structural, tribological, and biomedical applications.

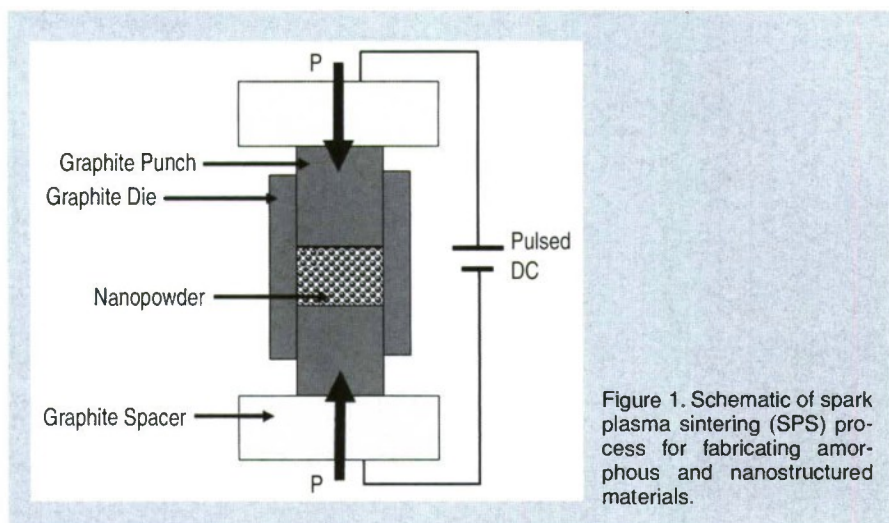


Figure 1. Schematic of spark plasma sintering (SPS) process for fabricating amorphous and nanostructured materials.

phous and nano-structured coatings has always been a challenge. For example, several efforts have been made in the past to fabricate amorphous coatings on crystalline substrates using various processes such as laser surface cladding¹⁴⁻¹⁷ and high velocity oxy-fuel coating/thermal spraying.^{18,19} Yue et al. reported laser cladding of Zr-based amorphous coating on magnesium alloy for structural applications.²⁰ The laser cladding resulted in the formation of crystalline phases in the amorphous matrix of the coating. Wong et al. also observed the formation of crystalline phases in Ni-Cr-B-Si coating laser clad on Al-Si alloy.²¹ Basu et al. also attempted laser cladding of the Fe-based amorphous coatings on steel substrates and observed formation of intermetallic phases in the coating.²² While laser surface cladding provides very high cooling rates (up to 10^6 K/s), most of these approaches have had limited success in retaining fully amorphous structure in the coatings. This can be primarily attributed to the dilution of the melt pool from the underlying substrate partially melted during laser processing. The rapid cooling rate associated with laser melting/cladding often results in refined dendritic microstructure. The formation of matrix grains with a size in the range of 100–200 nm is difficult with the achievable cooling rates in laser processing. However, laser processing can be used to fabricate the nanocomposite coatings by injecting nanoparticles into the laser melted pool.²³ While cold spraying techniques have been successfully used to fabricate structural amorphous coatings, the process is likely to be limited for the

coating of soft substrates due to efficient embedment of amorphous particles in these materials.²⁴ Electrodeposition techniques also present significant potential for fabricating amorphous, nanocrystalline, and nanocomposite coatings.²⁵ However, it is very difficult to fabricate thick coatings with uniform microstructure/texture/phase across the thickness. The process is also limited to only certain compositions of amorphous/nanocrystalline alloys (generally Ni-based alloys) depending on

the substrate materials. Thus, there is a tremendous drive to develop flexible processes that allow rapid fabrication of amorphous/nanostructured coatings of controlled thickness on a variety of substrates.

SPARK PLASMA SINTERING FOR SURFACE ENGINEERING

Spark plasma sintering (SPS) is rapidly emerging as a robust process for fabricating bulk shapes of amorphous and nanostructured materials. Spark plasma sintering is a novel powder consolidation technique rendering significant advantages to the processing of amorphous and nanocrystalline materials into configurations which were previously unattainable (Figure 1). The process involves application of uniaxial pressure and pulsed direct current to sinter the materials at a relatively lower temperature and within relatively short time compared to conventional hot pressing. Due to shorter processing times, the SPS process offers enormous possibilities of sintering highly dense nanocrystalline materials

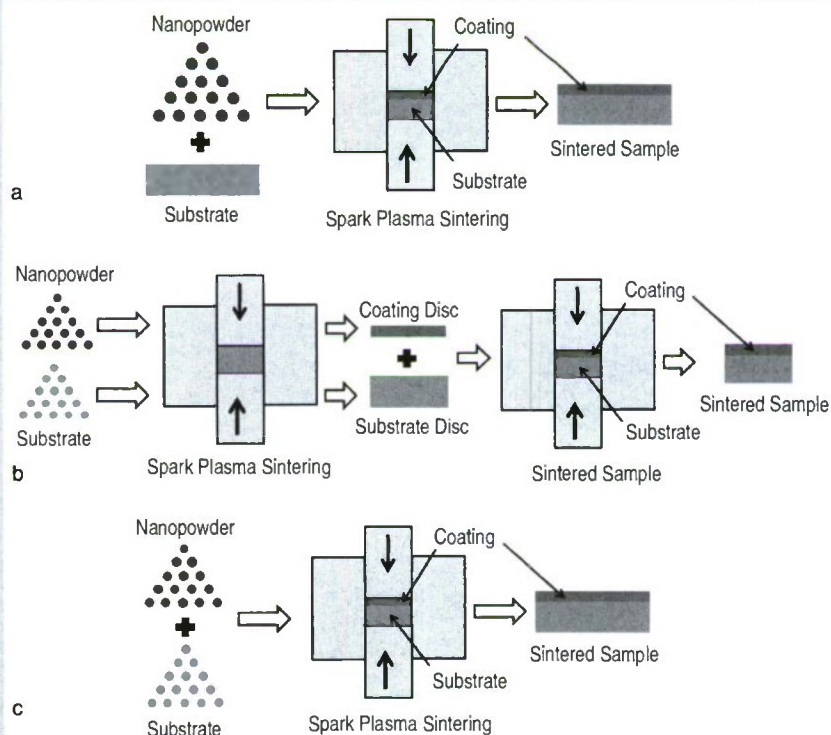
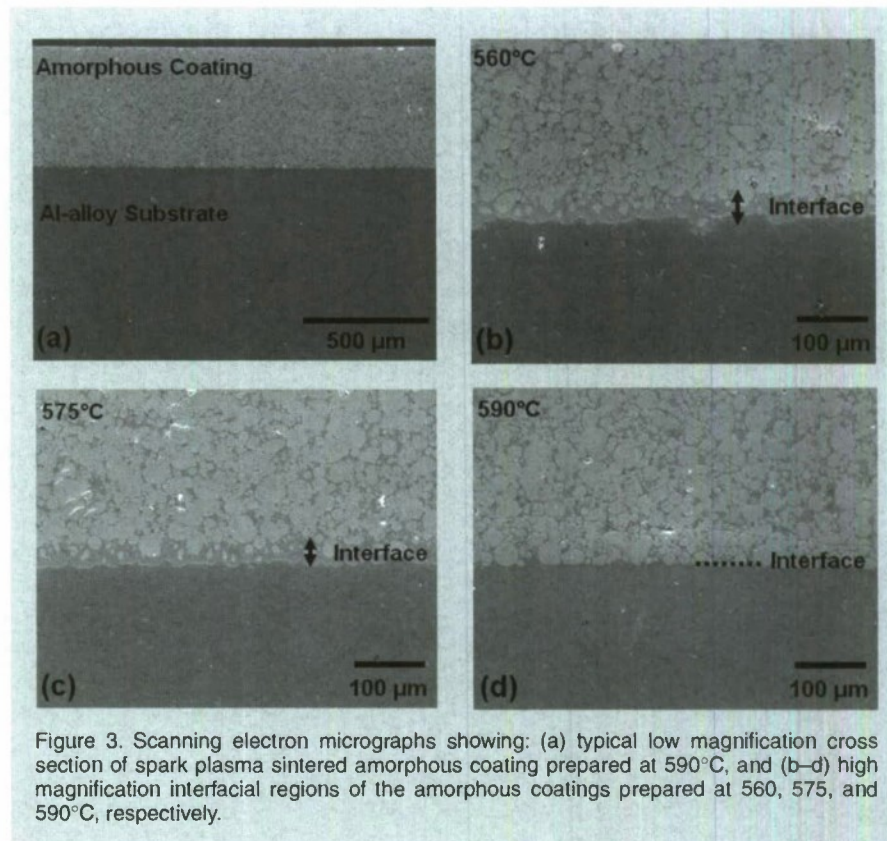


Figure 2. Various approaches for processing coatings using spark plasma sintering: (a) sintering of coating by directly loading powder of coating material on substrate disc; (b) fabrication of coatings by sintering coating and substrate discs separately followed by subsequent SPS sintering together; (c) fabrication of coating by sintering layers of substrate and coating powder.

without significant grain growth. Furthermore, sintering at relatively lower temperature allows the fabrication of amorphous phases without undesirable phase transformations (crystallization). In view of the attractive advantages of the SPS process, significant interests are now directed toward understanding the exact mechanisms of SPS. Joule heating is widely considered as a general mechanism during SPS.^{26–28} However, mechanisms involving formation of plasma between the particles are often suggested. Employing atomic emission spectroscopy, direct visual observation, and ultrafast in situ voltage measurement, a recent investigation has indicated that there is no plasma or sparking during the SPS process.²⁹ While exact mechanisms during SPS are still being debated, researchers are extending the unchallenging capabilities of the process for the fabrication of novel compositions and microstructures. Advanced materials such as nanocrystalline metals/alloys, nanoceramics, bulk metallic glasses, intermetallics, nanocomposites, and functionally graded materials have been successfully sintered to high density using SPS.³⁰

Spark plasma sintering also presents enormous possibilities for the processing of high performance coatings. Recently, spark plasma sintering has been used to produce Fe₃Al intermetallic coating on austenitic stainless steel for improving its wear and oxidation resistances.³¹ It was observed that reaction layers were formed at the interface of substrate and coating. The intermetallic coated samples exhibited marked improvement in high temperature oxidation resistance. Also, spark plasma sintering has been used to fabricate NiCoCrAlYTa coatings on nickel-based superalloy substrate.³² The prepared coatings were found to be dense and homogeneous with good adherence high strength interface. The presence of different phases like gamma (face-centered cubic Ni), gamma prime (Ni₃Al) and beta (NiAl) was observed. Spark plasma sintering has also been used by many researchers as a post spray treatment in order to make the coating more adherent, homogeneous, and dense. Thermally sprayed coatings are mostly porous which is beneficial at times and sometimes degrades the



performance of the coating. To densify these coatings, many techniques like heat treatments, laser treatments, and hot isostatic sintering have been used. Each of these techniques has its own disadvantages. For example, laser treatments produce many micro-cracks, and hot isostatic pressing takes a longer time which might lead to the generation of many new undesirable phases which affect the performance of the coatings. Prawara et al. have investigated post treatment of thermally sprayed ZrO₂-25 wt.% MgO coatings using spark plasma sintering.³³ It was observed that the SPS post-treated samples exhibited enhanced inter-lamellar contact and increased density compared to as-sprayed coatings.

Li et al. have also reported on using SPS technique as post spray treatment for plasma sprayed WC-Co coatings to compensate for the carbon lost during the thermal spray process.³⁴ Complete WC restoration at the coating surface was reported to be achieved by the SPS induced phase transformation. It has also improved the hardness of the sample surface. SPS has also been used for the fabrication of thin films on flexible metallic substrates for specific applications like semiconductors to improve the superconducting properties of the

films. In this context, YBCO superconducting films have been fabricated on copper substrates.³⁵ These films were found to possess improved superconducting properties with lower film porosity and higher crack density.

The simultaneous application of pressure and pulse current during spark plasma sintering also allows sintering of amorphous/nanocrystalline/nanocomposite powder on a variety of substrates without undesirable effects such as phase transformation/crystallization or grain growth. A schematic showing three possible approaches to processing of multi-scale coatings using SPS is presented in Figure 2. In approach 1, the powder to be coated is directly loaded on the substrate placed in a die followed by sintering between punches. In this approach, it is extremely important to select appropriate SPS temperature and pressure to prevent the plastic or liquid flow of substrate materials into the overlaid amorphous/nanostructured powder during sintering. In approach 2, coating material of required thickness is sintered separately as a disc. The disc is then fused with the substrate material using SPS. This approach is expected to result in a sharp coating/substrate interface due to high density of the starting discs. In

approach 3, powders of substrate and coating are sequentially loaded in the die followed by sintering of layered powders. This approach may lead to significant intermixing of the coating and substrate materials depending on the powder characteristics. The dies and punches used in SPS are often made of graphite for processing with low pressure (<100 MPa) and temperature up to 1,800°C. However, tungsten carbide dies and punches can be used for higher pressure (>100 MPa) up to 900°C. Depending on the material and processing temperature, inert gases or high vacuum may be needed to avoid undesirable reactions involving coating, substrate, and die/punch materials. Temperature dur-

ing SPS is often measured using thermocouple inserted in the die wall/punch (temperature < 1,200°C) or pyrometer (temperature > 1,200°C). Depending on the dimensions of the die/punch assembly, the temperature difference from the inside to outside surface of the die may be as high as 100°C. Hence, SPS processing parameters need to be carefully selected taking into consideration coating/substrate material properties and configuration of die/punches.

In the following sections, we present the results of our ongoing research on using spark plasma sintering for producing amorphous and nanostructured coatings for various applications, including structural, tribological, and

biomedical applications. The coatings were fabricated on metallic substrates by loading powder on the substrate discs before SPS processing (approach 1). Different coatings which were prepared using SPS include: iron-based amorphous coatings on aluminum alloy substrate; nanocrystalline alumina ceramic coatings on titanium substrate; nano hydroxyapatite (HA) coatings on titanium substrate; and nano HA + yttria-stabilized zirconia (YSZ) composite coatings on titanium substrate. The substrates used to deposit coatings were in the form of discs of ~20 mm diameter and ~5 mm thickness. A measured amount of coating material powder (amorphous, nano-alumina, nano-HA, or HA+YSZ composite powder) was loaded on the top surface of the substrate placed inside the graphite die followed by SPS sintering between graphite punches (approach 1). Commercially available SPS equipment (Model: 10-3; Thermal Technology, Santa Rosa, CA) was used for fabricating amorphous and nanostructured coatings on aluminum or titanium substrates. The schematic of SPS tooling which is used for making coatings is shown in Figure 1.

Spark Plasma Sintering of Amorphous Coatings

Amorphous coatings were prepared using starting amorphous powder of nominal composition $\text{Fe}_{48}\text{Cr}_{15}\text{Mo}_{14}\text{Y}_2\text{C}_{15}\text{B}_6$ with particle size in the range of 10–20 μm . The amorphous powder exhibited a distinct glass transition temperature (T_g) at 575°C followed by double exothermic crystallization (T_{x1} and T_{x2}) peaks above 600°C. The amorphous coatings were prepared on aluminum alloy substrate using spark plasma sintering at a uniaxial pressure of 50 MPa at three different temperatures (560, 575, and 590°C) well below the crystallization temperature of the given Fe-based amorphous alloy. A typical processing cycle consisted of three steps: rapid heating cycle with a rate of 100°C/min., holding for 15 min. at the processing temperature, and rapid cooling using nitrogen purging (cooling rate ~ 150°C/min.).

The typical microstructures of the cross section of the amorphous coatings prepared by spark plasma sintering are presented in Figure 3. The figure indi-

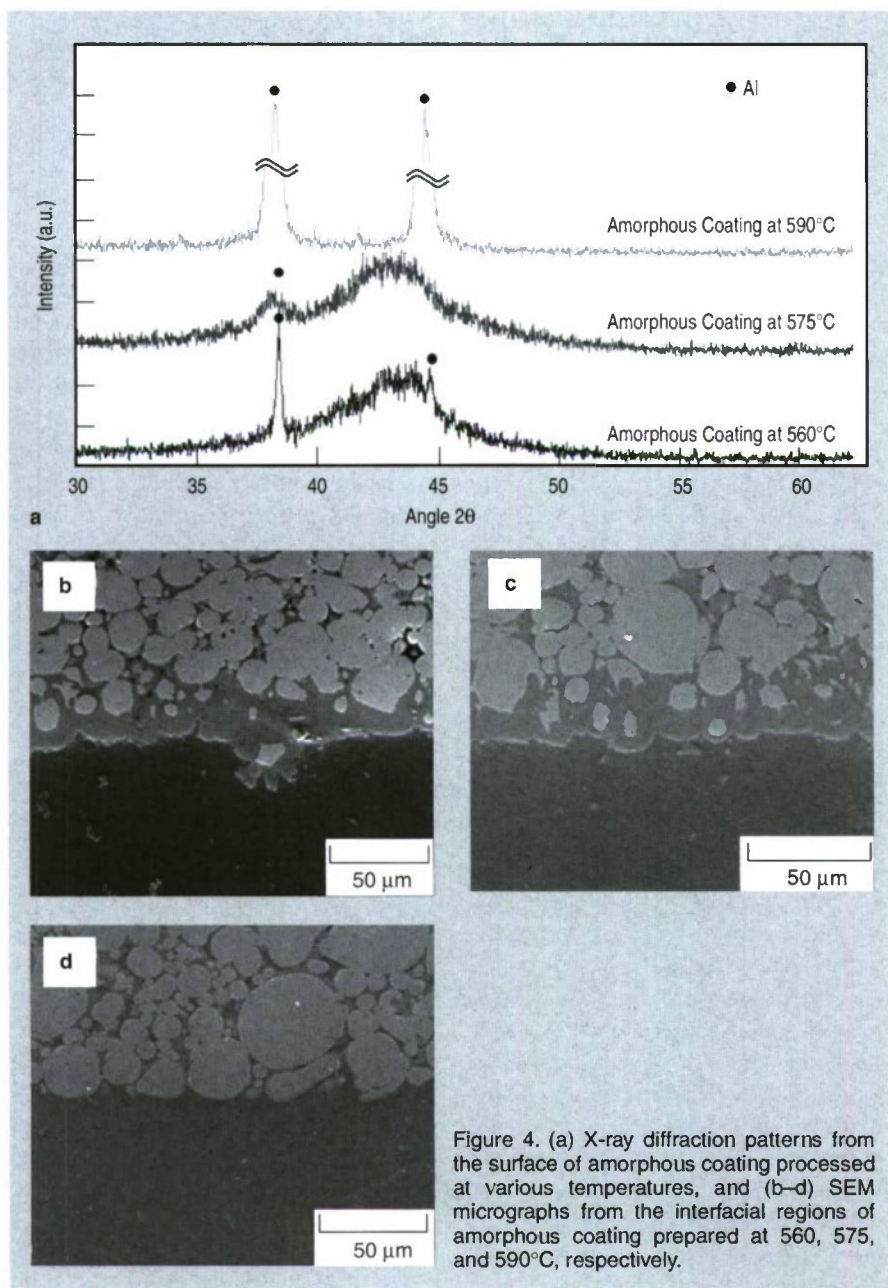
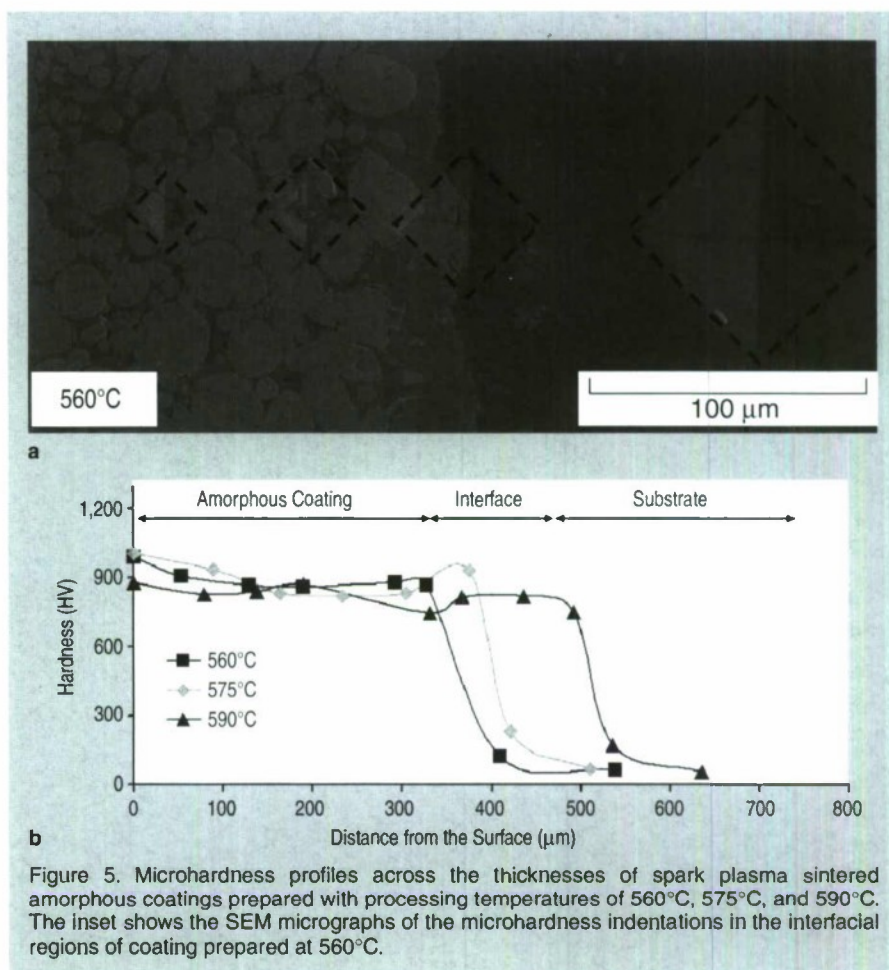


Figure 4. (a) X-ray diffraction patterns from the surface of amorphous coating processed at various temperatures, and (b–d) SEM micrographs from the interfacial regions of amorphous coating prepared at 560, 575, and 590°C, respectively.

cates that the coatings prepared at various processing temperatures (560, 575, and 590°C) are fully dense and exhibit very good bonding with the underlying aluminum substrates, as indicated by the absence of porosities at the interface. The average thickness of the coatings was around 400 μm . Figure 4a presents x-ray diffraction (XRD) patterns from the surface of sintered coatings prepared at 560, 575, and 590°C. The XRD patterns exhibit a broad peak corresponding to Fe-based amorphous alloy superimposed with crystalline peaks corresponding to aluminum alloy. The aluminum peaks in the case of 590°C are more intense when compared to aluminum peaks in cases of 560°C and 575°C. The presence of aluminum peaks in the XRD patterns indicate that the substrate has infiltrated into the amorphous coatings resulting in the formation of amorphous composite coating. The infiltration effects are more intense at higher processing temperature (590°C). The high magnification micrographs of the interface regions of the coatings prepared at various temperatures are presented in Figure 4b–d. The coatings prepared at lower temperatures (560 and 575°C) show a distinct interdiffusion layer about 25 μm thick along the interface. The smaller amorphous particles distributed within the interdiffusion layer can be easily seen. Surprisingly, the coatings prepared at higher temperature (590°C) don't show distinct interdiffusion layer at the interface. However, individual large particles near the interface show very thin ($\sim 1\text{--}2\ \mu\text{m}$) reaction layer on the particle surface (as indicated by lighter contrast). It seems that at higher temperature plastic deformation/flow assisted infiltration of aluminum into the overlaid amorphous powder is dominant. This enhanced flow of aluminum from surrounding amorphous particles prevents the build-up of the interdiffusion layer at the interface. The observation of aluminum as a major phase at the surface of the coatings prepared at 590°C is indicative of this enhanced infiltration effects (as indicated by XRD analysis).

Figure 5 presents the microhardness distribution along the depth of amorphous coatings prepared at various temperatures. The average hardness of the coatings prepared at 560, 575, and



590°C were 990, 1,007, and 880 HV, respectively. The higher surface hardness ($\sim 1,000$ HV) of the coatings prepared at lower temperatures (560 and 575°C) seems to be primarily due to presence of larger fraction of amorphous phase at the surface. The relatively lower surface hardness (880 HV) of the coatings prepared at higher temperature (590°C) is primarily due to presence of larger fraction of soft aluminum phase in the coating due to these enhanced infiltration effects. The high microhardness (800–1,000 HV) was retained along the 400 μm thickness of amorphous coatings followed by steep decrease at the interface region towards substrate. This trend is clearly indicated by the variation of indentation size across the interface (inset of Figure 5). In our previous investigation, we observed that the microhardness of SPS sintered fully amorphous/partially crystallized amorphous alloys was in the range of 1,200–1,350 HV.^{36,37} The relatively lower hardness (880–1,007 HV) of the amorphous coatings in the present investigation is primarily due to infiltration of aluminum substrate material in the overlaid amor-

phous powder bed. The coatings thus exhibit composite amorphous-crystalline microstructure, the crystalline phase being the infiltrated aluminum substrate material. However, no devitrification of the amorphous powder was observed. The surface hardness of the amorphous coatings is almost 10 times the hardness of the substrate aluminum material.

Spark Plasma Sintering of Nanoceramic Coatings

We have also attempted to use SPS for preparing nanoceramic coatings on titanium substrates using starting nanocrystalline alumina powder (particle size: 30–60 nm). The nanoceramic coatings were prepared at two different processing temperatures (1,250 and 1,375°C) with a pressure of 40 MPa and sintering time of 10 minutes. The nano alumina coatings exhibited very good bonding with the titanium substrate. The SEM micrographs from the polished surfaces of the coatings prepared at 1,250 and 1,375°C are presented in Figure 6. The surface microstructure consisted of ultrafine grains with some porosity. The XRD patterns from the surfaces

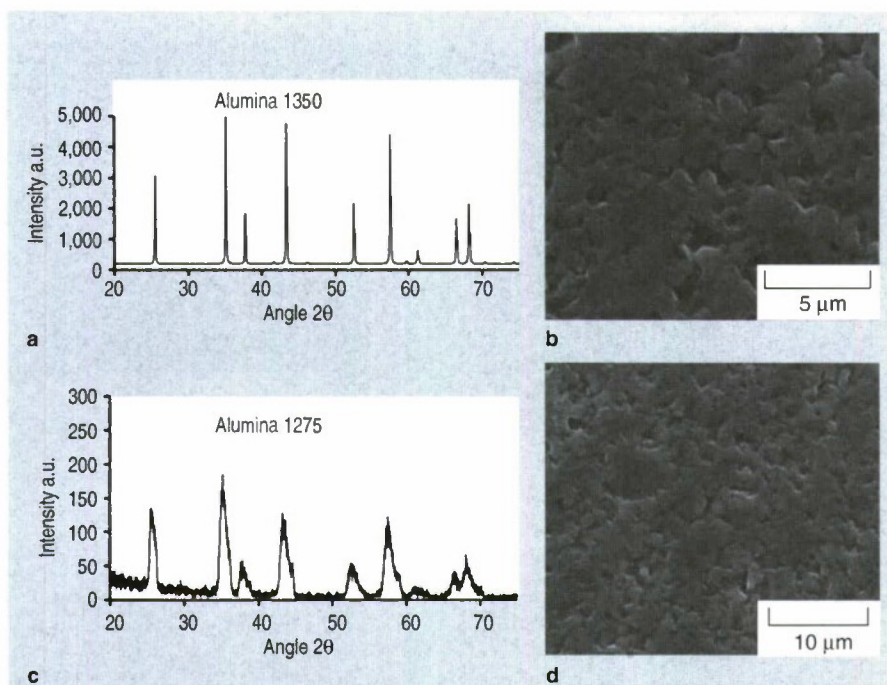


Figure 6. (a, b) X-ray diffraction pattern and SEM micrograph from the surface of alumina coating sintered on titanium substrate at 1,350°C, and (c, d) XRD pattern and SEM micrograph from the surface of alumina coating sintered on titanium substrate at 1,275°C.

of nano-alumina coatings are also presented in Figure 6. The XRD peaks corresponding to coatings prepared at 1,250°C are significantly broader than those corresponding to coatings prepared at 1,375°C. This indicates the increase in crystallite size with increasing SPS processing temperature. The nano alumina coatings prepared at 1,250 and 1,375°C showed average microhardness of 2,250 HV (~22 GPa) and 1,630 HV (~16 GPa), respectively. This decrease in the hardness with increasing SPS processing temperature seems to be a direct consequence of grain growth at higher SPS temperature (1,375°C). Thus, nanoceramic coatings with high hardness have been successfully processed using SPS. The microstructure and properties of the coatings are greatly influenced by SPS processing parameters such as temperature. Such nanoceramic coatings are expected to find wide applications where protections against wear, corrosion, or temperature are important.

Spark Plasma Sintering of Hydroxyapatite-based Nanocomposite Coatings

Recently, considerable research efforts have been directed towards the use of bioceramics as implant materials due to their excellent biocompatibility.^{38–40} HA ($\text{Ca}_{10}(\text{PO}_4)_6(\text{OH})_2$) con-

stitutes some 70% of the bone matrix and exists in the form of nanocrystallites (~20–80 nm long, 2–5 nm thick). Furthermore, bone extra cellular matrix (ECM) is also composed of nanometric protein components.⁴¹ Such nanostructured bone structure greatly influences the adhesion, proliferation and differentiation of mesenchymal stem cells, osteoblasts, osteoclasts, and fibroblasts.⁴² Thus mimicking the nanostructure of the bone in the artificial implants is expected to improve the bone cell functions. Thus, nano-HA not only represents compositional similarity but also dimensional similarity (and corresponding properties, such as topography, chemistry, wettability, and surface energy). Recent studies have indicated that nanostructured HA show

significantly greater osteoblast adhesion compared to conventional microstructured materials.⁴³ Such enhanced adhesion of osteoblast is reported to be due to increased adsorption of vitronectin on nanophase HA. The grain size and porosity of such nanophase HA is particularly important for the adhesion of osteoblasts. Thus, tailored nanophase HA can elicit specific desirable response from surrounding cells and tissues, and can be used as proactive biomaterials for improved implant life. Hence, some efforts have been made to explore the possibilities of using SPS for producing nano-HA based coatings (nano-HA and nano-HA+ 40 wt.% YSZ) on titanium substrates. The nano-HA coatings were synthesized using starting nanopowder (particle size: ~100 nm) with a SPS processing temperature of 1,000°C, a pressure of 35 MPa, and sintering time of 10 minutes. For preparing composite coatings, nano-HA and YSZ powder were mixed by ball milling for about an hour followed by SPS processing on a titanium substrate at a temperature of 1,150°C, pressure of 35 MPa, and sintering time of 10 minutes. The coatings exhibited very good bonding with the substrates and homogeneous surface microstructure. The broad peaks in the XRD pattern indicate that nanocrystalline HA structure were retained in the coatings prepared by SPS (Figure 7). The coating microstructure also shows some micro-porosity. Such microporosity on the implant is expected to improve the adhesion of bone cells. The x-ray diffraction analysis of the composite coatings indicated tetragonal zirconia and hydroxyapatite as major phases in the coating (Figure 8). No phase change

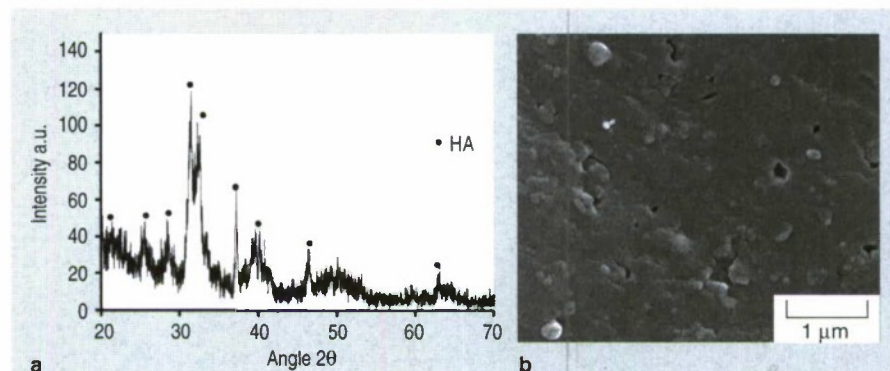


Figure 7. (a) X-ray diffraction pattern, and (b) SEM micrograph from the surface of nano HA coating sintered on titanium substrate at 1,000°C.

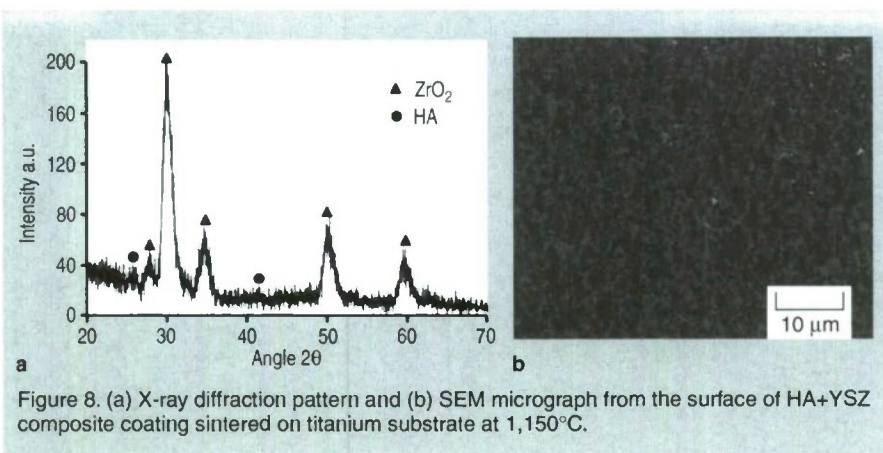


Figure 8. (a) X-ray diffraction pattern and (b) SEM micrograph from the surface of HA+YSZ composite coating sintered on titanium substrate at 1,150°C.

associated with HA in the composite coating was observed. The studies clearly showed very good interfacial adhesion between the composite coating and the substrate. The HA+YSZ composite coating exhibited improved hardness (530 ± 25 HV) compared to nano HA coating (420 ± 25 HV). While the coating exhibited very good bonding with the titanium substrates, some surface cracking was observed. Significant efforts are underway to characterize the properties (mechanical and biocompatibility) of these nano-HA based biocoatings prepared by SPS.

CONCLUSION

Various coatings including iron-based amorphous coating on aluminum alloy substrate, alumina nanocoating on titanium substrate, and hydroxyapatite based coatings (nano HA and nano HA+YSZ composite) on titanium substrate, have been successfully fabricated using SPS. The SPS process offers tremendous control over the phase and grain size of the coatings. The process can be effectively used to fabricate coatings over a range of thickness (few micrometers as in the case of HA coatings to few hundred micrometers as in case of amorphous coatings). Spark plasma sintering processed coatings exhibited homogeneous microstructure and stronger bonding with the substrates. The SPS process offers significant opportunities for fabricating engineered multi-scale coatings for various applications including structural, tribological, and biomedical applications. However, to realize the widespread use of SPS as a surface engineering technique, significant challenges need to be addressed. Some of these are:

- Current SPS technologies are ca-

pable of coating only small parts (<50 mm diameter) depending on the diameter of the die and type of materials being processed. Significant efforts need to be directed to develop the capabilities for coating parts of all sizes and complex shapes. Machine manufacturers are currently in the process of developing SPS machines with pressing capabilities of 200–250 tons and current capabilities of 40,000–60,000 A. These developments are expected to allow coating of samples up to 350 mm in diameter.

- Spark plasma sintering processing temperature should be less than transformation/melting temperature of the substrates to prevent undesirable phase transformations. While SPS allows sintering of the coating material at significantly lower temperature, this requirement limits the combination of coating and substrate materials that can be processed. The SPS seems to be more attractive for the one-step processing of net shaped coated parts than large area processing of coatings.

References

1. M. Miller and P. Liaw, editors, *Bulk Metallic Glasses* (New York: Springer, 2008).
2. H. Gleiter, *Nanostruct. Mater.*, 6 (1-4) (1995), pp. 3–14.
3. H. Gleiter, *Acta Mater.*, 48 (1) (2000), pp. 1–29.
4. W.L. Johnson, *Mater. Sci. Forum*, 225-227 (1996), pp. 35–50.
5. P.Y. Li et al., *Mater. Sci. Eng. A*, 449-451 (2007), pp. 1095–1098.
6. A.S. Edelstein and R.C. Cammarata, *Nanomaterials: Synthesis, Properties and Applications* (New York: Taylor and Francis, 1996).
7. J.R. Groza and R.J. Dowling, *Nanostruct. Mater.*, 7 (7) (1996), pp. 749–768.
8. N.B. Dahotre and S.P. Harimkar, *Laser Fabrication and Machining of Materials* (New York: Springer,

- 2007).
9. K. Balani et al., *Acta Mater.*, 20 (2008), pp. 5984–5994.
10. J.W. Dini, *Electrodeposition: The Materials Science of Coatings and Substrates* (Norwich, NY: Noyes Publication, 1993).
11. L.A. Dobrzanski et al., *J. Mater. Process. Technol.*, 175 (1-3) (2006), pp. 179–185.
12. T. Stollenhoff et al., *J. Therm. Spray Technol.*, 11 (4) (2002), pp. 542–550.
13. T. Burakowski and T. Wierzbach, *Surface Engineering of Metals: Principles, Equipment, Technologies* (Boca Raton, FL: CRC Press, 1999).
14. Q. Zhu et al., *Appl. Surf. Sci.*, 253 (2007), pp. 7060–7064.
15. I. Manna et al., *Surf. Coat. Technol.*, 201 (2006), pp. 434–440.
16. X. Wu and Y. Hong, *Surf. Coat. Technol.*, 141 (2001), pp. 141–144.
17. X. Wu et al., *Mater. Lett.*, 56 (2002), pp. 838–841.
18. J.C. Farmer et al., *J. Mater. Res.*, 22 (2007), pp. 2297–2311.
19. T. Parker et al., *Mater. Lett.*, 48 (2001), pp. 184–187.
20. T.M. Yue et al., *Mater. Lett.*, 61 (2007), pp. 209–212.
21. T.T. Wong and G.Y. Liang, *Mater. Charact.*, 38 (1997), pp. 85–89.
22. A. Basu et al., *Surf. Coat. Technol.*, 202 (2008), pp. 2623–2631.
23. L. Mingxi et al., *Appl. Surf. Sci.*, 252 (8) (2006), pp. 2882–2887.
24. L. Ajdelsztajn et al., *J. Therm. Spray Technol.*, 15 (4) (2006), pp. 495–500.
25. I. Gurrappal and L. Binder, *Sci. Technol. Adv. Mater.*, 9 (2008), 043001.
26. K.A. Khor et al., *Mater. Sci. Eng. A*, 356 (2003), pp. 130–135.
27. M. Omori, *Mater. Sci. Eng. A*, 287 (2000), pp. 183–188.
28. S.W. Wang et al., *Mater. Res. Bull.*, 35 (2000), pp. 619–628.
29. D.M. Hulbert et al., *Scripta Mater.*, 60 (2009), pp. 835–838.
30. R. Orru et al., *Mater. Sci. Eng. R*, 63 (2009), pp. 127–287.
31. A. Nishimoto and K. Akamatsu, *Plasma Processes Polym.*, 6 (2009), pp. S941–S943.
32. D. Oquab et al., *Adv. Eng. Mater.*, 9 (5) (2007), pp. 413–417.
33. B. Prawara et al., *Surf. Coat. Technol.*, 162 (2003), pp. 234–241.
34. H. Li et al., *Surf. Coat. Technol.*, 194 (2005), pp. 96–102.
35. Y. Kim et al., *J. Electron. Mater.*, 36 (10) (2007), pp. 1252–1257.
36. S.P. Harimkar et al., *J. Non-Cryst. Solids*, 355 (2009), pp. 2179–2182.
37. A. Singh and S.P. Harimkar, *J. Alloys Compd.*, 2010 (in press).
38. L.L. Hench, *J. Am. Ceramic Soc.*, 74(7) (1991), p. 1487.
39. S.M. Best et al., *J. Eur. Ceram. Soc.*, 28 (7) (2008), p. 1319.
40. A. El-Ghannam, *Expet. Rev. Med. Dev.*, 2 (1) (2005), pp. 87–101.
41. F.S. Kaplan et al., *Orthopedic Basic Science*, AAOS, ed. S.R. Simon, 7 (1994), pp. 127–184.
42. L. Zhang and T.J. Webster, *Nanotoday*, 4 (1) (2009), pp. 66–80.
43. T.J. Webster et al., *J. Biomed. Mater. Res.*, 51 (2000), pp. 475–483.

Mrinalini Mulukutla and Ashish Singh, research assistants, and Sandip P. Harimkar, assistant professor, are with the School of Mechanical and Aerospace Engineering, Oklahoma State University, Stillwater, OK 74078. Dr. Harimkar can be reached at (405) 744-5900; fax (405) 744-7873; e-mail sandip.harimkar@okstate.edu.

Electrophoretic Deposition of Hyaluronic Acid and Composite Films for Biomedical Applications

R. Ma, Y. Li, and I. Zhitomirsky

Hyaluronic acid (HYH) is a natural biopolymer, which has tremendous potential for various biomedical applications. Electrophoretic deposition (EPD) methods have been developed for the fabrication of HYH films and composites. New methods for the immobilization of drugs and proteins have been utilized for the fabrication of organic composites. Electrophoretic deposition enabled the fabrication of organic-inorganic composites containing bioceramics and bioglass in the HYH matrix. It was shown that the deposition yield, microstructure, and composition of the films can be controlled. Potential applications of EPD for the surface modification of biomedical implants and fabrication of biosensors are highlighted.

INTRODUCTION

New electrochemical methods have attracted increasing attention for the surface modification of biomedical implants. Electrochemical deposition of thin films and coatings offers the advantages of simple and low cost equipment, high purity of the deposited materials and the possibility of deposition on substrates of complex shape. Many investigations were focused on electrophoretic deposition (EPD) of hydroxyapatite (HA) and other bioceramics on metallic substrates.¹⁻³ Hydroxyapatite is an important material for biomedical implants, as its chemical composition is similar to that of the mineral phase of bone tissue. A complicating factor in the fabrication of ceramic films by EPD is sintering shrinkage, which usually results in deposit cracking. Moreover, it is important to avoid decomposition of HA and degradation of substrates during sintering at elevated temperatures. These problems can be addressed by

the development of composite films.

The combination of polymeric and

inorganic phases is a common feature of various natural materials, including bone, which can be considered as a composite, comprising collagen and HA crystals. Recently it was discovered that polysaccharides form interfaces between organic and inorganic components in bones and govern the crystallization of HA nanoparticles.⁴ This discovery has generated a new wave of interest in the fabrication of bone substitute materials containing natural polysaccharides. Moreover, polysaccharides are becoming increasingly important for the surface modification of biomedical implants.

Hyaluronic acid (HYH) is a naturally occurring anionic polysaccharide consisting of alternating units of glucuronic acid and N-acetylglucosamine.⁵ HYH presents at high concentrations in skin, joints and cornea.⁶ HYH is a bioactive material that has been associated with several cellular processes, including angiogenesis and the regulation of inflammation.⁷ In living tissue HYH usually combines with proteins to control various functions of the tissue.⁸ HYH coatings formed on surfaces of various implant materials provided improved biocompatibility and gliding resistance, reduced platelet adhesion and promoted new bone formation.⁹⁻¹² HYH has been utilized for the fabrication of drug eluting coatings for cardiovascular stents.¹³

Recent studies showed the feasibility of electrodeposition of HYH and composite HYH-HA films.^{14,15} The method offers the advantages of room temperature processing and paves the way for the fabrication of novel composite coatings containing other functional materials. The goal of this investigation was the development of electrochemical strategies for the EPD of composite

How would you...

...describe the overall significance of this paper?

The electrophoretic deposition method has been developed for the fabrication of nanocomposite coatings for biomedical applications. The nanocomposites contained advanced functional materials, such as bioceramics, bioglass, proteins and drugs in a biopolymer matrix. The method can be used for the fabrication of biomedical implants and biosensors.

...describe this work to a materials science and engineering professional with no experience in your technical specialty?

The feasibility of electrophoretic deposition of composites based on hyaluronic acid has been demonstrated. New electrochemical strategies have been developed for co-deposition of hyaluronic acid with bone-substitute materials, such as hydroxyapatite, and bioactive materials such as bioglass and bioceramics. It was shown that the method can be used for the fabrication of nanocomposite coatings containing proteins and drugs.

...describe this work to a layperson?

Hyaluronic acid is a natural biopolymer, which presents at high concentrations in skin, joints and cornea. Hydroxyapatite is an important material for biomedical implants, as its chemical composition is similar to that of the mineral phase of bone tissue. Bioglass and bioceramic glasses are materials which react with physiological fluids, forming hydroxyapatite layers on their surface. In this work biocomposite materials were obtained, containing hydroxyapatite, bioglass, bioactive ceramics, proteins and drugs in a hyaluronic acid matrix.

coatings containing other bioceramics, bioglass, heparin and salicylate drugs, and bovine serum albumin (BSA) protein in the HYH matrix.

See the sidebar for details on the electrodeposition of HYH films.

COMPOSITE MATERIALS CONTAINING DRUGS AND BSA PROTEIN

In this investigation heparin and salicylate were utilized as model drugs¹⁷⁻¹⁹ for the fabrication of composite films by EPD. Heparin is widely used as an anticoagulant drug¹⁷ due to its ability to accelerate the rate at which antithrombin inhibits serine proteases in the blood coagulation cascade, especially thrombin. However, the performance of heparin may vary significantly depending on many factors, such as the method of immobilization and the amount of heparin. Salicylate is a commonly used non-steroidal anti-inflammatory drug.²⁰ Significant interest has been generated in the development of composite materials with controlled release of heparin and salicylate, which were immobilized in the polymer matrix.^{17-19,21}

Heparin and salicylate are negatively charged in aqueous solutions. Therefore, anodic EPD has been utilized for the fabrication of composite films containing heparin and salicylate in a HYH matrix. Composite films were prepared from 0.5–3 gL⁻¹ HYNa solutions containing 0.5–2 gL⁻¹ heparin or salicylate. Figure Ab and c shows typical cross sections of the composite films prepared from aqueous solutions. The films were relatively dense and adhered well to stainless steel, platinum, titanium and graphite substrates. The SEM studies of the HYH-heparin and HYH-salicylate films prepared at different experimental conditions indicated that film thickness can be varied in the range of 0–20 µm by the variation of deposition time in the range of 0–10 min, and electric field in the range of 3–10 Vcm⁻¹.

BSA has been utilized as a model protein for the development of electrochemical methods for the incorporation of proteins into the HYH matrix. It should be noted that BSA contains cationic and anionic groups. The total charge of BSA depends on pH and

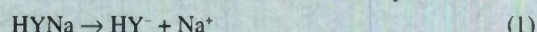
represents the sum of charges of all ionisable groups. It is known that BSA exhibits an isoelectric point²² at pH 5 and it is negatively charged at physiological pH. Electric field provided electrophoretic motion of anionic BSA in aqueous solutions at pH 7.4 towards the anode and resulted in accumulation of the BSA macromolecules at the anode surface. However, no anodic deposition was observed. This can be attributed to the pH decrease at the anode due to Reaction 2 and reversal of the BSA charge from negative to positive upon passing through the isoelectric point at the anode surface. It is suggested that

the charge reversal resulted in BSA-electrode electrostatic repulsion, which prevented film formation. However, composite films were obtained from the 0.5–3 gL⁻¹ HYNa solutions containing 0.1–1.7 gL⁻¹ BSA.

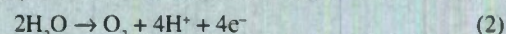
Deposition experiments performed from 3 gL⁻¹ HYNa solutions at electric field of 12 Vcm⁻¹ showed that the deposition rate of pure HYH was 0.15 mgcm⁻²min⁻¹. However, the deposition yield increased drastically after the addition of BSA to the HYNa solutions. The increase in BSA concentration from 0 to 1.7 gL⁻¹ in the 3 gL⁻¹ HYNa solutions resulted in increas-

ELECTRODEPOSITION OF HYH FILMS

Electrophoretic deposition of HYH was performed from sodium hyaluronate (HYNa) solutions in water or mixed ethanol-water solvent. It was suggested that the dissociation of sodium hyaluronate (HYNa) resulted in the formation of anionic HY⁻ species:



Electric field provided electrophoretic motion of the anionic HY⁻ species towards the anode surface, where the pH decreased owing to the electrochemical decomposition of water:



The charge compensation in the low pH region at the electrode surface resulted in the formation of hyaluronic acid films (HYH):

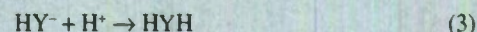


Figure Aa shows a typical cross section of HYH film prepared from aqueous 3 gL⁻¹ HYNa solution. Films thickness was varied in the range of 0–10 µm by the variation of the electric field in the range of 0–7 Vcm⁻¹ and deposition time in the range of 0–10 min. EPD resulted in the formation of uniform and adherent films on various conductive substrates, such as stainless steel, Ti and Ti alloys, graphite and platinized silicon wafers. The use of mixed ethanol-water (70% ethanol) solvent offers the advantage of reduced gas evolution attributed to the electrochemical decomposition of water.² In this case, higher electric fields can be applied, which are beneficial for the fabrication of composite materials, containing bioceramics and bioglass in the HYH matrix. On the other hand, composite materials containing drugs, proteins and enzymes must be prepared from aqueous solutions in order to avoid reactions of these materials with ethanol.¹⁶

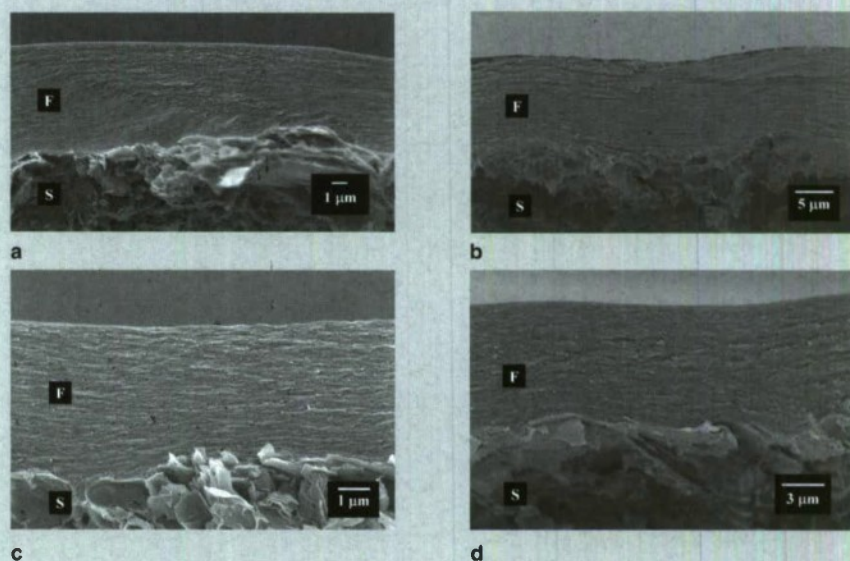


Figure A. SEM images of cross sections of (a) HYH, (b) HYH-salicylic acid, (c) HYH-heparin, and (d) HYH-BSA films, F-film, S-substrate.

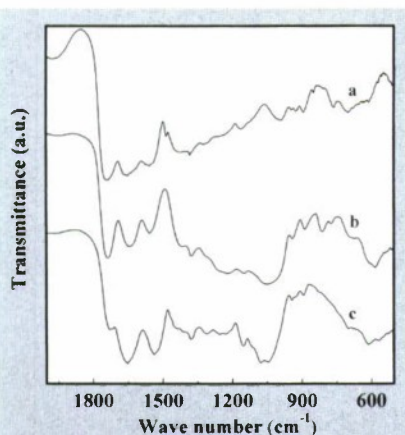


Figure 1. FTIR spectra of (a) HYH-salicylate, (b) HYH-heparin, and (c) HYH-BSA films.

ing deposition rate from 0.15 to 1.77 mgcm⁻²min⁻¹. The increasing deposition yield indicated co-deposition of HYH and BSA. The results indicated that charge reversal of BSA at the electrode surface promoted the deposition of composite films. It is suggested that the electrostatic attraction of positively charged BSA and negatively charged HY⁻ resulted in the precipitation of the HYH-BSA complexes^{8,23} and deposition of composite films. The complexes of hyaluronate and BSA were widely investigated in the literature in order to elucidate their functions in the living tissue. These studies^{8,23} showed the formation of insoluble HYH-BSA complexes below pH 5.

The co-precipitation of HYH and BSA can explain the significantly higher deposition rate obtained from mixed HYNa and BSA solutions compared to pure HYNa solutions. Figure 1 shows a typical cross section of a composite HYH-BSA film, prepared from 0.6 g L⁻¹ HYNa aqueous solution containing 0.4 g L⁻¹ BSA. The thickness of the HYH-BSA films prepared from 0.5–3 g L⁻¹ HYNa solutions containing 0.4–1.7 g L⁻¹ BSA was varied in the range of 0–20 μm by variation of the electric field in the range of 5–12 Vcm⁻¹ and deposition time in the range of 0–10 min.

Figure 1 shows Fourier transform infrared (FTIR) spectra for HYH-salicylate, HYH-heparin and HYH-BSA films. The FTIR spectrum of HYH-salicylate film (Figure 1a) showed characteristic amide I and amide II peaks of HYH at 1,658 and 1,555 cm⁻¹, respectively. The band at 1,740 cm⁻¹ in the spectrum of the film is related to the

stretching of the protonated carboxylic group of HYH.³⁴ The adsorption at 1,384 cm⁻¹ was attributed to the C-O-H deformation mode.²⁵ Similar peaks were observed in the spectrum of HYH-heparin (Figure 1b). The absorption band at 1,485 cm⁻¹ in the FTIR spectrum of HYH-salicylate film has been assigned to the C=C ring vibration mode of salicylate.²⁶ The adsorptions at 1,165 and 988 cm⁻¹ can be attributed to C-H bending modes.²⁷ The FTIR spectrum of HYH-heparin film showed absorptions at 1,222 and 1,037 cm⁻¹, which were attributed to SO_3^- asymmetric and symmetric stretching of heparin.²⁸ The sulfate half ester absorptions of heparin²⁸ were observed at 774 and 815 cm⁻¹. The FTIR spectrum of HYH-BSA film showed enhanced characteristic adsorption peaks at 1,656 cm⁻¹ attributed to amide I adsorption band and at 1,550 cm⁻¹ attributed to amide II adsorption band. Similar peaks were observed in the FTIR spectrum of BSA.^{29,30}

COMPOSITE HYH FILMS CONTAINING BIO-CERAMICS AND BIOGLASS

Titania, silica, HA and bioglasses are important materials for the fabrication of bioactive bone-substitute materials for biomedical implant applications. EPD method has been developed for the fabrication of composite coatings containing particles of bioactive ceramics, such as titania, silica, HA and bioglass in the HYH matrix. Ceramic powders of titania (anatase) with average particle size of 0.5 μm and amorphous silica with average particle size of 7 nm were purchased from Aldrich. Stoichiometric HA nanoparticles were prepared by a wet chemical technique described in a previous work.² Precipitation was performed at 70°C by the slow addition of a 0.6 M (NH₄)₂HPO₄ solution into a 1.0 M Ca(NO₃)₂ solution. The pH of the solutions was adjusted to 11 by NH₄OH. Stirring was performed during 8 h at 70°C and then 24 h at room temperature. The precipitate was washed with water and finally with ethanol. It has been previously reported³¹ that the average length of the needle-shape HA crystals, prepared by this method, is about 150 nm and the average aspect ratio is 8. The long axis of the needles corresponded to the

c-axis of the hexagonal HA structure. The average particle size of bioglass (45S5 powder, MO-SCI Corporation) was about 5 μm.

Titania, silica, HA and bioglass were dispersed in HYNa solutions in a mixed ethanol-water solvent. The adsorption of HY⁻ on the surfaces of the particles resulted in the electrosteric stabilization of the particles and provided negative charge for anodic EPD. Composite HYH-titania and HYH-silica films were obtained from 0.5–1 g L⁻¹ HYNa solutions in a mixed ethanol-water solvent (70% ethanol) containing 0.1–2 g L⁻¹ titania or 0.1–1 g L⁻¹ silica at electric fields of 15–25 Vcm⁻¹. It was found that the increase in the concentration of the silica or titania particles in the suspensions resulted in increasing particle concentration in the films. Figure 2 shows typical SEM images of surfaces of the composite films. The films were crack-free and contained particles of titania or silica. Silica particles showed significant agglomeration and non-uniform distribution in the HYH matrix. The agglomeration can be attributed to small particle size of the silica nanoparticles. It is suggested that particle agglomeration can be reduced by the use of dispersants.

EPD has also been used for the fabrication of composite HYH-nanoHA-bioglass films at room temperature. In

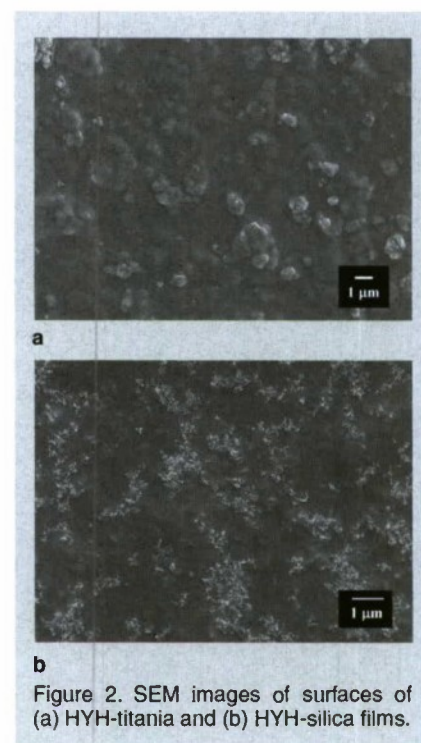


Figure 2. SEM images of surfaces of (a) HYH-titania and (b) HYH-silica films.

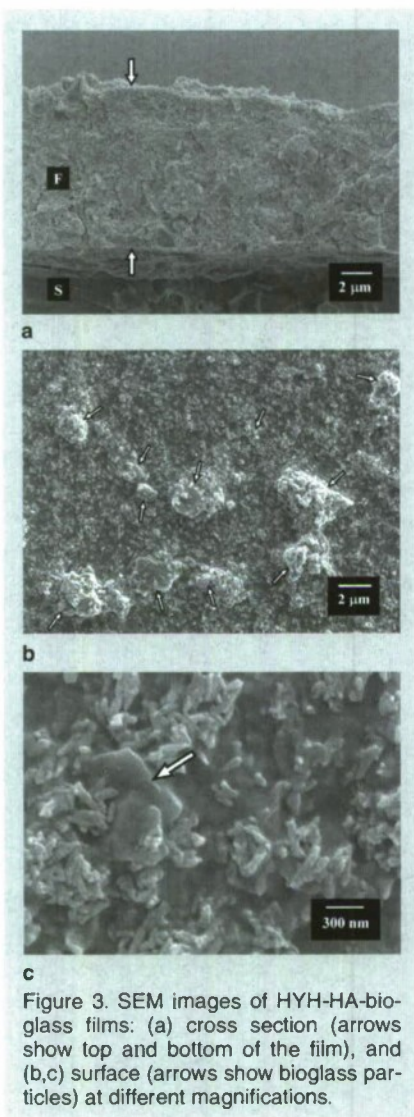


Figure 3. SEM images of HYH-HA-bioglass films: (a) cross section (arrows show top and bottom of the film), and (b,c) surface (arrows show bioglass particles) at different magnifications.

this approach, the problems related to the high temperature sintering of HA and bioglass deposits were avoided. It should be noted that the properties of sintered HA with large grain size are different from the properties of nanostructured HA in bones. Bioglass is a bioactive material, which readily reacts with physiological fluids, forming HA layers on its surface and creating tenacious bonds to hard and soft tissues through cellular activity. However, high temperature densification of bioglass can result in excessive crystallization, which may turn it into an inert material. The results of this investigations showed that HYH can be used as a common charging additive for the deposition of HA and bioglass. The use of HYH with good film forming and binding properties enabled the formation of adherent films containing HA

and bioglass in the HYH matrix. Figure 3a shows a cross section of a composite HYH-bioglass-HA film prepared from the 0.5 gL^{-1} HYN solution containing dispersed 0.15 gL^{-1} bioglass and 0.6 gL^{-1} HA. The deposition method enabled the formation of adherent films with thickness in the range of 0–20 μm . The SEM images of the surface of the films (Figure 3b,c) at different magnifications showed larger bioglass particles and smaller needle shape HA particles. The SEM results indicated co-deposition of bioglass and HA and the formation of composite HYH-bioglass-HA films. It is known that composite HA-bioglass materials exhibit high bioactivity³² due to the higher bioactivity of bioglass compared to HA.^{33,34}

CONCLUSIONS

Electrophoretic deposition has been utilized for the fabrication of composites, containing organic and inorganic functional biomaterials in the HYH matrix. The room temperature EPD method offers a possibility to utilize important functional properties of nanostructured bioceramics, bioglass and organic materials in the composite films. The results of this investigation pave the way for the fabrication of biomedical implants with improved biocompatibility, blood compatibility and bioactivity. The incorporation of heparin and salicylate into the HYH matrix can be useful for the fabrication of drug eluting coatings. The approach developed for the deposition of BSA can be further utilized for the deposition of other proteins and enzymes for applications in implants and biosensors.

ACKNOWLEDGEMENT

The authors gratefully acknowledge the financial support of the Natural Sciences and Engineering Research Council of Canada.

References

1. R. Damodaran and B.M. Moudgil, *Colloids and Surfaces A: Physicochemical and Engineering Aspects*, 80 (2-3) (1993), pp. 191–195.
2. I. Zhitomirsky and L. Gal-Or, *Journal of Materials Science: Materials in Medicine*, 8 (4) (1997), pp. 213–219.
3. P. Sarkar and P.S. Nicholson, *Journal of the American Ceramic Society*, 79 (8) (1996), pp. 1987–2002.
4. E.R. Wise et al., *Chemistry of Materials*, 19 (21)

- (2007), pp. 5055–5057.
5. M. Mason et al., *Biomaterials*, 21 (1) (2000), pp. 31–36.
6. K. Kakehi, M. Kinoshita, and S. Yasueda, *Journal of Chromatography B*, 797 (1-2) (2003), pp. 347–355.
7. J.B. Leach and C.E. Schmidt, *Biomaterials*, 26 (2) (2005), pp. 125–135.
8. S. Xu et al., *Chemical and Pharmaceutical Bulletin*, 48 (6) (2000), pp. 779–783.
9. K.Y. Suh et al., *Journal of Biomedical Materials Research Part B: Applied Biomaterials*, 72B (2) (2005), pp. 292–298.
10. H. Kito and T. Matsuda, *Journal of Biomedical Materials Research*, 30 (3) (1996), pp. 321–330.
11. M. Yoshikawa et al., *Materials Science and Engineering: C*, 27 (2) (2007), pp. 220–226.
12. T. Momose et al., *Journal of Biomedical Materials Research*, 59 (2) (2002), pp. 219–224.
13. L.-Y. Huang and M.-C. Yang, *Journal of Nanoscience and Nanotechnology*, 6 (9-10) (2006), pp. 3163–3170.
14. F. Sun and I. Zhitomirsky, *Surface Engineering*, 25 (12) (2009), pp. 621–627.
15. K. Grandfield et al., *Surface and Coatings Technology*, 203 (10-11) (2009), pp. 1481–1487.
16. B. Elysee-Collen and R.W. Lencki, *Biotechnology Progress*, 13 (6) (1997), pp. 849–856.
17. I. Capila and R.J. Linhardt, *Angewandte Chemie - International Edition*, 41 (3) (2002), pp. 390–412.
18. P. Taepaiboon, U. Rungsardthong, and P. Supaphol, *Nanotechnology*, 18 (17) (2007), 175102.
19. C. Ferrero et al., *Journal of Controlled Release*, 128 (1) (2008), pp. 71–79.
20. M.A. Saunders et al., *Journal of Biological Chemistry*, 276 (22) (2001), pp. 18897–18904.
21. N. Chinen et al., *Journal of Biomedical Materials Research - Part A*, 67 (1) (2003), pp. 61–68.
22. U. Böhme and U. Scheler, *Chemical Physics Letters*, 435 (4-6) (2007), pp. 342–345.
23. S. Xu et al., *Colloid and Polymer Science*, 283 (4) (2005), pp. 383–392.
24. A.L.R. Mercê et al., *Journal of Inorganic Biochemistry*, 89 (3-4) (2002), pp. 212–218.
25. J.A. Alkhrad et al., *Journal of Pharmaceutical and Biomedical Analysis*, 31 (3) (2003), pp. 545–550.
26. K.D. Dobson and A.J. McQuillan, *Spectrochimica Acta Part A: Molecular and Biomolecular Spectroscopy*, 56 (3) (2000), pp. 557–565.
27. B. Humbert, M. Alnot, and F. Quilès, *Spectrochimica Acta Part A: Molecular and Biomolecular Spectroscopy*, 54 (3) (1998), pp. 465–476.
28. F. Sun, X. Pang, and I. Zhitomirsky, *Journal of Materials Processing Technology*, 209 (3) (2009), pp. 1597–1606.
29. Y. Kang et al., *Carbohydrate Polymers*, 77 (2) (2009), pp. 244–249.
30. Z.G. Peng, K. Hidajat, and M.S. Uddin, *Journal of Colloid and Interface Science*, 271 (2) (2004), pp. 277–283.
31. F. Sun et al., *Colloids and Surfaces B: Biointerfaces*, 67 (1) (2008), pp. 132–139.
32. J.M. Gomez-Vega et al., *Biomaterials*, 21 (2) (2000), pp. 105–111.
33. D.L. Wheeler, M.J. Montfort, and S.W. McLoughlin, *Journal of Biomedical Materials Research*, 55 (4) (2001), pp. 603–612.
34. D. Krause et al., *Surface and Coatings Technology*, 200 (16-17) (2006), pp. 4835–4845.

R. Ma and, Y. Li, M.Sc. candidates, and I. Zhitomirsky, professor, are with the Department of Materials Science and Engineering, McMaster University, 1280 Main Street West, Hamilton, Ontario, Canada, L8S 4L7. Prof. Zhitomirsky can be reached at (905) 525-9140; fax (905) 528-9295; e-mail zhitom@mcmaster.ca.

Laser Process Effects on Physical Texture and Wetting in Implantable Ti-Alloys

Sameer R. Paital, Wei He, Claus Daniel, and Narendra B. Dahotre

Wetting is an important aspect for implantable biomaterials, as it affects the initial interaction with physiological fluids, which in turn dictates the protein adsorption, cell attachment, and tissue integration at the interface. In light of this in the present overview, surface engineering techniques based on laser processing of implantable titanium alloys for improved wettability and cell compatibility is discussed. Here three different laser processing techniques, laser interference patterning, continuous wave laser direct melting, and pulsed laser direct melting and the influence of each type of processing on the micro-texture evolution are studied. Finally, the effect of micro-textures on the wettability and thereby its in vitro bioactivity and in vitro biocompatibility is systematically discussed.

INTRODUCTION

Surfaces and Interfaces for Bone Tissue Engineering

The interface between the implanted biomaterial and the living tissue is the site of a variety of dynamic biochemical processes and reactions.¹ These numerous atomic and molecular level events at the interface modulate the surface chemistry and morphology of the implant material, which in turn influences its long-term durability and compatibility inside the body.¹ Under ideal situations, following implantation, a protein rich layer is supposed to be confirmed at the surface of an implant material as it further influences the cell attachment and tissue integration. The presence or the interaction of protein molecules depends on the wetting characteristic or the hydrophilicity of the implant material with the physiological fluids. The two most important factors that govern

the wetting of the implant material with the physiological fluids are the surface chemistry and surface morphology of

the implant material. Hence, there is a tremendous interest toward surface modification and effective design of such implantable materials so as to improve their hydrophilicity and thereby elicit a specific, desired, and timely response from the surrounding cells and tissues.

For bone tissue engineering applications, the most common design approach followed by various researchers is to mimic the functionality of the naturally occurring hierarchically organized hard tissue into the artificial implant material.²⁻⁵ It has been well understood that human bone is rich in calcium and phosphorous based hydroxyapatite (HA) phase at the nanoscale, and has a three-dimensional (3-D) extra cellular matrix (ECM) to support bone cells at the sub-micrometer scale.^{6,7} Hence, artificial biomaterials with biocompatible HA coatings on titanium based alloys, and engineered 3-D features at the meso-scale to support cells and tissue integration is becoming a reality. However, most of the surface engineering techniques⁸⁻¹⁰ used are "line of sight" methods: they either provide the appropriate surface chemistry (calcium and phosphorous based) or the 3-D topographic cue and lack in ability to achieve both simultaneously. Hence, in the present overview we demonstrate the laser-based surface engineering approach by which both an appropriate surface chemistry and regular 3-D topographic cues can be achieved simultaneously.

PULSED LASER SYNTHESIS OF TEXTURED Ca-P COATING

A pulsed laser is characterized by the short pulse duration (femtoseconds to milliseconds), high peak power, and intermittent delivery of the laser beam.

How would you...

...describe the overall significance of this paper?

This paper demonstrates the usage of high energy laser beams to synthesize biocompatible surfaces at various length scales for load bearing implant applications. It also demonstrates the significance of wetting phenomena for bioapplication and the use of laser surface engineering to achieve surfaces with tunable wetting characteristics.

...describe this work to a materials science and engineering professional with no experience in your technical specialty?

Fabricating and designing biomaterials to provide appropriate surface chemistry and surface morphology is a significant challenge for many materials scientists. To meet the above requirement we use a laser based direct melting and laser interference patterning technique. Here by using a high energy laser beam we provide calcium phosphate based bioactive textured coating on Ti-6Al-4V. This process only alters the surface chemistry without altering the bulk mechanical properties of the material.

...describe this work to a layperson?

Our work is mostly focused on synthesizing or designing artificial materials for load bearing implant applications. These materials are mostly used inside a body to replace a damaged hard tissue and thereby restore its function. Hence while designing these artificial materials for such applications, materials scientists are mostly concerned about mimicking the material as close as possible to the naturally occurring tissue and thereby make it more biocompatible.

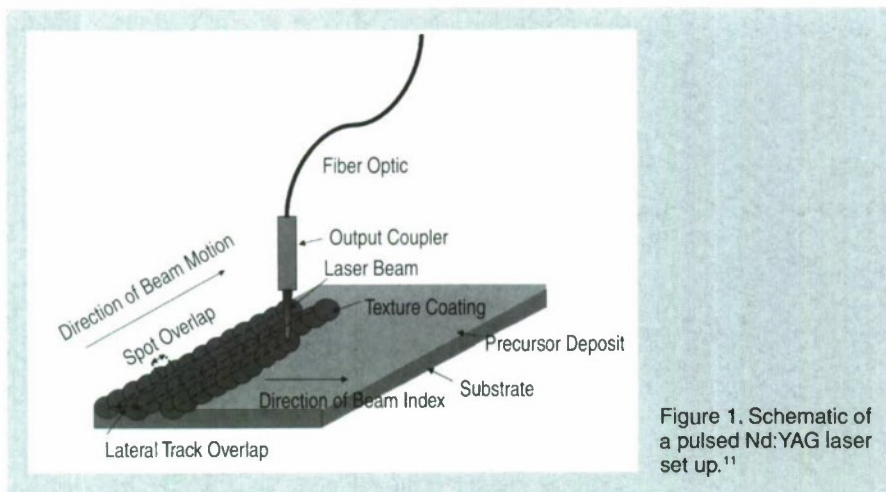


Figure 1. Schematic of a pulsed Nd:YAG laser set up.¹¹

During the impact of such ultra-short pulses a fine layer of material is melted and then is vaporized at the surface, forming a vapor jet. This jet induces a recoil pressure and the liquid metal underneath is pushed toward the edges of the impact. After the end of the laser pulse the liquid metal solidifies and forms a crater on the surface of a metal. The presence of such a crater due to pulsed laser irradiation generates a physical texture on the surface of a material (schematically shown in Figure 1¹¹) and can be considered as a 3-D topographic cue for cell adhesion. The presence of short duration pulses also results in high cooling rate and thereby meta-stable phases suitable for bio-application. Their beneficial effects were explored in the samples pre-sprayed with HA powder suspended in a water-based organic solvent (LISI) and scanned under a Lumonics JK701 model pulsed Nd:YAG laser. A metallurgical bonding at the coating/substrate interface and four different texture morphologies were obtained by varying the laser pulse frequency (10, 20, 30, and 40 Hz) and keeping the laser spot diameter (900 μm) and laser scan speed (50 cm min^{-1}) constant. These variations in frequency resulted in variations of 6%, 53%, 69%, and 76% crater overlap.

With an increase in pulse frequency there is an increase in crater overlap and hence varying surface textured morphology. Further, the 3-D morphological evolutions of the coatings (presented as insets in Figure 2¹¹) obtained using a confocal microscopic image indicate that the sample processed at 10 Hz possesses a relatively rough morphology as compared to the samples processed at higher frequencies. This is attributed to

the fact that for the samples processed at higher frequencies the crater overlap was substantially high as compared to the sample processed at 10 Hz. This increased crater overlap resulted in re-melting of the major portion of the prior crater thereby smoothing of the coating surface. The presence of such geometrically textured cues is expected to support bone cells and thereby induce bone ingrowth from the surrounding tissue.

The effect of surface morphology on its wetting behavior can be studied by the contact angle measurement of a simulated body fluid (SBF) subtended on these surfaces and by maintaining the SBF at 37°C and 7.4 pH. The composition and preparation of SBF solution was in ac-

Equations	
$w = \frac{\pi}{2 \sin\left(\frac{\beta}{2}\right)}$	(1)
$\cos \theta_c = \frac{w}{2\left(h^2 + \frac{w^2}{4}\right)^{\frac{1}{2}}} = \frac{1}{\sqrt{1 + \frac{4h^2}{w^2}}}$	(2)
$\cos \theta_c = \frac{1 - \phi}{R_f - \phi}$	(3)

cordance to References 11 and 12. The contact angle measurements carried out by a static sessile drop technique using a CAM Plus[®] contact angle goniometer (Chem Instruments, Inc. Fairfield, Ohio) indicated that all the laser-processed samples except for the sample processed at 10 Hz demonstrated an improved hydrophilic behavior as compared to the control Ti-6Al-4V (Figure 3a¹¹). Within the laser-processed samples, the sample processed at 40 Hz showed the maximum hydrophilicity to SBF with a contact angle of approximately 40°.

The improvement in hydrophilicity with increasing laser pulse frequency can be explained as per the schematic shown in Figure 3b.¹¹ A practical rough surface is assumed to have a cosine profile with a Gaussian distribution and is character-

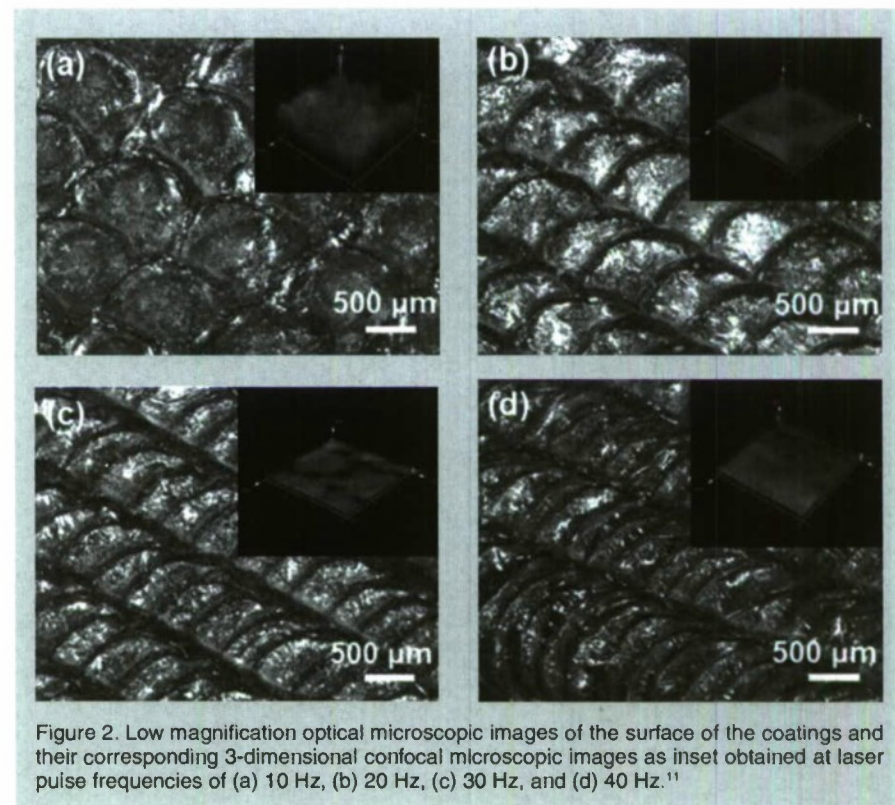
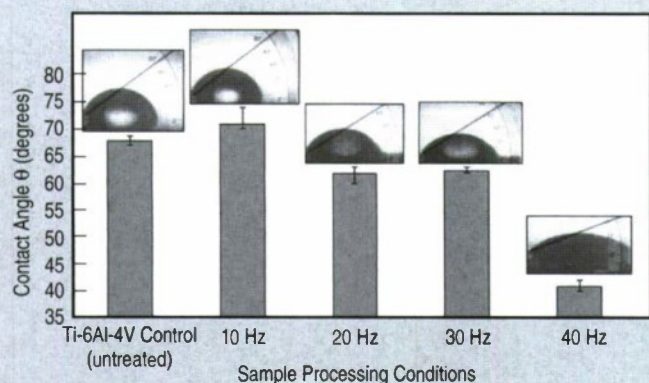
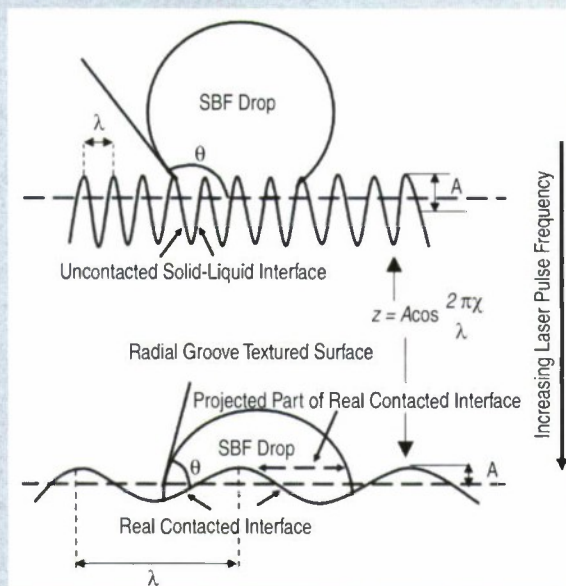


Figure 2. Low magnification optical microscopic images of the surface of the coatings and their corresponding 3-dimensional confocal microscopic images as inset obtained at laser pulse frequencies of (a) 10 Hz, (b) 20 Hz, (c) 30 Hz, and (d) 40 Hz.¹¹



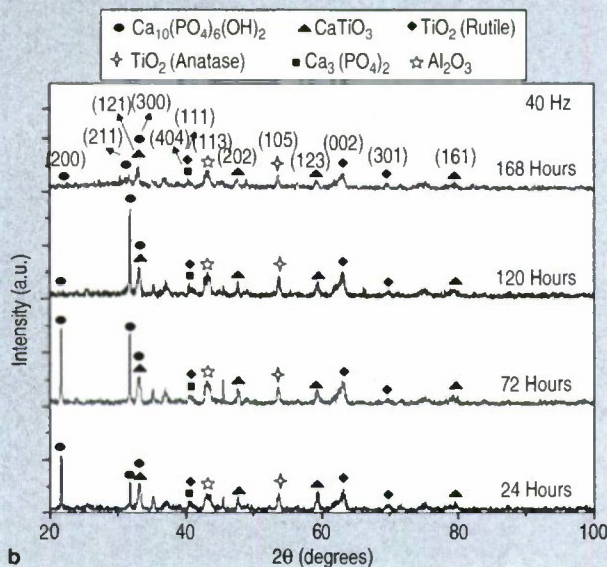
a



b



a

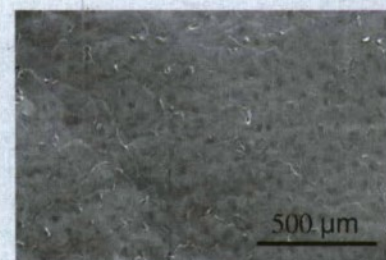


b

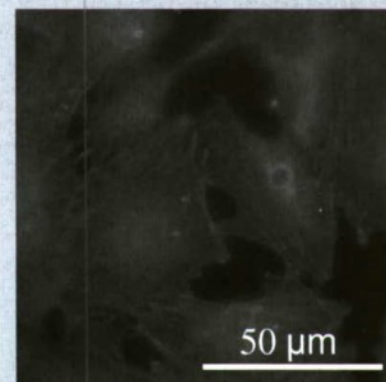
Figure 4. (a) An SEM micrograph of the 40 Hz processed sample revealing the precipitation of a whisker-like apatite phase following immersion in SBF for 1 day; (b) XRD spectra of the 40 Hz processed sample following immersion in SBF for different time periods.¹¹

ized by the texture parameter (σ_A/λ), where σ_A is the standard deviation of amplitude and λ the distance between two successive crests or troughs.^{11,13} From the confocal microscopy images (insets in Figure 2¹¹), it is clearly evident that at a laser pulse frequency of 10 Hz the surface had a rough morphology due to the minimal crater overlap. This resulted in a higher σ_A/λ value, leading to instability in wetting and increased contact angle. However, with an increase in laser pulse frequency there is increased remelting of the craters, resulting in a smoothing effect and lower σ_A/λ value. Hence when a liquid drop is placed on such a surface it easily overcomes the energy barriers associated with it and tries to wet it. Thus, an equilibrium state of wetting and thereby reduced contact angle is achieved on surfaces with lower σ_A/λ value.

As the samples processed at 40 Hz showed the maximum wettability, it was further studied for its in vitro bioactivity and in vitro biocompatibility. The in vitro bioactivity studies were carried out by soaking the sample in SBF and analyzing for the precipitation of an apatite ($\text{Ca}_{10}(\text{PO}_4)_6(\text{OH})_2$) like mineral



a



b

Figure 5. (a) An SEM morphology of the MC3T3-E1 osteoblast-like cells, and (b) cytoskeletal organization of the MC3T3-E1 osteoblast-like cells after culture for 7 days on the sample processed at 40 Hz.

layer. Following 24 hours of immersion in SBF the sample indicated for the precipitation of a whisker-like apatite phase (Figure 4a¹¹). XRD studies of the samples (Figure 4b¹¹)¹⁴ following immersion in SBF for different time periods indicated the presence of an apatite phase as evident from the characteristic HA maxima at $2\theta \sim 22.0^\circ$ and 31.75° corresponding to the planes (200) and (211), respectively. The presence of whisker-like morphology following 24 hours of immersion was attributed to heterogeneous nucleation of the hexagonal close packed (HCP) apatite crystal and subsequent growth of this HCP structure along the c axis (perpendicular to the close packed atomic plane) by the adsorption of Ca^{2+} and PO_4^{3-} ions from the super-saturated SBF solution. Also, from the XRD results (Figure 4b) it can be observed that as the immersion time is increased to 168 hours there is a decrease in intensity for the apatite peaks indicating a rapid change in the apatite crystallite size and thereby its mineralization behavior. The above results obtained from the SEM and XRD analysis for the 40 Hz sample therefore proved for its in vitro bioactivity.

The in vitro biocompatibility of the sample was assessed by cell attachment and cell proliferation of mouse pre-osteoblast MC3T3-E1 (subclone 14) cell line obtained from American Type Cell Culture Collection (ATCC, Manassas, VA, USA). The cell culture procedure, cell fixation for cell morphology analysis using SEM, and cell fixation for cytoskeleton organization using fluorescence microscope can be obtained

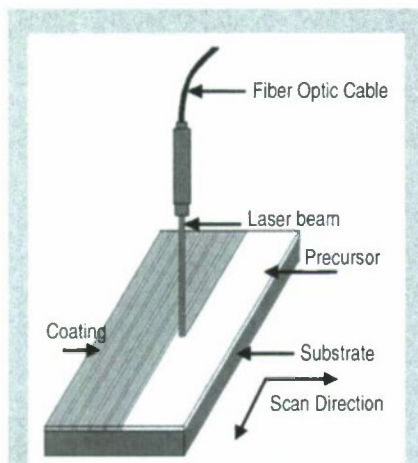


Figure 6. A schematic of a continuous wave Nd:YAG laser coating set up.¹⁴

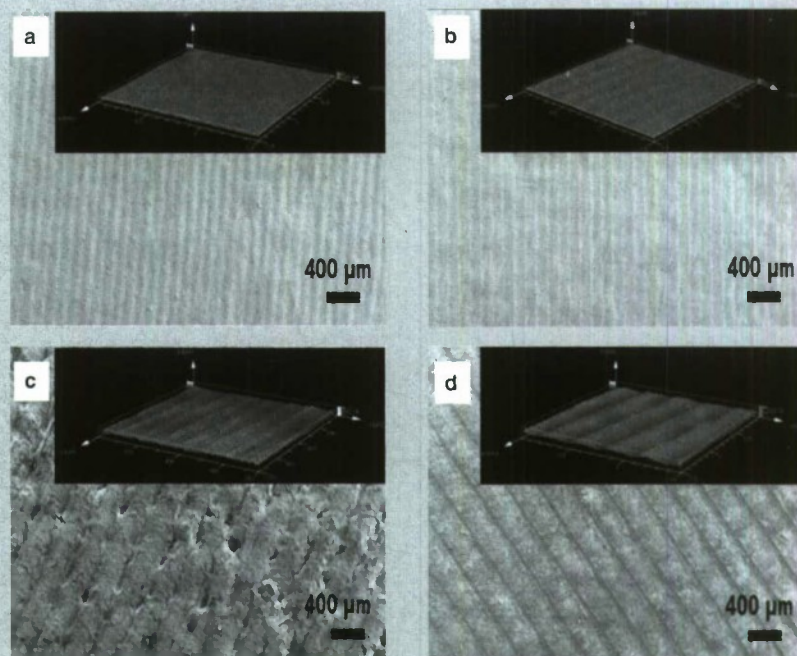


Figure 7. Low-magnification SEM images and their corresponding 3-D confocal microscopic images of the surface of coatings processed at (a) 137 J/cm², 100 μm line spacing, (b) 191 J/cm², 100 μm line spacing, (c) 137 J/cm², 200 μm line spacing, and (d), 191 J/cm², 200 μm line spacing.¹⁴

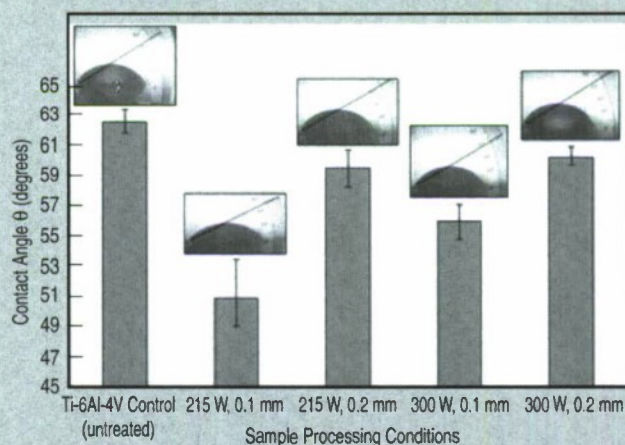


Figure 8. Contact angle variations and their corresponding shadow images of the SBF droplet on laser processed sample and control (untreated Ti-6Al-4V).

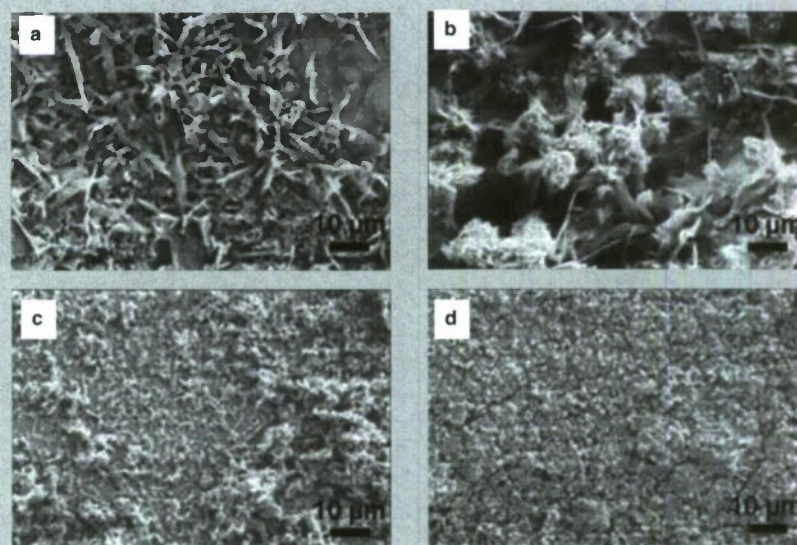


Figure 9. Scanning electron microscopy images of the sample processed at 137 J/cm², 100 μm line spacing following immersion in SBF for (a) 1 day, (b) 3 days, (c) 5 days, and (d) 7 days.¹⁴

from our previously published work.¹¹ The morphology of the MC3T3-E1 osteoblast-like cells after 7 days of culture on the 40 Hz processed sample appeared to be flattened, spread out uniformly, and strongly adhered with an elliptical and circular morphology (Figure 5a). The cytoskeletal organization of the osteoblast-like cells after 7 days culture indicated stressed actin filaments with well developed network of focal adhesion contacts (Figure 5b). Therefore, the pulsed laser processing technique holds the promise to synthesize bioactive and biocompatible textured CaP coatings on Ti alloys.

CW LASER-INDUCED DIRECT MELTING FOR TEXTURED CaP COATING

In a CW laser, the output power of the laser beam is constant with time. Hence direct melting using a CW laser is likely to produce more uniform thermal conditions within the beam-substrate interaction region. Further, as the beam is delivered in a continuous mode, direct melting and simultaneous scanning of a material surface results in a line pat-

tern rather than a crater as in the case of a pulsed mode operation. The laser scanning process in this case can be programmed to achieve line patterns with varying lateral track spacing and hence micro-textured patterns at varying length scales can be obtained. The schematic of such an operation is illustrated in Figure 6.¹⁴ The formation of such line patterned CaP surface is expected to provide contact guidance for directional attachment of bone forming cells and thereby improve its biocompatibility.

Keeping the above potential advantages in mind, the pre-coated samples were scanned under a CW Nd:YAG laser equipped with a fiber optic beam delivery system to obtain a metallur-

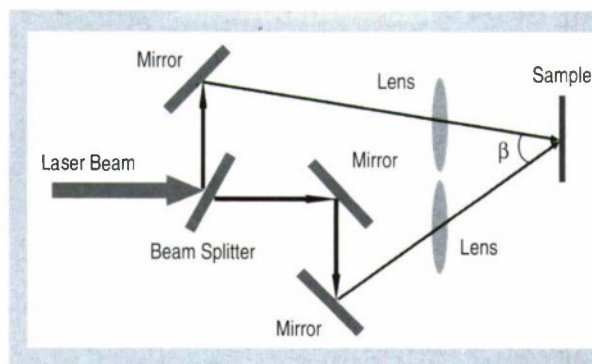


Figure 12. A schematic of the laser-based interference patterning technique.

gical bonding between the precursor ($\text{Ca}_{10}(\text{PO}_4)_6(\text{OH})_2$) and the substrate (Ti-6Al-4V). In the current work, two different laser fluences of 137 J/cm^2 and 191 J/cm^2 were used for each sideways line spacing ($100 \mu\text{m}$ and $200 \mu\text{m}$). A lateral or sideways spacing of 100 and $200 \mu\text{m}$ were chosen so as to match the length scale of the naturally occurring 3-D extra cellular matrix (ECM) present in the human bone.⁷ Irrespective of the laser fluence, the samples processed at $100 \mu\text{m}$ line spacing (Figure 7a and b¹⁴) have a smoother surface finish as compared to the samples processed at $200 \mu\text{m}$ spacing (insets of Figure 7c and d¹⁴) due to the increased overlap of melted layers as a result of reduced line spacing.

The wetting behavior of the textured CaP surface and control (untreated Ti-6Al-4V) obtained by a static sessile drop measurement technique indicated that the laser textured CaP surface has a significantly smaller value of experimental contact angle to SBF as compared to the control (untreated Ti-6Al-4V) (Figure 8). This improved hydrophilic behavior of the laser textured surface is attributed to the influence of surface texture and the presence of CaP phases evolved during laser processing. Further, within the laser processed parameters, it can be observed that the samples processed at $100 \mu\text{m}$ line spacing (irrespective of the laser fluences) has a significantly smaller value of experimental contact angle compared to the $200 \mu\text{m}$ line spaced samples. The improved hydrophilicity of the $100 \mu\text{m}$ line spaced samples can also be due to the significant overlap within the melted regimes that resulted in a smoothening effect and smaller texture parameter ($\sigma_A/\lambda \sim 0.01$) value as compared to the samples processed with $200 \mu\text{m}$ line spacing ($\sigma_A/\lambda \sim 0.02$). With a smaller σ_A/λ value, there is certain amount invasion of the liquid along the

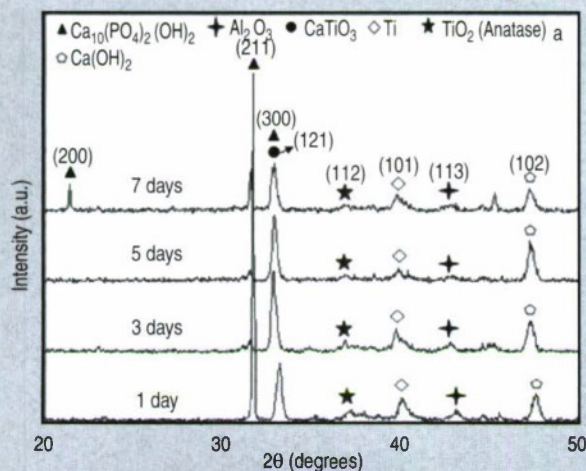


Figure 10. The XRD spectra of the samples processed at 137 J/cm^2 , $100 \mu\text{m}$ line spacing following immersion in SBF for different time periods.¹⁴

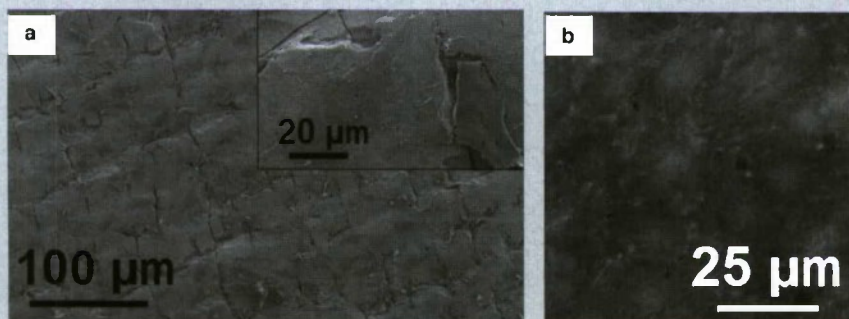


Figure 11. (a) The SEM morphology of the MC3T3-E1 osteoblast-like cells, and (b) cytoskeleton organization of the MC3T3-E1 osteoblast-like cells following culture for 1 day on the sample processed at 137 J/cm^2 , $100 \mu\text{m}$ line spacing.

textured surface and thereby improved wettability.

As the sample processed at 137 J/cm^2 and $100 \mu\text{m}$ line spacing has the most significant hydrophilic behavior, it was further selected to study for its in vitro bioactivity and in vitro biocompatibility. SEM analysis of the samples following immersion in SBF for four different time periods (1, 3, 5, and 7 days) is shown in Figure 9.¹⁴ After 1 day immersion in SBF (Figure 9a), characteristic whisker-like apatite crystallites are nucleated on the surface of the sample. As the immersion time is increased to 3 days the whisker-like crystallites gets covered with another mixed layer of whisker-like and nano

HA crystallites (Figure 9b). After 5 day immersion in SBF the layer is completely covered with nano crystallites of HA (Figure 9c) and at the end of the 7 days there is a thick mineralized layer of HA on the surface of the sample (Figure 9d). X-ray diffraction studies of the mineralized layers following immersion in SBF for 1, 3, and 5 days indicated the presence of characteristic HA peaks at $2\theta \sim 31.75^\circ$ corresponding to the plane (211) (Figure 10¹⁴). As the immersion time is increased to 7 days an extra HA peak at $2\theta \sim 21.82^\circ$ corresponding to the plane (200) is also evolved.

The morphology of the MC3T3-E1 osteoblast-like cells following culture

for 1 day on the samples processed at 137 J/cm^2 and $100 \mu\text{m}$ line spacing is shown in Figure 11a. The good adhesion of the osteoblast-like cells were characterized by the lamellipodia trying to extend and adhere along the grooves (inset of Figure 11a). The cytoskeleton organization of the osteoblast-like cells (Figure 11b) demonstrated uniform spreading with stressed actin filaments. The network of focal adhesion contacts along their edges can also be further proved for their strong attachment to the laser textured surface. Therefore, using a CW laser, textured CaP coatings with appropriate length scales can be synthesized for improved wettability, in vitro

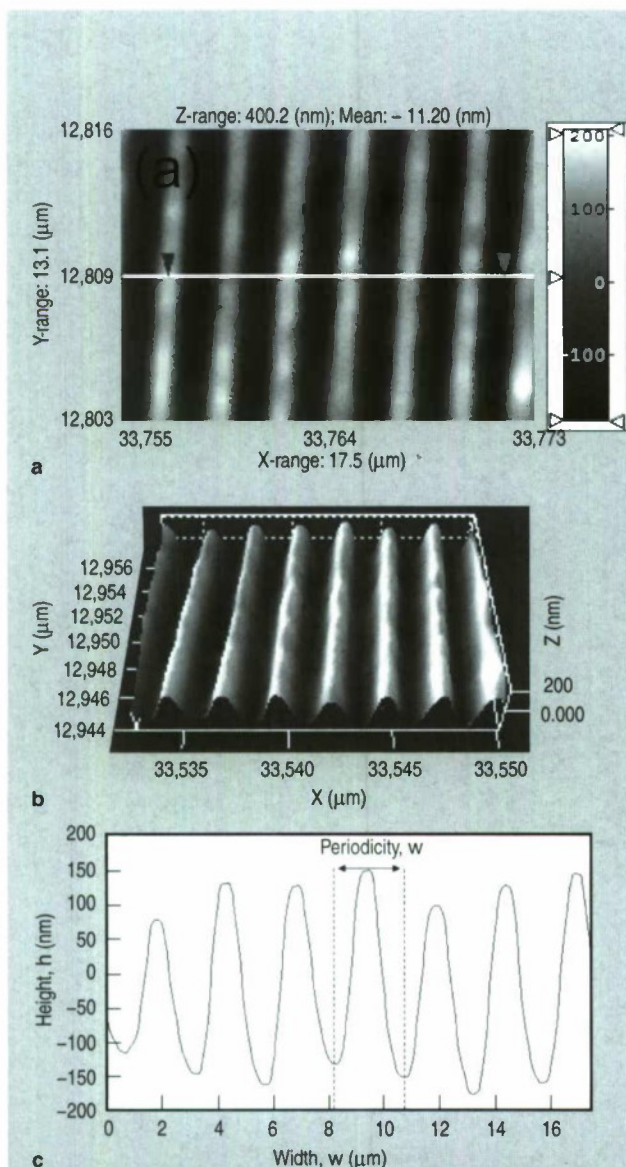


Figure 13. Groove pattern on Ti-6Al-4V by laser interference technique (760.35 mJ/cm^2): (a) 2-D morphological evolution, (b) 3-D morphological evolution, and (c) variation in height and width (across the line scan) of the features obtained using a one-step irradiation.¹⁷

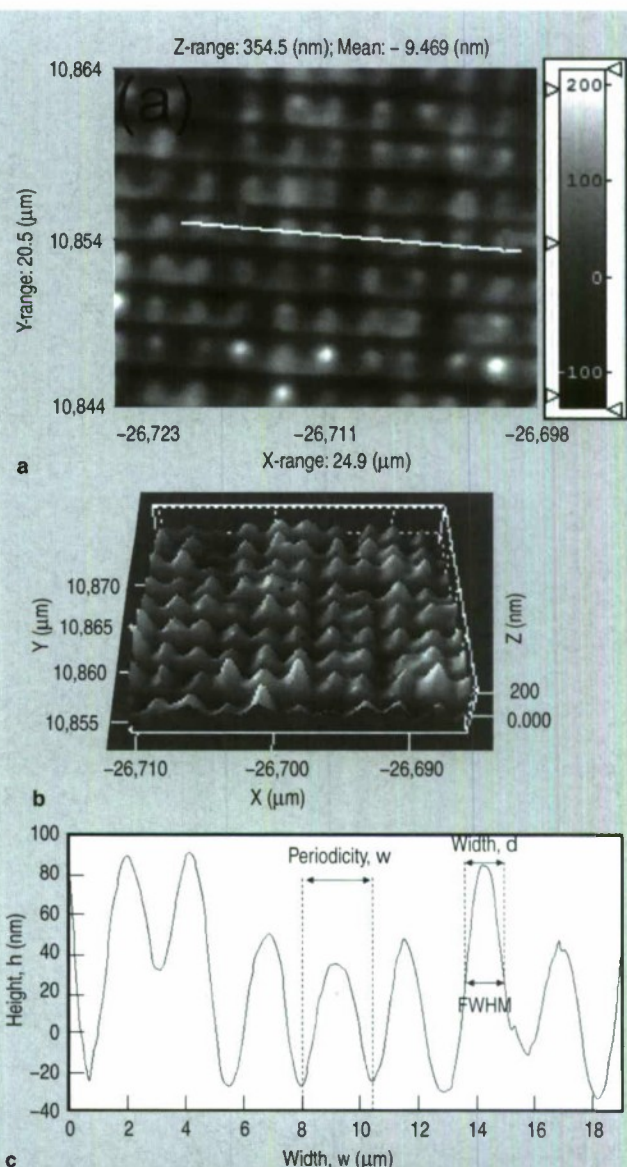


Figure 14. Pillar pattern on Ti-6Al-4V by laser interference technique (760.35 mJ/cm^2): (a) 2-D morphological evolution, (b) 3-D morphological evolution, and (c) variation in height and width at FWHM (across the line scan) of the features obtained using a two-step irradiation.¹⁷

bioactivity, and in vitro biocompatibility.

LASER INTERFERENCE TECHNIQUE FOR PATTERNING Ti-6Al-4V

In this technique, the primary laser beam is split into two coherent sub-beams, which were then guided using an optical assembly to produce interfer-

ence on the sample surface. The two interfering laser beams create a sinusoidal intensity distribution with high-and-low intensity lines. A detailed schematic setup of the interference patterning process is illustrated in Figure 12. The distance, w between the high intensity spots (periodicity) can be varied with the angle (β) between the beams as per the following Bragg equation (Equation 1 in

the table.^{15,16} The advantage associated with the present technique is that it creates periodic surface textures at length scales ranging from the micro to nano in a single-step process. Further, the process can also be controlled to mimic features close to size of the ECM or the pre-osteoblast cell size for their better adhesion and differentiation into bone cells.

In this preliminary work, laser interference patterned surface textures were obtained on Ti-6Al-4V samples and their influence on wettability was studied. The polished Ti-6Al-4V samples were interference patterned using a linear polarized third harmonic of a Q-switched Nd:YAG laser (Coherent Infinity, Santa Clara, CA, USA) operated at a wavelength of 355 nm. The pulse duration and repetition rate used in the present experiment were 2.5 ns and 10 Hz, respectively. The samples were irradiated under three different laser fluences of 362.26, 525.47, and 760.35 mJ/cm², while keeping the number of pulses as 5. Two different surface patterns (i.e. the groove and pillar-like) were obtained under each laser fluence. The 2- and 3-D morphological evolution of the groove-like feature obtained under a laser fluence of 760.35 mJ/cm² and the variation in height (h) and periodicity (w) of the grooves across the sample in x-direction are presented in Figure 13 a, b, and c, respectively.¹⁷ For obtaining the pillar-like features the samples irradiated with 5 pulses for a groove like pattern were rotated through 90° and irradiated once again with 5 pulses. Hence it was a two-step process for the pillar-like pattern, with the effective number of pulses being doubled compared to the groove-like pattern. The 2- and 3-D morphological evolution of the pillar-like feature obtained under a laser fluence of 760.35 mJ/cm² is presented in Figure 14a, b, respectively.¹⁷ From a line scan across the sample (Figure 14c¹⁷), it was observed that the width (d) at full-width-half-maxima (FWHM) and the periodicity (w) of the pillars were approximately 1.04 and 2.5 μ m, respectively. As described earlier in Equation 1, the periodicity (w) only depends on the angle (β) between the beams and hence the only physical feature which varied with laser fluence was the height (h) of the pillars and the grooves.

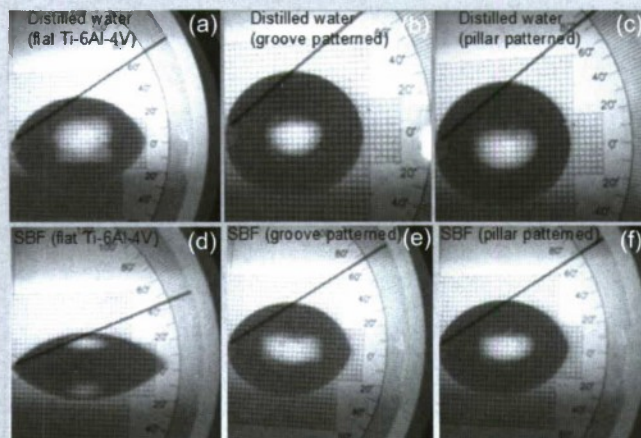


Figure 15. Light optical images of the distilled water droplet shadow on (a) flat Ti-6Al-4V, (b) groove patterned Ti-6Al-4V, (c) pillar patterned Ti-6Al-4V and light optical images of the SBF droplet shadow on (d) flat Ti-6Al-4V, (e) groove patterned Ti-6Al-4V, (f) pillar patterned Ti-6Al-4V.

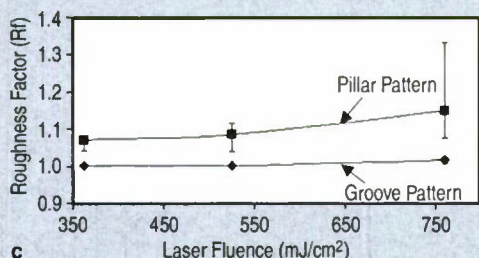
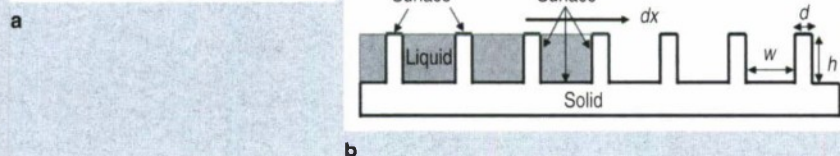
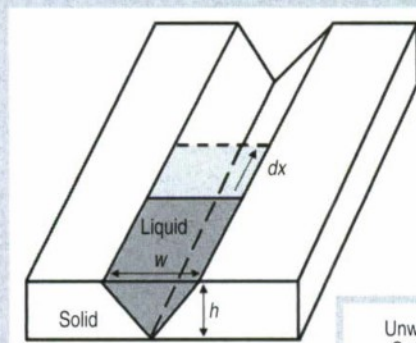
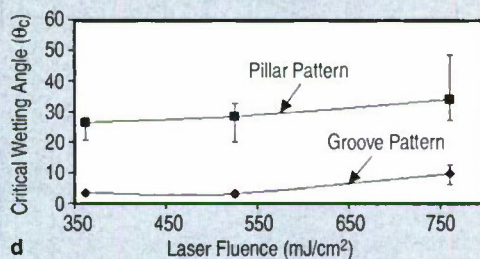


Figure 16. (a, b) A schematic illustration of liquid invasion into a groove pattern and pillar pattern and (c, d) variation in roughness factor, R_f and critical wetting angle, θ_c , with laser fluence for interference patterned samples.¹⁷



Contact angle measurements on both the groove- and pillar-like patterns were conducted using distilled water and SBF. It can be observed that irrespective of the samples processing conditions, the distilled water droplet (Figure 15a–c¹⁷) subtended a higher contact angle compared to the SBF droplet (Figure 15d–f¹⁷). Therefore, the presence of groove and pillar like features obtained using a laser interference technique with the present set of processing parameters resulted in tuning the surface towards a less hydrophilic behavior. This reduced wettability on the patterned surfaces can be explained based on the thermodynamic models as discussed below.

Here, for the ease of calculations, based on energy balance equations, the grooves are approximated to be of triangular type (Figure 16a¹⁷) and pillars to be of cylindrical type (Figure 16b¹⁷). Applying an energy minimum condition it can be hypothesized that liquid progression into a groove like pattern is favorable if the apparent contact angle θ^* or chemical angle θ is smaller than the critical angle θ_c for wetting, where θ_c is given as Equation 2.¹⁹ Therefore, for groove texture the critical angle for wetting depends on the roughness factor

$R_f = \sqrt{1 + \frac{4h^2}{w^2}}$ (ratio of the actual surface area to apparent surface area).

In contrast, a surface with an assembly of pillar-like patterns (Figure 16h) is characterized by Φ_s (solid fraction remaining dry) and roughness factor $R_f = 1 + 2h/d$ (ratio of the actual solid area to its projected area). The critical angle θ_c for wetting on such a surface is given as Equation 3.¹⁸ The roughness factor R_f was calculated for both groove and pillar patterns from the geometrical parameters (w , h , and d) of the features obtained using laser based interference technique, and plotted as a function of laser fluence (Figure 16c).¹⁷ It can be observed (Figure 16c) that there is a slight increase in R_f with increasing laser fluence for both the groove and pillar patterns, and R_f is higher for the pillar patterns compared to the groove pattern. This increased value of roughness factor ($R_f > 1$) for the pillar pattern is attributed to reduced width, d of the features as a result of the two-step

processing involved in this technique. Further, the critical wetting angle (θ_c) based on the above equations were calculated for the groove and pillar patterns respectively and plotted as a function of laser fluence (Figure 16d).¹⁷ The critical wetting angle (θ_c) increased with increasing laser fluence for both the patterns and the values of critical wetting angle (ranging from 3° to 48°) are smaller compared to the chemical or the Young's angle (θ , measured on the flat Ti-6Al-4V samples) obtained using both distilled water and SBF. As a result the condition for wetting ($\theta^* < \theta_c$) is not satisfied in both the cases (pillar and groove) and hence, the liquid dewets on both the patterns due to an increase in apparent contact angle (θ^*). Owing to the above reasons the samples were not further tested for its in vitro bioactivity and in vitro biocompatibility.

CONCLUSIONS

Three different laser-based surface modification techniques have been demonstrated to hold tremendous promise for improving the wettability of load-bearing implant alloys (Ti-6Al-4V). The samples processed by the pulsed and CW laser-based direct melting technique demonstrated an improved wettability with the SBF as compared to the control (untreated Ti-6Al-4V). Within the range of processing parameters employed in the present work, it was observed that there is an improved hydrophilicity with increasing laser pulse frequency for the pulsed laser direct melting. On the other hand, for the CW laser direct melting the samples demonstrated improved wettability with decreasing lateral track overlap. This improved wettability was attributed to the presence of appropriate CaP-based surface chemistry and 3-D topographic cues obtained using this technique. This improved wettability resulted in the precipitation of an apatite like phase following immersion in SBF and the attachment and spreading of the MC3T3-E1 osteoblast-like cells following culture for 1 day. The pulsed and CW laser direct melted samples therefore proved for its in vitro bioactivity and in vitro biocompatibility as a result of the improved hydrophilic-

ity. The groove and the pillar pattern obtained using the laser interference patterning technique with limited exploration of the parameters resulted in an increase in apparent contact angle.

ACKNOWLEDGEMENT

A part of this research has been performed at the Oak Ridge National Laboratory, managed by UT-Battelle, LLC, for the U.S. Department of Energy under contract DE-AC05-00OR22725 and has been sponsored by the Industrial Technologies Program for the Office of Energy Efficiency and Renewable Energy.

References

1. B.O. Palson and S.N. Bhatia, *Tissue Engineering*, 1st edition (New York: Pearson Prentice Hall, 2004), pp. 252–255.
2. D.A. Wahl and J.T. Czernuszka, *European Cells and Materials*, 11 (2006), pp. 43–56.
3. R.M. Streicher et al., *Nanomedicine*, 2 (6) (2007), pp. 861–874.
4. I. Sopyan et al., *Science and Technology of Advanced Materials*, 8 (1-2) (2007), pp. 116–123.
5. A. Kurella and N.B. Dahotre, *Acta Biomaterialia*, 2 (2006), pp. 677–683.
6. S.R. Paital and N.B. Dahotre, *Materials Science and Technology*, 24 (9) (2008), pp. 1144–1161.
7. M.M. Stevens and J.H. George, *Science*, 310 (18) (2005), pp. 1135–1138.
8. T. Blalock et al., *Surface and Coatings Technology*, 201 (12) (2007), pp. 5850–5858.
9. L. Clères et al., *Journal of Biomedical Materials Research Part A*, 49 (1) (1999), pp. 43–52.
10. A.R. Boyd et al., *Surface and Coatings Technology*, 200 (20-21) (2006), pp. 6002–6013.
11. S.R. Paital et al., *Journal of Materials Science: Materials in Medicine* (in press).
12. S.R. Paital and N.B. Dahotre, *Acta Biomaterialia*, 5 (7) (2009), pp. 2763–2772.
13. X.B. Zhou and J.Th.M. DeHosson, *Journal of Materials Research*, 10 (1995), pp. 1984–1992.
14. S.R. Paital et al., *Biofabrication* (in press).
15. C. Daniel et al., *Applied Surface Science*, 208-209 (2003), pp. 317–321.
16. A. Lasagni et al., *Advanced Engineering Materials*, 8 (2006), pp. 580–584.
17. N.B. Dahotre et al., *Philosophical Transactions of the Royal Society A* (in press).
18. J. Bico et al., *Electrophysics Letters*, 55 (2001), pp. 214–220.

Sameer R. Paital, graduate student, is with the Laboratory for Laser Materials Synthesis and Fabrication, Materials Science and Engineering Department, University of Tennessee at Knoxville; Wei He, assistant professor, is with the Mechanical Aerospace and Biomedical Engineering Department, University of Tennessee at Knoxville; and Claus Daniel, senior scientist, is with the Materials Science and Technology Division, Oak Ridge National Laboratory, Oak Ridge, TN. Narendra Dahotre, professor and chairman, is with the Department of Materials Science and Engineering, University of North Texas, Denton, TX, 76207. Dr. Dahotre can be reached at (940) 565-2031; fax (940) 565-4824; e-mail narendra.dahotre@unk.edu.

Characteristics of Hemocompatible TiO₂ Nano-films Produced by the Sol-gel and Anodic Oxidation Techniques

C.E. Schvezov, M.A. Alterach, M.L. Vera, M.R. Rosenberger, and A.E. Ares

Hemocompatible films can be obtained by different techniques which must produce a smooth surface and a desired combination of crystal structure including rutile and anatase structures. Two of the simplest techniques include sol-gel and anodic oxidation. The characteristics of the films associated with the process variables are presented. The most important characteristics of the films are thickness, structure, roughness, and mechanical properties such as adhesion and wear resistance.

INTRODUCTION

Significant advances in biomedical technology in recent decades have greatly improved the health and social integration of people of all ages. One of these technologies is in the field of implants with different functions in the body, such structural materials (e.g., bone implants) or critical functional devices (e.g., heart valves and pacemakers). This progress required advances in materials technology, and efforts are continuing in the search for better materials to improve performance. There is a requirement of biocompatibility which, in the case of devices in contact with blood, is hemocompatibility. This short review presents some advances in the production of hemocompatible titanium alloys coated with titanium dioxide.

COATINGS

Coatings of metals and alloys are widely used to incorporate or improve tribological, biological, corrosion, or aesthetic properties into a component. The choice of the substrate material and type of coating for implants is a complex issue and depends on many aspects, such as the place in the body where they are implanted and where they must

have full biocompatibility, such as tissue integration, hemocompatibility, and tribological and mechanical properties adequate to the desired performance.¹

In the case of tribological properties, wear resistance and a low friction coefficient of a coating increase the lifetime of a component.² The tribological properties necessary in the coating are associated with those needed in the specific device implanted on humans. The required properties are also related to the type of tissue with which the device is in contact, where the coating must integrate and also have the mechanical and tribological performance according to the specific requirements. For instance, in hip and dental implants the device is in contact with both hard (cortical bones) and soft tissue (trabecular bones and muscles). In other cases, like in heart valves, stents, hemodialysis equipment, and pacemakers the most important property is biocompatibility, where the device must be biologi-

cally inert in the blood stream.³

Tribological thin coatings can be produced by physical or chemical methods and the process must produce a coating which must satisfy certain conditions like the relation between hardness of the coating and the substrate, the thickness, the surface roughness, adhesion, and size and hardness of the debris produced by wear,⁴ which in the case of orthopedic implants are most demanded.

In the case of implanted mechanical heart valves, hemocompatibility becomes the most relevant requirement in which the wear and fracture fatigue in the moving hinge are also of major concern because failure could be fatal.

TITANIUM AND TiO₂ COATING

Titanium and its alloys are among the most used material in bone implants as well as heart valve parts,^{5,6} stents, hemodialysis equipment, and pacemakers.³ The use of titanium alloys is expected to increase in the future due to their superior biocompatibility, corrosion resistance, and specific strength compared to other metallic alloys.⁶ Pure Ti, Ti-6Al-4V, and vanadium- and aluminum-free titanium alloys containing non-toxic elements like Nb, Ta, and Zr have tensile strength between 500 and 1000 MPa, elongation between 10 and 20%, and module of elasticity between 55 and 85 GPa.⁶

However, titanium may be dissolved by physiological fluids releasing ions in vivo and may be accumulated in adjacent tissues or transported to distant organs by the blood stream.⁷ This indicates that the oxide layer of TiO₂ formed naturally is not sufficiently protective under wear and therefore additional coating must be deposited in order to

How would you...

...describe the overall significance of this paper?

This paper presents a review of two of the most simple techniques to produce hemocompatible nano-films and their characterization, particularly thickness and crystal structure. The techniques are sol-gel dip coating and anodic oxidation and the film is titanium oxide.

...describe this work to a layperson?

The need of new and better hemocompatible materials for use in prosthetic human devices require the investigation of alternatives such as those presented in the paper. Titanium dioxide is a good candidate and the methods to produce these protective films are discussed. The methods are simple and efficient.

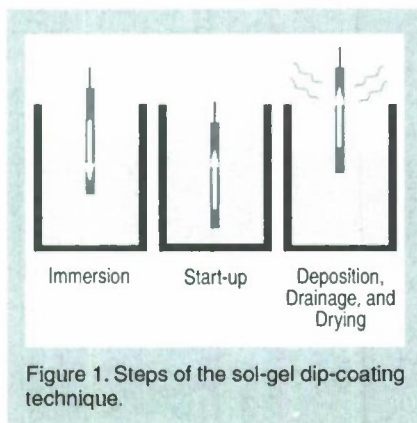


Figure 1. Steps of the sol-gel dip-coating technique.

improve the tribological properties and also improve hemocompatibility of the implant.

TiO₂ is the natural selection for coating a titanium prosthesis. The methods to produce films of TiO₂ reported in the literature include thermal oxidation, anodic oxidation, magnetron sputtering, cathodic arc deposition, plasma immersion ion implantation (PIII), ion beam-enhanced deposition (IBED), and the sol-gel process.^{7,8}

The choice of the method depends on the type of implant and surface requirements according to the tissue and cells in contact and its lifetime expectancy which result in design parameters. There is no general theory for process selection and the performance of a given coating must be proven under conditions as close as possible to the final application.²

In particular a rough porous film of TiO₂ on titanium has been proven to have good osseointegration.⁹ In some cases surface modification produced by sandblasting,^{9,10} acid etching,^{9,10} a combination of both,^{9,10} deposition of calcium phosphate, or hydroxyapatite coatings by ion implantation can also improve biocompatibility.¹⁰ The process route may include first, the treatment of the titanium alloy substrate surface and then, production of the coating by one of the most accessible methods such as thermal or anodic oxidation or the sol-gel technique. On the other hand, hemocompatibility requires smooth surface finishing; in such cases the substrate surface must be smooth since a thin film may reproduce the roughness of the substrate. In some cases, such as in dental applications, rough and smooth surfaces are required in different parts of the implant.⁹

HEMOCOMPATIBILITY

According to Buddy D. Ratner,¹¹ "There is no clear consensus as to which materials are 'blood compatible'," and "There are no standardized methods to assess blood compatibility." Nevertheless a hemocompatible material could be defined one with a surface that is unable to activate the platelet coagulation system or generate alteration or damage in the blood components.³

In this case the surface plays a crucial role, as properties must be maintained during the whole process until it reaches the surgery room and during service in the human body. The qualification of the hemocompatibility is performed by *in vitro* and *in vivo* testing. *In vitro* investigations include clotting time measurements, platelet adhesion, and hemolysis analysis.¹² *In vivo* testing requires the implantation of the component in animals and then in humans with a rigorous protocol.

In general the main factors affecting hemocompatibility are surface roughness, superficial energy, corrosion resistance, and surface electric charge.^{1,3} Roughness increases the surface contact area with blood and may favor blood coagulation¹³ and very smooth surface roughness (3–4 nm) inhibits thrombogenicity.¹⁴ Measurement of clotting time on rutile coating, grown by thermal oxidation, shows that the anti-clotting properties increase when the coating thickness increase from 40 nm to 350 nm.¹⁵

At present there is substantial effort to produce suitable TiO₂ coatings which have been demonstrated to have better blood compatibility than low-temperature isotropic pyrolytic carbon (LTIC), which is widely used in the production of mechanical heart valves,^{5,16} and also diamond-like carbon (DLC) films.^{17,18} The TiO₂ has shown to have better hemocompatibility properties due to its semiconductor properties.¹⁸

The films can be deposited by the techniques mentioned above. In the cases of IBED^{11,16} and PIII^{18,19} the techniques permit doping of the films with others elements which may modify beneficially the physical structure of the material and the physicochemical properties due to changes in the electrical double layer between the surface and the biosystem.¹

In the case of TiO₂, the crystal struc-

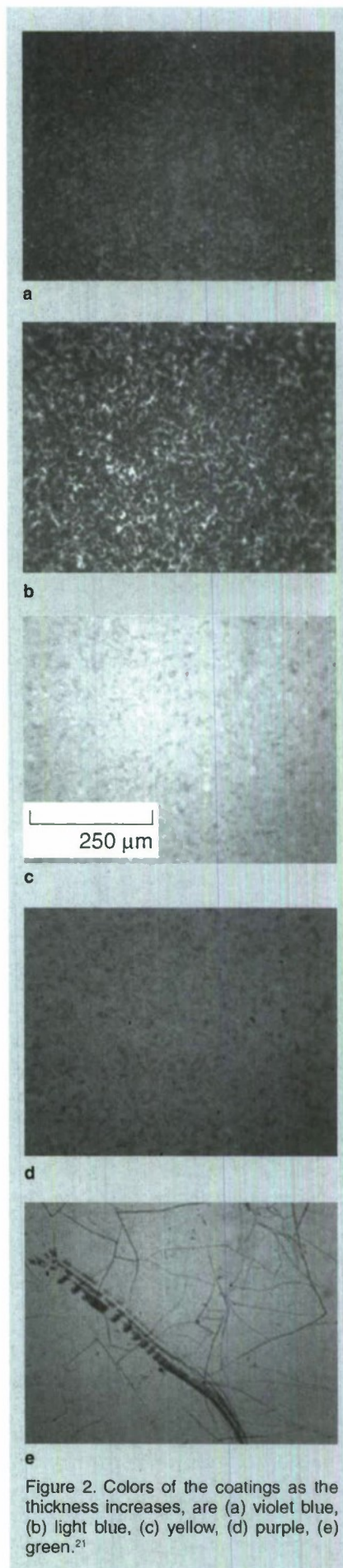


Figure 2. Colors of the coatings as the thickness increases, are (a) violet blue, (b) light blue, (c) yellow, (d) purple, (e) green.²¹

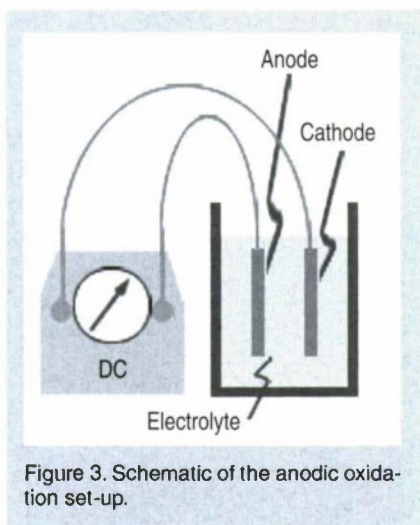


Figure 3. Schematic of the anodic oxidation set-up.

ture of the film is also very important. For instance, the dissolution of titanium metal ions from rutile is one order of magnitude lower than that from anatase.¹⁵ So far, a mixed composition of each crystal structure, rutile and anatase, is preferable for blood compatibility.¹⁸ Research is ongoing to produce nanofilms with these characteristics employing two accessible methods based on sol-gel and anodic oxidation techniques which are presented next.

SOL-GEL DIP-COATING AND ANODIC OXIDATION TECHNIQUES

The sol-gel dip-coating and anodic oxidation techniques are two of the most inexpensive and reliable techniques available today.

Sol-gel Dip-coating

The sol-gel dip-coating technique consists of three main steps as illustrated in Figure 1: immersion of a substrate to be coated in a sol containing particles of the coating material; start-up and withdrawal of the substrate at slow velocity to permit drainage of the sol; and drying of the film. The next step consists of the heat treatment for crystallization.^{8,20} With this technique it is possible to control the film thickness by the withdrawal velocity, number of layers, sol concentration and sol aging time and crystal structure by heat treatment and thickness.^{8,14,20}

Coatings between 25 and 205 nm were obtained and x-ray diffraction analysis determined that the crystal structure is a combination of anatase and rutile phases where the rutile phase increases with the heat treatment temperature.^{8,14}

Table I. Color and Thickness of the Anodic Oxide Films Obtained at Different Voltages³⁰

V	Color	t [nm]
10	Golden	27.21
20	Purple	48.00
30	Light blue	70.46
40	Light green	92.25
50	Yellow	112.64

The thicknesses of the coatings are associated qualitatively with the color due to light interference, which can be observed by the naked eye (Figure 2).⁸

Anodic Oxidation

The anodic oxidation technique schematically shown in Figure 3 is simple to mount and has been extensively applied and studied.^{8,22–29} The anode is made of the metal or alloy to be coated and the cathode is made of a noble metal like platinum, both immersed in an electrolyte. Oxidation occurs by reactions such as those proposed for titanium and the oxide could be formed by either constant voltage or current. The following reactions have been proposed in the literature:²⁸

- Ti / TiO₂ interface: $\text{Ti} \Leftrightarrow \text{Ti}^{+2} + 2\text{e}^-$
- TiO₂ / electrolyte interface: $2\text{H}_2\text{O} \Leftrightarrow 2\text{O}^{2-} + 4\text{H}^+$ (oxygen ions react with titanium to form oxide); $2\text{H}_2\text{O} \Leftrightarrow \text{O}_2 (\text{gas}) + 4\text{H}^+ + 4\text{e}^-$ (oxygen gas evolves)
- In both interfaces: $\text{Ti}^{+2} + 2\text{O}^{2-} \Leftrightarrow \text{TiO}_2 + 2\text{e}^-$

The process can be controlled by the following parameters: concentration of the electrolyte, current density, anodic voltage, temperature, agitation speed, time and surface area ratios of cathode to anode. In a 1M H₂SO₄ solution used as electrolyte and using different constant voltages (V) it is possible to produce coatings of different thickness (t) as with the sol-gel technique. The relation among voltage, color, and thickness is shown in Table I³⁰ and Figure 4.³¹

It has been found that thickness and crystal structure are related.²⁴ Although that relationship is unclear, the possible sequence is amorphous/unknown, anatase, anatase and rutile and rutile phases as thickness increases. Anatase and rutile could alternatively be obtained by heat treatment.²⁹

Another important result of this tech-

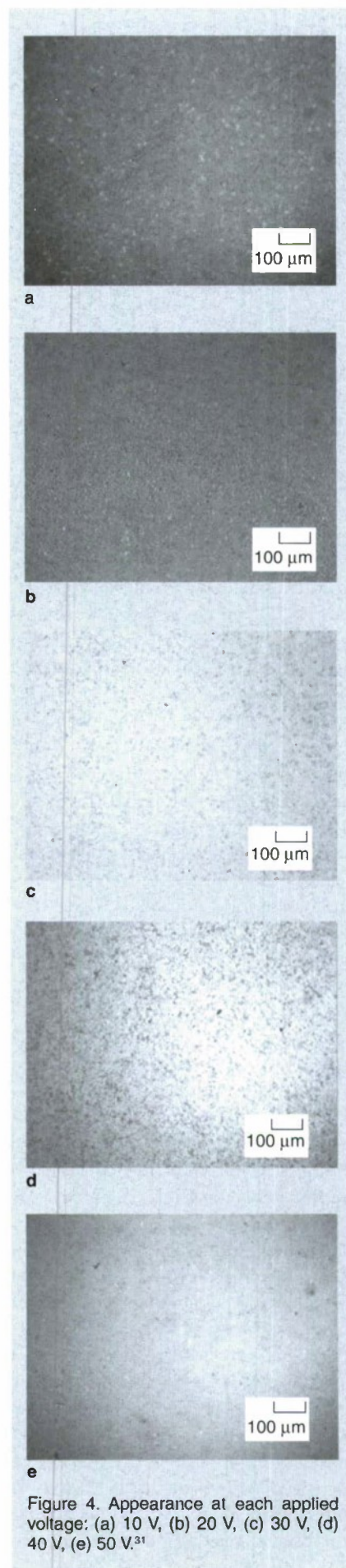


Figure 4. Appearance at each applied voltage: (a) 10 V, (b) 20 V, (c) 30 V, (d) 40 V, (e) 50 V.³¹

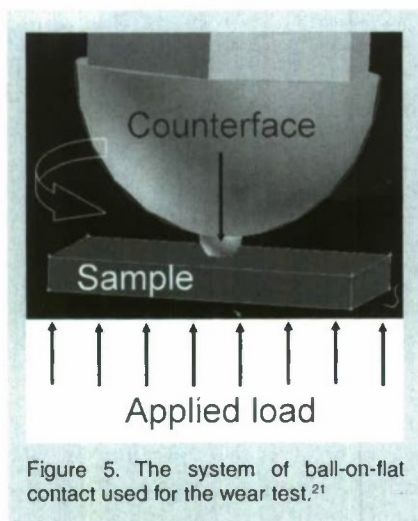


Figure 5. The system of ball-on-flat contact used for the wear test.²¹

nique is that at higher voltages the film increases porosity and therefore be suitable for osseointegration.^{27,31} It has also been found that the thickness depends on the texture of the substrate and could vary from grain to grain.^{25,32}

ADHESION AND WEAR PROPERTIES

Implants in a blood stream such as a heart valve or a stent not only must satisfy hemocompatibility criteria but also must have certain mechanical properties according to the required performance. In the case of heart valves the TiO₂ coating must have a good adhesion and moving parts must wear at a rate comparable with the expected valve lifetime.

Assays were performed on TiO₂ coatings obtained by both techniques using a scratch test to measure adhesion³³ and a ball-on-flat test for wear. In the case of adhesion an increasing load applied at a 2N/mm rate and up to 10N did not produce failure of anodic oxide films in the whole range of thicknesses listed in Table I. In the case of sol-gel dip-coatings the coating adhesion increases with the number of deposited layers and temperature of the heat treatment.³⁴

In the wear tests, a rotating ball-on-flat device was used in order to approximate the movement of a pivot in a prosthetic heart valve, as shown in Figure 5. Lubricated tests were performed, employing a 6.35 mm in diameter glass ball as counterface. A constant 7 rpm and 1 N in load^{8,35} were chosen to perform the test; this value exceeds more than 50 times the stress calculated on the valve pivot. Optical microscopy was used to characterize the film before and after the wear test.

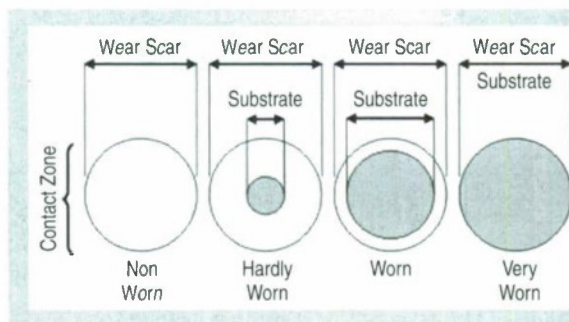


Figure 6. Wear scar categories utilized in the tests.³⁴

As a measure of wear, a qualitative scale has been proposed and utilized as shown in Figure 6,³⁵ where the shaded area is the area of the coating which has been removed due to wear. It is found that tri-layer films are more resistant when each layer has a high temperature heat treatment that assures the crystallization of them.

CONCLUSIONS

Coating continues to be a very active area of research with a substantial amount of effort directed to produce better implants, in particular those which require hemocompatibility properties. Titanium alloys coated with titanium oxide nano-films is one of the suitable combinations for implants where hemocompatibility properties are required as well as good mechanical and tribological behavior.

Anodic oxidation and sol-gel techniques, which are two of the most simple to implement and control, can be used to produce nano-films with mechanical and tribological properties with overall qualities to build implants. Testing of the coatings requires specific systems which reproduce as much as possible the in-vivo conditions.

References

1. R. Thull, *Biomolecular Engineering*, 19 (2-6) (2002), pp. 43–50.
2. S. Hogmark, S. Jacobson, and M. Larsson, *Wear*, 246 (2000), pp. 20–33.
3. M. Schaldach, *Electrotherapy of the Heart* (Berlin: Springer-Verlag, 1993).
4. K. Holmberg, H. Ronkainen, and A. Matthews, *Ceramics International*, 26 (2000), pp. 787–795.
5. O.N. Amerio et al., *Revista Argentina de Cirugía Cardiovascular*, 4 (2006), pp. 70–76.
6. M. Niinomi, *Materials Science and Engineering A*, 243 (1998), pp. 231–236.
7. Y.X. Leng et al., *Surface and Coatings Technology*, 156 (2002), pp. 295–300.
8. D. Velten et al., *Journal of Biomedical Materials Research Part A*, 59(1) (2001), pp. 18–28.
9. C.N. Elias et al., *Journal of the Mechanical Behavior of Biomedical Materials*, 1 (2008), pp. 234–242.
10. H.-J. Oh et al., *Surface and Coatings Technology*, 198 (2005), pp. 247–252.
11. B.D. Ratner, *Biomaterials*, 28 (2007), pp. 5144–5147.
12. "Biological Evaluation of Medical Devices. Selection of Test for Interactions of Blood, STANDARD ISO 10993-4 (Geneva, Switzerland: International Organization for Standardization, 2006).
13. T. Hasebe et al., *Diamond & Related Materials*, 16 (2007), pp. 1343–1348.
14. J.-X. Liu et al., *Thin Solid Films*, 429 (2003), pp. 225–230.
15. N. Huang et al., *Journal of Biomaterials Applications*, 8 (1994), pp. 404–412.
16. X. Wang et al., *Surface and Coatings Technology*, 128-129 (2000), pp. 36–42.
17. X. Liu, P.K. Chu, and C. Ding, *Materials Science and Engineering R*, 47 (2004), pp. 49–121.
18. N. Huang et al., *Biomaterials*, 24 (2003), pp. 2177–2187.
19. I.A. Tsyganov et al., *Nuclear Instruments and Methods in Physics Research B*, 257 (2007), pp. 122–127.
20. C.J. Brinker and A.J. Hurd, *Journal of Physics III France*, 4 (1994), pp. 1231–1242.
21. M.A. Alterach et al., *Anales de la Asociación Física Argentina*, 20 (2008) pp. 147–153.
22. A. Aladjem, *Journal of Materials Science*, 8 (1973), pp. 688–704.
23. M.V. Diamanti and M.P. Pedferri, *Corrosion Science*, 49 (2007), pp. 939–948.
24. Z. Xia et al., *Electrochemistry Communications*, 9 (2007), pp. 850–856.
25. M.V. Diamanti, M.P. Pedferri, and C.A. Schuh, *Metallurgical and Materials Transactions A*, 39 (2008), pp. 2143–2147.
26. Y.T. Sul et al., *Biomaterials*, 23 (2002), pp. 491–501.
27. X. Cui et al., *Dental Materials*, 25 (2009), pp. 80–86.
28. K.-H. Kim and N. Ramaswamy, *Dental Materials Journal*, 28(1) (2009), pp. 20–36.
29. R. Palombari et al., *Solar Energy Materials & Solar Cells*, 71 (2002), pp. 359–368.
30. M.L. Vera et al., *Anales AFA 2009*, in press.
31. M.L. Vera et al., *Supplemental Proceedings, Volume 2: Materials Characterization, Computation, Modeling and Energy* (Warrendale, PA: TMS, 2010), pp. 625–632.
32. M.L. Vera et al., *SAM-CONAMET 2009: 9º Congreso Internacional de Metalurgia y Materiales* (Buenos Aires, Argentina, 19–23 Octubre 2009, Actas en edición), <http://www.cnea.gov.ar/samconamet2009/>.
33. S. Jacobsson et al., *Scratch Testing*, *ASM Handbook 18* (Materials Park, OH: ASM International, 1997), pp. 820–837.
34. M.A. Alterach et al., *Supplemental Proceedings, Volume 2: Materials Characterization, Computation, Modeling and Energy* (Warrendale, PA: TMS, 2010), pp. 609–616.
35. W. Zhang et al., *Ceramics International*, 35 (2009), pp. 1513–1520.

Carlos Enrique Schvezov, professor and researcher, Maria Laura Vera and Miguel Angel Alterach, Ph.D. students, Mario Roberto Rosenberger, researcher, and Alicia Esther Ares, associate professor and researcher, are with the Department of Materials, Modeling and Metrology at the University of Misiones and CONICET, 1552 Azara St. (3300) Posadas, Misiones, Argentina. Dr. Schvezov can be reached at +54 3752427491 ext: 153; fax: +54 3752425414; e-mail: schvezov@fceqyn.unam.edu.ar.

Effect of Current Density on the Pulsed Co-electrodeposition of Nanocrystalline Nickel-copper Alloys

Mansi Agarwal, Vinod Kumar, S.R.K. Malladi, R. Balasubramaniam, and Kantesh Balani

Author's Note: Co-author R. Balasubramaniam passed away on Dec. 9, 2009.

Nanocrystalline coatings have become an essential component of single and multilayer electronic packaging, ship building, mining, magnetorestrictive applications, etc. In the current work, nanocrystalline Ni-Cu films were synthesized by pulsed electrodeposition using a citrate bath. Cathodic polarization experiments were carried out for optimization of bath composition to co-deposit nanocrystalline Ni-Cu films. Depositions were optimized between the current density range of 0.05–0.25 A·cm⁻² to achieve a uniform equiaxed coating with a target Ni content of greater than 70% owing to their superior corrosion resistance and enhanced hardness.

INTRODUCTION

In recent decades, interest in the synthesis of nano-sized materials has increased because it was found that decreasing the size of crystals below a threshold value may result in a large change of magnetic, mechanical, electrical, optical, and corrosion properties.^{1–4} Nowadays, in order to fabricate nanocrystalline metallic films, many deposition techniques are available, such as sputtering, molecular beam epitaxy, vacuum evaporation, sol-gel, thermal spray, etc.⁵ But all these methods require high precision process control, which demand higher capital cost and incur huge material waste. But electrodeposition is an established and inexpensive technology among other fabricating processes which is accomplished by fabricating metallic alloys using low-temperature synthesis from aqueous solutions.⁶ This has an advantage of preparation of films over a large surface area without impairing materi-

als purity in a relatively shorter period of time. In the electrodeposition process, the film properties mainly depend on deposition conditions, e.g., current density, deposition potential, bath type and electrolyte pH.^{2,6–9} By tailoring the electrochemical deposition conditions as well as physical parameters such as thickness, the substrate type,

and orientation, it is possible to control and optimize the electrodeposited films (such as coating thickness, cluster size, etc.).^{3,10} Conventionally direct current (dc) electrodeposition could be only possible above a critical current density, whereas nanosized Ni-Cu alloy deposits require the application of much higher current densities, which normally leads to cracks in films.^{6,10} In comparison to conventional dc electrodeposition, pulse electrodeposition provides more uniform and crack-free deposits with required properties.^{6,10}

Ni and Cu have identical crystal structure, face-centered cubic (fcc), and almost the same atomic radius (Ni~0.125 nm and Cu~0.128 nm), which is approximate to 2.4% misfit, so it becomes feasible to synthesize solid solution of Ni-Cu strain free films by electrodeposition.¹⁰ The pulse electrodeposited nanocrystalline (nc) Ni-Cu alloys receive great attention, both as single layer and multilayer films, due to their magnetoresistive properties, enhanced mechanical properties, and improved corrosion resistance.^{2,8,10,11} However, it is important to note that superior corrosion resistance can only be possible when the nc films are dense and defect free.⁸

In the current work, nanocrystalline Ni-Cu films were pulse electrodeposited on Cu substrates using a sulfate bath. During synthesis of nanocrystalline Ni-Cu films, the current density was varied in order to vary film composition, thickness, and cluster size of the nanocrystalline Ni-Cu alloys. A composition of greater than 70% Ni is targeted to achieve enhanced corrosion resistance and hardness.^{2,8,11} Enhanced Ni content has shown to enhance the hardness of the co-electrodeposited Ni-Cu films. X-ray diffraction (XRD)

How would you...

...describe the overall significance of this paper?

Nanocrystalline Ni-Cu coatings are essential for myriad applications such as enhanced corrosion resistance and improved hardness in magnetorestrictive coatings, layered electronic packaging, mining, etc. Novel electrolytic bath achieving Ni-Cu co-deposits via variation of current density has been attained.

...describe this work to a materials science and engineering professional with no experience in your technical specialty?

Co-electrodeposition of the nanocrystalline Ni-Cu coatings has been achieved using a single electrolytic bath by controlling the current density of the deposition. Superior nanocrystalline coatings (size 18–31 nm) with enhanced Ni content (>70%) have been achieved, eliciting superior corrosion resistance and hardness.

...describe this work to a layperson?

Superior Ni-Cu coatings, with improved corrosion resistance and hardness, have been developed on an annealed copper substrate. The composition of the co-deposits can be tailored using a single electrolytic bath just by changing the current density of the electrodeposition. These coatings can be used in single and multilayer electronic packaging, magnetorestrictive applications, mining, and ship building applications.

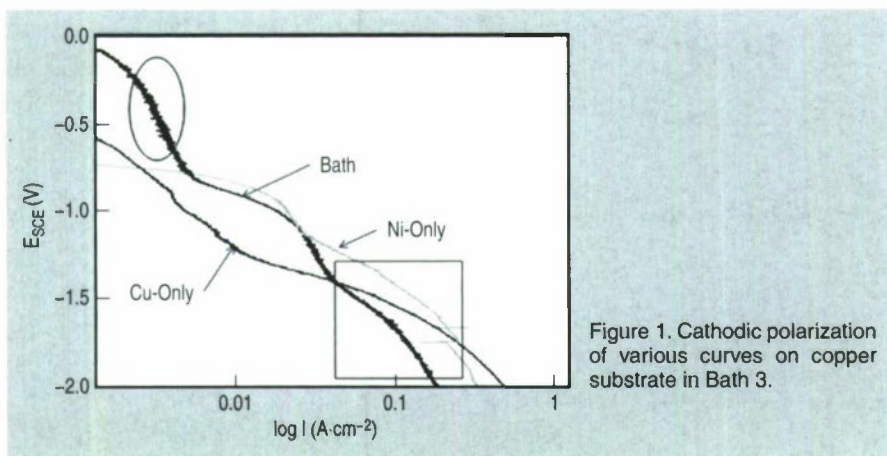


Figure 1. Cathodic polarization of various curves on copper substrate in Bath 3.

has been utilized to evaluate micro-strain in the deposits via calculation of average lattice constant in the pulsed co-electrodeposited polycrystalline Ni-Cu films.⁸ The transmission electron microscope (TEM) has confirmed the nanocrystalline nature of the NiCu deposits. The novelty of this work lies in assessing the deposition pattern of both Ni and Cu in isolation, and inducing a complexing agent for impeding the Cu deposition and achieving Ni-Cu co-deposits via variation of current density in a modified electrolytic bath.

See the sidebar for experimental details.

RESULTS AND DISCUSSION

Co-electrodeposition of the Ni-Cu Films

Initially, the cathodic polarization experiment was conducted by adopting two electrolytic baths: (i) removing the Ni-source (i.e. retaining 0.02M $\text{CuSO}_4 \cdot 5\text{H}_2\text{O}$, and using Pt as anode instead of commercial grade Ni anode to avoid Ni deposition), and (ii) removing the Cu-source (i.e., retaining 0.2 M $\text{NiSO}_4 \cdot 7\text{H}_2\text{O}$) with citrate complexing agent (0.2 M $\text{Na}_3\text{C}_6\text{H}_5\text{O}_7 \cdot 2\text{H}_2\text{O}$, tri-sodium citrate), see Figure 1. These depositions allow their comparison when both the Cu and Ni sources are present in the electrolytic bath (bath 3). It can be observed that the net polarization curve (of bath 3), Figure 1, is a result of the combined response from that of individual polarization curves of Cu and Ni. Additionally, it is to be noted that the standard reduction potential for Cu (+ 0.34 V, SHE) is far apart from that of Ni (−0.25 V, SHE). Hence a complexing agent is required in order

to co-deposit both of these metals simultaneously.⁸

The region marked in the oval (Figure 1) shows the effect of complexing agent which enhances the diffusion region (and impedes Cu-deposition) so the Cu reaction curve intersects the Ni reaction curve. Decrease in the deposition kinetics also indicates that Cu-alone will not get preferentially deposited. Beyond this region (i.e. current densities higher than that at crossover $\sim 0.008 \text{ A}\cdot\text{cm}^{-2}$), deposition of both Cu and Ni occur simultaneously, thereby representing the region of interest in order to obtain co-deposits of Cu and Ni. From this diagram, it can be noted that at lower current densities the expected percentage of Cu in the deposit should be relatively higher, while at higher current densities the expected percentage of Ni should be higher. Hence the

experiments were carried out at current densities from 0.05–0.25 $\text{A}\cdot\text{cm}^{-2}$ to obtain a range of co-deposited Ni-Cu compositions.

Microstructural Characterization of Co-Electrodeposited Ni-Cu

The cross-sectional morphology of the co-deposited Ni-Cu is presented in Figure 2a–d, showing good adherence of the coating with the annealed Cu substrate. The inset shows the overall coating morphology and deposit thickness. Deposition times were decreased with the increasing current density in order to achieve coatings in the range of 25–80 μm for their comprehensive phase and microstructure analysis (Table II). It can be observed that inhomogeneous deposit result at a current density of 0.05 $\text{A}\cdot\text{cm}^{-2}$ (Figure 2a), whereas thick deposits at a current density of 0.15 $\text{A}\cdot\text{cm}^{-2}$ lead to sub-surface cracking of the deposit (Figure 2b). Even at higher current density of 0.20 $\text{A}\cdot\text{cm}^{-2}$, the equiaxed structure is maintained (Figure 2c), but further increase in the current density of 0.25 $\text{A}\cdot\text{cm}^{-2}$ has been shown to destruct the equiaxed grain structure (Figure 2d).

The XRD analysis of the deposits (Figure 3) revealed the overlapping Ni-Cu peak-shifts indicating the formation of solid solution. Peak-shifts toward higher 2θ with increasing current density indicate lowering of the lattice parameter. As per Vegard's law, with

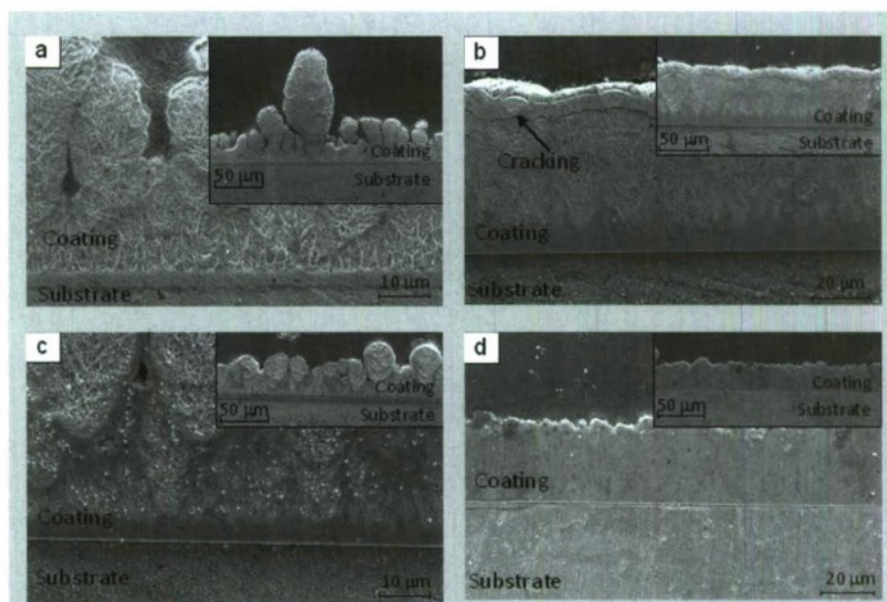


Figure 2: Co-electrodeposited Ni-Cu coatings on an annealed substrate at current density of (a) 0.05 $\text{A}\cdot\text{cm}^{-2}$, (b) 0.15 $\text{A}\cdot\text{cm}^{-2}$, (c) 0.20 $\text{A}\cdot\text{cm}^{-2}$, and (d) 0.25 $\text{A}\cdot\text{cm}^{-2}$.

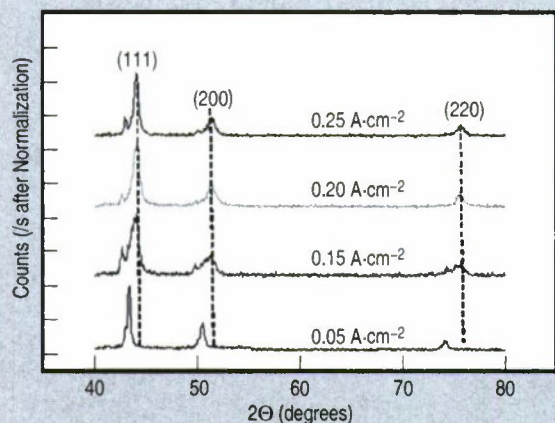


Figure 3. X-ray diffraction spectrum of electrodeposited coatings showing overlap of the indexed planes of Cu/Ni phases.

increasing current density, the lattice parameter reaches from that of pure Cu (3.615 Å) toward that of Ni (3.523 Å), indicating the formation of Ni-Cu solid solution.⁶ Correspondingly, electrodeposition has induced lattice strain to the order of only less than 1%, Table I, since the annealed Cu substrate has a matching lattice parameter (3.615 Å). Thick and uniform deposits resulted in

higher strains (Table I) as observed in coatings deposited at current density of 0.15 and 0.25 A·cm⁻². Eventually, cracking of the film is also observed at current density of 0.15 A·cm⁻² (Figure 2b). The crystallite size evaluated from the Scherrer equation varies between 18–31 nm, with the minimum crystallite size depicted by deposition at current density of 0.20 A·cm⁻². Mar-

ginal increase in the crystallite size at a current density of 0.25 A·cm⁻² might be expected due to dominant Ni content of the deposit experiencing lattice strain mismatch being imposed by the annealed Cu substrate.

The morphology of grain clustering is shown in Figure 4. The colonies are largely equiaxed in nature and vary between 3–15 μm. No phase contrast could be observed in the backscattered electron images (not shown here) since Cu and Ni lie adjacent to each other in the periodic table. The variation in colony size as a function of current density is shown in Table II. The difference in morphology arises because lower current density allows only a few crystals to nucleate, and high deposition time allows the growth of grains leading to their impingement leading to preferential growth of selected few crystals. Hence the clusters are bigger (~10.35 μm) at a current density of 0.05 A·cm⁻² when compared to that (~6.12 μm) at a

EXPERIMENTAL DETAILS

Electrodeposition of Ni-Cu Alloys

All depositions were carried out in a double-walled cell, connected to the constant temperature bath maintained at 55°C (Figure A). The double-walled cell was placed on the magnetic stirrer and the electrodes were connected to the potentiostat (model 263A, Princeton Applied Research, USA) as shown in Figure A, for pulsed current deposition using constant temperature bath (Julabo F-32, Germany), magnetic stirrer (SCHOTT, Germany). Virtual potentiostat interface allowed variations of the parameters of pulse deposition, such as the on-time (t_{on}), off-time (t_{off}), duty cycle, period, and time of deposition using a user-interface program. Duty cycle is defined as ($t_{on} / t_{on} + t_{off}$) given in percentage, and the period of deposition is the sum of t_{on} and t_{off} usually in milliseconds.^{11,12} In the present study, a square wave pulse generator program was used for defining the deposition current.

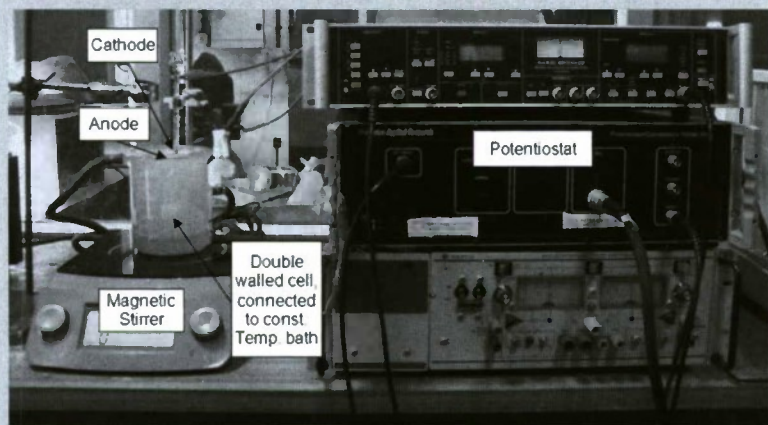


Figure A. Experimental setup showing double walled cell placed on the magnetic stirrer and the connection of the electrodes to the potentiostat.

Initially mild steel was used as a substrate for coating deposition, but mild steel exhibited cracking of the coating, and as a result, peeling. Cracking of the coating was attributed to the stress in the substrate (due to lattice strains), thus, annealed mild steel was chosen as a substrate. However, there was a decrease in the total weight of the cathode after every deposition, which was attributed to the spontaneous double decomposition reaction (i.e., $Fe + Cu_2^{+2} \rightarrow Fe^{+2} + Cu$). Consequently, annealed Cu (size 20 × 20 mm) was chosen as the substrate because of its excellent adherence to Ni and Ni based alloys.^{13,14} A polished and ultrasonically cleaned cold rolled Ni (size 10 cm × 2 cm × 3 mm) was used as the anode. Using Ni as anode ensured enrichment of the Ni ions in the bulk electrolyte, as the anode gets consumed during the deposition. According to the literature two electrolytic baths were tried for the co-deposition of Ni and Cu (Table A).

Bath 1 showed good deposits but the current efficiency⁹ obtained was low since coatings were very thin (<10 μm) even for prolonged deposition time (>240 min.), whereas bath 2 resulted non-uniform deposits. It was deduced that the bath inefficiency of bath 1 could have been due to the low concentration of both Cu^{+2} and Ni^{+2} ions in the solution. Hence an experimental bath was synthesized (bath 3) where the concentrations of Cu and Ni ions were increased by a factor of ten, Table A. To control the Cu and Ni content in the electrodeposition, current densities in the range of 0.05–0.25 A·cm⁻² were used at a duty cycle of 20% and time period of 30 ms.

Potentiodynamic Polarization for Selection of Optimized Current Density

Usually, potentiodynamic polarization experiments are carried out to study the electrochemical behavior of metals in particular solutions, and are carried out in ei-

current density of 0.05 A.cm^{-2} . Since the successive deposition develops on the predeposited clusters, cluster size can be a dominant feature in deciding surface roughness.¹⁵ The deposited coatings in the current work were very shiny and reflective, but their surface roughness was not evaluated.

As expected, higher concentration of the Ni can be observed with increasing current density, Table II (also see Figure 1). It is also reported in the literature that the dominant ferromagnetic coating (Ni-dominated) or diamagnetic coatings (Cu-dominated) can be tailored via pulsed electrodeposition.⁶ Moreover, the combined effect of composition (with varying current density) and finer grain size (due to Hall Petch relationship) in enhancing the hardness is observed in Table II. Owing to solid solution strengthening, higher hardness is observed with increasing Ni content in the Cu matrix ($\sim 150\text{--}170 \text{ H}_{\text{V0.01}}$) when compared to

Table I. Coating Thickness, Crystallite Size, and Strain in the Co-electrodeposited Ni-Cu Coatings

Current Density (A.cm^{-2})	Deposition Time (min.)	Coating Thickness (μm)	Crystallite Size* (nm)	Lattice Parameter (\AA)	Lattice Strain*
0.05	785	10–140	26	3.618 ± 0.002	+0.0012
0.15	200	70–80	31	3.562 ± 0.003	–0.0094
0.20	100	25–70	18	3.548 ± 0.001	–0.0053
0.25	50	30–40	27	3.552 ± 0.001	–0.0084

* The crystallite size and lattice strain showed a standard deviation of $\pm 10\%$

that of pure Cu or with lower ($<70\%$) Ni content ($\sim 65 \text{ H}_{\text{V0.01}}$). This trend is also observed by Pellicer,² and such coatings are targeted for their superior corrosion resistance as well.^{8,11}

Sample preparation for TEM involved dissolving the substrate in the chromic acid solution. Though the coating was covered with a paint coating of nitro-cellulose in order to prevent the damage, absence of pitting or any damage to the coating affirmed the formation of Ni-Cu solid solution.

This implication is justified because presence of free Cu in the coating otherwise would have been dissolved as well in the chromic acid. Thereby, non-dissolution of the electrodeposited coating affirmed formation of solid-solution in the co-electrodeposited Ni-Cu film (confirmed after observing varying lattice parameter with increasing Ni content as per Vegard's law).

Transmission electron microscope images of co-deposited Ni-Cu coating at a current density of 0.02 A.cm^{-2}

ther flat or round bottom cells, without agitating the electrolyte. In this case, the potentiodynamic polarization experiments were carried out with stirring in order to understand the nature of reduction reactions that take place on the cathode surface.⁸ More importantly, the aim was to determine the range of current density for co-depositing Ni-Cu alloys. The polarization experiments were performed in the same cell set-up that was used for deposition. Annealed Cu substrate served as the working electrode, saturated calomel electrode (SCE) as the reference electrode, and commercial-grade Ni as counter electrode. The deposition was carried out using bath 3 electrolyte (Table A), at a scan rate of 1 mV/s . All the experiments were conducted without stabilizing the open circuit potential (OCP) because deposition begins immediately after the substrate is immersed in the solution under normal conditions. The potential was scanned ranging from the as-immersed OCP value to $2,000 \text{ mV}$. The bath temperature was maintained at 55°C and the electrolytic bath was agitated by continuous stirring at 300 rpm .

Characterization of Co-Electrodeposited Nanocrystalline Ni-Cu Films

X-ray diffraction was done (using Cu-K α radiation in SEIFERT, ISO-DEBYEFLEX-2002 Diffractometer) to confirm the phase purity and the formation of solid solution in the electrodeposits. All samples were scanned at the rate of 3 degrees/min , in the range of $40\text{--}80$. Consequently, Scherrer equation was utilized to evaluate the crystallite size while removing the instrumental broadening via using a standard Si sample. To analyze the morphology, surfaces of the co-electrodeposited Ni-Cu alloys on an annealed Cu substrate were observed using a scanning electron microscope (Carl Zeiss

EVO50). Compositional analysis of the deposits was done with an EDAX detector (Oxford Instruments model 8100, England).

To correlate the composition and hardness, Vickers microhardness testing was done at five random locations to evaluate the hardness in the cross section of the deposits at a load of 10 g with a dwell time of 15 s .

The grain sizes were confirmed using bright field and dark field imaging in a transmission electron microscope. (TEM, FEI Tecnai 2007) operated at 200 kV . Selected area diffraction patterns (SADP) in the TEM further confirmed polycrystalline nature of the deposits. The annealed Cu substrate was chemically dissolved using an aqueous solution of chromium trioxide (250 g/L) and $98 \text{ wt.}\% \text{ H}_2\text{SO}_4$ (20 mL/L). Successively, the stripped Ni-Cu deposit was cleaned using an ultrasonic cleaner (Transsonic digitals, Singapore) in distilled water for 10 min . and then thoroughly cleaned in acetone. Discs of 3 mm diameter were cut using spark erosion, and twin jet polished ($20 \text{ vol.}\% \text{ perchloric acid}$ and $80 \text{ vol.}\% \text{ methanol}$) for creating electron transparency in the center of the discs.

Table A. Electrolyte Bath Compositions Utilized for the Co-deposition of Ni-Cu

	Composition	Concentration	Parameters	Reference
Bath 1	$\text{NiSO}_4 \cdot 7\text{H}_2\text{O}$	0.002 M	Temp. 55°C	6
	$\text{CuSO}_4 \cdot 5\text{H}_2\text{O}$	0.02 M		
	$\text{Na}_3\text{C}_6\text{H}_5\text{O}_7 \cdot 2\text{H}_2\text{O}$	0.2 M		
Bath 2	$\text{NiSO}_4 \cdot 7\text{H}_2\text{O}$	0.475 M	$\text{pH} = 9.0$ (Maintained using NH_3 addition) Temp: 20°C	8, 11
	$\text{CuSO}_4 \cdot 5\text{H}_2\text{O}$	0.125 M		
	$\text{Na}_3\text{C}_6\text{H}_5\text{O}_7 \cdot 2\text{H}_2\text{O}$	0.2 M		
Bath 3	$\text{NiSO}_4 \cdot 7\text{H}_2\text{O}$	0.2 M	Temp. 55°C	Current Work
	$\text{CuSO}_4 \cdot 5\text{H}_2\text{O}$	0.02 M		
	$\text{Na}_3\text{C}_6\text{H}_5\text{O}_7 \cdot 2\text{H}_2\text{O}$	0.2 M		

Table II. Colony Size and Chemical Composition Variation with Resulting Hardness of Co-electrodeposited Ni-Cu Films

Current Density (A·cm ⁻²)	Colony Size (μm)	Cu (%)	Ni (%)	Average Hardness (H _{v0.01})
0.05	10.35 ± 0.85	87.1 ± 7.1	12.9 ± 6.9	65.9 ± 8.6
0.15	8.49 ± 0.36	62.3 ± 8.7	37.7 ± 8.4	129.5 ± 11.9
0.20	6.83 ± 0.48	25.8 ± 4.9	74.2 ± 4.9	168.9 ± 17.3
0.25	6.12 ± 0.42	22.6 ± 3.0	77.4 ± 3.0	149.0 ± 15.9

revealed that the Ni-Cu grains in the observed section plane were nanocrystalline (~20 nm), largely equiaxed, and frequently contained twins (Figure 5). The formation of these twins can be attributed to the effects of epitaxy or pseudomorphism, by which the deposit tends to follow the structure present in the substrate.^{6,8,9} The selected area diffraction ring pattern of the electrodeposited Ni-Cu, as shown in the inset of Figure 5, confirms the polycrystalline nature of the deposit.

The crystallite size of the deposit ~20 nm is similar to that obtained from x-ray diffraction Scherrer equation. Since the nanocrystallines resist the deformation owing to indentation, higher hardness can be envisaged (Table II). Further, the nanoprobe EDAX was utilized to extract chemical composition at various regions (not presented here). Similar chemical composition observed both in a large area (of 200 × 200 nm) and individual spots (~7 spots) confirm that the composition of

spots is similar to that of a larger area (i.e., the grains are not individual deposits of isolated Cu and isolated Ni but form a solid solution).

CONCLUSIONS

The enhanced content of Ni with increasing current density of deposition allows controlling the composition of deposits in terms of achieving enhanced hardness (~149 H_{v0.01}) in comparison to that of low Ni-Cu deposits (~66 H_{v0.01}). Colony-type morphology commonly observed in electrodeposits tends to depend on the current density and deposition times. Consequently, the films can be tailored to yield ferromagnetism (Ni-dominant) or diamagnetism (Cu-dominant) nature merely by varying current density in a single electrolytic bath used for electrodeposition.

Transmission electron microscopy revealed the nanocrystalline nature (~18–31 nm) of the electrodeposits affirming Ni-Cu solid solution strength-

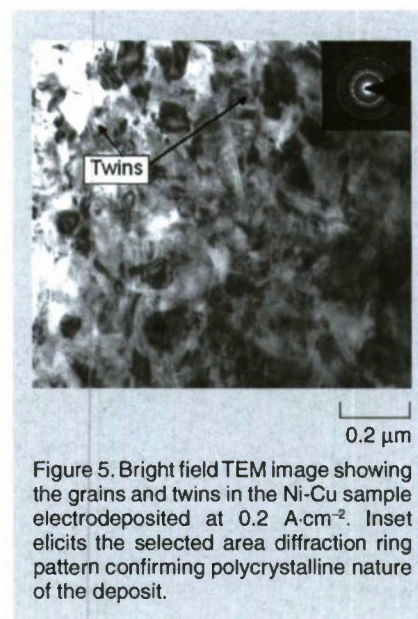


Figure 5. Bright field TEM image showing the grains and twins in the Ni-Cu sample electrodeposited at 0.2 A·cm⁻². Inset elicits the selected area diffraction ring pattern confirming polycrystalline nature of the deposit.

ening to result enhanced hardness with increasing Ni content.

ACKNOWLEDGMENT

KB acknowledges ISRO grant-2009 of space technology cell (STC) at IIT Kanpur to partially support this work.

References

1. V.P. Gilbin, B.V. Kuznetsov, and T.N. Vorobyova, *J. Alloys & Compounds*, 386 (2005), pp 139–143.s.
2. E. Pellicer et al., *Proc. in the International Conference on Advanced Materials* (Zurich: IRIS, 2009), p. R513.
3. H. Natter and R. Hempelmann, *Electrochimica Acta*, 49 (2003), pp 51–61.
4. M. Troyon and L. Wang, *Appl. Surf. Sci.*, 103 (1996), pp. 517–523.
5. T. Miyake et al., *Thin Solid Films*, 397 (2001), pp. 83–89.
6. I. Baskaran et al., *Mater. Lett.*, 60 (2006), pp. 1990–1995.
7. X. Chui and W. Chen, *J. Electrochemical Society*, 155 (2008), pp. K133–K139.
8. S.K. Ghosh et al., *Surf. Coat. Tech.*, 126 (2000), pp. 48–63.
9. R.Y. Ying, *J. Electrochem. Soc.: Electrochem. Sci. Tech.*, 135 (1988), pp. 2957–2964.
10. M. Alper et al., *J. Alloys & Compounds*, 453 (2008), pp. 15–19.
11. M. Cherkaoui et al., *Surf. Coat. Tech.*, 34 (1988), pp. 243–252.
12. N. Ibl, *Surf. Tech.*, 10 (1980), pp. 81–104.
13. A.G. Ives et al., *Electrochimica Acta*, 15 (1970), pp. 1797–1801.
14. H.L. Gaiser and G.N.V. Wyk, *Thin Solid Films*, 15 (1973), pp. 163–172.
15. S. Ruan and C.A. Schuh, *Scripta Mater.*, 59 (2008), pp. 1218–1221.

Mansi Agarwal, Vinod Kumar, and S.R.K. Maladi, research scholars, R. Balasubramaniam (deceased), and Kantesh Balani, associate professor, are with the Department of Materials and Metallurgical Engineering, Indian Institute of Technology Kanpur, Kanpur 208016, India; Professor R. Balasubramaniam passed away on December 9, 2009. Prof. Balani can be reached at +91-512-259-6194; e-mail kbalani@iitk.ac.in.

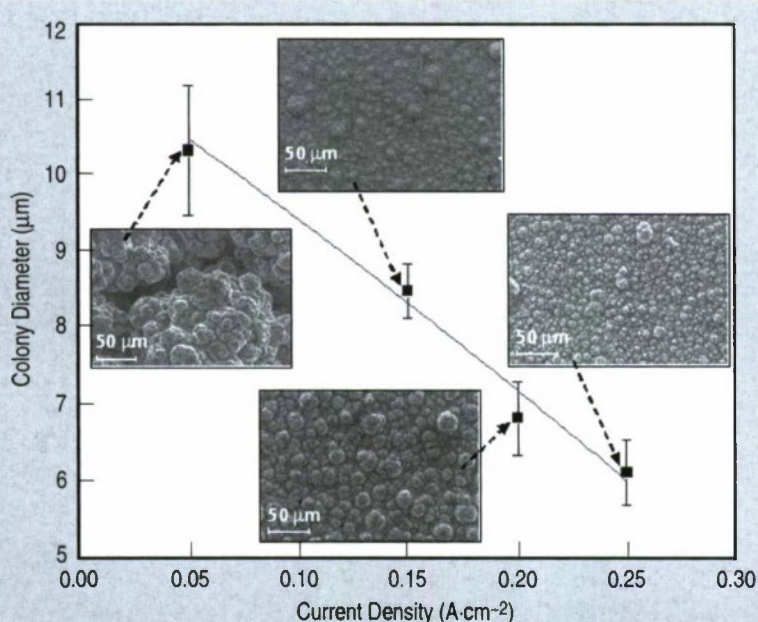


Figure 4. Variation in the colony size observed on the top surface of the deposits as a function of current density.

Symposia Proposals and Abstract Submissions: For TMS-sponsored meetings, symposia proposals and abstracts must be submitted through ProgramMaster, the on-line TMS conference and proceedings management system. The system can be accessed at www.tms.org. Using the Meetings & Events pulldown menu, select the Upcoming TMS Meeting for which you wish to submit a symposia proposal or an abstract, and follow the on-line instructions. The society especially encourages the submission of "hot-topic" symposia or special-session proposals on timely or developing subjects. To advance an idea, use the symposium creation form in ProgramMaster. Additional information can be acquired from the TMS Technical Support Services Department, 184 Thorn Hill Road, Warrendale, PA 15086; (724) 776-9000, ext. 212; fax (724) 776-3770.

Electronic Materials Conference 2010 (EMC 2010)

*June 23–26, 2010
Notre Dame, Indiana*

Electronic materials are defined as relating to, produced, or operated by the controlled flow of electrons through a semiconductor, gas, or free space along with those relating to devices, systems, or circuits that employ components such as vacuum tubes, integrated circuits, or transistors in their design. The TMS Electronic Materials Conference is the premier annual forum on the preparation and characterization of electronic materials. Held in conjunction with the Device Research Conference, technical symposia topics include: chemical and biological sensors; materials, interfaces, and integration; dilute nitride semiconductors; epitaxy; flexible and printed thin film electronics; ionic conductors for solid oxide fuel cells and batteries; low-dimensional structures: quantum dots, wires, and wells; nanotubes and nanowires; narrow bandgap semiconductors; antimonides and other materials; organic-inorganic hybrid photovoltaics; solar cell materials and devices; thermoelectrics and thermionics; and several others. **Contact:** TMS Meeting Services, 184 Thorn Hill Road, Warrendale, PA 15086; (724) 776-9000, ext. 243; email: mtgserv@tms.org; www.tms.org/Meetings/Specialty/EMC10/home.aspx.

1st TMS-ABM International Materials Congress

*July 26–30, 2010
Rio de Janeiro, Brazil*

Held in conjunction with 65th Annual Congress of ABM (Brazilian Metallurgical, Materials and Mining Association) and the 18th International Federation for Heat Treatment and Surface Engineering Congress, this inaugural congress will feature seven

proposed symposia covering important contemporary issues in materials science and engineering. This congress builds on the TMS Alliance of the Americas initiative to work together with Society partners in South America and Canada. Technical symposia themes include: Characterization and Application of Biomaterials; Composite Materials; Computational Modeling and Advanced Characterization; Dynamic Behavior of Materials; Light Weight Materials for Transportation; Processing and Properties; Materials and Society; and Mechanical Properties of Materials with Emphasis on Grain-size Effects. A plenary lecture and more than 25 posters will also be presented. **Contact:** Meeting Services, TMS, 184 Thorn Hill Road, Warrendale, PA 15086; (724) 776-9000, ext. 243; e-mail: mtgserv@tms.org; www.tms.org/meetings/specialty/ABM-TMS/home.aspx.

7th Pacific Rim International Conference on Advanced Materials and Processing —PRICM 7

*August 1–5, 2010
Cairns, Australia*

This international conference is the 7th in a series devoted to advanced materials and processing. The conference, which is held every three years, is jointly sponsored by the Chinese Society for Metals (CSM), The Japan Institute of Metals (JIM), The Korean Institute of Metals and Materials (KIM), Materials Australia (MA), and The Minerals, Metals & Materials Society (TMS) and is organized in rotation. The purpose of PRICM is to provide an attractive forum for the exchange of scientific and technological information on materials and processing. The symposia will cover such topics as advanced steels and processing, advanced high temperature structural materials, light metals and alloys, bulk metallic glasses and nanomaterials, advanced ceramics,

energy generation harvesting and storage materials, and others. **Contact:** Ms. Helen Woodall, Materials Australia, Suite 205, 21 Bedford Street, North Melbourne, VIC 3111, Australia; +61-9326-7266; e-mail: helen@materialsaustralia.com.au; www.materialsaustralia.com.au/scripts/cgiip.exe/WService=MA/ccms.r?PageID=19070.

5th International Conference on Very High Cycle Fatigue 2011 (VHCF-5)

*June 27–July 1, 2011
Berlin, Germany*

The Fifth International Conference on Very High Cycle Fatigue resumes the successful series of previous conferences (1998/Paris, 2001/Vienna, 2004/Kusatsu, 2007/Ann Arbor) on the latest very high cycle fatigue research. The objective of the conference is to provide a worldwide platform for scientific communication, discussion and activities for all those interested in both fundamental aspects and practical applications. The conference aims to bring together researchers from various engineering disciplines such as mechanical engineering, civil engineering, power plant engineering, automotive and transportation, aerospace, microelectronics and other branches, all faced with failure phenomena and their prevention, in order to exchange their experiences and to gain more comprehensive understanding. The conference will comprise invited key-note lectures, contributed oral presentations and posters on the following scientific topics: fundamental, physics and mechanisms; parameters; experimental methods, and applications to components and structures. **Abstracts are due October 1, 2010.** **Contact:** Dr. Christina Berger, TU Darmstadt, MPOA u. Inst. Fur Werkstoffkunde, Grafenstr. 2, D-64283 Darmstadt, Germany; +49-615-116-2151; e-mail: berger@mpa-ifw.tu-darmstadt.de; www.vhcf5.de.



TRACE ELEMENT ANALYSIS

5 Day Turnaround

- High Purity Metals & Alloys
- Ceramics
- Glasses
- Semiconductors
- Thick Films
- Carbon, Graphite
- High Temperature Alloys

Utilizing State of the Art Techniques

- Glow Discharge Mass Spectrometry (GDMS)
- Inductively Coupled Plasma Mass Spectrometry (ICPMS)
- Inductively Coupled Plasma Optical Emission Spectrometry (ICP-OES)
- Spark Source Mass Spectrometry (SSMS)
- Combustion and Inert Gas Fusion Methods (LECO)

Northern Analytical Laboratory

13 Delta Drive Unit #4
Londonderry, NH 03053

Tel: 603-434-8400 • Fax: 603-434-8500
E-Mail: NALABS@northernanalytical.com
Website: www.northernanalytical.com

ACT Aluminum Casting Technology, LLC

Professional Consulting Services: Project, Metallurgy, Field Service,
Engineering of Casting Equipment & upstream/downstream Operations

Contact: JOHN V. GRIFFIN, P.E.

7 Lone Cedar Way Office: (1) 201-767-9044
Old Tappan, New Jersey 07675 Fax: (1) 201-750-2279
United States E-mail: johnvj@optonline.net

James E. Hoffmann and Associates Co.
P.O. Box 420545
Houston, Texas USA 77242-0545

JAMES E. HOFFMANN, FIMM, P.E.

CONSULTING EXTRACTIVE METALLURGICAL ENGINEER
NON FERROUS, RARE, AND PRECIOUS METALS

BUS (281) 493-9441 E-MAIL: jehentp@aol.com
FAX (713) 780-0761

Read by thousands
of the field's leading
professionals and
decision-makers,
JOM can deliver an
impressive international
audience, both in print
and online.

The new TMS
Media Kit
is now available.

To request your copy,
contact ads@tms.org

Check out the TMS media kit at
<http://www.tms.org/pubs/journals/JOM/ads.html>

ISO-9001 and ISO-17025 Certified

Analytical Services & Reference Standards
SEM/X-ray, Electron Microprobe, Surface
Analysis (Auger) Metallography, Particle
Size Counting & Surface Roughness

Quantitative analysis of small amounts of material in
concentrations to 10 ppm, surface oxides, stains &
cleanliness, corrosion, diffusion, reverse engineer-
ing, elemental mapping, diffusion gradients (carbon,
nitrogen, etc.) Get your data by e-mail. Digital
micrographs and elemental maps. We manufacture
traceable standards for magnification (SEM, OM,
etc.) and over 240 pure elements, alloys, glasses
and compounds for micro-analysis.

Put our years of experience to work on your specimens!



**GELLER
MICROANALYTICAL
LABORATORY**

426e Boston St. (Rt. 1), Topsfield, MA 01983-1216
978 887-7000 fax: 887-6671 www.gellermicro.com

micron inc.

ANALYTICAL SERVICES

3815 LANCASTER PIKE

WILMINGTON, DE 19805

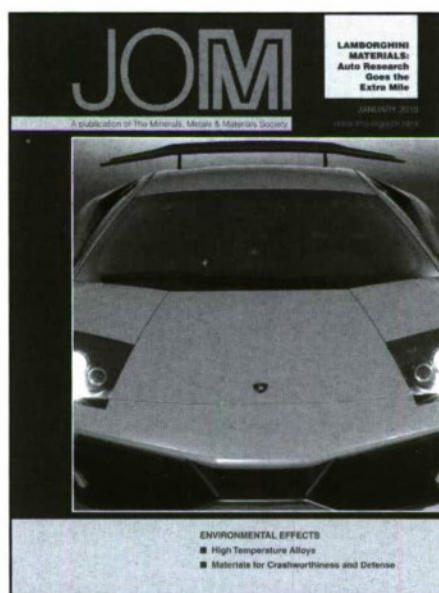
302-998-1184, FAX 302-998-1836

micronanalytical@compuserve.com
WWW.MICRONANALYTICAL.COM

TMS

Your Professional Partner
for Career Advancement

www.tms.org



Thermophysical Properties Instruments & Testing Services

- Thermal Expansion
- Thermal Conductivity
- Thermal Diffusivity
- Specific Heat Capacity
- -180°C to 2800°C Range

Anter Corporation 1700 Universal Road Pittsburgh, Pa 15235-3998
Tel: 412.795.6410 Fax: 412.795.8225 E-mail: sales@anter.com

ISO9001: 2000 Certified
www.anter.com/jom



Worldwide experience in
technology development

FLOGEN Technologies

9 Non-Ferrous and Ferrous Metallurgy, Inorganic and
Organic Chemistry, Environment and InfoTechnology etc
9 Thermodynamic and kinetic quantification of slags,
mattes, metals, etc., smelting, converting and refining
process development and optimization, modeling and
simulation, Atomic Absorption Spectrometry, minor
and trace element analysis, electroanalytical techniques
(biosensors), heavy metal pollution analysis, analytical
quality assurance, mercury speciation, etc.

www.flogen.com

5757 Decelles Ave., Suite 511 Tel: (514) 344-8786
Montreal, Quebec Fax: (514) 344-0361
Canada H3S 2C3 Email: secretary@FLOGEN.COM

MATERIALS SCIENCE

Materials & Metallurgical
Testing, Analysis & Consulting

TEM, SEM, EDX, XRD, WDXRF, AES,
NIR, m-FTIR, PLM/PCM, AA, ICP, GC/MS

Materials Characterization
Metallurgical Analysis

XRD Phase Analysis

Failure Analysis

Product Comparison

Contamination Analysis

Surface Analysis

Forensic Analysis

Chemical Analysis

Mechanical Testing

R&D Support and Consulting

20 Years Of Experience

www.EMSL.com
800.220.3675



Adaptive, Active Air Quality, Environmental Monitoring
Industrial Hygiene, Lead, Mercury, Formaldehyde, Environmental Chemistry
CORPORATE LABORATORY
107 HADDON AVENUE
WESTMONT, NJ



The Minerals, Metals & Materials Society Marketplace is the information resource providing you with a one-stop resource to find many products and information.

www.tmsmarketplace.com

TMS



MULTIVIEW

**Another TMS Member Benefit:
Materials Technology@TMS**

www.materialstechnology.tms.org/TECpage.asp

**Your resource for technology
overviews, news stories, downloadable
resources, and links.**

JOM is looking for volunteer book reviewers for its Book Review Program, which publishes reviews of recent materials science and engineering publications on the JOM web site. Participants keep any book they review, provided a publication-quality review is submitted in a timely manner.

If you'd like to participate, here's how:

- Go to www.tms.org/pubs/journals/JOM/review-request.html
- Read the review program guidelines and submit your request using the form provided
- If your request is approved, JOM will mail you the book
- Go to www.tms.org/pubs/journals/JOM/review-form.html to submit your review within 90 days

Questions?

Telephone (724) 776-9000, ext. 228

Fax (724) 776-3770 • E-mail jom@tms.org

METALLURGIST

GE Transportation

Erie, PA

Provide technical leadership on the selection & processing of materials for the components & systems engineered & produced by GE Transportation. Products include large medium speed diesel engines; electrical traction systems for locomotives, off highway propulsion & gear drive systems

Responsibilities:

- Mat'l selection, mfg methods of engine components & failure analysis of failed components
- Design review processes, identifying risks & ensuring technical quality of engine component/system design
- Extensive knowledge in metal forming/processing (castings, forgings & fabrications), principally ferrous systems & aluminum/copper, mat'ls & process specification authorship for metallic components
- Drive & maintain consistent use of DFSS/DFR methodology

Qualifications:

- BS Metallurgical Eng'gr or Mat'l Science
- Min 5 yrs exp in metallurgical
- Knowledge of Int'l mat'ls & process specifications systems (ASTM, ISO, EN)
- Mat'l labskills: SEM operation, optical microscopy & photography NDE backgrd

GE is working for a better future. Are you ready? For more than 125 years, GE has been respected for its performance & innovative spirit. GE people worldwide are dedicated to turning imaginative ideas into leading products & services that help solve some of the world's toughest problems. Come see what you can achieve with GE Transportation! For more information or to apply, go to www.ge.com/careers & search job number 1162857.

I'VE SPECIALIZED FOR 31 YEARS

in the placement of Metallurgical, Materials, and Welding Engineers in the areas of R&D, Q.C. Production, Sales & Marketing, nationwide. My background as a Met. Eng. can help you! Salaries to \$190K. Fees paid by Co. Call/Send/E-mail Resume:

Michael Heineman, Meta-Find, Inc.; P.O. Box 610525, Bayside, NY, 11361; Phone (212) 867-8100; E-mail mikeh@meta-findny.com; Web: www.meta-findny.com

**If you have a key position to fill,
JOM Classified Advertising can help you
track down that special individual with
the right qualifications and background to
match your needs.**

**Metallurgists • Researchers •
Educators • Managers**

Find the job you're looking for in the
JOM Materials Resource Center.

**Job postings are updated
weekly online at**

<http://www.tms.org/classifieds.html>

Multi-society Publication Underscores MSE Role in Securing Energy Solutions

Lynne Robinson

The importance of materials science and engineering to meeting both short- and long-term energy challenges is the focus of "Advanced Materials for Our Energy Future," a new publication released as a collaborative initiative of TMS, the American Ceramic Society (ACerS), the Association for Iron & Steel Technology (AIST), ASM International (ASM), and project leader, the Materials Research Society (MRS). Developed as a reference tool for policy makers, media professionals, and educators, the booklet provides a broad overview of materials research and development areas that have been identified as having the greatest potential for creating new energy sources or more effectively conserving current ones.

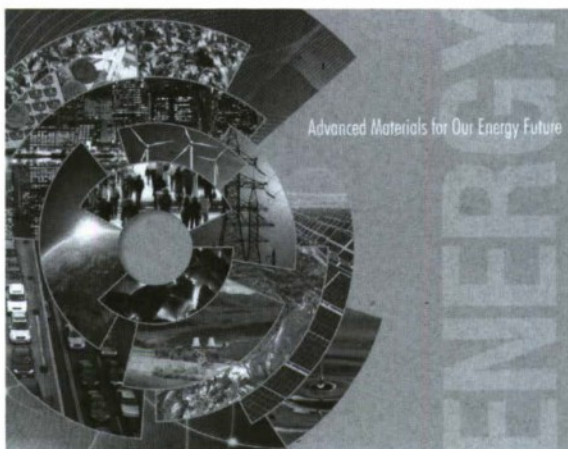
Iver Anderson, senior metallurgist at Ames Laboratory and chair of the TMS Materials and Society Committee, was a member of the joint society committee that researched and prepared the publication. "I believe there is a general misconception by the public that everything has been invented related to energy technologies and it's just a matter of pulling something off the shelf," he said. "A key message we tried to convey is that there are extremely important developments that need to be made in materials science to enable these technologies to go forward."

Other TMS members who served on the "Advanced Materials" committee were Gregory J. Hildeman, formerly of Solar Power Industries, Inc., and Subodh K. Das, Phinix, LLC.

"The collaboration among the committee members from the various societies was excellent," said Hildeman. The end product of the committee's efforts, Hildeman continued, "is an

effective communication tool explaining the important role that materials have played in advancing current fossil and nuclear energy sources, as well as sustainable, renewable energy such as solar, wind, geothermal, biofuels, and hydrogen fuel cells."

Anderson noted that the committee felt it was important to present the



realm of energy possibilities. "There is a wide variety of ways that we can succeed in securing our energy future. The best solution, however, is going to be a set of choices, not just one or two options," he said. "There are very definite plans to accomplish this, but it will only happen with a sustained, long-term research effort."

Participation in the development of "Advanced Materials for Our Energy Future" is one of a series of projects recently undertaken by TMS as part of its strategic commitment to facilitating materials solutions to energy challenges. In February, TMS convened an Energy Materials Blue Ribbon Panel as the first phase of a project commissioned by the Department of Energy (DOE) Industrial Technologies Program (ITP). The Panel's Vision Report, due to be published in July, will identify areas where new materials and processing breakthroughs

can lead to transformational advances in energy efficiency, energy security, and carbon emission reductions. In the second phase of the project, four Technical Working Groups will be formed over the summer to develop roadmaps for each of the cross-cutting materials science and engineering areas identified in the Vision Report. A final report consolidating these roadmaps and addressing interdependencies will be published by the end of 2010.

In a related effort, TMS and ASM International have come together to form the Energy Materials Initiative, a program that utilizes energy education, energy events, and an on-line "Energy Materials Network" to support the exchange of information and ideas on energy materials issues and technologies.

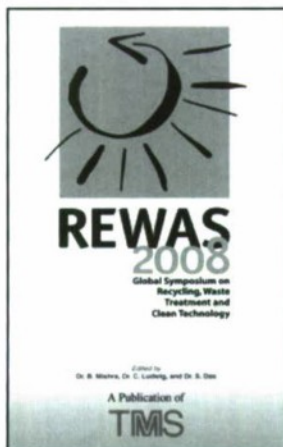
Like the Energy Materials Initiative, "An important element of the 'Advanced Materials' project is the cooperation among the materials societies in such a vital area," said Warren H. Hunt, Jr., TMS executive director. "TMS is committed to working with our sister societies to achieve synergistic benefits for the profession, leveraging our collective 'energy'."

"Advanced Materials for Our Energy Future" was provided to policy makers during Congressional visits in April, with plans for wider distribution in the works. On the potential impact of the publication, Anderson commented, "Hopefully, we have presented these various energy strategies in a way that will enable them to be broadly discussed and eventually will lead to real action in implementing them."

The complete version of "Advanced Materials for Our Energy Future" can be downloaded at energy.tms.org/.

Lynne Robinson is a news and feature writer for TMS.

Visit the Knowledge Resource Center to reserve your copy today!



REWAS 2008: Global Symposium on Recycling, Waste Treatment and Clean Technology

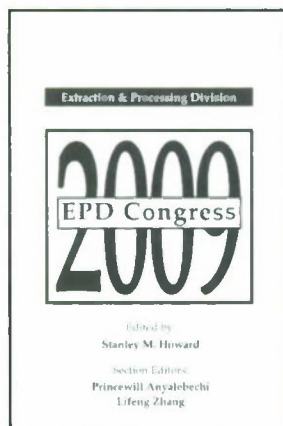
by B. Mishra, C. Ludwig, and S. Das, editors

The 2008 Global Symposium on Recycling, Waste Treatment and Clean Technology (REWAS 2008) is the third in a series of international conferences to address the continuing globalization of environment protection through progress in recycling technology, re-engineering of the production system, and clean technologies. The conference incorporates the Fifth International Symposium on Recycling of Metals and Engineered Materials and R'08 - the World Congress on the Recovery of Materials and Energy for Resource Efficiency. Technical topics covered in the conference proceedings include:

- Aluminum By-product Recovery and Secondary Production
- Automotive Recycling
- Case Studies in the Development of Waste Treatment Technologies
- Clean Technology and Re-engineering of Current Processes
- Composite Materials
- Design and Engineering of Waste Treatment Plants
- Economic Evaluation of Waste Treatment Strategies
- Electronic Waste
- Environmental Issues Related to Waste Storage and Recycling
- Ferrous Metals
- General Recycling and Solid Waste Processing
- Heavy-Metal Containing Waste
- Nonferrous Metals
- Precious and Rare Metals
- Radioactive Waste
- Refractory Metals
- Remediation of Contaminated Soil and Industrial Sites
- Resources, Monitoring and Characterization of Waste
- Treatment of Liquid and Gaseous Effluents
- Waste Conversion and Reutilization

TMS Member price \$64

TMS Student Member price \$49



EPD Congress 2009 (CD-ROM)

by S. Howard, Editor P. Anyalebechi, L. Zhang, Section Editors

This book contains up-to-date information regarding the process metallurgy community, which convened the Extraction & Processing Division Congress at the TMS 2009 Annual Meeting & Exhibition. It covers the science, technology and industrial practice of the processing of ores and the treatment and minimization of wastes. Subjects include advances in roasting and sintering; aqueous processing; energy conservation in metals extraction and materials processing; materials processing fundamentals; pyrometallurgy; recycling; and developments in rare earth science and technology.

TMS Member price \$159

TMS Student Member price \$124

To order these or related publications, contact TMS:

E-mail publications@tms.org • Phone (724) 776-9000, ext. 256 • Fax (724) 776-3770



SIMPLIFIND

Tap into the incredible network of The Minerals, Metals & Materials Society with The Minerals, Metals & Materials Society Marketplace. Powered by MultiView, the Guide gives materials and metallurgy professionals a faster and easier way to find great vendors.

Simplifind your search today at
tmsmarketplace.com.

TMS


MULTIVIEW